Extracellular Stimulation of Individual Electrogenic Cells with Micro-Scaled Electrodes

Von der Fakultät für Elektrotechnik und Informationstechnik
der Rheinisch-Westfälischen Technischen Hochschule Aachen
zur Erlangung des akademischen Grades eines Doktors
der Ingenieurwissenschaften genehmigte Dissertation

vorgelegt von

Diplom-Ingenieur
Stefan Eick
aus Mönchengladbach

Berichter: Universitätsprofessor Dr.rer.nat A. Offenhäusser
Universitätsprofessor Dr.rer.nat W. Mokwa

Tag der mündlichen Prüfung: 7. Januar 2010

There's no thrill in easy sailing when the skies are clear and blue,
there's no joy in merely doing things which anyone can do.
But there is some satisfaction that is mighty sweet to take,
when you reach a destination that you never thought you'd make...

---

author unknown

Abstract

The interface between biological and electronic information processing within bioelectronic hybrid systems is an exciting field of research. From an application point of view, it offers the possibility to develop and improve neuroprosthetic devices, e.g. for medical use. In basic neuroscience it enables the investigation of dissociated neuronal cultures or brain slices to elucidate the development, plasticity, and information processing of neuronal networks. To this end, systems and devices for stable long-term investigations with multiple interfaces for extracellular recording and stimulation on a single-cell level are desirable to gain precise access to the network or tissue. The main focus of this work was to study the extracellular stimulation of individual electrogenic cells *in vitro* with surface-embedded microelectrodes.

For this purpose, a new electrophysiological system, including devices and a versatile and customizable amplifier, was developed. The novel amplifier is comprised of a general main amplifier for impedimetric and electrophysiological experiments and multiple headstages specialized for individual chip types including *multi-electrode arrays* (MEAs) and integrated chips combining stimulation electrodes and recording field-effect transistors. The amplifier was tested and integrated in a patch-clamp setup for intracellular recordings. Microelectrodes with *sputtered iridium oxide films* (SIROFs) for improved stimulation capabilities were developed in an iterative process. With low impedance and high charge storage capacity, the rough and porous SIROF electrodes showed electrochemical properties superior to conventional gold or platinum electrodes. The biocompatibility and stability of the devices was shown by repeated use for cell growth, electrophysiological experiments, and cleaning of the chips.

The new setup and devices were used for experiments with rat cortical neurons and electroactive cell lines. Single Human Embryonic Kidney 293 cells with the $Na_V1.4$ sodium channel could be stimulated to the point of pseudo-*action potential* (AP) excitation in a controlled manner. The data was analyzed and compared to numerical simulations to investigate stimulation mechanisms and the influence of experimental parameters on stimulation success. For the first time, iridium oxide microelectrodes were successfully employed for extracellular stimulation of individual neurons from a dissociated culture. Two basic stimulation mechanisms were identified, which could both lead to a self-amplifying depolarization of the membrane potential and the excitation of APs. In addition, successful

recordings of electrical activity from the HL-1 cardiac myocyte-like cell line were performed.

The developed MEAs and SIROF layers showed excellent electrochemical properties, stability, and biocompatibility, and were successfully applied for extracellular stimulation and recording. Hence, they represent an ideal system for the bidirectional communication with electrogenic cells *in vitro*.

Zusammenfassung

Die Schnittstelle zwischen biologischer und elektronischer Informationsverarbeitung in bioelektronischen Hybridsystemen ist ein faszinierendes Forschungsfeld. Neben medizinischen Anwendungen, wie der Entwicklung und Verbesserung von Neuroprothesen, ermöglicht es grundlegende Untersuchungen an dissoziierten neuronalen Kulturen oder Gehirnschnitten. Ziel dieser Untersuchungen ist es die Entwicklung, Plastizität und Informationsverarbeitung von neuronalen Netzwerken aufzuklären. Hierfür werden stabile Systeme und Bauelemente für Langzeituntersuchungen mit zahlreichen Einzelzell-Schnittstellen für extrazelluläre Stimulation und Ableitung benötigt, um präzisen Zugriff auf das Netzwerk von Zellen oder Gewebe zu erhalten. Im Fokus dieser Doktorarbeit stand dabei die Untersuchung der extrazellulären Stimulation von einzelnen elektrisch aktiven Zellen *in vitro* mit oberflächengebundenen Mikroelektroden.

Zu diesem Zweck wurde ein neues elektrophysiologisches Messsystem, inklusive Bauelementen und einem vielseitigen und anpassbaren Verstärker, entwickelt. Dieser Verstärker besteht aus einem allgemeinen Hauptverstärker für impedimetrische und elektrophysiologische Experimente und mehreren Vorverstärkern. Jeder Vorverstärker ist auf jeweils einen speziellen Chiptyp abgestimmt, wie z.B. Multielektrodenchips (Englisch: *multi-electrode array*, MEA) oder integrierte Chips mit Mikroelektroden für Stimulation und Feldeffekttransistoren für Ableitungen. Der neu entwickelte Verstärker wurde getestet und in einen Patch-Clamp Aufbau für intrazelluläre Ableitungen integriert. In einem iterativen Prozess wurden Mikroelektroden mit einer Iridiumoxidbeschichtung (Englisch: *sputtered iridium oxide film*, SIROF) zur Verbesserung der Stimulationseigenschaften entwickelt. Im Vergleich zu konventionellen Gold- und Platinelektroden hatten die rauen und porösen SIROF-Elektroden eine geringere Impedanz, eine höhere Ladungsspeicherkapazität und damit insgesamt verbesserte elektrochemische Eigenschaften. Durch wiederholte Zellkulturen, elektrophysiologische Experimente und Reinigung konnten die Biokompatibilität und die Stabilität der Chips nachgewiesen werden.

Das neue Setup und die neuen Elektroden wurden für Experimente mit Neuronen aus dem Kortex der Ratte und anderen elektrisch aktiven Zelllinien angewendet. Einzelne *Human Embyronic Kidney 293* Zellen mit dem $Na_V1.4$ Natriumkanal konnten auf kontrollierte Art und Weise bis zur Auslösung von Pseudo-*Aktionspotentialen* (APs) stimuliert werden.

Um Stimulationsmechanismen und den Einfluss von experimentellen Parametern auf den Stimulationserfolg zu untersuchen, wurden die Messdaten analysiert und mit numerischen Simulationen verglichen. Erstmals wurden Iridiumoxidelektroden erfolgreich für die extrazelluläre Stimulation von einzelnen Neuronen aus einer dissoziierten Kultur angewendet. Zwei grundlegende Stimulationsmechanismen konnten identifiziert werden, welche beide zu einer selbstverstärkenden Depolarisation des Membranpotentials und der Auslösung eines APs führen konnten. Zusätzlich wurde erfolgreich elektrische Aktivität von der *HL-1* Herzmuskelzelllinie abgeleitet.

Die entwickelten MEAs und SIROF Schichten zeigten hervorragende elektrochemische Eigenschaften, waren stabil und biokompatibel und wurden erfolgreich für die extrazelluläre Stimulation und Ableitung angewendet. Folglich bilden sie ein ideales System für die bidirektionale Kommunikation mit elektrisch aktiven Zellen *in vitro*.

Contents

Chapter 1

Introduction

> Twenty years from now you will be more disappointed by the things that you didn't do than by the ones you did do. So throw off the bowlines. Sail away from the safe harbor. Catch the trade winds in your sails. Explore. Dream. Discover.
>
> *Mark Twain (American humorist, writer and lecturer, 1835-1910)*

The origins of neuroscience as well as the first description of electrical phenomena can be traced back to the ancient Egyptians and Greeks. The first written reference to the brain in the history of mankind can be found in an Egyptian papyrus from the seventeenth century B.C., which describes the medical case of two patients with skull fractures [1]. The first researcher known to study electrical phenomena was the Greek philosopher Thales of Miletus. Around 600 B.C. he made several observations of electrostatic effects such as the attractive force between hair or other light objects and amber after it was rubbed with a cat's fur [2,3]. The words "electric" and "electricity" both derived from *elektron*, the Greek word for amber. Although the bioelectric effect of shocks by electric fish was already known to the Egyptians around 4000 B.C. [4], it took until the end of the eighteenth century A.D. until a connection between the function of nerve and muscle cells and electricity was found.

In 1791, Luigi Galvani published his finding of frog leg muscle contraction upon touching an exposed nerve and the muscle with a bimetallic rod. The contraction was accompanied by electric sparks, which he assumed originated in the frog leg. He called the phenomenon "animal electricity". His finding was further investigated and partly refuted by Alessandro Volta, who proposed the "metallic electricity" generated at the connection between the two metals as the origin of the electricity. He proposed that the biological tissue only acted as indicator for the electricity stored in the bimetallic system. While Volta's experiments led to his development of the first battery and paved the way for electrical engineering, Galvani can be deemed discoverer of bioelectricity, initiating the field of electrophysiology [5].

One of the greatest achievements in the history of electrophysiology and the understanding of cellular electrical activity was the work of Alan Hodgkin and Andrew Huxley. In 1952, they published a series of articles on the function of the neuronal cell membrane and introduced an electrical equivalent circuit model to describe neural signal generation. The model includes membrane potential dependent conductivities for sodium and potassium ions, which enable the simulation of the time course of an action potential [6–10]. Hodgkin and Huxley proposed the existence of ion channels, which was finally confirmed by the development of the patch-clamp technique and its application for current measurements on single ion channels in 1976 by Erwin Neher and Bert Sakmann [11]. For their work, Hodgkin and Huxley as well as Neher and Sakmann were awarded with the Nobel Prize in Physiology or Medicine in 1963 and 1991, respectively.

Although the patch-clamp technique is still state-of-the-art and the method of choice for investigations of single cells and very small cellular networks, it also has some limitations. First of all, the technique is invasive and leads to cell death after a very short experimental time, usually less than one hour. Furthermore, patch-clamp experiments are performed with macroscopic measurement probes, which require a bulky mechanical setup and hence limit the number of simultaneously measurable cells. For those reasons, the patch-clamp technique cannot be utilized for long-term measurements or investigations of more than a couple of cells. However, time and multiple recording sites are necessary to understand the development, plasticity, and information processing of neuronal networks, or even more abstract mechanisms such as memory formation or pattern recognition. Enabled by advances in the semiconductor industry, new planar chips with a high number of sensors in the micrometer scale were developed and further improved for electrophysiological investigations of larger networks of neurons over periods of days, weeks, or even months. In the 1970s, *multi-electrode arrays* (MEAs), usually composed of structured thin conducting layers on silicon or glass substrates, were developed and used for extracellular recordings from cultured cells *in vitro* [12, 13].

About the same time, an alternative sensor approach with arrays of *field-effect transistors* (FETs) was introduced [14] and utilized for electrophysiological measurements [15, 16]. The first FET recordings from single neurons were achieved in the 1990s [17, 18]. FETs are active devices that can detect extracellular signals via a non-ohmic charge transfer, which changes the current flow through the transistor. While the first FETs were silicon-based devices, other materials such as aluminum gallium nitride [19] and surface-conductive diamond [20] have been developed and applied for extracellular recording, as well. Recent developments in the field of FETs include silicon nanowire transistors [21–23] and highly integrated transistor arrays produced in *complementary metal-oxide-semiconductor* (CMOS) production processes with on-chip signal amplification and processing [24, 25].

Despite their promising characteristics for recording devices and compatibility to highly efficient CMOS production processes, FETs have one severe disadvantage in comparison to microelectrodes. In order to allow a thorough investigation and manipulation of neuronal networks, it is necessary to establish devices for the bidirectional communication with the cell, including extracellular stimulation. Although excellent studies on the capacitive stimulation of electrogenic cells with electrolyte-oxide-semiconductor capacitors have been conducted [26–30], this method still requires separate devices for stimulation in addition to the recording FET. Novel approaches for truly bidirectional devices such as silicon nanowire transistors [21] or *floating-gate* FETs [31] are still in their infancy and not regularly used. On the other hand, MEAs have already been established for electrophysiological studies with extracellular recording and stimulation of dissociated networks of neurons [32–38], brain tissue slices [39–42], and retina explants [43, 44]. Nevertheless, continuous research and development is aimed at further improving and tapping the full potential of MEAs as devices for bidirectional communication with neurons.

Recently approached technological challenges in the field of MEAs include CMOS-based high-density arrays with on-chip signal amplification and processing [45–47], three-dimensional sensor arrays [41], as well as new electrode materials and surface modifications for improved electrochemical properties. Novel electrode materials or surface modifications such as deposited carbon nanotubes [48–50] or electrically conducting polymers [51, 52] are being developed to achieve electrodes with a low impedance and a high charge storage capacitance. Standard materials like gold, platinum, and the transparent indium tin oxide - in their plain or platinized forms - have mostly been superseded by electrode materials such as *titanium nitride* (TiN) or *iridium oxide* (IrO_x), which combine excellent electrochemical characteristics and high mechanical stability to withstand cleaning procedures. While TiN has already become a standard electrode material for bidirectional electrophysiological investigations on the level of single cells or networks of neurons *in vitro* [37, 40, 53, 54], the usage of IrO_x has been focused on the development of stimulation electrodes for *in vivo* applications in the central or peripheral nervous system and especially the retina [55, 56]. A comparison to TiN revealed equivalent or even superior electrochemical properties of IrO_x as an electrode material for safe stimulation [57].

Due to the immense progress in electronic technology and computational methods for data storage and analysis, significant advances towards understanding network electrophysiology or even complex brain operations and functions have recently been made [58]. Furthermore, the research on MEAs also inspired the development of neuroprosthetics such as cochlea implants [59,60], retina prostheses [61], and deep brain stimulators [62,63]. Nevertheless, the research and development of new methods in neuroscience is still stimulated and driven by the desire to understand complex biological processes in the brain and com-

bining the strengths of information processing in biology and advanced microelectronic systems. For the realization of advanced bioelectronic applications such as specialized and highly sensitive biosensors or prostheses for the restoration of human senses or limbs, it is not only necessary to investigate biological signaling in neuronal networks. It is equally important to understand the interfaces between electrodes and individual cells and to develop new devices with improved properties for stimulation of and recording from dissociated cultures, tissues slices, or complete organs.

The main goal of this thesis was to develop a new system for the extracellular stimulation of electrogenic cells *in vitro*. This includes novel MEA chips and an electrophysiological setup with a new amplifier system in hard- and software. The MEAs produced contain an array of 64 gold microelectrodes with a diameter of 50 µm and *sputtered IrO_x films* (SIROFs) for reduced impedance and improved charge storage capacity. In the scope of a research project, these SIROF stimulation electrodes were integrated with recording FETs in one chip for the bidirectional interfacing of cells. A versatile amplifier system, which can be used for electrophysiological experiments with MEAs, FET chips, and combinations of both, was designed for maximum flexibility and number of applications with a single apparatus. The new system was then applied for the stimulation of individual cells from a *Human Embryonic Kidney 293* (HEK293) cell line and rat cortical neurons with simultaneous intracellular recordings using the patch-clamp method. The acquired data was analyzed and compared to simulations to investigate stimulation mechanisms and the influence of experimental parameters on the stimulation success.

This thesis is structured as follows: **Chapter 2** presents the electrophysiological fundamentals of neuronal cells and a basic introduction to the intra- and extracellular methods available to communicate with those cells. In the last section, the model for extracellular stimulation and a numerical solution used in this thesis for the simulation of the passive effects of stimulation pulses on the cell membrane is introduced. **Chapter 3** deals with the design and characterization of the various MEAs and the chips integrating microelectrodes and FETs, which were produced and used in the scope of this thesis. In the first two sections of **Chapter 4**, two amplifier systems and their respective measurement setups are introduced. These two systems are the basis for the newly developed multifunctional amplifier system, which is presented with the corresponding electrophysiological setup for stimulation experiments in the third section. **Chapter 5** gives the results and discussions of the electrophysiological experiments performed in this thesis, including the successful stimulation of rat cortical neurons. Also, the results and implications of the simulations of the passive responses to extracellular stimulation and the comparison to measurements with HEK293 cells are presented here. Finally, **Chapter 6** summarizes the conclusions of this thesis and gives an outlook on future system improvements and applications.

Chapter 2

Fundamentals and Theory

> Success is neither magical nor mysterious. Success is the natural consequence of consistently applying the basic fundamentals.
>
> *Jim Rohn (American entrepreneur, author, and motivational speaker, 1930-)*

This chapter aims to introduce the fundamental biological and (bio-)physical basics in this thesis. Since the investigated topic is situated at the interface between neurobiology and microelectronics, the fundamentals can only give a brief overview of several aspects of this interdisciplinary field. Nevertheless, references will help the reader to find literature for a deeper study of fields of particular interest.

The first two sections of this chapter will deal with *electrogenic* cells, the basics of *electrophysiology* and the standard intracellular electrophysiological measuring method. In the third section, the electric properties of interfaces between solids (especially metals) and liquids will be elucidated. The final two sections will deal with the extracellular devices and methods to electrically interface cells.

2.1 Electrophysiology and Electrically Active Cells

Electrophysiology deals with the study of electrical properties and the measurement of voltage change or electric current in biological systems. This includes a great variety of systems such as single ion channels in cell membranes, individual or networks of electrically active cells, tissues or even complete organs like the brain or the heart. For the investigation of the interface between cells and microelectronics, it is very important to understand the fundamentals underlying the electrophysiological mechanisms in individual cells.

In this work, several electrically active cell types (rat cortical neurons and cell lines) were used for electrophysiological experiments. The cell types used and their culture, including protocols, are introduced and presented in Appendix C. Since biological information

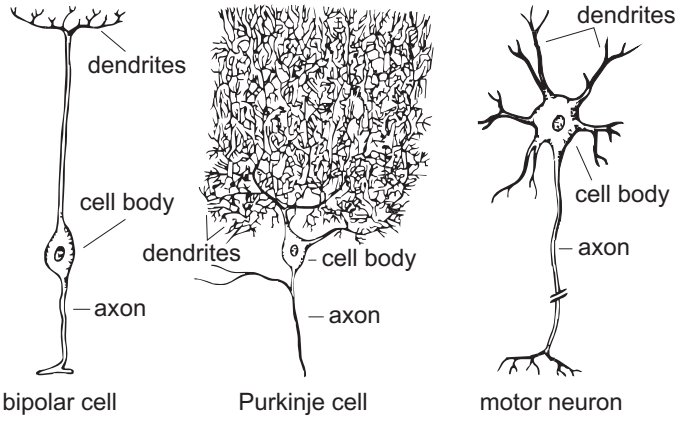

Figure 2.1: Three neuron types illustrating the various morphologies of nerve cells with different functions. The figure was adapted from [1].

processing is mostly mediated by the interaction between neuronal cells, the basic mechanisms of neuronal electrical activity are well established and will also be introduced here. The basic task of neuronal cells and especially networks of neurons is to receive, process, store, and relay signals [64, 65]. The complexity of these neuronal networks varies widely from organism to organism, with the *central nervous system* (CNS) of vertebrates reaching an extraordinary complexity with a very high number of neurons. For example, the human CNS consisting of the brain and the spinal cord, contains approximately 100 billion neurons [66], which each are connected to up to 100,000 other neuronal cells [1].

All neurons can basically be described as consisting of four functional units: the *dendrites* form the receptive input for signals from other cells, which are processed in the *soma* or cell body and relayed along the *axon*. Finally, the *axon terminals* form the signaling output of the neuron and pass information about the processed data to subsequent cells. Axon terminals and dendrites come together to form *synapses*, the interfaces for data processing from one cell to another. Although these basic functional units are common to all nerve cells, the specific morphology of the various types of neurons can vary significantly with the function of the cell. While the size of the soma varies in a rather narrow range from 10 µm to 100 µm, the number of connections to other cells and especially the length of the axon can differ greatly, from 100 µm to 1 m [66]. Three different kinds of neurons are depicted in Figure 2.1 to exemplify these differences. In the retina of the eye, bipolar cells gather information from the sensory cells and function as primary link to the processing brain areas. In contrast, Purkinje cells process inputs from a large number of nerve cells, while motor neurons are instead specialized to quickly transport information over long distances from the CNS to innervated muscles. Despite those differences in morphology and function, all neurons share the same fundamental principles concerning the generation and processing of electric potentials and pulses. This electrical activity and information processing of cells will be briefly introduced in the following subsections.

2.1.1 Cell Membrane and Ion Channels

All cells are surrounded and separated from their extracellular environment by an approximately 5 nm thick cell membrane [64] (Figure 2.2), which is mainly formed by a bilayer of *phospholipids* - *amphiphilic* molecules with a *hydrophilic* head and a *hydrophobic* tail group. Because of their hydrophobicity, the unpolar tails align to each other and build the center of the membrane, while the hydrophilic heads point towards the outside and build the interface to the liquid solution on both sides of the membrane. Because of the hydrophobicity of the inner layer, the membrane is an impermeable barrier to ions, water and hydrophilic molecules. Nevertheless, movement of most membrane compartments within each or both layers is not inhibited and results in the image of the cell membrane as a two dimensional liquid [64].

In addition to the phospholipids, the membrane also integrates proteins and, on a small scale, carbohydrates. The proteins can either be attached to the hydrophilic head groups as peripheral proteins, or span through the whole membrane as integral proteins [66]. Some of these integral proteins enable the transport of various substances like water, nutrients, waste, signaling molecules or ions through the membrane, resulting in a semi-permeable barrier between the intracellular and the extracellular domain. Particularly, the permeability of the cell membrane to inorganic ions (K^+, Na^+, Cl^-) is mediated by a protein group called ion channels (Figure 2.3) and is important for the electroactive properties of cells. Most importantly, the permeability for a certain ion species is not necessarily constant over time, but can vary significantly by opening or closing of specific ion channels. This opening and closing can be mediated by several different cues or *gating mechanisms* of ion channels [1,64]. The two most important gating mechanisms of ion channels are introduced in Figure 2.3. A *ligand-gated* ion channel is depicted on the left side of the figure. The ion channel opens when a certain messenger molecule (the ligand) binds to a highly specific receptor in a pocket of the ion channel. This binding causes a conformational change of the channel, opening it for the passage of one or several ion species. *Voltage-gated* ion channels on the other hand experience a conformational change of the channel domain, when the

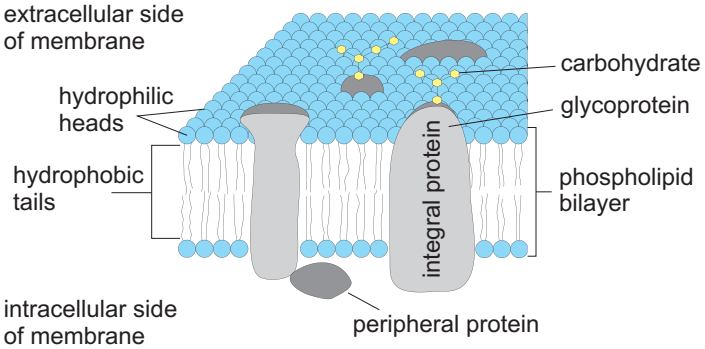

Figure 2.2: Simplified schematic of a vertebrate cell membrane in cross section. Integral proteins incorporated into the phospholipid bilayer allow the highly selective passage of water, ions and larger molecules. The figure was taken from [25].

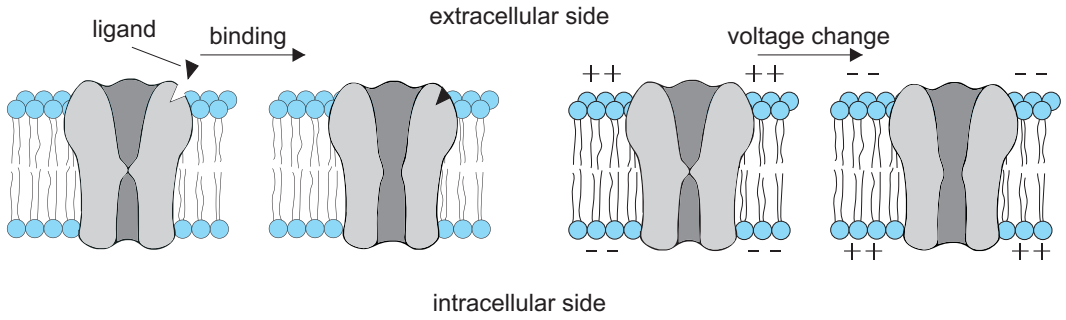

Figure 2.3: Schematic of the two main gating mechanisms for ion channels. The ion channel on the left side opens when a special mediating molecule called ligand binds to a receptor on the channel protein. A potential change across the cell membrane causes the opening of the channel on the right. The figure was adapted from [1].

electric potential across the membrane close to the channel is inverted. Both of these kinds of ion channels are very important for the electric activity and its propagation in neuronal cells, as will be explained in the next subsections.

Most ion channels utilize varying pore sizes, charge distributions and binding sites in the channel to guarantee a high specificity of the permissible ions [1, 64]. While the transport through ion channels is purely passive and follows the electrochemical gradient of the ion species, ion pumps can also actively transport ions against their electrochemical gradient under consumption of energy.

2.1.2 Resting Potential

A cell's *membrane potential* (v_M) is defined as the difference between the intracellular and the extracellular potential (v_{IC} and v_{EC}, respectively). For most electrophysiological measurements, the extracellular space is held at the reference potential $v_{EC} = 0$ V, resulting in an equivalence of membrane potential and intracellular potential:

$$v_M = v_{IC} - v_{EC} \Rightarrow v_M = v_{IC}. \tag{2.1}$$

Investigating the membrane potential of a neuron, one usually finds the cell in a resting state with a constant negative intracellular potential. This *resting potential* can be explained by the semi-permeable nature of the cell membrane and differences in the ion concentration inside and outside of the cell, causing a charge separation with excess negative charges inside and positive charges outside of the cell. Table 2.1 gives some typical values for important *ion concentrations* inside and outside ($[i]_{in}$ and $[i]_{out}$, respectively) of a mammalian neuron. Although the concentration differences between intra- and extracellular regime for individual ion species can be very high, the total charge difference is close to zero.

Ion species	Intracellular concentration (mmol/l)	Extracellular concentration (mmol/l)
Na^+	15	150
K^+	150	5
Ca^{2+}	10^{-4}	2
Cl^-	10	120
A^-	100	0

Table 2.1: Typical intra- and extracellular concentrations of important ion species for a mammalian neuron. A^- represents large negatively charged organic molecules including amino acids for which the cell membrane is impermeable [65]. Despite the high concentration differences between intra- and extracellular regime for individual ion species, the total charge difference is close to zero.

Considering a cell membrane permeable for only a single *ion species* i, an electric potential would be necessary to maintain an imbalance of the ion concentration inside and outside of the cell. In steady state, this *equilibrium potential* or *Nernst potential* (E_0^i) causes a flux of ions which exactly counteracts the osmotic ion flow along the concentration gradient. The *Nernst equation* can be used to calculate the equilibrium potential:

$$E_0^i = -\frac{RT}{z^i F} \cdot \ln \frac{[i]_{in}}{[i]_{out}}, \tag{2.2}$$

where R and F are the universal gas constant and the Faraday constant, T is the absolute temperature, and z^i the valence of the ion species i. For the special case of only a single involved ion species with given constant ion concentrations, this equilibrium potential would be equivalent to the resting potential. If more than one ion species is involved, it has to be considered how well the different types of ions can pass the cell membrane. The ion with the highest *permeability* (P^i) has the biggest impact on the combined resting potential.

For a neuronal cell in the resting state, the permeability is highest for potassium ions. Taking the values from Table 2.1, an equilibrium potential of -91.2 mV with respect to a grounded extracellular regime can be calculated at a temperature of 37 °C. However, if the real resting potential is measured experimentally, it is usually found to differ from the equilibrium potential for K^+ ions by several millivolts. The *Goldmann-Hodgkin-Katz equation* can be used to get a much better estimation of the experimental membrane potential at rest by considering more than one ion species and their respective permeabilities:

$$v_M = -\frac{RT}{F} \cdot \ln \frac{P^K[K^+]_{in} + P^{Na}[Na^+]_{in} + P^{Cl}[Cl^-]_{out}}{P^K[K^+]_{out} + P^{Na}[Na^+]_{out} + P^{Cl}[Cl^-]_{in}}. \tag{2.3}$$

In literature [1], a typical ratio of 1:5:20 for permeabilities for sodium, chloride and potassium respectively can be found in the resting state.

Before moving on to the mechanism of signal generation in neurons, one important remark has to be stated. For the preservation of the resting potential, no energy is con-

sumed since no net charge transfer takes place. Nevertheless, the initial establishment of the ion imbalance can only be achieved by consumption of energy [66]. This is done by one of the previously mentioned ion pumps, which continuously transports potassium ions into the cell and sodium ions out of the cell. Under decomposition of one *adenosine triphosphate* (ATP) molecule (an energy reservoir of the cell), the electrogenic *sodium-potassium-exchanger* transports three sodium ions and two potassium ions against their electrochemical gradient through the cell membrane [64]. This mechanism is also used to reestablish the initial concentrations if the membrane potential is disturbed or altered.

2.1.3 Action Potentials

Considering just the cell's resting potential, a transport or processing of signals cannot be explained. *Action potentials* (APs) [1] are ion-mediated electric pulses that occur at local areas of a cell membrane and can propagate along the membrane to relay information. An action potential (Figure 2.4) can occur, when the membrane potential is increased towards more positive values (*depolarization)* from the resting potential, which is usually between -60 mV and -70 mV for neurons [1]. Upon reaching a certain threshold voltage, fast voltage-gated sodium channels in the cell membrane open, rapidly increasing the permeability of the cell membrane for sodium ions. This leads to a fast influx of sodium along its electrochemical gradient into the cell, further depolarizing it towards the equilibrium potential of sodium (approximately +60 mV). At the same time, but with slower time dynamics, voltage-gated potassium channels also open, causing a slower and prolonged efflux of potassium ions out of the cell. While the potassium permeability stays increased for several milliseconds, the fast sodium channels close again very rapidly and therefore stop the further influx of sodium ions into the cell. Instead, the ongoing efflux of potassium ions causes a *repolarization* of the membrane potential towards, or even beyond (*hyperpolarization*), the initial resting potential, until also the potassium channels slowly close again. After closing, the fast sodium channels inactivate and cannot open again (*refractory period*) until the initial resting potential is reinstated by ion diffusion and transport of sodium and potassium ions by ion pumps like the sodium-potassium exchanger.

In summary, a neuronal AP is a characteristic of the cell membrane and occurs as an inversion of the membrane potential and recovery to its initial state during a time period of just a few milliseconds. Additionally, APs follow the *all-or-nothing principle*, meaning that any depolarization above the threshold causes the excitation of a complete AP with full amplitude (as long as the membrane is not in the refractory period). A subthreshold depolarization, on the other hand, does not cause an AP and just disappears by ion diffusion within a short time period.

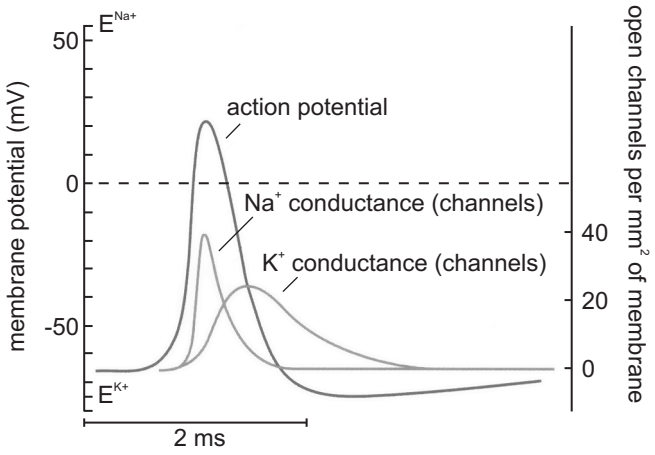

Figure 2.4: Membrane potential and conductances for sodium and potassium ions during a neuronal action potential. The figure was adapted from [1].

In 1952, Hodgkin and Huxley introduced an equivalent circuit which can be used to model the electrical behavior of the cell membrane [10]. An expanded version of the original circuit (called *Hodgkin-Huxley element*) is depicted in Figure 2.5.

Since the cell membrane itself is a barrier to ions, it acts as a capacitor to separate charges with the *membrane capacitance* (C_M). The equivalent circuit includes ionic currents for the different ion species i, which are modeled by voltage sources equal to the respective equilibrium potentials (E_0^i) and resistors with a conductance (G_M^i) representing the permeability of the membrane for the ion species. Since the permeability for sodium and potassium ions varies significantly with the opening and closing of the respective ion channels (see Subsection 2.1.1), the conductivities for sodium and potassium ions are modeled as adjustable resistors. The currents for all other ion species including chloride are summed up as leakage currents with a constant conductance (E^L, G^L). Finally, two current sources (i^{K+}, i^{Na+}) are included to represent the sodium-potassium exchanger, which actively transports sodium and potassium ions through the cell membrane. The membrane capacitance and conductivities are usually given in specific values, which are normalized

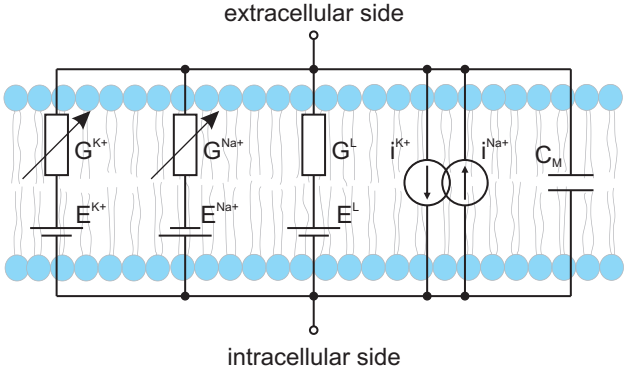

Figure 2.5: Equivalent circuit for the electric properties of a neuron's cell membrane. The basic circuit was originally proposed by Hodgkin and Huxley [10]. Two current sources were added to take into account the sodium-potassium exchanger. The figure was adapted from [25].

by the area of the cell membrane (A_M):

$$c_M = \frac{C_M}{A_M}, \tag{2.4}$$

$$g_M^i = \frac{G_M^i}{A_M}. \tag{2.5}$$

The complete specific membrane conductivity can then be calculated as:

$$g_M = \sum_i g_M^i. \tag{2.6}$$

A typical value for the specific membrane capacitance is $c_M = 1\ \mu\text{F/cm}^2$ [1]. While an artificial lipid bilayer without any proteins proves to be a very good insulator ($g_M = 10\ \text{nS/cm}^2$), the specific conductivity of natural cell membranes with membrane proteins can vary from $g_M = 100\ \mu\text{S/cm}^2$ to $g_M = 1\ \text{S/cm}^2$ [67].

2.1.4 Signal Propagation and Processing

APs are a characteristic attribute of neuronal cell membranes, which occur locally at a certain fraction of the membrane. However, neuronal functions such as signal transport and processing require the propagation of the AP along the membrane, which is possible by *electrotonic conduction*. When the membrane has been depolarized to the point of AP excitation at one point on the axon, the depolarization passively spreads to nearby areas along the axon. This again causes the adjacent membrane areas to also reach the threshold of AP generation. In this way, action potentials can automatically spread along the whole length of an axon and thus transport the signal through the cell [1]. A one-directional signal transmission and suppression of signal oscillations is established by the refractory period at the end of an AP, which prevents a direct second excitation shortly after an AP has passed an area of the axon.

The electrotonic conduction can only explain how an AP propagates within one cell, but not between cells, since there is no direct connection of the cytoplasm. In order to transport a signal between two neurons, *chemical synapses* transform the electrical signal into chemical transmitters, which then transport the signal to another neuron as depicted in Figure 2.6.

At a chemical synapse, two neurons are separated by a *synaptic cleft* with a size of about $20 - 40$ nm [1], interrupting the direct electrotonic transmission of a signal. When the AP arrives in the axon terminal of the *presynaptic cell*, voltage-gated calcium channels are opened, causing an influx of Ca^{2+} ions into the cell. The rising calcium concentration

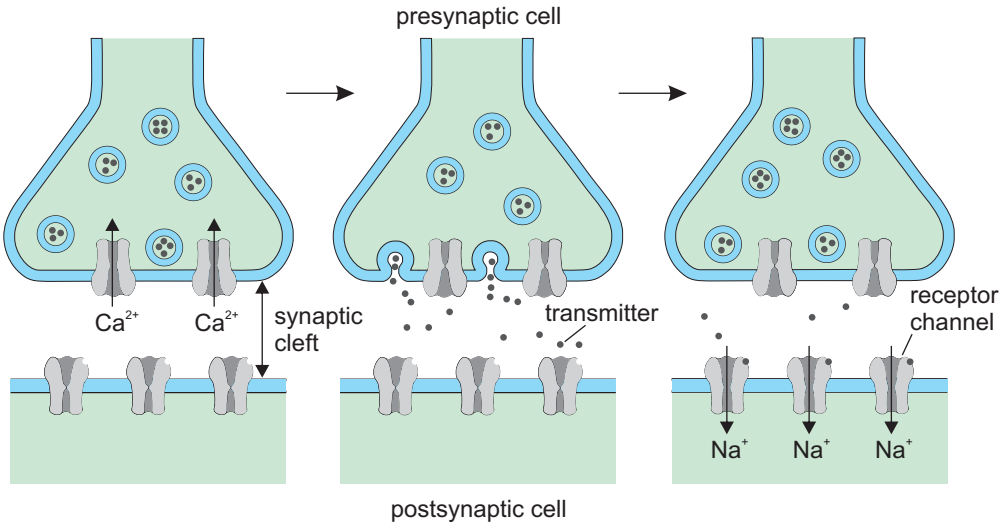

Figure 2.6: Unidirectional signal transmission from a presynaptic neuron to a postsynaptic cell by a chemical synapse. The electric signal is transformed to a chemical signal by neurotransmitter release at the presynaptic membrane. By diffusion, the transmitters reach the postsynaptic membrane and cause opening of ion channels. By influx of positively charged ions, the postsynaptic membrane is depolarized causing an electric propagation of the signal. The figure was adapted from [1].

causes the fusion of vesicles containing *neurotransmitter* with the presynaptic membrane. The neurotransmitters are released into the synaptic cleft and diffuse to the membrane of the *postsynaptic cell*, where they can bind to ligand-gated receptor channels. Depending on the kind of synapse, the channels either open or close and increase or decrease the conductance of the postsynaptic membrane for a depolarizing or hyperpolarizing ion species. In Figure 2.6, the receptors open a sodium channel, which causes a depolarizing influx of sodium ions, which can trigger signal propagation in the postsynaptic cell. This form of signal transmission between cells is purely unidirectional, and the original state of the synapse can be reestablished by active reuptake of the neurotransmitters by the presynaptic cell. The speed of synaptic transmission at a chemical synapse is limited by the diffusion and the reuptake of the neurotransmitters. This *synaptic delay* is on the order of a few hundred microseconds up to several milliseconds [1].

By the combination of several depolarizing (*excitatory*) or hyperpolarizing (*inhibitory*) synapses, signal processing is possible. Within the dendritic tree and the soma of a neuronal cell, the excitatory and inhibitory signals from up to 100,000 synapses can be summed and processed to a combined output signal of the cell. Additionally, weighting of the different inputs by differently developed synapses (e.g. with a varying amount of released neurotransmitters) is also possible. The signal summation is again done by electrotonic conduction of all the input signals on the way to the soma. At the *axon hillock* (were the axon starts at the cell body), the summed signals are transformed into an outgoing train

of APs [1]. A higher sum of input signals transforms into a higher AP output frequency. Nevertheless, the maximum output frequency is limited by the refractory period of the cell membrane.

Finally, it should be mentioned that there also exist *electrical synapses*, where a direct connection between two adjacent cells is established by so-called *gap junctions*. In contrast to chemical synapses, these synapses are usually bidirectional and almost without any delay.

2.2 Intracellular Recording and Stimulation

The standard electrophysiological method for recording and control of electrical activity in neurons and other electrogenic cells is the *patch-clamp technique*. It was developed in the 1970s by Erwin Neher and Bert Sakmann [11, 68].

There are three configurations of the patch-clamp technique for the measurement of single channel activity (*cell-attached*, *outside-out*, or *inside-out*), which are explained in the literature in detail [69]. However, since all the measurements done in this work were made to analyze the activity of the complete cell, only the *whole-cell* configuration will be explained here (Figure 2.7).

As a first step, the micropipette is filled with a patch solution, which resembles the intracellular fluid of the cell. After inserting a *silver/silver chloride* (Ag/AgCl) patch electrode, overpressure is applied to the micropipette to prevent any influx of extracellular fluid or contamination of the micropipette tip with dust or dirt particles. While approaching the cell with micromanipulators under optical control with a microscope, the resistance between the patch electrode and a second Ag/AgCl wire immersed in the extracellular electrolyte solution is continuously monitored. This bath electrode, or reference electrode, is used to ground the electrolyte solution. The measured value for the resistance is in the range of a few megaohms and mainly reflects the resistance against the ion flux through the micropipette tip. Therefore, the value depends on the size of the pipette opening. As soon as the tip gets in close proximity to the cell membrane (Figure 2.7.a), an increase of the resistance due to the partial coverage of the pipette opening and a slight infolding

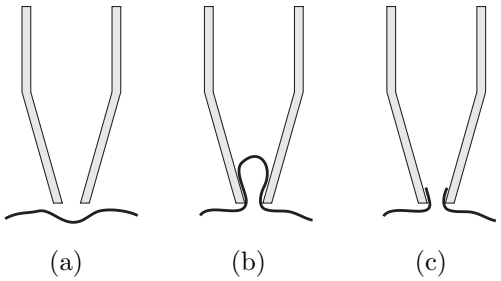

Figure 2.7: Configuration of the patch-clamp pipette at different stages in establishment of the whole-cell configuration. The cell membrane is approached, until a slight indentation in the membrane can be observed (a). In the cell-attached configuration (b), the membrane is sucked into the pipette and finally ruptured for the whole-cell mode (c).

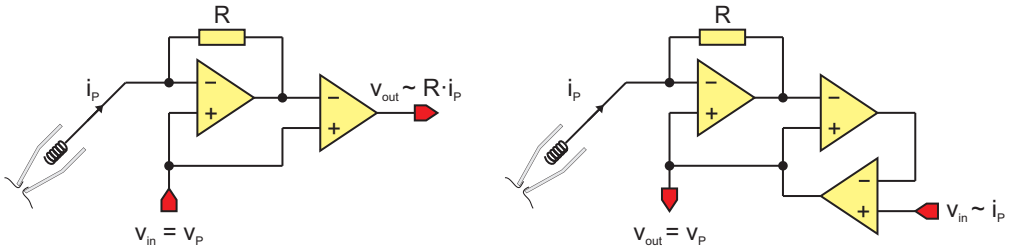

(a) voltage-clamp (b) current-clamp

Figure 2.8: Simplified electronic circuits for the voltage- (a) and current-clamp (b) mode for electrophysiological measurements with the patch-clamp technique. The Figures were adapted from [69].

of the membrane can be observed. At that point, the overpressure is released, causing the membrane to be sucked into the opening of the micropipette (Figure 2.7.b). This complete coverage of the pipette opening causes the so-called *giga seal*, the increase of the resistance to several gigaohms. In this cell-attached configuration, the membrane patch in the pipette opening can be ruptured by either shortly and carefully applying underpressure or a voltage pulse to the patch pipette. If the cell is not damaged by this process, the final whole-cell configuration is reached, where the intracellular space is directly contacted and ionic currents through the whole cell membrane can be measured (Figure 2.7.c).

Once the whole-cell configuration is achieved, two basic measurement modes can be used for the electrophysiological analysis of the cell (Figure 2.8). In the *voltage-clamp* (VC) mode (Figure 2.8.a), the membrane potential of the cell is clamped to the user-defined *pipette potential* (v_P) by an *operational amplifier* (OPA). The current which flows through the cell membrane also flows through the patch electrode (*pipette current* i_P) and is converted into an equivalent output voltage by a differential amplifier. This configuration is usually used to investigate the current responses of a cell to defined changes in the membrane potential. In the *current clamp* (CC) mode (Figure 2.8.b), another OPA is used to modify the circuitry in a way that the pipette (and membrane) current is clamped to a user-defined value. In this case, the output voltage of the differential amplifier is used as the controlled value, which is proportional to the desired pipette current. The output voltage of this circuit is now proportional to the pipette (and membrane) potential. The CC mode is usually used to investigate action potentials of a cell as a response to injected current.

It has to be mentioned that the complete circuitry of a patch-clamp amplifier is much more complex and includes compensation circuitry for several parasitic parameters of the experimental setup. A good introduction to the patch-clamp technique with suggestions for further reading is given by Numberger and Draguhn [69] or in the “Axon Guide” [70].

2.3 Solid/Liquid Interfaces

In order to understand the working principle of metal electrodes in electrolyte solutions, we first have to look at the fundamentals of the solid/liquid and especially the metal/electrolyte interface. Once a metal comes into contact with an electrolyte solution, an interface between the solid and the liquid phase is formed. On the one hand, the metal's chemical equilibrium is changed from the initial state in vacuum, and a new equilibrium has to be reached. On the other hand, the isotropy of the bulk electrolyte solution is disturbed by the introduction of a solid boundary, since any ion or dipole close to the interface will orientate differently than in the bulk solution.

Several models have been proposed for the resulting structure at the interface between liquid and metal. In 1879 [71], Helmholtz proposed the adsorption of a layer of ions from the electrolyte at the metal surface, which compensates any surface charge of the metal. The resulting *electrical double layer* or *Helmholtz layer* is located directly at the surface of the metal with an approximate dimension of about 0.1 nm. It can be modeled as a capacitor with a *Helmholtz capacitance* (C_H). However, electrochemical measurements showed that this capacitance is not constant in a real experiment, but depends on the *surface potential* (Φ_0) of the metal.

At the beginning of the last century, Gouy and Chapman further modified the model by considering the thermal movement of ions [72, 73]. Instead of a capacitor-like double layer, they proposed a diffuse layer of ions with local anion and cation concentrations, which depend on the *potential* (Φ) in the solution. In a first approximation, the potential itself exponentially decays with the distance from the surface in accordance to a length constant called *Debye length* (L_D). The Debye length is a measure for the spatial expansion of the diffusive layer and depends on the *temperature* (T) and the *bulk ion concentration* (n_0):

$$L_D \sim \sqrt{\frac{T}{n_0}}. \tag{2.7}$$

The diffuse layer proposed by Gouy and Chapman also results in a charge separation that again can be modeled as a capacitor, this time with the *Gouy capacitance* (C_G). Although the Gouy-Chapman model qualitatively describes a dependence of the capacitance on the potential, it is limited to monovalent salt solutions with low concentrations.

A more general model was introduced by Stern in 1924, who combined both previous models to the *Gouy-Chapman-Stern model* (Figure 2.9) with an inner *Stern layer* (corresponding to the Helmholtz layer), and an outer diffusive layer [75]. He furthermore pointed out that the position of the Helmholtz layer will vary with the ion species attracted to the surface. Some ions may be able to lose their water molecule sheaths and approach the surface much closer than other ions. Therefore, two layers were introduced representing

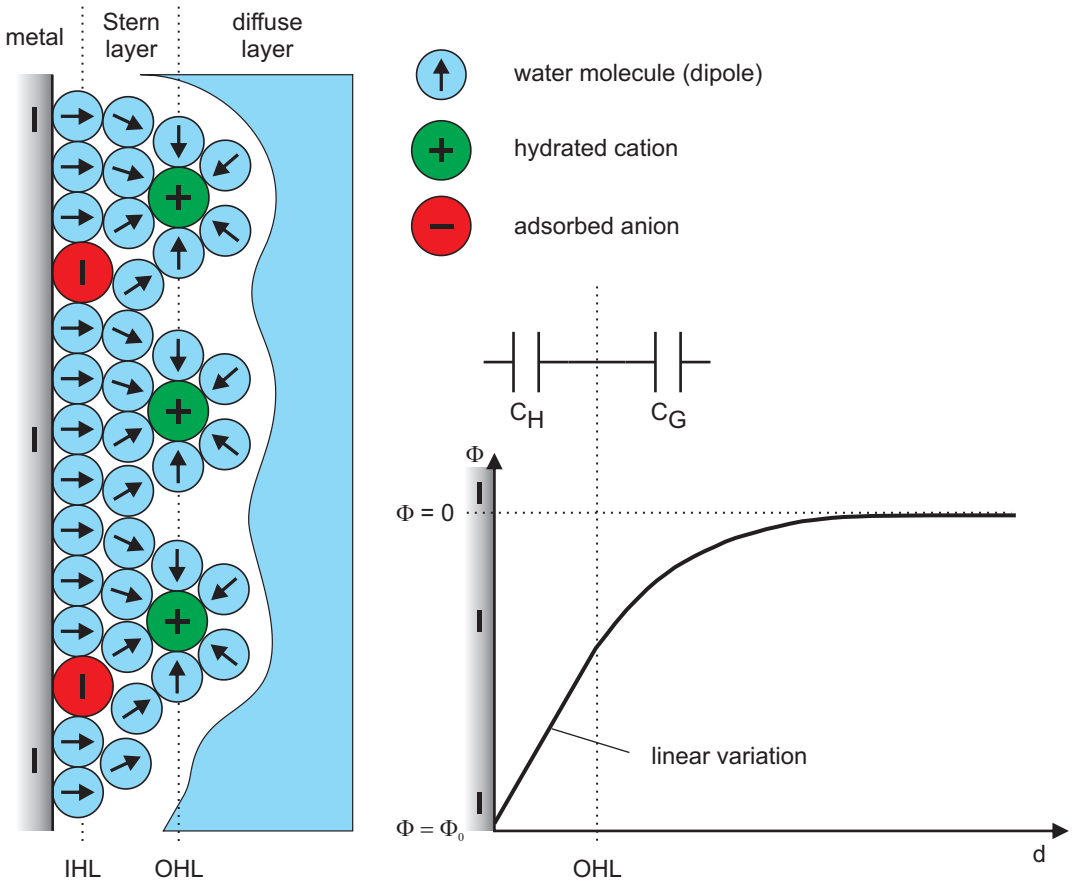

Figure 2.9: Gouy-Chapman-Stern model of the electrical double layer at the metal/electrolyte interface. The two parts of the figure are explained in the text and were adapted from [74].

the closest ion layer (*inner Helmholtz layer*, IHL), and the layer formed by ions with the biggest water sheath (*outer Helmholtz layer*, OHL) [74].

While the potential linearly decreases within the Stern layer, it exponentially decays to zero within the diffuse layer. The resulting *double layer capacitance* (C_{DL}) is given by the serial connection of Gouy and Helmholtz capacitance:

$$C_{DL} = \frac{C_H \cdot C_G}{C_H + C_G}. \tag{2.8}$$

and depends significantly on the electrolyte's ion concentration.

As an example, the *specific double layer capacitance* (c_{DL}) for a planar gold surface can reach values up to $c_{DL} = 40\ \mu\text{F/cm}^2$ [76]. For a more detailed insight into the physics and mathematics of the Helmholtz, Gouy-Chapman, and Gouy-Chapman-Stern model, the interested reader is referred to the literature [74, 76–78].

Finally, it has to be mentioned that an insulator (and especially an oxide) in contact with an electrolyte solution also forms an electrical double layer. This is especially important when insulated sensors, like *field-effect transistors* (FETs), are used in electrolyte solutions.

The surface of the gate-oxide of a FET carries a surface charge, which is dependent on the kind of insulator and the pH-value of the solution. The site-binding model for the *electrolyte-oxide-semiconductor* (EOS) interface allows a quantitative description of the chemical reactions at the oxide surface [79]. In brief, for every oxide there is a pH-value at which the surface is neutral (*point of zero charge*). For higher or lower pH-values, the surface is negatively or positively charged, respectively. In the case of a *ion sensitive FET* (ISFET), the resulting surface potential influences the conductance of the transistor channel and can thus be measured. If the electrolyte solution contains any other ions than hydronium (H_3O^+) or hydroxide (OH^-), these ions are also attracted or repelled by the surface charge as described by the Gouy-Chapman-Stern model.

2.4 Extracellular Recording

This section will briefly present available devices for extracellular recording signals from neurons and other electrogenic cells *in vitro*. Furthermore, models for the interpretation of recorded data will be introduced.

2.4.1 Devices and Methods for Extracellular Recording

Most devices utilized for extracellular recording from cells are currently fabricated in two-dimensional arrays of sensors on a planar chip surface, which can be used to grow and interface dissociated cultures of electrically active cells. Alternatively, these devices can also be used to record signals from explants or tissue slices. For all these devices, the basic mechanism of signal transduction is the detection of a voltage drop in the cleft between the cells or tissue and the recording device. The voltage drop is caused by the flow of ions from (or to) the cell membrane and through this cleft during the activity of the cell. Besides the properties of the recording devices and the cells, the geometry of this cleft is especially important for the quality of the signal transduction and has been investigated optically and electrically [80–86].

The simplest approach to such a sensor chip is a *multi-electrode array* (MEA) - a two-dimensional array of micrometer-sized metal electrodes [12,13,32]. The microelectrodes can detect the voltage drop in the cleft and are connected to an amplifier system to amplify and filter the signal for further processing. One big advantage of MEAs is the simple fabrication process, which is explained in detail for the sensors used in this thesis in Appendix A. In brief, a metal layer is deposited on a planar substrate and structured by optical lithography into sensor spots, contact lines and bond pads. The whole chip is then passivated against the electrolyte by an insulating layer, and only the bond pads and sensor spots are opened by another lithography and an etch process. In order to achieve better signal coupling, it is

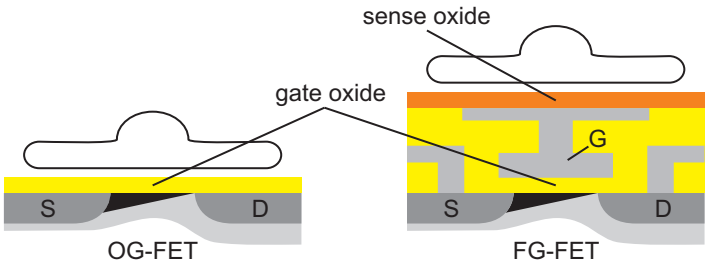

Figure 2.10: Schematics of an open-gate field-effect transistor (left) and a floating-gate field-effect transistor (right) for extracellular recording of signals from electrically active cells. The figure was taken from [25].

important to have a low input impedance of the microelectrodes. A reduction of the input impedance can be achieved by the introduction of surface topology or by using materials with a high specific double layer capacitance (see Section 2.3). The MEAs used in this thesis are introduced and characterized in detail in Chapter 3.

A main disadvantage of MEAs is that the number of sensor spots is limited by the number and length of the contact lines. With an increasing array size, the sensor pitch (distance between the sensors) has to be increased to allow the feed through of the contacts from the inner electrodes. Furthermore, long contact lines increase the noise introduced to the system before the first amplification stage. For this reason, MEAs with a higher number of sensors than 64 are rarely found. Using a *complementary metal-oxide-semiconductor* (CMOS) process with microelectrodes and on-chip amplification and filtering, this problem has been partially overcome to build CMOS-MEAs with higher sensor numbers [45, 87]. Nevertheless, the minimum sensor size is still limited by the fact that the input impedance of the electrode needs to be low enough to allow detection of signals.

Using active devices, such as FETs, an even higher density of sensors can be achieved, since these devices represent an amplifier by themselves [24,25,88]. However, this only holds true if the *signal-to-noise ratio* (SNR) of the transistors is good enough to enable a clear differentiation of the cell signals from the noise. Cell signal detection by FETs is usually achieved by setting the device to its operating point with a high transconductance and recording the current through the channel of the transistor. Any voltage drop in the cleft between cell and sensor spot caused by cell activity will change the channel conductance and thus the measured current. Two different kinds of transistor configurations can be used for cell signal detection (see Figure 2.10).

With an *open-gate FET* (OG-FET) [16–18], the cells are directly cultured on the gate oxide above the inversion channel of the transistor. Any cell activity will cause a voltage drop in the cleft between cell and gate oxide, directly modify the gate potential and cause a measurable change in the channel current. The name OG-FET derives from the missing gate contact in comparison to a standard *metal-oxide-semiconductor* FET (MOSFET).

For a *floating-gate FET*(FG-FET) [89–91], the gate contact is not missing, but instead remains without any contact at a floating potential. The top side of this floating gate forms a sensing area and is covered by an insulating layer. This sandwich-like structure

has several advantages in comparison to the OG-FET. The sensing area can be designed to fit to the geometry of the cells being investigated in shape and size, while the transistor gate can be optimized in its dimensions for optimal functionality of the device. Furthermore, the device lifetime is increased due to the protection of the sensitive transistor channel from penetrating ions from the electrolyte solution. Finally, the FG-FET is well suited for fabrication in a standard CMOS process.

Recently, a new kind of transistor based on silicon nanowires has been developed and successfully employed for the recording of cell signals [21, 23]. The capabilities of those devices in terms of sensor density and signal-to-noise performance are very promising, but further investigations of the new systems are needed to reveal the true capabilities of nanowire sensors.

2.4.2 Models for Extracellular Recording

The simplest approach to model the interface between an electrogenic cell and a device for extracellular recording is the *point-contact model* [92]. In this model, the contact between cell and sensor is described by a single point in the junction or cleft by the *junction potential* (v_J). A simple equivalent circuit of the point-contact model for the coupling between a neuron and a FET is depicted in Figure 2.11.

The cell membrane is divided into two parts: the *junction membrane* or *attached membrane* (AM) that is in direct contact to the sensor surface, and the *free membrane* (FM). Both parts of the membrane are modeled by Hodgkin-Huxley elements as introduced in Figure 2.5 with membrane capacitances C_{AM} and C_{FM}, voltage-dependent conductances G^i_{AM} and G^i_{FM}, and equilibrium potentials $E^i_{AM,0}$ and $E^i_{FM,0}$. The cleft between cell and

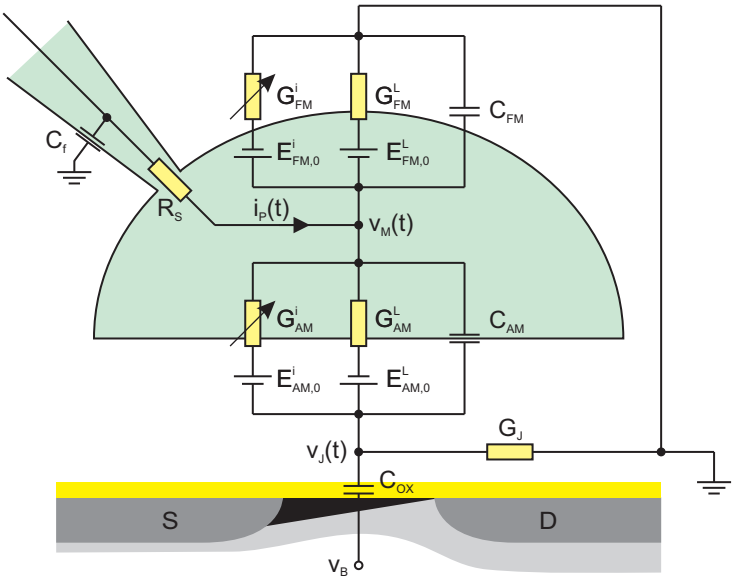

Figure 2.11: Point-contact model for extracellular recording of signals from an electrically active cell with an OG-FET. The cell is located in a grounded electrolyte solution on the sensor surface. The transistor bulk voltage is taken to be zero.

sensor and it's conductance for ion flow is represented by the *seal conductance* or *junction conductance* (G_J). G_J strongly depends on the cleft geometry [80, 82, 83], which again is strongly influenced by the cell type and any kind of surface treatment such as protein coating. The transistor itself is just modeled by its sensing *gate oxide capacitance* (C_{OX}), and the transistor *bulk voltage* (v_B) is assumed to be zero. Although these parameters are sufficient to describe the basic characteristics of the cell-transistor coupling, it is useful for in-depth investigations to use a patch-clamp pipette with the *pipette capacitance* C_f and *series resistance* R_S to measure or control the intracellular potential (equivalent to the membrane potential) by the pipette current (i_P).

Using Kirchhoff's current law, the time course of the junction potential ($v_J(t)$) can be related to a varied membrane potential ($v_M(t)$):

$$\begin{aligned} C_{OX} \cdot \frac{dv_J(t)}{dt} + G_J v_J(t) = C_{AM} \cdot \frac{d(v_M(t) - v_J(t))}{dt} \\ + \sum_i G^i_{AM}(v_M(t) - v_J(t) - E^i_{AM,0}). \end{aligned} \tag{2.9}$$

The following three approximations can be applied to simplify the expression [93]:

- The capacitive current through the transistor's gate oxide is considered negligible:

$$C_{OX} \cdot \frac{dv_J(t)}{dt} \approx 0. \tag{2.10}$$

- The variation of the junction potential is very small in comparison to the membrane potential:

$$v_M(t) - v_J(t) \approx v_M(t). \tag{2.11}$$

- The ion concentration in the cleft is considered to be homogeneous and equal to the ion concentration in the bulk solution, resulting in an equal equilibrium potential:

$$E^i_{AM,0} \approx E^i_0. \tag{2.12}$$

With these three approximations, Equation 2.9 can be simplified to:

$$v_J(t) = \frac{1}{G_J} \left(C_{AM} \cdot \frac{dv_M(t)}{dt} + \sum_i G^i_{AM}(v_M(t) - E^i_0) \right). \tag{2.13}$$

When considered as the gate potential variation of the measuring transistor, this equation for $v_J(t)$ gives a very basic and crude estimation of the expected signal from a given membrane potential change, which can easily be calculated or simulated. In the case of metal electrodes, similar considerations with slight modifications can be used to derive

equivalent equations. Nevertheless, the approximations made result in a lack of accuracy when fitting calculations and measured data in some characteristic parts of the signal for most experimental configurations. Therefore, several augmentations to the model have been proposed.

The *sheet-conductor model* [94] expands the investigation from a single point to a two-dimensional disk corresponding to the cleft between a cell and sensor. The junction potential is then described by a more complex cable equation. Although this enables the investigation of two-dimensional variations in the junction potential, the resulting accuracy of the simulation is not significantly improved.

A very promising approach to a better model introduces two new components. Firstly, the diffusion of ions in the cleft causes a concentration gradient of the different ion species and an electrodiffusive potential [95–97]. Secondly, the ion sensitivity of the transistor gate oxide varies for different ion species and therefore influences the surface potential [96, 98]. Accounting for both influences helps improve the fit between model and experiment.

2.5 Extracellular Stimulation

The final section of this chapter deals with extracellular stimulation and the devices that can be used for stimulation of electrically active cells. Here, the stimulation model applied in this thesis for the analysis of experimental data will be introduced.

2.5.1 Devices and Methods for Extracellular Stimulation

For the extracellular stimulation of electrogenic cells, the aim is to depolarize the cell membrane of the stimulated cell by application of stimulation pulses until voltage-gated sodium channels in the membrane open and allow the influx of sodium ions. This influx causes a self-amplifying depolarization, finally leading to an action potential. Therefore, it is important to establish a reliable, biocompatible, and functional cell-electrode interface by using electrode materials that can deliver a high amount of charge into the electrolyte solution without causing any damage to the cells or the electrode itself. Two basic approaches can be used to achieve this task.

In the first approach, insulated electrodes are used for the purely *capacitive stimulation* of cells. Here, the application of voltage steps or ramps to the stimulating device causes a purely capacitive displacement current across the interface between electrode and electrolyte. Of the microelectronic devices used for extracellular recording (see Subsection 2.4.1), two kinds are also utilized for purely capacitive extracellular stimulation. Besides their interesting capabilities for signal recording, FG-FETs can also be used for stimulation [25, 31] by application of stimulation pulses to the floating gate. In order to keep

the gate floating for recording, the stimulation contact should have a high off impedance. This can be achieved either by a capacitor [31], or a switch realized by transistors [25]. For FG-FETs, the stimulation mechanism is purely capacitive, since the sensor oxide represents an insulator preventing any Faradaic charge transfer. Additionally, first studies with nanowire transistors reveal promising results for capacitive stimulation as well [21]. As in the case of recording, nanowire stimulation has to be studied further to analyze its mechanism and efficiency. In addition to FG-FETs and nanowire transistors, there are also devices that are exclusively used for the purely capacitive stimulation of electrogenic cells. Several excellent studies on oxide capacitors [99] and their successful application for stimulation have been reported by Fromherz and colleagues [26–30, 100].

As a second approach, metal electrodes can be used for a combination of capacitive and *Faradaic stimulation*. In this case, an additional Faradaic current by electrochemical reactions across the solid/electrolyte interface significantly increases the charge transfer from the electrode to the electrolyte. However, care has to be taken not to cause any irreversible electrochemical reactions that can harm the device and the stimulated cells or tissue. Harmful electrochemical reactions usually occur if the *safe electrochemical window* (SECW) for the stimulator material is exceeded. This includes gas evolution by water electrolysis, substantial pH-value changes, or metal dissolution [101–105]. If the potential is kept within the SECW, materials such as platinum (Pt) and iridium (Ir) allow reversible faradaic reactions like hydrogen atom plating (Equation 2.14) or oxide formation and reduction (Equations 2.15 to 2.18), which add substantially to the charge storage capacity without causing any damage [104]:

$$Pt + H^+ + e^- \rightleftharpoons PtH, \tag{2.14}$$

$$Pt + H_2O \rightleftharpoons PtO + 2H^+ + 2e^-, \tag{2.15}$$

$$Ir + H_2O \rightleftharpoons IrO + 2H^+ + 2e^-, \tag{2.16}$$

$$Ir + 2H_2O \rightleftharpoons IrO_2 + 4H^+ + 4e^-, \tag{2.17}$$

$$Ir_2O_3 + H_2O \rightleftharpoons 2IrO_2 + 2H^+ + 2e^-. \tag{2.18}$$

Despite the recent advances in the development of insulating materials with a high specific capacitance [99, 106] for purely capacitive stimulation, the maximum current across the electrode-electrolyte interface is still very low in comparison to metallic electrodes. Therefore, all devices with insulating materials for the purely capacitive stimulation are not yet established for regular use. On the other hand, MEAs with metal electrodes have a long history of usage for the *in vitro* extracellular stimulation of single or networks of dissociated neurons [32–38, 46, 53, 54, 107] and brain slices or tissue explants [39–44]. Nevertheless, continuous research and development in the field of novel materials and surface

modifications for metal microelectrodes is aimed at optimizing the cell-electrode interface for bidirectional communication with electrogenic cells.

In the past, various materials such as platinum [41], gold-plated *indium tin oxide* (ITO) [35], and *titanium nitride* (TiN) [37, 40, 53, 54] have been used for microelectrodes both for stimulation and recording of cell signals. In order to reduce the electrode impedance, platinum [46], ITO [34, 107], and gold [32, 33, 36, 38, 39] electrodes have been platinized before usage for stimulation and recording. Recent developments in the field of electrode materials and surface coatings include carbon nanotubes [48–50] and electrically conducting polymers [51, 52].

A very promising material, which has already a history of application in neuroprosthetics [55, 60, 61] is iridium and especially *iridium oxide* (IrO_x), which can be formed by electrochemical activation of iridium [42, 57, 108–110] or by reactive sputtering from iridium in an oxidizing plasma [56, 111–116]. For stimulation electrodes, IrO_x results in low impedance and high charge storage capacity in comparison to other electrode materials. This is caused by its porous surface structure, greatly enhancing the electrode surface area, and a fast reversible faradaic reaction between the Ir^{3+} and Ir^{4+} oxide states [104, 105, 114]. Furthermore, it is highly biocompatible and very stable in electrolyte solutions [104, 110] making it an ideal material for the interfacing of neuronal tissue and cultured networks. Despite the long history in the field of neuroprosthetics, neither activated nor sputtered IrO_x films (SIROFs) have so far been applied for electrophysiological experiments with dissociated neuronal cell cultures using MEAs. Recently, a first study on extracellular recordings from a brain slice with SIROF MEAs has been reported, though [42].

Extracellular stimulation can be achieved using either current- or voltage-controlled stimulation pulses. While current-controlled stimulation enables precise definition of the current density and injected charge during the pulse, the sensor potential is not directly controlled or limited during stimulation. Therefore, great care has to be taken not to exceed the SECW. For voltage-controlled stimulation, the sensor potential is predefined, but the current density and amount of injected charge is not controlled in this case. Thus, voltage-controlled stimulation directly allows preventing harmful reactions at the electrode, while stimulation pulses have to be chosen carefully for current-controlled stimulation to achieve this task [54].

2.5.2 Models for Extracellular Stimulation

This section will introduce a model for extracellular stimulation, which can be applied to stimulation with MEAs, FG-FETs or capacitors. Very similar to the approach for recording (see Subsection 2.4.2), the stimulation of cells can also be modeled by assuming a point-contact model with the cleft between cell and device approximated by a single

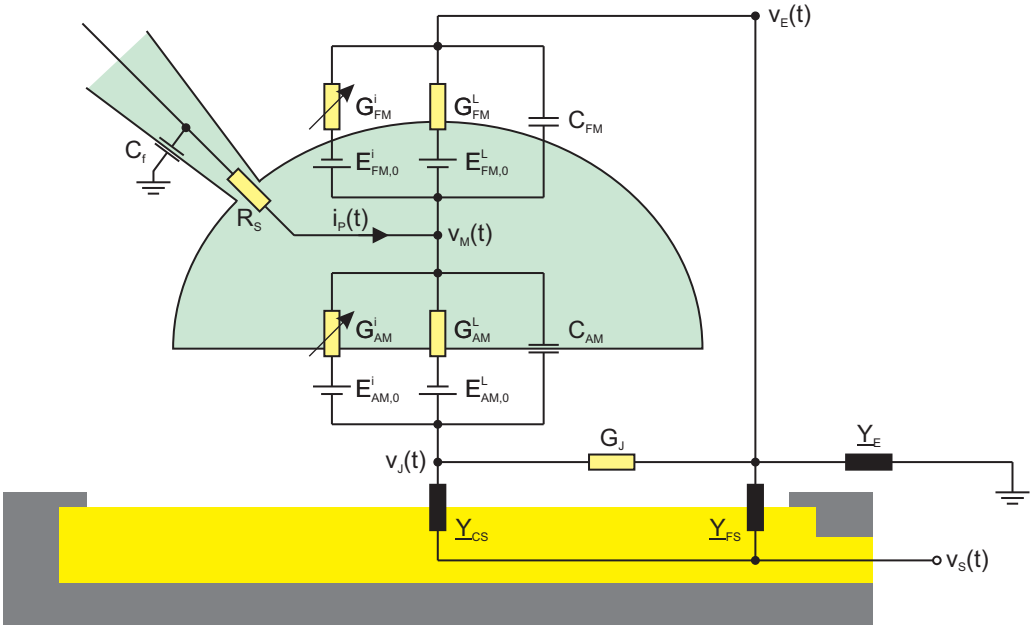

Figure 2.12: Generalized two-domain stimulation model for extracellular stimulation of electrically active cells. The cell is divided into two membrane domains described as Hodgkin-Huxley elements. It is electrically contacted by a patch-clamp pipette and located on a part of the stimulator characterized by its admittance. The admittance of the grounded electrolyte solution and the bath electrode are included in the model as well.

point with junction potential v_J. This model was first used by Fromherz and Stett in a very basic version to explain the capacitive stimulation with oxide capacitors [26] and further developed as the *two-domain stimulation model* by the same group [29,30]. In order to present a model that can be applied to stimulation with MEAs, capacitors, and FETs, a more generalized equivalent circuit for the model is introduced in Figure 2.12.

A cell located on a part of a generalized stimulator is divided into an attached and free membrane domain (AM and FM) with surface areas A_{AM} and A_{FM}. Like in the model for extracellular recording, both membrane domains are again described as Hodgkin-Huxley elements with membrane capacitances C_{AM} and C_{FM}, voltage-dependent conductances G^i_{AM} and G^i_{FM}, and equilibrium potentials $E^i_{AM,0}$ and $E^i_{FM,0}$. In order to monitor and analyze the cell's response to stimulation, the intracellular potential v_M is monitored simultaneously by a patch-clamp pipette with the pipette capacitance C_f, series resistance R_S, and pipette current i_P. As in the extracellular recording model, the cleft between cell and stimulator is represented by the junction conductance (G_J). In order to keep the model generally applicable for various kinds of devices, the stimulator is represented by its complex *stimulator admittance* $\underline{Y}_S$. Since the size of the stimulated cells is usually smaller than the size of the stimulator, it is also divided into the *covered* and the *free stimulator* (CS and FS) with the admittances $\underline{Y}_{CS}$ and $\underline{Y}_{FS}$. To account for any voltage drop in the electrolyte solution and at the reference electrode during stimulation, the electrolyte and

the electrode are described by the admittance $\underline{Y}_E$. With theses parameters, the equivalent circuit can be used to model the time course of any potential change in the cell ($\Delta v_M(t)$), the junction ($\Delta v_J(t)$), and in the electrolyte solution close to the cell ($\Delta v_E(t)$) as response to a potential change at the stimulator ($\Delta v_S(t)$).

This model can be used to analyze data from both voltage-clamp and current-clamp experiments with the patch-clamp amplifier. For voltage-clamp experiments, it has to be considered that the intracellular potential v_M is kept constant by the patch-clamp pipette. For current-clamp experiments on the other hand, only the change of the current through the patch pipette is kept zero, resulting in the fact that all current injected by the stimulation through the attached membrane must also flow through the free membrane. Since the aim of this thesis was to investigate the excitation of APs in neurons, the current-clamp mode was used for most experiments and will also be the basis of the following calculations for the model.

In order to estimate the response of a cell to a given stimulation pulse, it is important to understand that the membrane potential at the attached and the free membrane ($v_{AM}(t)$ and $v_{FM}(t)$) are, in the case of extracellular stimulation, not equivalent to the intracellular potential ($v_M(t)$). Since the membrane potential is defined as the difference between the intracellular and the extracellular potential (compare Equation 2.1), the potential at both membrane domains is significantly different:

$$v_{AM}(t) = v_M(t) - v_J(t), \tag{2.19}$$

$$v_{FM}(t) = v_M(t) - v_E(t). \tag{2.20}$$

For a given potential change at the stimulator, at least part of this potential change will drop across the two cell membrane domains, resulting in different changes for $v_M(t)$, $v_J(t)$, and $v_E(t)$. Obviously, the sign of the potential change will always be the same for all three potentials, while its amplitude will be highest for $\Delta v_J(t)$, and lowest for $\Delta v_E(t)$:

$$|\Delta v_J(t)| \geq |\Delta v_M(t)| \geq |\Delta v_E(t)|, \tag{2.21}$$

where the changes can only be equal if the complete voltage drop is zero. Equations 2.19 to 2.21 again explain the name “two-domain stimulation model”. Because of the relation of the three potential changes, the changes at the two membrane domains, $\Delta v_{AM}(t)$ and $\Delta v_{FM}(t)$, always have opposite signs. Therefore, any stimulation pulse applied to the stimulator will cause a depolarization of one membrane domain and hyperpolarization of the other domain. Both mechanisms can lead to the excitation of APs in the stimulated cell if the threshold for opening fast sodium channels is exceeded in one membrane domain [29].

To allow a comparison of modeled potentials to measurements and a discussion of the

results, two final remarks about the model have to be made:

- Since the model handles the potential at each membrane domains with a single potential, the values for $v_J(t)$ and $v_E(t)$ represent the average of the potential in the cleft and in the electrolyte close to the cell, respectively. Estimations of the spatial variations of both potentials by a stimulation model equivalent to the *sheet-conductor model* (compare Subsection 2.4.2) predict local potential changes of twice the amplitudes of the averaged values [29, 30].

- When comparing measured and modeled data, it has to be considered that the recorded intracellular potential reflects the difference between intracellular potential and system ground, which is very different to the membrane potential at the free and the attached membrane. Any discussion must especially consider a substantial voltage drop in the electrolyte solution and at the bath electrode during fast stimulation pulses. Furthermore, the intracellular potential recorded by the patch-clamp amplifier (pipette potential v_P) will also deviate from the real intracellular potential due to a filtering effect caused by the electronics.

Analytical Solution in the Time Domain

In the following, an analytical approach for the application of this model to stimulation with microelectrodes is introduced. For this purpose, the model is modified by three simplifications resulting in the equivalent circuit shown in Figure 2.13:

- The generalized admittances of both parts of the stimulator are each replaced by a parallel circuit of a capacitor and a resistor, representing the double layer capacitance (C_{CS} and C_{FS}) and the faradaic processes at the electrode (G_{CS} and G_{FS}). This corresponds to a simple model of a metal electrode in contact with an electrolyte solution.

- The bath electrode and the electrolyte solution are represented by just a single resistor with conductance G_E. This means that any capacitive compartment of the electrode is omitted.

- The model is applied to calculate the fast passive changes of the potential at the cell membrane, omitting the membrane conductivities for the different ion species. Therefore, both membrane domains are modeled by a capacitor (C_{AM} and C_{FM}). This simplification means that only the direct impact of a stimulation pulse on the membrane potential at the membrane domains can be calculated. Nevertheless, since

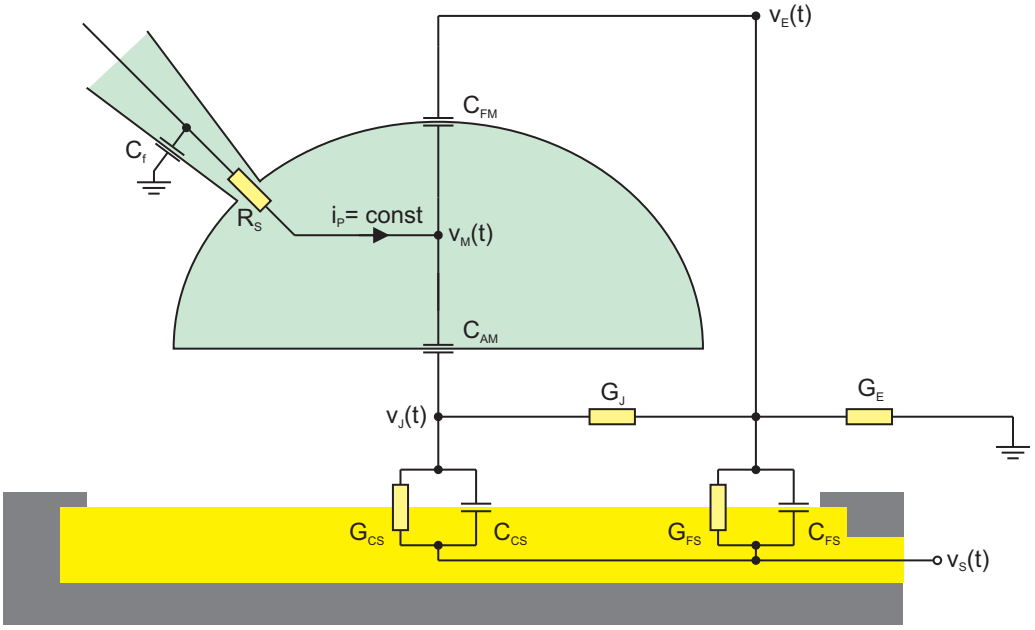

Figure 2.13: Simplified two-domain stimulation model for an analytical approach to describe the extracellular stimulation of a current-clamped cell with a microelectrode.

in most cases the aim of the stimulation is to passively raise the membrane potential (of at least one membrane domain) above the threshold for AP excitation, this simplified circuit can still be used to estimate the stimulation effect.

Since the intracellular potential is monitored simultaneously with a patch-clamp pipette in current-clamp mode, the pipette current is kept constant during the experiment. Based on this simplified circuit, a system of three differential equations can be established by the application of Kirchhoff's current law:

$$C_{AM} \cdot \frac{d(v_J(t) - v_M(t))}{dt} = C_{FM} \cdot \frac{d(v_M(t) - v_E(t))}{dt}, \tag{2.22}$$

$$\begin{aligned} G_{CS}(v_S(t) - v_J(t)) + C_{CS} \cdot \frac{d(v_S(t) - v_J(t))}{dt} = \\ G_J(v_J(t) - v_E(t)) + C_{AM} \cdot \frac{d(v_J(t) - v_M(t))}{dt}, \end{aligned} \tag{2.23}$$

$$\begin{aligned} G_E v_E(t) = G_{FS}(v_S(t) - v_E(t)) + C_{FS} \cdot \frac{d(v_S(t) - v_E(t))}{dt} \\ + G_J(v_J(t) - v_E(t)) + C_{FM} \cdot \frac{d(v_M(t) - v_E(t))}{dt}. \end{aligned} \tag{2.24}$$

Considering the area ratio of the attached and the whole membrane, as well as the covered and the whole stimulator (A_{CS} and A_S), the scaling parameters α and β can be

introduced:

$$\alpha = \frac{A_{AM}}{A_M}, \qquad 1 - \alpha = \frac{A_{FM}}{A_M}, \tag{2.25}$$

$$\beta = \frac{A_{CS}}{A_S}, \qquad 1 - \beta = \frac{A_{FS}}{A_S}. \tag{2.26}$$

Together with Equations 2.19 and 2.20, Equation 2.22 can thus be simplified to:

$$-\alpha \cdot \frac{dv_{AM}}{dt} = (1 - \alpha) \cdot \frac{dv_{FM}}{dt}. \tag{2.27}$$

This equation directly reveals the relation between the change of the potential at the free and the attached membrane: the changes have an opposite sign and are scaled by the ratio of the corresponding membrane area to the complete membrane area. This actually means that free and attached membrane act like a capacitive voltage divider to any voltage drop across the cell, which is caused by an external stimulus.

The Equations 2.22 to 2.24 and 2.27 together build a system of differential equations, which can now be used to calculate the time course of $v_M(t)$, $v_J(t)$, $v_E(t)$, $v_{AM}(t)$, and $v_{FM}(t)$ in response to a given stimulation signal $v_S(t)$ analytically. As an example for a simple stimulation signal, a potential step with amplitude V_S^0 at the stimulator can be expressed with the *Heaviside step function* $\epsilon(t)$:

$$v_S(t) = V_S^0 \cdot \epsilon(t). \tag{2.28}$$

These equations together with boundary conditions for the start values of the voltages have to be fed to a *computer algebra system* to get analytical solutions for all required potentials for comparison to measured data. However, there are some severe drawbacks to this analytical approach:

- Analytical solutions for the system can only be calculated for rather simple stimulation input signals such as single voltage steps or ramps.

- Even for these simple input signals, the computation time is unreasonably high and results in rather bulky and confusing equations, which are difficult to handle.

- Also for simpler systems with only a pure capacitor as stimulation device, further simplifications or approximations have to be made to get easy-to-handle equations. For example, the influence of the free stimulator [29, 30], or the voltage drops at the electrolyte solution and the bath electrode [29] have to be omitted.

- If a new circuit element has to be introduced (e.g. if a more complex equivalent circuit for the stimulator is used), the whole system of equations has to be derived and solved again, usually becoming even more complex.

- Especially for fast stimulation signals, a deviation of the measured intracellular potential from the real value due to a filtering effect of the patch-clamp amplifier cannot be easily included into the calculations.

For all these reasons, a different approach for the modeling of the extracellular stimulation was developed in this thesis. Instead of calculating analytical solutions in the time domain for the involved potentials, a numerical solution in the frequency domain is used.

Numerical Solution in the Frequency Domain

In engineering, signal processing [117, 118] offers the possibility to analyze analog, time-discrete and digital signals not only in the time domain, but also in the frequency domain. The application of *Fourier-transform*, *Laplace-transform*, or *z-transform* gives the user powerful tools to solve differential equations describing *linear time-invariant* (LTI) systems like electric circuits of passive resistors and capacitors. As a convention, all quantities in the frequency domain as opposed to the time domain are written in upper instead of lower case in this thesis.

A LTI system can well be described in the frequency domain by its complex *frequency response* $\underline{H}(\omega)$:

$$\underline{H}(\omega) = \frac{\underline{V}_{out}(\omega)}{\underline{V}_{in}(\omega)} = |\underline{H}(\omega)| \cdot e^{j\varphi(\omega)}, \tag{2.29}$$

with j and $\omega = 2\pi f$ being the imaginary unit and the angular frequency, respectively. The frequency response therefore gives a complex-valued factor, by which an input signal $\underline{V}_{in}(\omega)$ has to be multiplied in the frequency domain to get the output signal $\underline{V}_{out}(\omega)$. The frequency response can also be given by its magnitude $|\underline{H}(\omega)|$ and phase $\varphi(\omega)$.

In this thesis, the input signal of our stimulation model is numerically transfered into the frequency domain by *discrete Fourier transform* (DFT) and multiplied with the calculated frequency responses of the system for the different desired output potentials. Finally, these output potentials are transformed back into the time domain by inverse DFT (iDFT). For the involved calculations, a *numerical calculation environment* (MATLAB, The MathWorks, Inc., Natick, USA) is used. For an excellent introduction to signal processing with MATLAB, the user is referred to Kammeyer and Kroschel [119].

In the following, the equivalent circuit presented in Figure 2.12 will be used to derive the frequency responses for the calculation of the different output voltages. Of the simplifications made in the analytical model, only the limitation to the fast passive potential

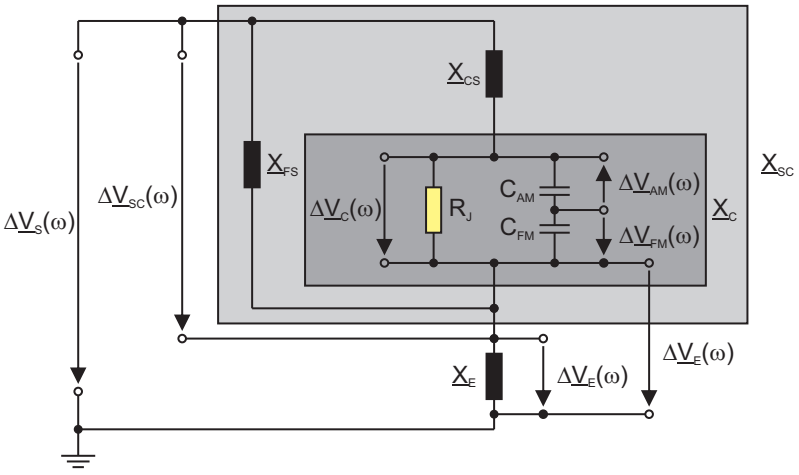

Figure 2.14: Modified equivalent circuit of the two-domain stimulation model for extracellular stimulation. The circuit is used to derive the equations for the frequency response to calculate the relevant voltages within the system. The interior of the dark and light gray boxes are combined to the cell impedance ($\underline{X}_C$) and to the stimulator-cell impedance ($\underline{X}_{SC}$).

changes at both membrane domains will be used for the numerical solution, meaning that the membrane conductivities for the different ion species are omitted. As previously stated, this simplified circuit can still be used to investigate extracellular stimulation and if the applied pulse is sufficient to raise the membrane potential above the threshold for AP excitation. Figure 2.14 shows the resulting modified equivalent circuit, which is used for the derivation of the frequency response equations (the circuit was rearranged to give a better overview of the relation between the various voltages).

Since the calculation of frequency responses is more easily done with impedances ($\underline{X} = \underline{Y}^{-1}$) than with admittances, the covered and free stimulator, as well as the electrolyte solution and the bath electrode are represented by their respective impedances ($\underline{X}_{CS}$, $\underline{X}_{FS}$, and $\underline{X}_E$) instead of their admittances. These impedances can be adapted to the model for the respective electrode material and the desired complexity. For the example in the analytical solution, the impedance of the covered and free stimulator would each be stated as the parallel circuit of a resistor and a capacitor:

$$\underline{X}_{CS/FS} = \frac{R_{CS/FS}}{1 + j\omega R_{CS/FS} C_{CS/FS}}, \tag{2.30}$$

and the impedance of electrolyte and bath electrode would correspond to a simple resistor ($\underline{X}_E = R_E$).

The influence of the cell is modeled by the capacitance of the attached and free membrane domain (C_{AM} and C_{FM}) and the junction resistance $R_J = G_J^{-1}$. The complete impedance of the cell including the junction resistance can be combined to the cell impedance $\underline{X}_C$:

$$\underline{X}_C = \frac{R_J}{1 + j\omega R_J C_M^*}. \tag{2.31}$$

C_M^* represents the *effective cell membrane capacitance* and is constituted by the serial

connection of the two membrane domain capacitors:

$$C_M^* = \frac{C_{AM} \cdot C_{FM}}{C_{AM} + C_{FM}}. \tag{2.32}$$

The impedance of the complete construct including the cell impedance and both parts of the stimulator are merged to the stimulator-cell impedance $\underline{X}_{SC}$:

$$\underline{X}_{SC} = \frac{(\underline{X}_{CS} + \underline{X}_C) \cdot \underline{X}_{FS}}{\underline{X}_{CS} + \underline{X}_C + \underline{X}_{FS}}. \tag{2.33}$$

Using all those elements of the equivalent circuit, the frequency responses for the various interesting voltage changes in the system can now be stated by analyzing three subcircuits corresponding to three complex voltage dividers. Firstly, the applied change in the stimulation voltage $\Delta\underline{V}_S(\omega)$ is divided into the voltage drop at electrolyte solution and bath electrode ($\Delta\underline{V}_E(\omega)$) and the voltage drop across the stimulator-cell impedance ($\Delta\underline{V}_{SC}(\omega)$):

$$\underline{H}_E(\omega) = \frac{\Delta\underline{V}_E(\omega)}{\Delta\underline{V}_S(\omega)} = \frac{\underline{X}_E}{\underline{X}_E + \underline{X}_{SC}}, \tag{2.34}$$

$$\underline{H}_{SC}(\omega) = \frac{\Delta\underline{V}_{SC}(\omega)}{\Delta\underline{V}_S(\omega)} = \frac{\underline{X}_{SC}}{\underline{X}_E + \underline{X}_{SC}}, \tag{2.35}$$

Secondly, the voltage change $\Delta\underline{V}_{SC}(\omega)$ is divided between the impedance of the covered stimulator and the cell and can be used to calculate the voltage drop across the whole cell ($\Delta\underline{V}_C(\omega)$):

$$\underline{H}_C(\omega) = \frac{\Delta\underline{V}_C(\omega)}{\Delta\underline{V}_S(\omega)} = \underline{H}_{SC}(\omega) \cdot \frac{\Delta\underline{V}_C(\omega)}{\Delta\underline{V}_{SC}(\omega)} = \frac{\underline{X}_{SC}}{\underline{X}_E + \underline{X}_{SC}} \cdot \frac{\underline{X}_C}{\underline{X}_C + \underline{X}_{CS}}. \tag{2.36}$$

Finally, the two capacitors representing the cell membrane domains again divide the voltage change $\Delta\underline{V}_C(\omega)$ as a capacitive voltage divider, with the resulting $\Delta\underline{V}_{AM}(\omega)$ and $\Delta\underline{V}_{FM}(\omega)$ directly corresponding to the voltage drops across the attached and the free membrane. The sign of the voltage drop at the attached membrane is negated to fit to the electrophysiological definition of the membrane potential (compare Equation 2.1 and the

direction of the arrows symbolizing the voltage drops in Figure 2.14):

$$\begin{aligned}\underline{H}_{AM}(\omega) &= \frac{\Delta\underline{V}_{AM}(\omega)}{\Delta\underline{V}_S(\omega)} = \underline{H}_C(\omega)\cdot\frac{\Delta\underline{V}_{AM}(\omega)}{\Delta\underline{V}_C(\omega)} \\ &= \frac{\underline{X}_{SC}}{\underline{X}_E+\underline{X}_{SC}}\cdot\frac{\underline{X}_C}{\underline{X}_C+\underline{X}_{CS}}\cdot\frac{-C_{FM}}{C_{AM}+C_{FM}},\end{aligned} \tag{2.37}$$

$$\begin{aligned}\underline{H}_{FM}(\omega) &= \frac{\Delta\underline{V}_{FM}(\omega)}{\Delta\underline{V}_S(\omega)} = \underline{H}_C(\omega)\cdot\frac{\Delta\underline{V}_{FM}(\omega)}{\Delta\underline{V}_C(\omega)} \\ &= \frac{\underline{X}_{SC}}{\underline{X}_E+\underline{X}_{SC}}\cdot\frac{\underline{X}_C}{\underline{X}_C+\underline{X}_{CS}}\cdot\frac{+C_{AM}}{C_{AM}+C_{FM}}.\end{aligned} \tag{2.38}$$

Using the equations for the frequency responses $\underline{H}_E(\omega)$, $\underline{H}_{AM}(\omega)$, and $\underline{H}_{FM}(\omega)$, the voltage drops at the electrolyte solution and bath electrode ($\Delta\underline{V}_E(\omega)$), as well as both membrane domains ($\Delta\underline{V}_{AM}(\omega)$ and $\Delta\underline{V}_{FM}(\omega)$) can easily be calculated from any frequency-domain transformed stimulation signal ($\Delta v_S(t)$ or $\Delta\underline{V}_S(\omega)$) by simple multiplication:

$$\Delta\underline{V}_E(\omega) = \underline{H}_E(\omega)\cdot\Delta\underline{V}_S(\omega), \tag{2.39}$$

$$\Delta\underline{V}_{AM}(\omega) = \underline{H}_{AM}(\omega)\cdot\Delta\underline{V}_S(\omega), \tag{2.40}$$

$$\Delta\underline{V}_{FM}(\omega) = \underline{H}_{FM}(\omega)\cdot\Delta\underline{V}_S(\omega). \tag{2.41}$$

As can easily be seen in Figure 2.14, the change in the intracellular potential that is recorded with the patch pipette, is equal to the sum of the change in the voltage drop at electrolyte and bath electrode and free membrane ($\Delta\underline{V}_M(\omega) = \Delta\underline{V}_E(\omega) + \Delta\underline{V}_{FM}(\omega)$). Finally, the time-domain equivalents of all the interesting voltages and especially the pipette potential can be calculated by iDFT, and used for comparison with measured data and analysis of the system.

As mentioned before, the patch-clamp pipette and amplifier can have the effect of a low-pass filter on the measured signal. One big advantage of the solution in the frequency domain is that this filter can easily be applied by multiplication of the calculated membrane potential with the filter's frequency response to get the change in the resulting pipette potential $\Delta\underline{V}_P(\omega)$. Alternatively, this filter can also be included in the numerical simulations in the time domain. Another advantage is that more complex models for the impedance of the stimulator or bath electrode and electrolyte (e.g. including *constant phase elements*) can easily be included in the system. However, the solution in the frequency domain is limited to linear systems (because of the Fourier transform). Therefore, it is impossible to directly include the voltage-dependent opening state of ion channels in the cell membrane, which limits the absolute scope of the simulations in comparison to a different approach using the finite element method [120, 121]. Nevertheless, the model requires less com-

putational time and can be used to quickly investigate and predict the passive membrane potential changes caused by any stimulation pulse, thus enabling an estimation of the pulse effect on the opening state of the channels.

Chapter 3

Device Design and Characterization

There is no failure except in no longer trying...

Elbert Hubbard (American writer, publisher, artist, and philosopher, 1856-1915)

This chapter deals with the various chip types used in this thesis. In the first section, the different *multi-electrode arrays* (MEAs) will be introduced and characterized with *scanning electron microscope* (SEM) imaging, *electrochemical impedance spectroscopy* (EIS), and *cyclic voltammetry* (CV). The second section will deal with a new kind of microelectronic chip integrating both microelectrodes and *field-effect transistors* (FETs). The various steps in the processing of these chip types are described in detail in Appendix A.

Data sets from EIS and CV measurements presented in this chapter were collected at a resolution higher than is feasible to print with markers for every data point. Therefore, a subset of the data is shown for every measurement in a way that the markers do not overlap and are equally spaced, while a solid line represents the whole data set.

3.1 64-Electrode MEAs

In the scope of this thesis, MEAs have been designed, processed, characterized, and applied in electrophysiological experiments on single electrogenic cells from dissociated cultures *in vitro*. The work was especially aimed at producing arrays of porous, low-impedance *iridium oxide* (IrO_x) electrodes and investigating the extracellular stimulation of individual cells in defined experimental conditions. In order to lower the impedance, the electrode surface of standard gold (Au) MEAs was coated with *sputtered IrO_x films* (SIROFs) for improved stimulation capabilities. In several iterations, the design, process steps, and material properties of the chips where modified and optimized, resulting in multiple generations of IrO_x MEAs with different properties.

3.1.1 Standard Gold and Modified Iridium Oxide MEAs

Standard MEA Chip Design

Before this thesis, only standard gold MEAs were available in our institute for electrophysiological experiments [122]. Those standard MEAs are designed as an array of 8 × 8 gold microelectrodes (Figure 3.1.b) with a pitch of 100 or 200 µm and electrode diameters of 6, 8, 10, 20, or 30 µm. Additionally, some chips were produced with twelve stimulation electrodes, three in every corner of the array, with diameters of 50 or 100 µm. An encapsulated chip and the design of the electrode array are depicted with a photograph and two *differential interference contrast* (DIC) images in Figure 3.1. The gold contact lines leading to the bond pads of the chips are covered and protected against the electrolyte solution by a passivation stack. The stack is composed of a layer of *silicon nitride* (Si_3N_4) sandwiched between two layers of *silicon oxide* (SiO_2) (ONO stack). The detailed production process and a cross section of the final MEA structure (Figure A.1) can be found in the appendix (Subsection A.1.1). After processing, the chips are glued to a carrier structure and encapsulated with polymers to protect the electric contacts from shortcuts. In the same step, a dish with a volume of approximately 600 µl is formed around the sensor area as a vessel for cell culture (Figure 3.1.a). The packaging process including the formation of the culture dish is explained in Section B.1 of the appendix. This basic type of MEA will be referred to as the zeroth MEA generation.

In an effort to reduce the impedance and increase the charge transfer capabilities of the electrodes, standard gold MEA wafers were coated with a SIROF stack consisting of a 20 nm titanium (Ti) adhesive layer and a 300 nm porous IrO_x layer in a sputtering post-process [123], which resulted in the first generation of MEAs with a grainy porous IrO_x electrode surface. The post-process is described in the appendix (Subsection A.1.2), and the final layer structure of these MEAs can be seen in Figure A.2. Figure 3.2 shows a SEM

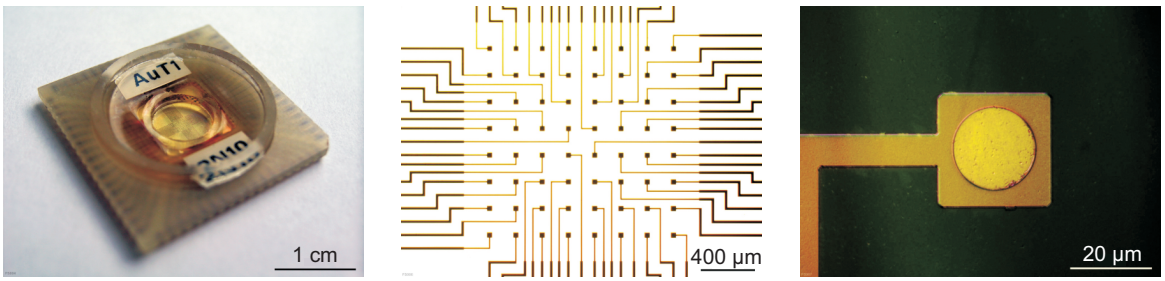

(a) (b) (c)

Figure 3.1: Standard gold MEA encapsulation and chip design. (a) Photograph of fully encapsulated MEA with carrier. Two DIC images show a magnification of the sensor array (b) and a single gold electrode with a diameter of 20 µm (c).

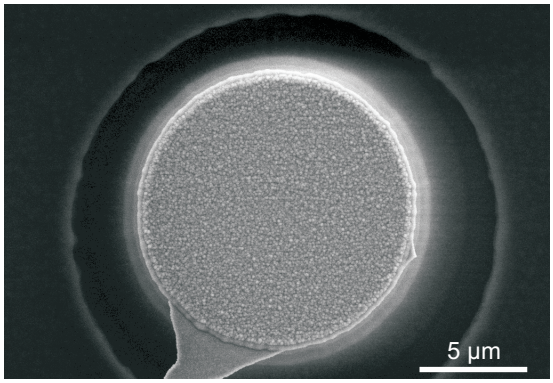

Figure 3.2: SEM image of a first generation IrO_x electrode. The grainy surface structure can clearly be seen. The image was taken from [123].

image of an IrO_x electrode. The MEAs were encapsulated in the same way as the standard gold MEAs, electrochemically characterized, and used for electrophysiological experiments.

Standard and Modified MEA Characterization

Coating of an electrode with a film of IrO_x can significantly increase the surface area of an electrode and thus cause an increase of the electrode's capacitance. At the same time, the *charge storage capacity* (Q_{CSC}) of the electrode is significantly increased by reversible electrochemical reactions as already mentioned in Subsection 2.5.1. Both characteristics reduce the impedance and increase the stimulation capabilities of the coated electrode significantly. In this work, the values for Q_{CSC} always correspond to the cathodal charge storage capacity, which is the integral of the negative current taken from a CV measurement [105, 124]. The electrochemistry of iridium and its oxide in contact with electrolytes has been studied in detail [57,108,109,111,113,114,125,126], with an elaborate summary given in [114]. An important characteristic of IrO_x is the fact that its charge storage capacity and the impedance can be further improved by activation of the electrode with repetitive potential cycling within the *safe electrochemical window* (SECW) of the material [108,114].

As can be seen in Figure 3.2, the surface enlargement in comparison to the flat gold electrodes (compare Figure 3.1.c) is due to a grainy and porous surface topology. The thickness of the complete sputtered stack, which was produced in the first sputtering run, was determined using a surface profiler (P-10, KLA-Tencor Corporation, San Jose, USA). With a thickness of 360 nm, the adhesive layer and SIROF together were found to be slightly thicker than the desired 320 nm. Table 3.1 shows the stack composition as well as the desired and measured stack thicknesses for all sputtering runs used in this thesis.

This first MEA generation was produced in the scope of a diploma thesis [123]. A brief summary of the first chip characterization from this study will be given here. Firstly, the electrodes were investigated optically using SEM images. For that purpose, unencapsulated chips were cleaned by sonication in a mixture of 50 % (v/v) ethanol and acetone,

sputtering run	Chip types (chip generations)	Stack composition	Desired thickness (nm)	Measured thickness (nm)
1^{st}	MEA 64 (1,2)	Ti/IrO_x	320	360
2^{nd}	MEA 64 (3) Mi-BeSAN MEA (3)	Ti/Pt/IrO_x	470	475
3^{rd}	MEA 64 (4) Mi-BeSAN MEA (4,5)	Ti/Pt/IrO_x	420	380
4^{th}	Mi-BeSAN MEA (5)	Ti/Pt/IrO_x	420	385
5^{th}	MEA 64 (4)	Ti/Pt/IrO_x	420	384

Table 3.1: SIROF stack composition and thickness for all sputtering runs (see also Table A.2) done in the scope of this thesis. The stack thickness was measured with a surface profiler.

coated with a $10 - 20$ nm thick gold layer by sputtering (SCD004 Sputter Coating Unit, Balzers AG, Liechtenstein) and introduced to the SEM (LEO1550, Carl Zeiss SMT AG, Oberkochen, Germany). Although most electrodes showed dense SIROF layers with a grainy and porous surface, some electrodes exhibited ruptured or detached stacks. The origin of these defects could not be determined with absolute certainty, but the lift-off process used for structuring the IrO_x layer was identified as a possible cause.

Secondly, EIS and CV measurements were conducted using a three electrode setup with a frequency response analyzer (1260A Impedance/Gain-Phase Analyzer, Solartron Analytical, Farnborough, UK) and a potentiostat/galvanostat (PAR 283, AMETEK Princeton Applied Research, Oak Ridge, USA) to characterize the electrochemical properties of the SIROF electrodes. After imaging in the SEM, the impedance of the SIROF electrodes was measured before and after electrochemical activation by repetitive potential cycling in physiological saline solution (unbuffered aqueous 0.9 % (w/v) NaCl) at room temperature from -0.65 V to $+0.95$ V against a Ag/AgCl reference electrode. An impedance reduction and increase of the charge storage capacity during the activation procedure could be detected. In comparison to standard gold electrodes, the SIROF electrodes proved to have a charge storage capacity up to three orders of magnitude higher and a reduced impedance. Even in comparison to electrochemically platinized gold electrodes ("platinum black", platinization procedure adapted from Thiébaud et al. [127] and described on page 39), the charge storage capacity was higher [123].

For a further comparison of the electrochemical properties of the standard gold MEAs and the first generation IrO_x MEAs, another series of EIS measurements was conducted in the scope of this work. All further electrochemical measurements (EIS and CV) were performed with another three electrode setup with a potentiostat/galvanostat (Autolab PGSTAT100, Eco Chemie B.V., Utrecht, Netherlands) and a frequency response analyzer module (Autolab FRA2, Eco Chemie). Unless stated differently, one or several electrodes of

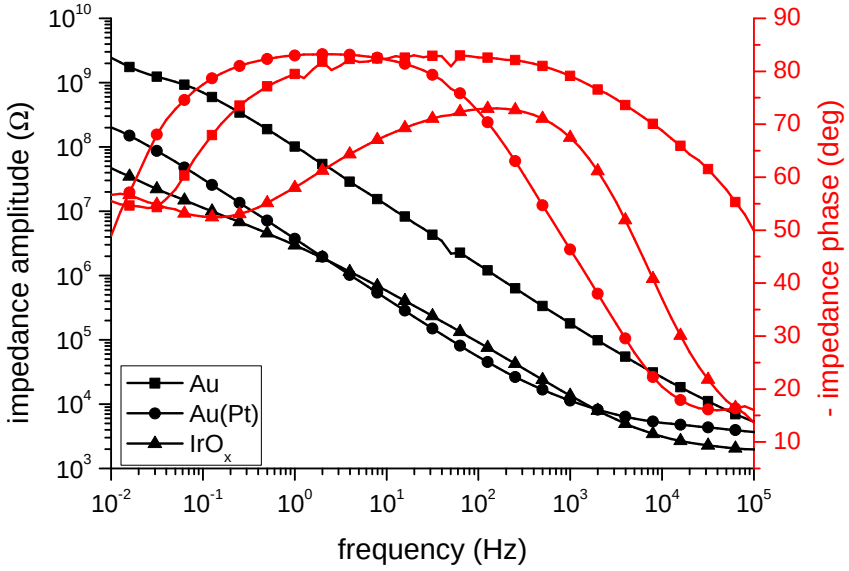

Figure 3.3: Comparison of the impedance for a gold electrode before and after platinization, as well as an IrO_x electrode from the first MEA generation after activation with cyclic voltammetry. Magnitude and phase of the impedance is shown for the electrodes, which had a diameter of 100 µm.

a MEA were used as working electrode, a platinum (Pt) wire with a surface area much larger than the area of the working electrode was used as counter electrode, and a Ag/AgCl wire was used as a quasi reference electrode. Counter and reference electrodes were immersed in electrolyte solution (saline as above) in the culture dish on top of the encapsulated MEA chip. The measurements were done either *against the potential of the Ag/AgCl wire* (vs. SSE, in this thesis done for CV) or *with respect to open circuit potential* (w.r.t. OCP, here used for EIS). For EIS, a sinusoidal input signal with an amplitude of 10 mV was used to characterize the complex impedance of the working electrode and the electrolyte solution.

Figure 3.3 shows the results of EIS measurements for a standard gold electrode and a SIROF electrode of the first MEA generation, both of which had a diameter of 100 µm. Before the impedance scan, the SIROF electrode was activated by 50 cycles from −0.7 V to +0.7 V vs. SSE (CV) with a scan rate of 100 mV/s. Usually, the *safe electrochemical window* (SECW) of IrO_x is considered covering a larger potential range than ±0.7 V vs. SSE [114–116, 126, 128]. However, this range was chosen for all CV experiments within this thesis to stay sufficiently far away from the potentials of gas evolution and to prevent damage to the electrodes in accordance with literature [56, 57, 125].

Additionally, the results of another impedance scan of the same gold electrode after deposition of platinum black are included in Figure 3.3, as well. The electrode was platinized with a procedure adapted from Thiébaud et al. [127]. Briefly, the potential of the gold sample was continuously cycled from 0.1 to −1.0 V for 50 times in the potentiostat with a solution containing 1 to 2 % potassium hexahydroxyplatinate (Platinum 3745 Solution, Engelhard - CLAL Deutschland GmbH, Dreieich, Germany) with a scan rate of 100 mV/s.

Comparing the two impedance scans for the gold electrode, it can easily be seen that the impedance is reduced by the platinization by more than one order of magnitude. However,

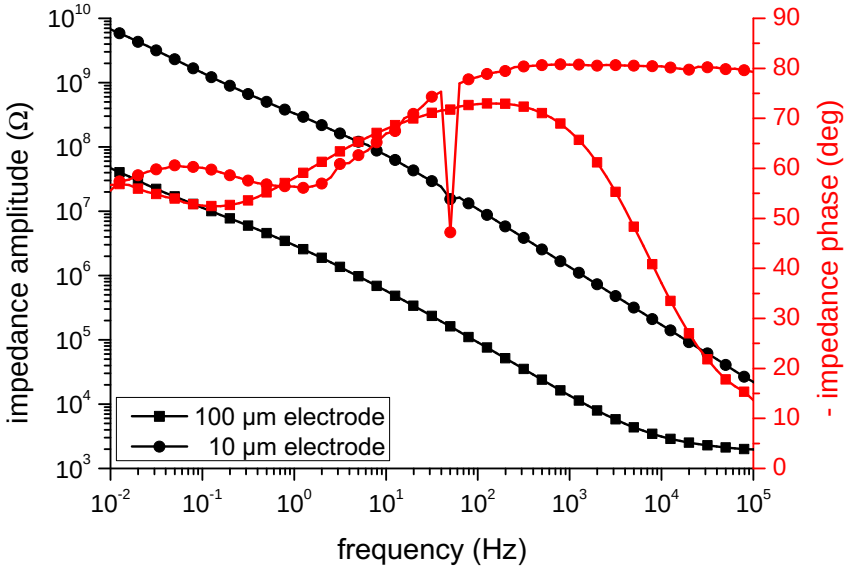

Figure 3.4: Comparison of the impedance for 10 and 100 µm IrO_x electrodes of the first MEA generation after activation by cyclic voltammetry. The magnitude and the phase of the impedance is shown for both electrodes.

in the frequency range above 20 kHz, the impedance measurements become dominated by the resistance of the bath electrolyte between the working and the counter electrode, causing convergence of both scans. The reduced impedance of the electrode arises from an increase in the surface area due to the deposited platinum black [127]. The impedance of the activated IrO_x electrode is in the same range as the impedance of the platinized gold electrode and thus also significantly reduced in comparison to the impedance of the plain gold electrode of the same size. Similar to the scans from the gold electrode, the high-frequency impedance is dominated by the resistance of the bath electrolyte. However, the distance between working and counter electrode was smaller for this measurement, explaining the slightly reduced impedance above 20 kHz. In the frequency range between approximately 2 Hz and 2 kHz, the IrO_x electrode has an impedance that is slightly higher than the impedance of the platinized electrode. In the frequencies below 2 Hz however, the impedance is increasingly dominated by a resistive component with a value below the impedance of the platinized gold electrode. This resistive component and reduced impedance can be explained by the typical faradaic processes at the surface of the IrO_x electrode (see Subsection 2.5.1).

A comparison of the impedance of two activated IrO_x microelectrodes with diameters of 10 and 100 µm is presented in Figure 3.4. As expected, the impedance of the smaller electrode is significantly higher compared to the 100 µm electrode. Basically, it resembles the course of the impedance of the bigger electrode multiplied by an approximate factor of 100 (in accordance with the 100-fold reduced electrode area), but the resistance of the bath electrolyte is negligible in comparison to the increased impedance and does not influence the high frequency range. The kink at the 50 Hz mains frequency is caused by electromagnetic interference. Table 3.2 gives an overview of impedance values at characteristic frequencies

Electrode type and [diameter] (µm)	Impedance at 100 Hz (Ω)	Impedance at 1 kHz (Ω)
Au [100]	$1.47 \cdot 10^6$	$1.76 \cdot 10^5$
Au(Pt) [100]	$5.25 \cdot 10^4$	$0.93 \cdot 10^4$
IrO_x [100]	$8.94 \cdot 10^4$	$1.16 \cdot 10^4$
IrO_x [10]	$1.08 \cdot 10^7$	$1.35 \cdot 10^6$

Table 3.2: Exemplary impedance values at 100 and 1000 Hz of zeroth generation gold and platinized gold (Au(Pt)) electrodes, as well as first generation IrO_x electrodes as determined from the EIS measurements. The impedance of the electrolyte solution (in the order of a few kΩ) was estimated from the impedance at high frequencies and subtracted.

taken from the scans in Figures 3.3 and 3.4.

Figure 3.5 shows the last cycle of the activation of a 100 µm and a 10 µm IrO_x electrode used for the impedance scans in Figure 3.3 and 3.4. Using this last scan for both electrodes, the specific cathodal charge storage capacity (q_{CSC}) was calculated as the integral of the negative current divided by the electrode area [105,124]. The resulting values of 4.91 (100 µm electrode) and 7.91 mC/cm^2 (10 µm electrode) are well within the range of literature values for activated IrO_x [57,104,105,108–110,112] and show the functionality of the SIROF electrodes. The observed increased q_{CSC} of the smaller electrode can be explained by nonuniform current distributions and transport limitations for larger electrodes [105].

In summary, the MEAs of the first generation contained a sufficient number of working activated IrO_x electrodes with good electrochemical properties to perform electrophysiological measurements. The protein-coated (compare Appendix C) ONO passivation stack had already been shown to be biocompatible and to allow the growth of electrogenic cells [122,129,130]. Also, the biocompatibility of IrO_x layers had been shown in the past [110], and was again proven by the growth of cortical rat neurons on the IrO_x MEAs of the first generation [123]. Therefore, extracellular stimulation experiments with rat cortical

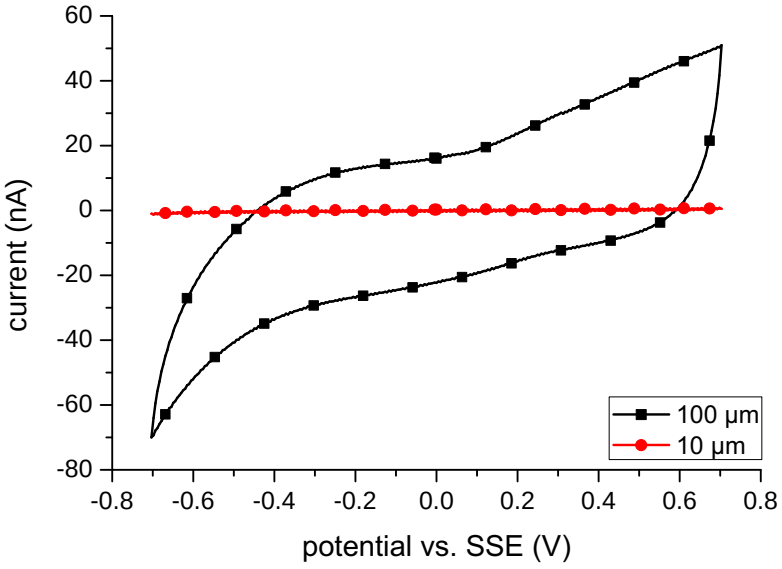

Figure 3.5: Fiftieth scan of cyclic voltammograms of SIROF electrodes with a diameter of 10 and 100 µm from the first MEA generation. The scan was done with a scan rate of 100 mV/s and used for calculation of the electrode's cathodal charge storage capacity.

neurons could be conducted with these MEAs as described in Section 5.1.

In the scope of repetitive cell cultures with the first generation MEAs, it was found that the SIROF coatings of the electrodes were not sufficiently stable and detached with increasing time under cell culture conditions. In combination with the initial detachment problems caused by the lift-off process, the yield of working electrodes was found unsatisfactory. Additionally, the number of available gold MEA wafers for post-processing was strictly limited to a small stock, since passivation with the ONO stack was no longer available for the production of new MEAs (compare Subsection A.1.2). For both reasons, new processes for the production of more stable SIROF MEAs with a dense and stable passivation layer were developed and investigated.

3.1.2 New Iridium Oxide MEAs

New MEA Chip Design

As described more thoroughly in the appendix (see Subsection A.1.2), the second and the third generation of MEAs did not result in reliably working IrO_x MEAs that could be used for electrophysiological measurements. Briefly, the second generation was produced with a new passivation layer composed of the resist Parylen C, which was not mechanically stable enough for repetitive cell cultures. The third generation of MEAs was therefore produced with a new passivation made of six alternating layers of Si_3N_4 and SiO_2 (NONONO stack). Although this passivation layer proved to be stable and dense [131], the MEAs could still not be used since the SIROF stack detached from the electrode surface during cell culture.

A solution for this problem was found for the fourth MEA generation by inverting the process steps for the passivation and SIROF stack deposition. After structuring of the bond pads, contact lines, and electrodes, the SIROF stack consisting of 20 nm titanium, 100 nm platinum and 300 nm IrO_x was deposited on the electrodes. The titanium promotes adhesion to the electrodes, and the platinum forms a protective layer against the electrolyte solution, which otherwise could diffuse through the porous IrO_x and cause oxidation of the titanium. After that, the chips were passivated with a 850 nm thick NONONO stack that was then opened at the bond pads and electrodes. Details about the process can be found in Subsection A.1.2, and the resulting layer structure of the fourth generation MEAs can be found in Figure A.3.

The design of the fourth generation IrO_x MEAs is depicted in the form of the three process masks in Figure 3.6. Like the MEAs of the zeroth and first generation, the new chips were designed as arrays of 8×8 gold microelectrodes (see Figure 3.6.b). A sensor pitch of 200 µm between the electrodes was chosen. This time, the electrode diameters were kept at 50 µm for all electrodes on all chips (see Figure 3.6.c). The increased electrode size was

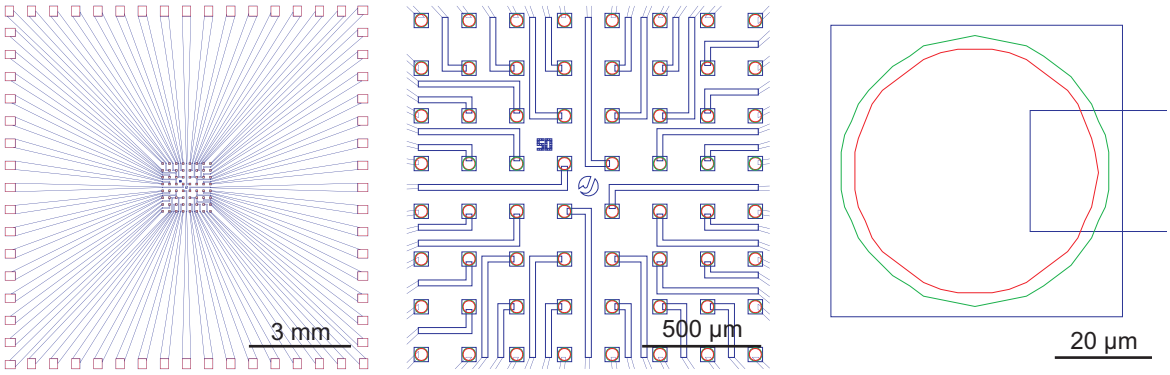

(a) (b) (c)

Figure 3.6: Process masks of fourth generation MEAs with IrO_x electrodes shown for the complete chip (a), the active sensor area with all 64 electrodes (b), and one single electrode (c). The blue mask is used to structure the metalization for bond pads, contact lines, and electrodes. The SIROF stack deposition is structured with the green mask, and the bond pads and electrodes are opened after passivation using the red mask.

chosen to get a higher yield of electrogenic cells completely positioned on a single electrode for a defined experimental condition for extracellular stimulation. Before electrochemical characterization and electrophysiological experiments, the chip encapsulation was again done in the same way as for standard MEAs, resulting in final chips with a cell culture chamber similar to the old MEAs depicted in Figure 3.1.a.

New MEA Characterization

The fourth generation MEAs used for the electrophysiological measurements introduced in Chapter 5 were coated with the SIROF deposited in the third sputtering run (see Table 3.1). The measured stack thickness of 380 nm was a little thinner than the expected (420 nm), most likely indicating a thinner platinum and IrO_x layer.

As a first step to characterize the new MEAs, non-encapsulated chips were again investigated by SEM. Figure 3.7 shows two exemplary SEM images of a SIROF electrode from a fourth generation MEA. The electrodes were completely covered with a dense IrO_x layer. Especially at higher magnification of the electrode surface (see Figure 3.7.b), the porous SIROF is clearly visible.

The new process flow resulted in an excellent yield of microelectrodes with a dense IrO_x layer completely covering the underlying substrate. In contrast to previous MEA generations, almost no defects, such as cracks or detachment of the SIROF stacks, could be found in the SEM.

To characterize the electrochemical behavior of the new IrO_x electrodes, EIS and CV were utilized as described for the zeroth and first generation MEAs. In a first step, the

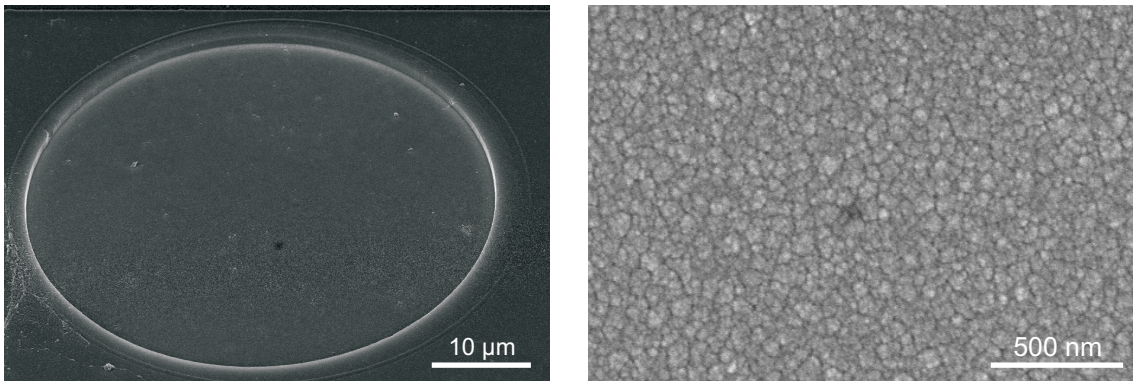

(a) (b)

Figure 3.7: SEM images of SIROF electrode of the fourth MEA generation. For a complete electrode (a), and especially for a magnification of the IrO_x surface (b), the grainy structure of the SIROF surface can be seen.

SIROF stack was investigated and compared to other materials by performing EIS with large unstructured samples that were processed in the same sputtering run as the MEAs. Figure 3.8 shows the results of EIS scans of an untreated SIROF sample, a plain gold sample, and a gold sample after deposition of platinum black (platinization done as described for MEAs in Subsection 3.1.1). All three samples had a surface area of 0.5 cm^2 in contact with the electrolyte solution.

In the frequency range up to a few hertz, the impedance of the platinized gold sample is approximately a factor of 40 lower than the impedance of the plain gold sample, indicating a significantly increased surface area and double layer capacitance. For higher frequencies, the impedance scans become dominated by the resistance of the electrolyte solution in the experimental configuration, concealing the impedance of the metal-electrolyte interface.

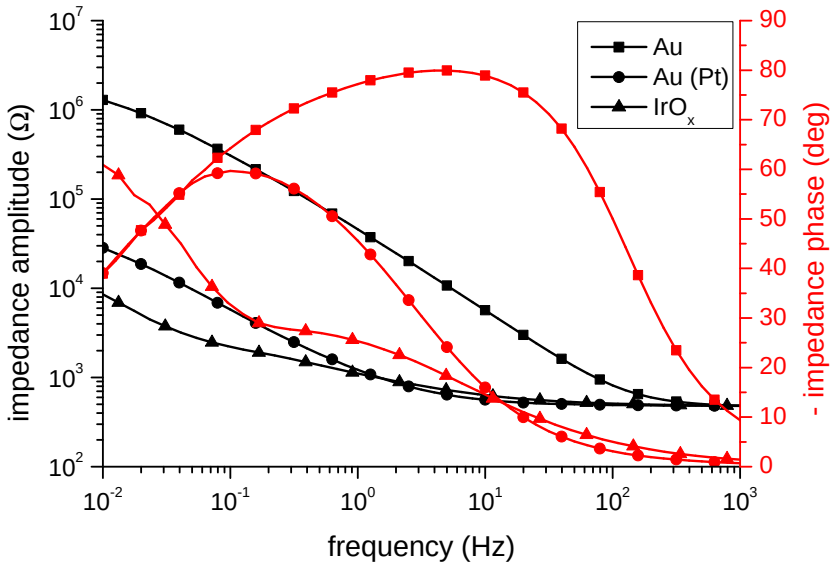

Figure 3.8: Comparison of the impedance of a plain and platinized gold sample, as well as an untreated SIROF sample. Magnitude and phase of the impedance is shown for all three samples, which had a surface area of 0.5 cm^2.

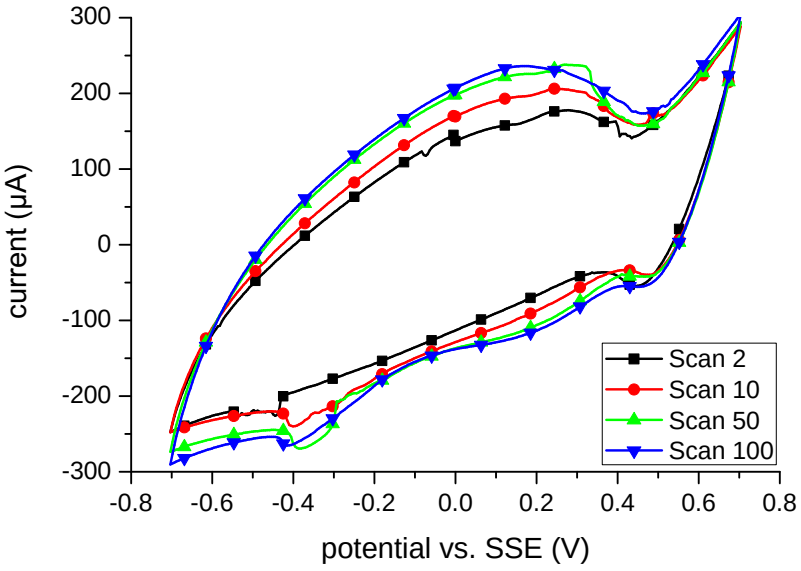

Figure 3.9: Selected cycles from a cyclic voltammetry measurement during the activation of a 0.5 cm^2 IrO_x sample with 100 cycles and a scan rate of 100 mV/s. The increase in the charge storage capacity gradually weakens from cycle to cycle.

Despite this strong decrease of the impedance caused by the platinization, the interface between the untreated SIROF and the electrolyte shows an even lower impedance than the platinum black. Especially in the low frequency regime, a further decrease by a factor of 3 to 4 can be observed, which is attributed to a combination of a significantly increased surface area of the sample, a high double layer capacitance, and a faradaic contribution to charge transfer across the interface.

As already stated in Subsection 3.1.1, the impedance of IrO_x electrodes can be further reduced through activation by continuous potential cycling [108, 114]. To investigate this behavior for our IrO_x electrodes, the potential of the SIROF samples was cycled between -0.7 V and $+0.7$ V vs. SSE (CV) for 100 cycles with a scan rate of 100 mV/s. Figure 3.9 shows four selected scans of the CV performed to activate the sample used for the EIS measurement presented in Figure 3.8. In the course of the cycles, the current flowing across the SIROF/electrolyte interface increases indicating a growing charge storage capacity due to the activation. Calculating the specific cathodal charge storage capacity from the scans shown in Figure 3.9, an increase from 3.84 mC/cm^2 in the second scan to 4.72 mC/cm^2 in scan number 100 is found. With an increasing number of cycles, the change in q_{CSC} from one scan to the next decreases gradually. The increase in the current during the first ten scans is approximately the same as the change during the next 40 scans. Subsequents scans showed no substantial change in the charge storage capacity anymore until the hundredth cycle. Thus, it was concluded that 50 cycles suffice for initial activation of the SIROF layers.

After activation of the sample, another EIS measurement was done as presented in Figure 3.10. It can easily be seen that the impedance of the electrode is even further reduced by the potential cycling. Also, the shape of the EIS curve changes slightly in the

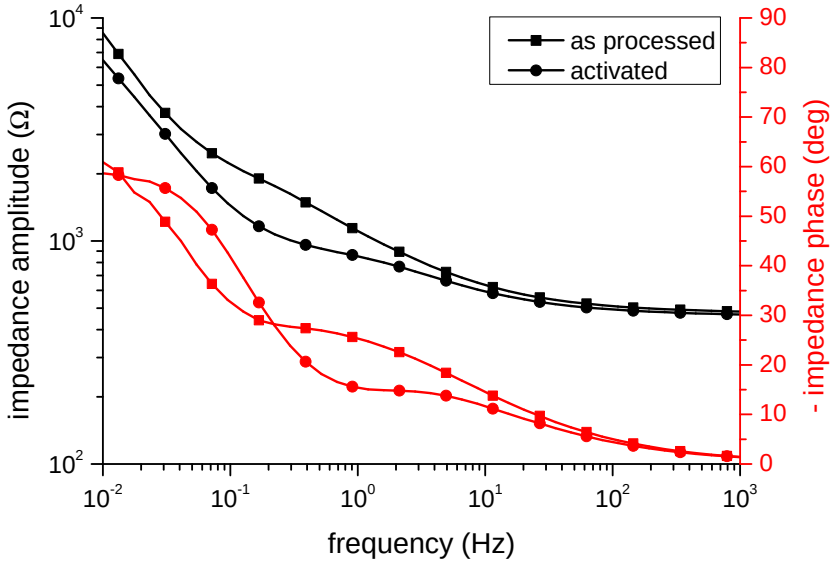

Figure 3.10: Comparison of the impedance of an untreated and an activated SIROF sample with a surface area of 0.5 cm^2. The magnitude and phase are shown for both samples.

frequency range between approximately 30 mHz and 10 Hz. The untreated IrO_x has an elevated impedance in that frequency range, which can be commonly found in porous electrode materials like IrO_x [109, 113, 114, 132, 133]. During the cycling process, this elevated impedance is reduced, which can be explained by a change in the morphology and porosity of the SIROF stack.

The results of the first electrochemical investigations with the large samples suggest a low-impedance interface between the untreated and especially the activated SIROF stack and the electrolyte solution. Even in comparison to platinized gold, the SIROF exhibits a lower impedance and promises to be nicely suited for stimulation electrodes. The specific cathodal charge storage capacity corresponds to literature values and is even slightly higher than for the first generation IrO_x MEAs.

Electrochemical measurements were conducted for electrodes of the fourth generation MEAs and again compared to other electrode materials. The impedance of a freshly encapsulated SIROF electrode is depicted in comparison to a gold electrode of the same size in Figure 3.11. The gold electrode was processed in the same way as the IrO_x electrode, but without the sputtering step for deposition of the SIROF stack. After the EIS measurement, the gold electrode was coated with platinum black as described before (see page 39) and measured again. Without any electrochemical pretreatment, the impedance of the new IrO_x electrode is very similar to the impedance of the plain gold electrode and less than a factor of two lower across the whole frequency range. The platinized gold electrode on the other hand shows an impedance, which is significantly reduced by almost two orders of magnitude in comparison to the plain gold and by more than one order of magnitude compared to the untreated IrO_x electrode. This unexpectedly high impedance was observed before for untreated SIROF MEAs [134], and most probably originates from residues of the

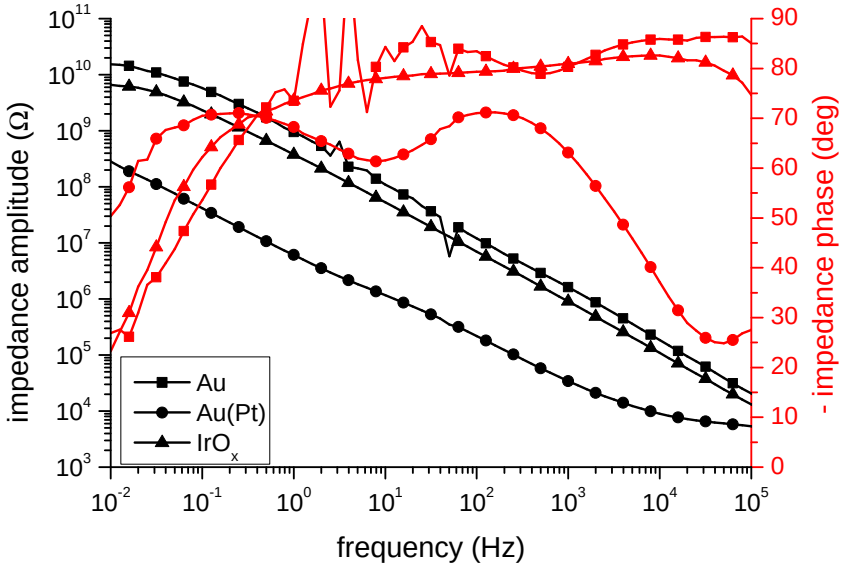

Figure 3.11: Comparison of the impedance for a plain and a platinized gold electrode, as well as a freshly encapsulated IrO_x electrode of the fourth MEA generation. Magnitude and phase of the impedance is shown for all electrodes, which had a diameter of 50 µm.

process steps after SIROF deposition that remain on the electrode surface. As shown in this subsection, this initial impedance can easily be reduced by a process called *pretreatment* or *conditioning* [134], which is equivalent to the procedure for activation of the IrO_x: the electrode potential is cycled between −0.7 V and +0.7 V vs. SSE (CV) for a few cycles with a scan rate of 100 mV/s. Due to the potential change during the conditioning, the electrodes are cleaned from all process residues, and by extending the number of cycles to 50, the activation of the SIROF electrodes can be included in the same step.

Figure 3.12 shows an impedance scan of the same electrode after conditioning and activation as described above in comparison to the initial impedance. After the electrochemical treatment, the impedance of the SIROF/electrolyte interface is reduced by more than one order of magnitude and qualitatively resembles the course of the impedance for a 0.5 cm^2

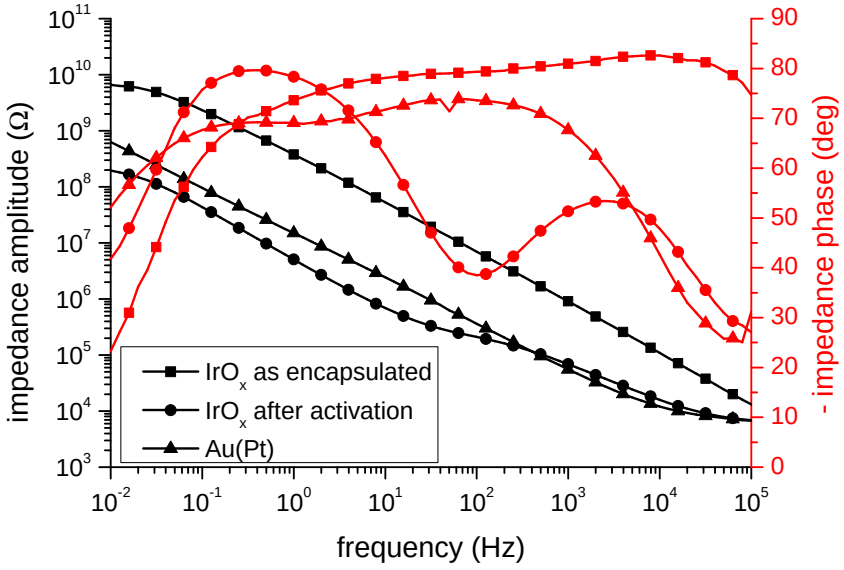

Figure 3.12: Comparison of the impedance of an IrO_x electrode of the fourth MEA generation before and after conditioning and activation by potential cycling, as well as a platinized gold electrode. Magnitude and phase of the impedance is shown for all scans, and all electrodes had a diameter of 50 µm.

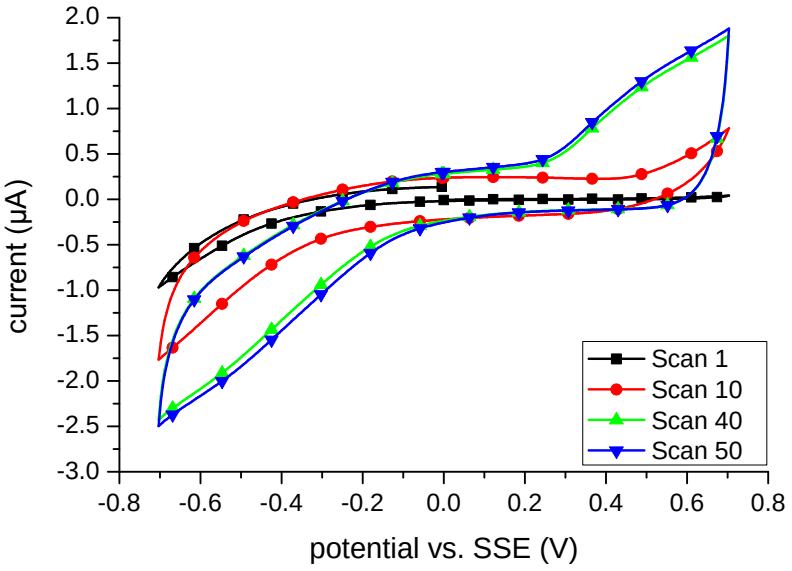

Figure 3.13: Selected cycles from a voltammetry measurement during the activation of all 64 electrodes (50 µm) of a fourth generation IrO_x MEA by 50 cycles with a scan rate of 100 mV/s. The current initially increases strongly as associated with the conditioning of the electrodes. The activation in the following cycles causes a further increase, which gradually plateaus with higher scan numbers.

IrO_x sample (compare Figure 3.10). Even in comparison to the platinized gold electrode, the impedance is lower for most frequencies after the conditioning and activation.

Four selected cycles during the process of the conditioning and activation of a complete array of 64 electrodes is shown in Figure 3.13 to visualize the change of the charge storage capacity during the electrochemical treatment. During the first few scans, the flowing current significantly increases as the residues from the production process are cleaned off from the electrodes (conditioning). After approximately 10 cycles, the further activation of the IrO_x only causes a slow further increase in q_{CSC}, which gradually plateaus with a rising number of cycles. Calculation of q_{CSC} from the activation of all 64 electrodes of 15 MEAs resulted in an initial value of 1.74 ± 0.62 mC/cm^2 (first scan) and a final value of 7.15 ± 1.73 mC/cm^2 after 50 cycles. This value is even higher than the value for the 0.5 cm^2 sample, which can again be explained by nonuniform current distributions and transport limitations for larger electrodes [105].

As can be seen in Figure 3.14, the impedance of the SIROF electrodes after conditioning and activation is consistent for electrodes at various positions in the array and between different MEAs. The impedance of the SIROF electrodes is significantly lower than the impedance of gold electrodes, and in the range of or even lower than the impedance of platinized gold electrodes. Table 3.3 gives a summary of the impedance magnitude at 100 and 1000 Hz of the fourth generation MEA electrodes with plain and platinized gold, as well as conditioned and activated SIROF.

Summing up the results from electrochemical characterization of the new fourth generation SIROF MEAs, it can be stated that the new electrodes exhibit a high charge storage capacity and an impedance that is significantly lower than the impedance of plain gold electrodes and on the same order of magnitude or even lower than the the impedance of

Electrode type	Impedance at 100 Hz (Ω)	Impedance at 1 kHz (Ω)
Au	$1.76 \cdot 10^7$	$1.88 \cdot 10^6$
Au(Pt)	$3.56 \cdot 10^5$	$4.93 \cdot 10^4$
IrO_x	$(2.48 \pm 0.37) \cdot 10^5$	$(6.98 \pm 0.94) \cdot 10^4$

Table 3.3: Impedance values at 100 and 1000 Hz of fourth generation MEA electrodes with a diameter of 50 µm. Exemplary values are given for plain and platinized gold electrodes, and mean values ± standard deviation (n=5) are given for conditioned and activated SIROF electrodes as determined from the EIS measurements. The impedance of the electrolyte solution (in the order of a few kΩ) was estimated from the impedance at high frequencies and subtracted.

platinized electrodes of the same size. Although both kinds of low-impedance electrodes need an electrochemical preparation step (platinization or conditioning and activation), the SIROF electrodes have the substantial advantage of mechanical stability. The platinization of the gold electrodes is easily destroyed mechanically during the standard cleaning protocol (see Section B.3), and a new platinization is required before every cell culture. On the other hand, the IrO_x electrodes can be cleaned and re-used for several cell cultures. Additionally, the platinum black has the further disadvantage that it is visualized as a dense black area in DIC images, making it difficult or even impossible to see single cells and perform patch-clamp experiments for simultaneous intracellular measurements.

Besides the necessity for good electrochemical properties of the electrodes, it is extremely important that the materials used for electrodes, passivation and packaging of the MEAs are stable under cell culture condition, biocompatible, and allow the growth of the investigated cells. The first results of a biocompatibility study are shown in Figure 3.15 in the form of SEM images of fixed rat cortical neurons on material samples and uncoated chips. The

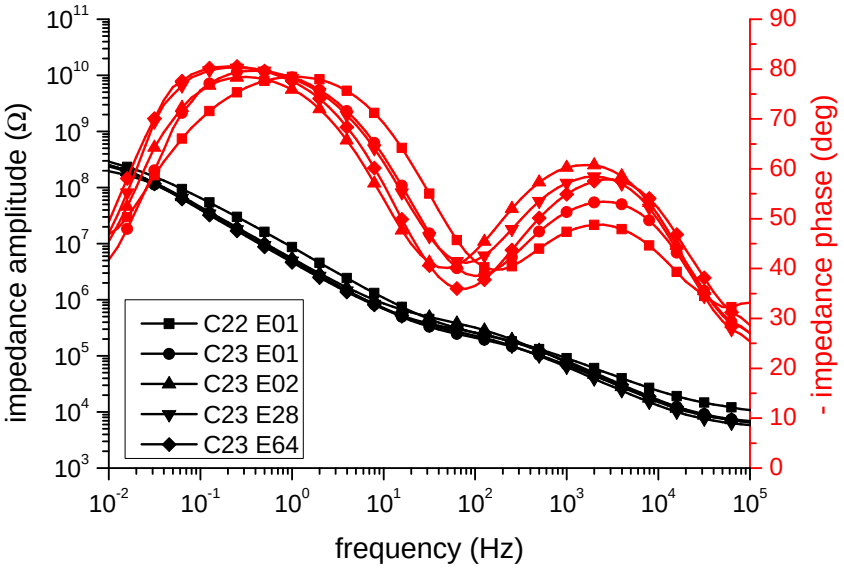

Figure 3.14: Impedance of several 50 µm fourth generation IrO_x electrodes after conditioning and activation. The impedance is found to be very similar for electrodes in various positions at the edges and in the center of the sensor arrays and also for two different chips. Magnitude and phase of the impedance is shown for all scans.

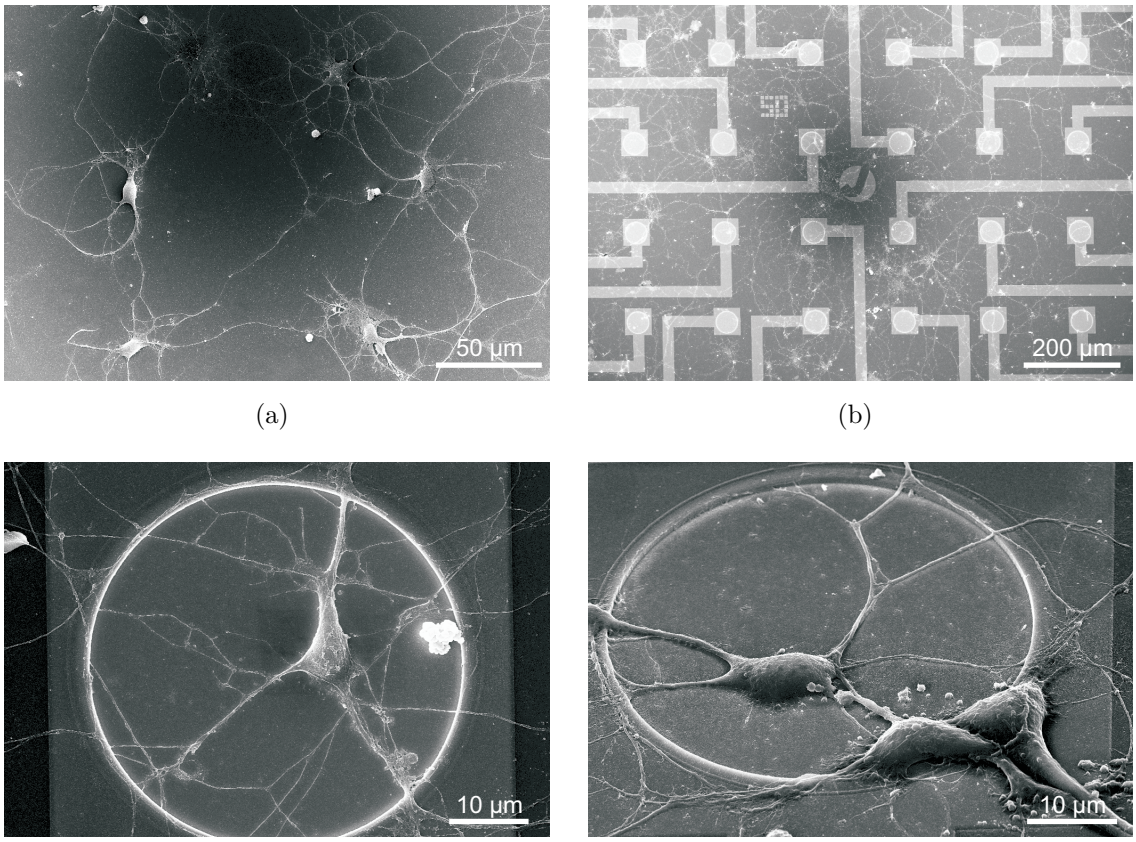

(a) (b)

(c) (d)

Figure 3.15: SEM images of DIV 6 to 7 fixed rat cortical neurons on a sample with NONONO passivation (a) and non-encapsulated SIROF MEAs of the fourth generation (b-d). The cells grew nicely on the samples and the SIROF MEAs, forming a dense network of cells and possible interconnects by their processes (a-b). Examples of the desired situation of a single cell located on a 50 µm IrO_x electrode for extracellular stimulation is shown in perpendicular view (c) and with a tilt angle of 45° (d).

fixing and imaging of the cells was done as described in Section C.1 of the appendix.

In a first step, the biocompatibility of the NONONO stack used for the passivation of the electrodes was tested by growing rat cortical neurons on large samples coated with the passivation stack [131]. The NONONO samples were coated with a protein mixture, and the cells were cultured on the samples as described in the appendix (see Section C.1) for more than one week, which is long enough to perform electrophysiological measurements on single cells. After 6 to 7 *days in vitro* (DIV), the cells were found nicely attached and growing on the NONONO surface (see Figure 3.15.a). They showed distinct neurite outgrowth and formed a dense network of processes which could potentially form synapses between the cells. A similar growth behavior was found on non-encapsulated IrO_x MEAs of the fourth generation (Figure 3.15.b). The cells also attached nicely to the surface and could be cultured for more than one week. Since the stimulation experiments introduced

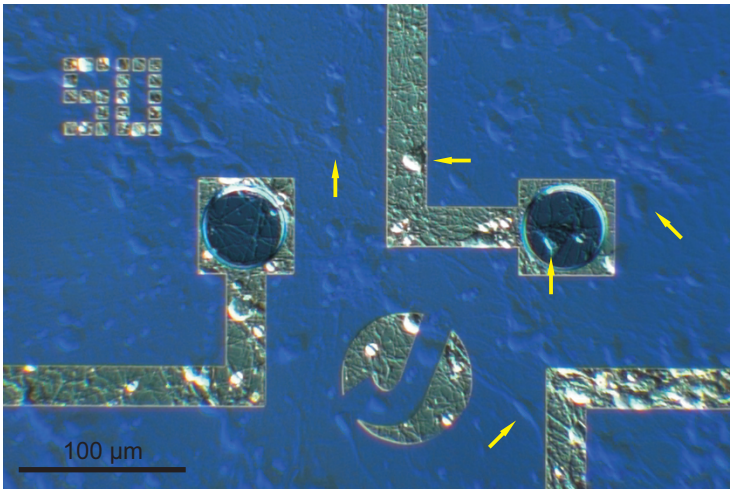

Figure 3.16: DIC image of rat cortical neurons (DIV 6) growing on the surface of a fourth generation SIROF MEA. A high number of cells with a dense networks of cell processes can be seen, indicating a healthy neuronal culture. Yellow arrows indicate the position of some of the cell bodies on the chip surface.

in Chapter 5 were usually done at DIV 6 or 7, the cells were also fixed on those days. At that time, the cells already grew a dense network of cell processes with possible neurite interfaces for synapse formation. Figure 3.15.c and 3.15.d show the experimental condition used for single-cell extracellular stimulation experiments with a 50 µm IrO_x electrode as introduced in Section 5.2.

Also after encapsulation, the chips of the fourth MEA generation were suited to culture rat cortical neurons. Figure 3.16 shows a DIC image of a part of the surface of a SIROF MEA with a culture of rat cortical neurons (DIV 6) directly before an electrophysiological experiment was conducted. A high number of cells can be seen on the whole chip surface including the passivated gold contact lines as well as the electrodes. The cells exhibit a high number of neurites, indicating a healthy neuronal culture.

To further investigate the experimental situation during extracellular stimulation and the layer structure of the SIROF electrodes, *focused ion beam* (FIB) cuts (CrossBeam 1540 XB, Zeiss SMT) of fixed cells on fourth generation MEA electrodes were made and investigated by SEM imaging (LEO1550, Zeiss SMT). Figure 3.17 shows two SEM images of a FIB cut. The cell body was completely located on the microelectrode, with some cell processes growing out of the electrode area (see Figure 3.17.a). A magnification of the interface between cell, electrode, and the underlying electrode layers was made to investigate the thickness of the materials in the SIROF stack (see Figure 3.17.b). In accordance with the thickness measurements from the surface profiler, the overall SIROF stack thickness was found to be approximately 360 to 370 nm, consisting of 220 nm IrO_x, 120 nm platinum and roughly 25 nm titanium. The thickness of the gold layer from the basic electrode metalization was found to be 210 nm. As already stated, the SIROF stack was thinner than expected from the process parameters (compare Table 3.1 and Subsection A.1.2), and especially the IrO_x layer thickness could be slightly increased for future processes.

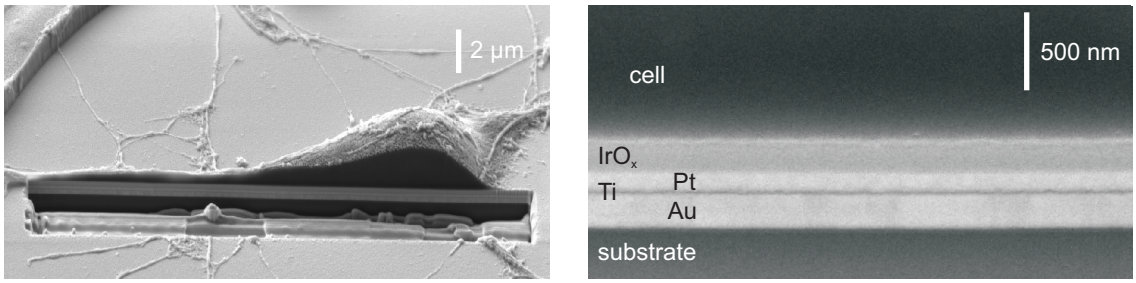

(a) (b)

Figure 3.17: SEM images of FIB cut through a fixed rat cortical neuron on a 50 µm SIROF electrode. The complete cell body was attached to the IrO_x microelectrode, with some neurites growing out of the electrode area (a). A magnified view of the electrode layers and the interface between the cell body and the electrode reveal the different material layers of the SIROF stack. Both images were taken at an angle of 54°.

3.1.3 Summary and Discussion of the Results

MEAs with 64 microelectrodes carrying functional SIROFs for *in vitro* studies with electrogenic cells were produced and characterized concerning their surface structure and electrochemical properties. The first three advanced generations of MEAs had unstable SIROF layers, which detached during ongoing exposure to electrolyte solutions. This problem could be overcome by alterations of the production process for the fourth generation IrO_x MEAs, which proved stable in electrolyte solutions over several weeks of repeated cell culture.

Using SEM imaging, the surface structure of the functional SIROFs on the microelectrodes for the first and fourth MEA generations was found to be rough and porous, greatly increasing the electrochemically active surface area. The imaged microporous surface structure was comparable to IrO_x surfaces presented in other studies [42, 57, 114]. As shown in several publications, the surface roughness severely depends on the production process and can be further increased for even larger surface areas by variation of process parameters such as number of activation cycles and oxygen flow during sputtering [114, 116, 135]. Nevertheless, the surface structure and roughness found for the SIROFs on the MEAs used in this work was promising for their electrochemical properties.

Examination of the MEAs with CV and EIS measurements revealed the high charge storage capacity and the low impedance caused by the increased surface area and the faradaic charge transfer at the SIROF surface. With values between roughly 4 and 8 mC/cm^2, the cathodal charge storage capacity of the microelectrodes was found to be higher than for other electrode materials such as plain and platinized gold, platinum, and *titanium nitride* (TiN) and within the range (roughly 1 to 25 mC/cm^2) of other IrO_x film electrodes [57, 104, 105, 108–110, 112]. Even higher values for the charge storage capacity, more

than 100 mC/cm^2, have been reported in the past [56, 114, 126, 135]. Nevertheless, the achieved charge storage capacity severely depends on several material and experimental parameters such as the film thickness, the electrolyte solution, the number of activation cycles, and the potential range used for the calculation of the delivered charge. The variation of these parameters between publications complicates a comparison.

The results of the EIS measurements proved the low impedance of the SIROF microelectrodes in the whole frequency range investigated. The impedance was significantly reduced in comparison to plain and in the same range as or lower than the impedance of platinized gold electrodes. A comparison to literature values for TiN electrodes with a similar size also reveals equivalent impedance scans [54, 57].

In addition to the good electrochemical properties, the SIROF MEAs of the fourth generation were also found to be biocompatible and mechanically stable. They could be used for several cell cultures and electrophysiological experiments with subsequent application of a cleaning procedure. This constitutes a significant advantage over platinized electrodes, since the platinization is usually removed during the chip cleaning step and has to be renewed after every cell culture.

In summary, the fourth generation MEAs with SIROF electrodes were shown to be well suited for extracellular electrophysiological measurements *in vitro* and especially the stimulation of electrogenic cells. This was proven by successful extracellular stimulation of individual neurons from dissociated cultures, and the extracellular recordings of action potentials from HL-1 cells, as presented in Sections 5.2 and 5.4 of this thesis.

3.2 Mi-BeSAN Chips

In the scope of the research project "Mikroelekronische Bauelemente zur Stimulation und Ableitung von Neuronen" (Mi-BeSAN) funded by the "Deutsche Forschungsgemeinschaft" (DFG), a chip for the non-invasive investigation of neuronal networks *in vitro* was developed. The Mi-BeSAN chip implemented the combination of p-type FETs for recording and SIROF microelectrodes for stimulation of electrically active cells. Previously, both devices had been characterized individually and tested and were now integrated on a single chip to combine their advantages for the bidirectional coupling of cells. A similar approach with separated devices for stimulation and recording had already been taken by Stett et al. with a combination of silicon transistors and capacitors [136].

The production process of this chip [131, 137] is a combination of a process for a planar p-type FET, which was developed and characterized in the scope of a diploma thesis [84], and the process for the SIROF MEAs already introduced in this thesis. The ultra-flat p-FET design is necessary and especially well-suited for the further processing of the mi-

croelectrodes in close proximity to the FET gate. The Mi-BeSAN chip process itself is explained in the appendix of this thesis (see Section A.2), and the complete process flow can be found in the diploma thesis by Kotman [131].

3.2.1 Mi-BeSAN Chip Design

Like the process, the design of the Mi-BeSAN chip is also based on the planar p-FETs developed in preliminary work [84]. Additionally, the chips carry SIROF microelectrodes located in direct proximity to the gate area of the FETs.

Three different experimental electrode designs were chosen and processed for three different chip configurations (see Figure 3.18). The various colors represent several important masks, which are being used in the production process. The transistor and electrode contact lines are shown in light blue and magenta, respectively. The brown color indicates the position of the deposited IrO_x, which is slightly larger than the underlying basic metalization. The dark blue areas represent the mask for final opening of the passivation. For this mask, the dark blue square in the center of each chip is only framed to show the underlying structure of the gate plateau as well as the implanted drain and source areas indicated in orange and red, respectively. While the button (Figure 3.18.a) and the ring (Figure 3.18.b) electrodes just realize a geometry surrounding the gate area with two different electrode sizes, the quad configuration (Figure 3.18.c) actually consists of four individually addressable electrodes.

Figure 3.19 shows the two basic designs of the Mi-BeSAN chips. For the button and the ring electrode chips, the sensor spots are arranged in an 4 × 4 array as shown for the ring

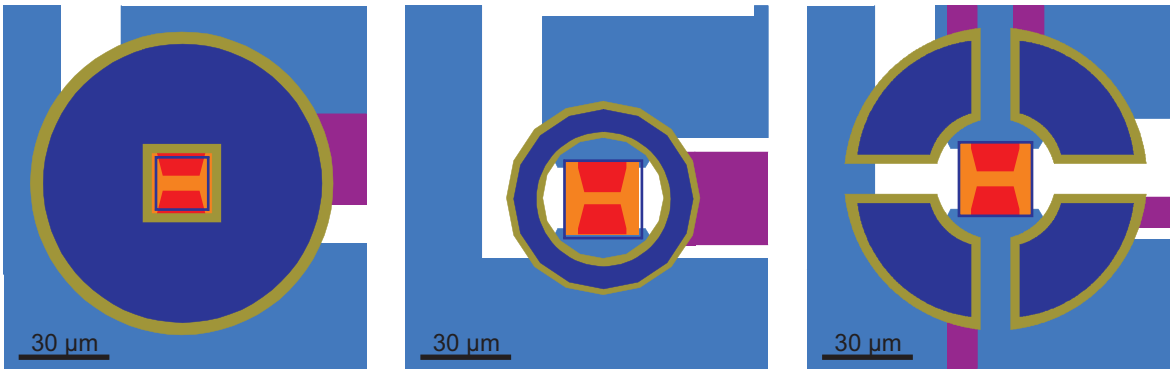

(a) button electrode (b) ring electrode (c) quad electrode

Figure 3.18: Button (a), ring (b), and quad (c) electrode configurations of the Mi-BeSAN chips. The contact lines of the transistors and electrodes are shown in light blue and magenta, the gate plateau and the implanted drain and sources areas in orange and red, respectively. The IrO_x is denoted brown, and the opening through the passivation is indicated by the dark blue areas and the interior of the dark blue square in the center of each chip.

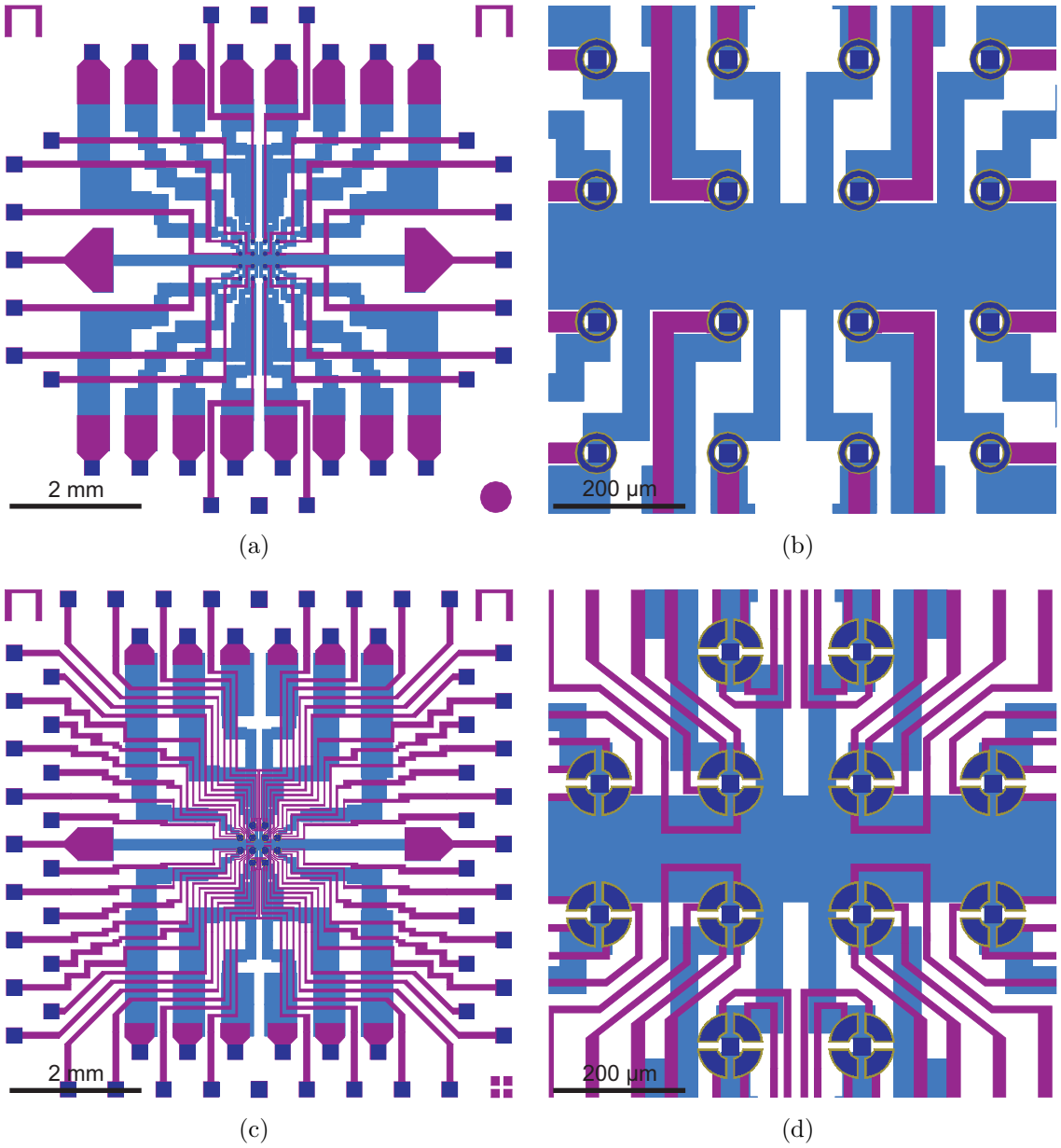

Figure 3.19: Whole chip (a and c) and magnification of the sensor array (b and d) for the two different basic Mi-BeSAN designs. The ring electrode chips (a and b) are arranged in an array of 4×4 interfacing spots with one FET and one electrode each equivalent to the button electrode layout. The quad electrode chips (c and d) have only 12 interfacing spots with one FET and four electrodes each. The colors are according to the same masks as shown in Figure 3.18.

electrode chips in Figures 3.19.a and 3.19.b. The chips with the quad electrode design (see Figure 3.19.c and 3.19.d) carry a reduced number of 12 interfacing spots (with 12 FETs and 48 electrodes) on each chip, since the amplifier systems are limited to 64 channels. The colors in Figure 3.19 indicate the same process masks as shown in Figure 3.18. Table 3.4 gives a summary of the differences between the different kinds of Mi-BeSAN chips, including the surface area of one single electrode.

Table 3.4: Summary of the differences in the three Mi-BeSAN chip designs.

Chip type	Number of FETs	Number of electrodes	Electrode surface (cm^2)
Button	16	16	$5.97 \cdot 10^{-5}$
Ring	16	16	$1.48 \cdot 10^{-5}$
Quad	12	48	$9.04 \cdot 10^{-6}$

At the beginning of the Mi-BESAN project, the process for the SIROF microelectrodes had not been implemented and tested for functionality and stability. Therefore, the three chip designs were first tested for structuring and stability with a simplified process, implementing only the microelectrodes on plain glass or silicon substrates.

3.2.2 Characterization of Mi-BeSAN MEAs

The simplified process for the Mi-BeSAN MEAs is very similar to the process used for standard 64-electrode MEA fabrication and is explained in Subsection A.1.3 of the appendix. As explained there, the first Mi-BeSAN MEAs were processed together with the third and fourth generation of standard 64-electrode MEAs. These third and fourth generation Mi-BeSAN MEAs were built up and encapsulated as described in Section B.2, and tested for their stability under cell culture conditions in the scope of a diploma thesis [131].

Figure 3.20.a shows a DIC image of four electrodes of a third generation button electrode chip after seven days of cell culture with rat cortical neurons. While the button electrode on the top left looks perfectly flat with cells growing across the IrO_x surface, the other three

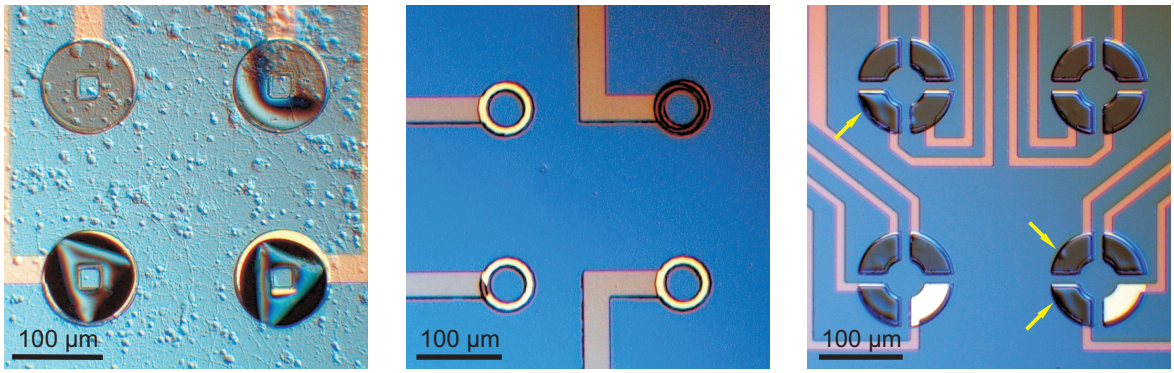

(a) (b) (c)

Figure 3.20: DIC images showing detachment of the grey SIROF stack from third generation Mi-BeSAN MEA electrodes with button (a), ring (b), and quad (c) design. After seven days in cell culture with rat neurons, cambering and undulation of the SIROF stacks could be observed (a). After several days of cell culture and cleaning of the chip surface with ethanol and a cotton swab, some of the SIROF stack detached completely (b and c). Yellow arrows show additional defects suggesting that further detachment can be expected (c).

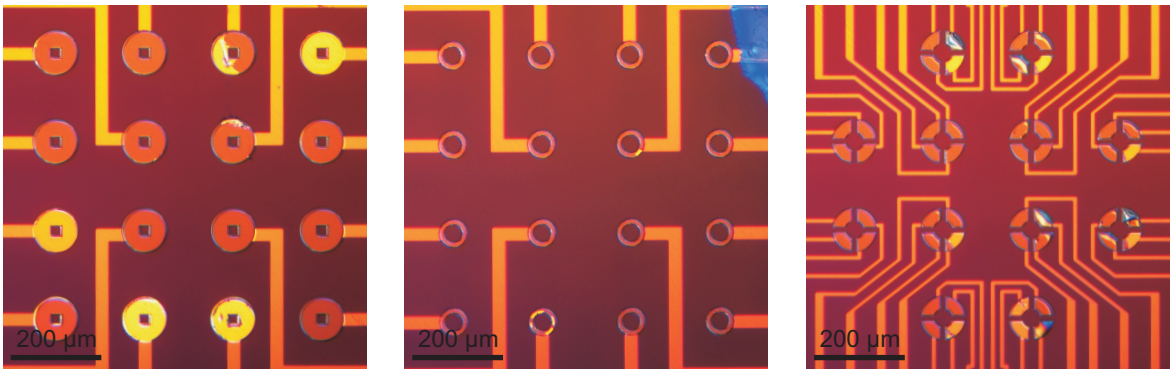

(a) (b) (c)

Figure 3.21: Also for the fourth generation of Mi-BeSAN MEAs, a detachment of the SIROF stack after one week of cell culture and cleaning could be seen for button (a), ring (b), and quad (c) electrodes. Bright yellow areas on the electrodes indicate spots, where the SIROF stack is already peeled off. The blue contamination in the top right corner of the ring electrode chip (b) is resist from the encapsulation procedure.

electrodes all show signs of SIROF stack detachment. The stack seems to camber, undulate, and detach from the gold surface of the basic metalization underneath. Investigating ring and quad electrodes, a similar behavior could be observed. Figures 3.20.b and 3.20.c show DIC images of four ring electrodes and four times four quad electrodes, respectively, after several days of cell culture with rat neurons and subsequent cleaning with a cotton swab and ethanol. On both chip types, several of the electrodes lost the SIROF stack and revealed the metalization underneath. Especially for the quad electrodes, small defects of the remaining IrO_x electrodes can already be seen, indicating further detachment (see yellow arrows in Figure 3.20.c). Although the SIROF stack initially remained on the surface for some of the electrodes in each array, further detachment from more and more electrodes occurred with repeated cell culture periods. Nevertheless, a few initial experiments and a successful extracellular stimulation were conducted with a Mi-BeSAN ring electrode (see Section 5.3).

Analyzing the ongoing detachment, it was assumed to be caused by the deposition of the SIROF stack as the final step in the production process on top of the otherwise finished MEAs (compare Subsection A.1.3). Therefore, the process order was changed for the fourth generation of Mi-BeSAN MEAs. The SIROF stack was deposited on the basic metalization before the final deposition and opening of the passivation layer.

Unfortunately, the fourth generation Mi-BeSAN MEAs also showed detachment of the SIROF stack after one week of cell culture and subsequent cleaning for all chip designs as shown in Figure 3.21. Again, the detachment was more severe with increasing time under cell culture conditions. Furthermore, the chips did not perform as well electrochemically.

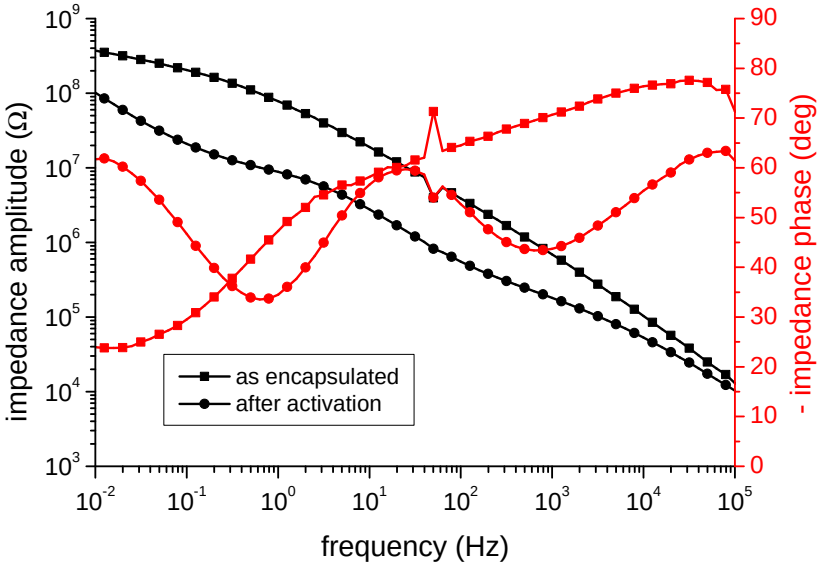

Figure 3.22: Comparison of the impedance of a fifth generation Mi-BeSAN IrO_x button electrode before and after conditioning and activation by potential cycling. Magnitude and phase of the impedance is shown for both scans.

Electrochemical investigations of the Mi-BeSAN MEA electrodes were conducted to compare their behavior to the standard 64-electrode MEAs of the fourth generation. While the standard MEAs could be activated by cyclic voltammetry and subsequently showed a significantly decreased impedance in comparison to gold electrodes, this could not be observed for the fourth generation Mi-BeSAN MEAs. Instead, EIS measurements revealed impedance values which could be expected from plain gold surfaces without functional IrO_x coating.

The reason for the detachment was finally attributed to the process step for opening the passivation of the microelectrodes. The original masks for IrO_x deposition and passivation opening were designed with an identical geometry. Therefore, a small misalignment of the mask for opening the passivation causes the exposure of the edges of the SIROF stack to the electrolyte solution. Hence, the titanium adhesion layer beneath the platinum oxidizes and causes detachment of the platinum and the IrO_x.

To circumvent this, the aperture for the opening of the passivation layer was reduced in size as indicated in Figure 3.18. Thus, the fifth generation of Mi-BeSAN MEAs was opened with the new mask and found stable in electrolyte solution and under cell culture conditions. The quality of the electrodes with the new process then needed to be validated.

To show the functionality of the SIROF electrodes, electrochemical measurements were conducted. Figure 3.22 shows the results of typical impedance measurements of a Mi-BeSAN button electrode before and after conditioning and activation with cyclic voltammetry. After conditioning and activation (procedure described in Subsection 3.1.1), the impedance of the electrode is significantly reduced in the whole frequency range and roughly resembles the course of the impedance scans of other activated IrO_x samples and electrodes as shown in Figures 3.10 and 3.12. From the cyclic voltammetry, an increase in the spe-

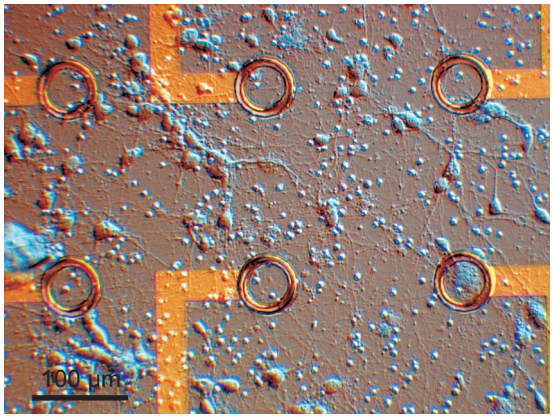

Figure 3.23: DIC image of rat cortical neurons (DIV 7) growing on the surface of a fifth generation SIROF Mi-BeSAN MEA. The cells grow with a dense network of processes indicating a healthy neuronal culture.

cific cathodal charge storage capacity from initial 1.58 mC/cm^2 to 3.24 mC/cm^2 in the fiftieth cycle could be calculated. Although this value is smaller then the q_{CSC} found for the 50 µm electrodes, it still shows the functionality of the Mi-BeSAN electrodes and lies within the range of literature values. Similar results could be acquired with ring and quad electrodes, implying that the fifth generation Mi-BeSAN SIROF electrodes can be used for stimulation.

As already shown for previous chip generations in the scope of a diploma thesis [131], the SIROF Mi-BeSAN MEAs also offered a high degree of biocompatibility and allowed the culturing of rat cortical neurons. Figure 3.23 shows a DIC image of an encapsulated Mi-BeSAN ring electrode with a DIV 7 neuronal culture to visualize the healthy growth of cells on the devices.

3.2.3 Characterization of Complete Mi-BeSAN Chips

With the SIROF microelectrodes and the planar p-type FET [84] tested separately, the processing of the complete Mi-BeSAN chips as presented in Figures 3.18 and 3.19 could be performed. The FETs were fabricated with the Mi-BeSAN FET process as described in Subsection A.2.1. The final step of the FET process was the deposition of aluminum to the implanted contact lines of the drain and source contacts. In order to show the functionality of the devices, several transistors were characterized electronically before the electrode process was started using a probe station with a semiconductor characterization system (Model 4200-SCS, Keithley Instruments, Cleveland, USA). The results of the characterization for one representative FET are depicted in Figure 3.24.

Figure 3.24.a shows the output characteristics of the FET. The *drain-source current* (i_{DS}) is plotted against the *drain-source voltage* (v_{DS}) for five constant values between 0 and −4 V of the *gate-source voltage* (v_{GS}). The resulting graph shows a typical course for the output characteristics of a p-type FET with a linear and a saturation region. However, a non-vanishing i_{DS} for $v_{GS} = 0$ V shows that the transistor channel does not completely

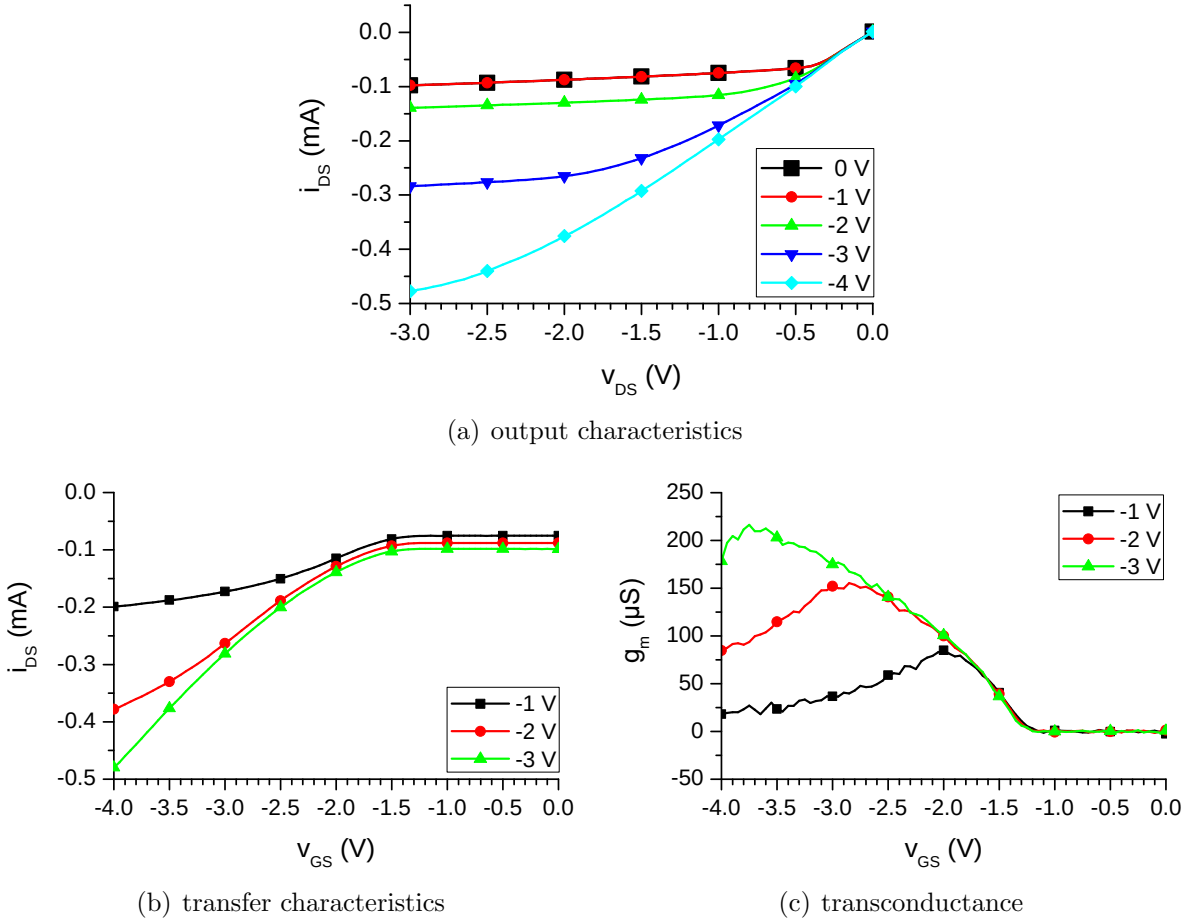

(a) output characteristics

(b) transfer characteristics

(c) transconductance

Figure 3.24: Electronic characterization of the Mi-BeSAN FET after aluminum deposition. The output (a) and transfer characteristics (b) were measured using a probe station. The transconductance (c) was calculated from the transfer characteristics by differentiation. For clarity of the graphs, only every tenth measured value is included with a marker. The solid lines encompass all data points.

close as desired. This can be explained by boron ion diffusion to the channel area during the annealing step after source and drain implantation, which causes an unwanted residual conductivity of the channel area. Sine the traces for $v_{GS} = 0$ V and $v_{GS} = -1$ V are almost identical, it can be concluded that the threshold voltage for the complete opening of the channel is lower than -1 V.

The same non-vanishing channel current can also be seen in the transfer characteristics (see Figure 3.24.b), which show i_{DS} in dependence on v_{GS} for v_{DS} equal to -1 V, -2 V, and -3 V. The graph shows that the threshold voltage for the opening of the channel is approximately -1.5 V, which fits very well to the threshold voltages determined for the planar p-type FETs developed in preliminary work [84].

For extracellular recording of cell signals, a FET is usually operated at an operation point with a high *transconductance* (g_m), i.e. where a small change of v_{GS} causes a maximum

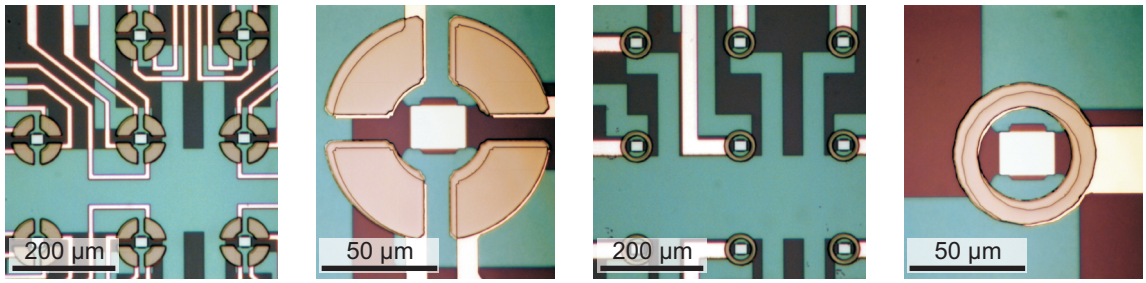

(a) (b) (c) (d)

Figure 3.25: DIC images with overviews of parts of the sensor arrays (a,c) and magnifications of one sensor area (b,d) for Mi-BeSAN chips with quad (a,b) and ring electrode configurations (c,d) after metalization and SIROF stack deposition.

change in i_{DS}. By differentiation of the transfer characteristics, g_m was calculated and plotted in Figure 3.24.c. The transconductance traces show a typical shape with a distinct maximum for every value of v_{DS}. The maximum value for g_m of roughly 220 µS also equates to values determined for previously developed planar p-type FETs for cell recordings [84]. Therefore, the FETs can still be used for extracellular recording of signals from electrogenic cells, although the transistor channels cannot be closed completely.

After the characterization of the FETs, the second part of the Mi-BeSAN process for the production of the SIROF microelectrodes was started (see Subsection A.2.2). The metalization and SIROF stack deposition was conducted, and the chips were investigated optically before the final passivation of the chip surface.

Figure 3.25 shows DIC images taken from quad and ring electrode Mi-BeSAN chips before the deposition of the passivation layers. As visualized in the images, the metalization and SIROF stack deposition was conducted successfully to form the stimulation electrodes around the arrays of recording FETs, the contact lines, and the bond pads. The magnifications of single quad (see Figure 3.25.b) and ring electrode sensor spots (see Figure 3.25.d) show only a slight misalignment of the deposited SIROF in relation to the basic metalization. This misalignment is noncritical, since the subsequent passivation of the chip surface covers the free gold areas and the edges of the SIROF stack and thus prevents any contact with the electrolyte solution. The final opening of the electrodes through the passivation layer is smaller than the size of the SIROF electrodes.

The final process steps including the chip surface passivation and opening of the sensor areas were conducted and finished just within the scope of this thesis. However, in order to determine and elaborate the full potential of the Mi-BeSAN chips, a complete characterization of the encapsulated chips and the application for electrophysiological experiments with electrogenic cells still has to be performed. Nevertheless, the satisfying electrochemical properties and the successful application of the preliminary Mi-BeSAN MEAs for stimula-

tion of a neuron (see Subsection 3.2.2 and Section 5.3) suggest the adequacy of the SIROF electrodes for the extracellular stimulation of electrogenic cells. Additionally, the properties of the working planar p-type FETs shown in this subsection are similar to previous planar recording FETs and should enable the recording of action potentials from electrogenic cells. In combination with the newly developed amplifier system (see Section 4.3), this yields a powerful tool for the bidirectional communication with electrogenic cells and especially neurons.

Chapter 4

Amplifiers and Experimental Setups

There's a setup here and I'm stuck in the middle of it!

Lance Armstrong (American cyclist, 1971-)

The purpose of this chapter is to introduce all custom amplifier systems and experimental setups that were used for the electrophysiological measurements in this work. The first two sections will briefly present the systems available at the beginning of this work and used for the first measurements. This includes the individual amplifiers for stimulation and recording with *multi-electrode arrays* (MEAs), as well as potentiometric and impedimetric recording with *field-effect transistors* (FETs). In the third section, the novel combined amplifier system is introduced, which was developed within the scope of this thesis.

4.1 MEA Stimulation Amplifier

In previous work [122, 129, 130], a 64-channel readout system with headstage and main amplifier for extracellular recordings with MEAs (see Section 3.1) was developed and optimized for interfacing electrogenic cells. The headstage performs a first amplification by a factor of ten and carries a 68-pin socket for contacting the encapsulated MEA chips and another socket for a Ag/AgCl reference electrode. The main amplifier has two further ten-fold amplification stages and a high-pass filter to suppress drift of the output voltage.

In an effort to introduce a first test system capable of extracellular stimulation as well as recording of cell signals with microelectrodes, the existing system was further modified by Schindler [25]. A new headstage was built with a decoder controlling a set of switches, which can be used to connect every single electrode either to the input of the first amplification stage for recording or to a stimulation channel. Due to limited space on the *printed circuit board* (PCB), the headstage could only be equipped for the 16 center and the 4 corner

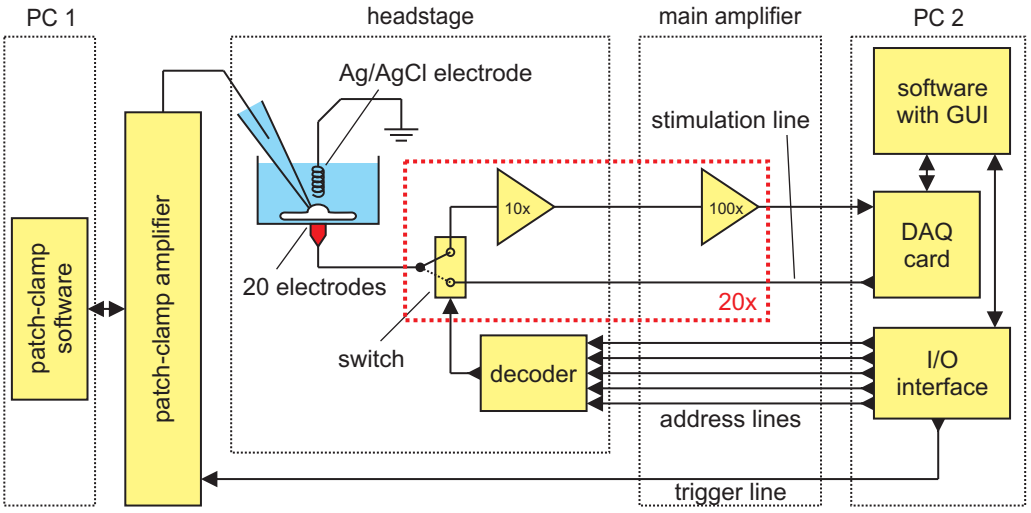

Figure 4.1: Schematic of electrophysiological setup with modified 20-channel MEA amplifier system. Besides the main amplifier and the headstage, the setup contains two personal computers and a patch-clamp amplifier. The figure was adapted from [25].

electrodes in the 64-electrode array. One main amplifier was slightly modified to be able to pass the data lines for control of the decoder and the stimulation line to the headstage. Thus, it can still be used with a standard 64-channel headstage purely for recording, or with the new headstage for bidirectional interfacing. The address bits of the decoder are controlled via a digital *input/output* (I/O) interface (PCI-6503, National Instruments Corp., Austin, USA). For recording experiments, a *data acquisition* (DAQ) card (PCI-6071E, National Instruments) is used to sample the output voltage of the last amplifier stage for 20 (new headstage) or all 64 channels (conventional system). In the case of a stimulation experiment, the same DAQ card is used to generate the stimulation voltage pulse, which is applied to the selected electrode via the main amplifier and the headstage.

Figure 4.1 shows a schematic of the electronic components involved in stimulus generation and data acquisition from the experimental setup with the modified MEA amplifier system. In order to monitor the success of the extracellular stimulation, a patch-clamp amplifier (EPC 10 Double, HEKA Elektronik Dr. Schulze GmbH, Lambrecht, Germany) is used to intracellularly measure the membrane potential or current of the stimulated cell during the experiment. The patch-clamp probes carrying the micropipettes for contacting the cells are controlled by micromanipulators and a manual control unit (SM-5, Luigs & Neumann Feinmechanik und Elektrotechnik GmbH, Ratingen, Germany). For imaging and visual control of the cell position and the micropipette movement during the experiment, an upright microscope (Axiotech Vario, Carl Zeiss Microimaging GmbH, Göttingen, Germany) with an immersion objective (UMPlanFl 20x, Olympus Corp., Tokyo, Japan) and a digital camera (AxioCam MRc, Carl Zeiss) is used. The microscope's z-position is also controlled by a micromanipulator with a manual control unit (SM-6, Luigs & Neumann).

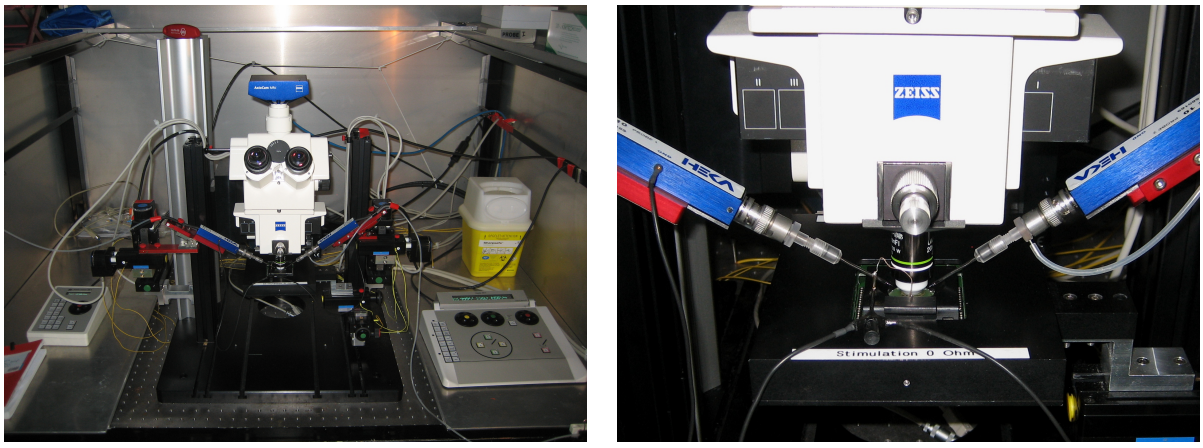

(a) (b)

Figure 4.2: Photographs of the electrophysiological setup with modified 20-channel MEA amplifier system. Since electrophysiological measurements are sensitive to vibrations and electromagnetic distortion, the system is set up in a Faraday cage on a vibration-isolation table (a). The headstage is mounted underneath an immersion objective for optical control of the experiment (b). Two micromanipulator-controlled patch-clamp pipettes can be used to contact cells located on the MEA chip.

The recording with the patch-clamp amplifier is started by a trigger pulse generated by the digital I/O interface. To minimize any distortion of the measurement by environmental influences, the setup is positioned in a custom-made Faraday cage on a vibration-isolation table (VH3648W-OPT, Newport Corp., Irvine, USA). Two *personal computers* (PCs) are used to run the patch-clamp software (TIDA 5.20, HEKA Electronics), the imaging software (AxioVision, Carl Zeiss), as well as a custom-made *graphical user interface* (GUI) for the stimulation control. The GUI was created with a graphical programming language (LabVIEW 8, National Instruments). Photographs of the complete setup and a magnification of the modified headstage with two patch-pipettes underneath the microscope are presented in Figure 4.2.

4.2 Portable FET Amplifier Box

As a second system for extracellular interfacing of electrogenic cells and for biosensor applications, FETs are frequently used in our institute. Previously, a two-stage 16-channel amplifier system for device characterization and long-term potentiometric measurements (also called *direct current* (DC) measurements) had been developed [138] and used for measurements with rat neurons [18] and cardiac myocytes [139].

Besides potentiometric measurements, our ISFETs are also frequently used for impedimetric measurements (also called *alternating current* (AC) measurements), which can e.g.

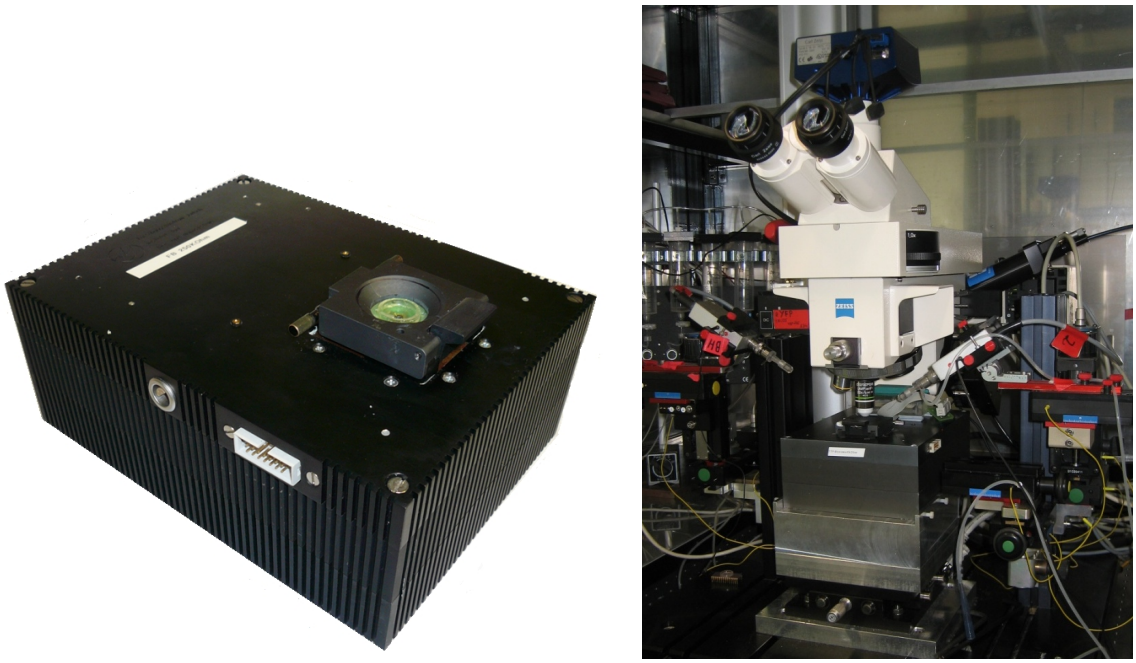

(a) (b)

Figure 4.3: Photographs of portable FET amplifier box (a) and electrophysiological setup with amplifier box mounted in Faraday cage on vibration-isolation table (b). Optical control of any measurements with cells on the FET chips can be achieved by a microscope with an immersion objective. Two micromanipulator-controlled patch-clamp pipettes can be used for comparative intracellular measurements during experiments with the amplifier system.

be utilized for biomolecule detection [140–142] or cell adhesion investigation [84,86]. Therefore, the FET amplifier system was reengineered in several steps [86, 141, 142] to enable both potentiometric or impedimetric measurements of 16 FETs with the same setup. Furthermore, the whole amplifier system was consolidated into one small box (Figure 4.3.a) for a high portability and easy handling of the system.

A basic circuit diagram of the readout electronics of the amplifier system is given in Figure 4.4. Two switches are used to choose between impedimetric and potentiometric measurements. In the DC readout mode (both switches in lower position (dotted line) in Figure 4.4), all 16 transistors can be characterized simultaneously by measuring the drain-source current while varying the potential at the *source* (S) and *drain* (D) contacts (v_{source} and v_{drain}), and grounding the *gate* (G). The gate potential corresponds to the potential of the electrolyte solution which is contacted by a Ag/AgCl wire. The drain-source currents are transformed into output voltages by *current-to-voltage converters* (first amplification stage) with 10 kΩ feedback resistors. The devices are set to an *operating point* (OP) in the saturation regime, where a small change in the gate potential causes the largest change possible in the drain-source current of the transistor. After setting the OP, the constant output voltage offsets of the current-to-voltage converters are of no particular

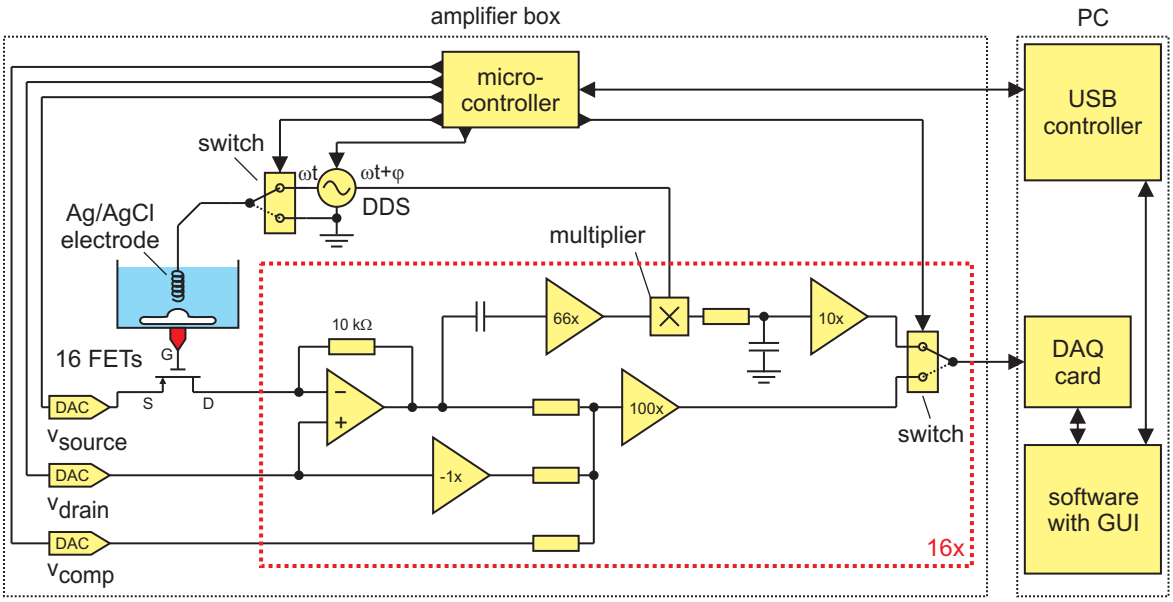

Figure 4.4: Schematic of measurement setup with portable FET amplifier system controlled by personal computer. Two switches can be used to set the system to impedimetric or potentiometric measurement mode.

interest and are compensated by *digital-to-analog converters* (DACs) applying individual *compensation voltages* (v_{comp}) for each channel, separately. Time-dependent potentiometric measurements of the gate potentials can be conducted by recording changes in the output voltages, which are further amplified by a factor of 100 in a second amplification stage.

For impedimetric readout (both switches in top position (solid line) in Figure 4.4), the system contains 16 independent phase-selective amplifiers, which are utilized to measure the frequency-dependent *transistor transfer function* (TTF) of the system including amplifiers, devices and possible biomolecules or cells [86,140]. The FETs are operated in the same OP as for DC readout, and the scan of the transfer functions is done by feeding a sinusoidal test signal with 10 mV amplitude and varying frequency from 1 Hz to 1 MHz to the Ag/AgCl reference electrode. *Direct-digital-synthesis* (DDS) devices are used to provide the AC test signals with exact amplitude, *angular frequency* (ω) and *phase* (φ). Frequency-selective amplification is conducted by 16 separate capacitively decoupled amplification cascades with frequency-multipliers. The output voltage is generated by averaging the output of the frequency multipliers over several oscillation periods. As an alternative to the frequency scan, the AC signal can also be measured continuously at a constant frequency to directly detect changes in the transfer function at that particular frequency [86].

FET chips are mounted to the box by a 68-pin socket that includes a Peltier element for temperature control of the chips during measurements (e.g. to keep the temperature at 37 °C for mammalian cells). The complete amplifier system, including the switches, DDS devices, and DACs, is operated by a microcontroller, which communicates to the

operating PC via a *universal serial bus* (USB) connection. For fast readout of all 16 channels with a sampling rate of up to 10 kHz, the *analog-to-digital converters* (ADCs) of a DAQ card (e.g. PCI-6071E, National Instruments) are used. The software and GUI for system control, chip characterization, and potentiometric as well as impedimetric recording were implemented in a text-based programming language (Delphi 5, Borland Software Corporation, Austin, USA). Besides the stand-alone usage of the amplifier system for purely extracellular measurements, the box can also be mounted to an electrophysiological setup (Figure 4.3.b) to combine extracellular FET measurements with intracellular recordings using a patch-clamp amplifier. This configuration is similar to the combined measurements with the MEA system presented in Figure 4.1 and additionally contains an X-Y table (M-401, Newport Corp., Irvine, USA) for positioning the amplifier box underneath the microscope.

4.3 BioMAS - Combined System for FETs and MEAs

In the past, several generations of amplifier systems for electrophysiological and impedimetric measurements with MEAs and FETs have been developed, continuously optimized, and adapted with new functionalities. The previous two sections briefly introduced the state-of-the-art systems, which were available for MEAs (Section 4.1) and FET chips (Section 4.2). However, due to the ongoing development, almost all existing amplifiers and setups in our institute differed in hardware and software (e.g. in specifications, functionalities, grade of documentation, GUI, and programming language used). This confusing jungle of equipment caused long training periods for new students and inconsistent data formats for processing and analysis.

In the scope of the research project Mi-BeSAN (see also Section 3.2) and this thesis, a new amplifier system for electrophysiological measurements *in vitro* with chips containing both FETs and microelectrodes had to be developed. The Mi-BeSAN chip was designed to carry FETs for extracellular recording of signals, and microelectrodes for extracellular stimulation. To prevent a further complication of the equipment pool, it was decided to design a new amplifier capable of merging the previous systems and consolidating as many functionalities as possible. Figure 4.5 shows a schematic of the new *Bioelectronic Multifunctional Amplifier System* (BioMAS), which is aimed at versatility in applications and allowing future user customization.

BioMAS is realized as a system consisting of one generalized main amplifier, which can be connected by two cables to one of several specialized headstages adapted to the chip kind to be used (FET chips, MEAs, or Mi-BeSAN chips with both FETs and microelectrodes). Standardized heads carrying a 68-pin chip socket with a heater unit can be plugged in to all

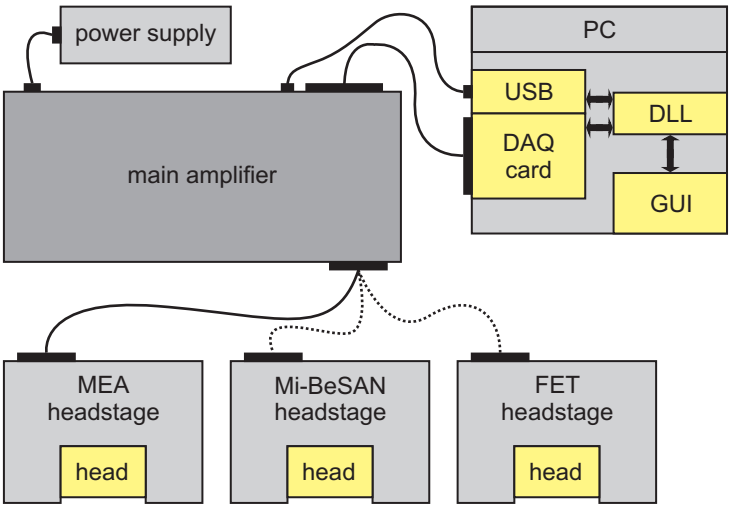

Figure 4.5: Basic schematic of new multifunctional amplifier system for electrophysiological experiments with FETs, MEAs and combinations of both kinds of devices. A personal computer is used for data acquisition and control of the main amplifier, which is connected to one of several application-adapted headstages.

headstages for measurements. Alternatively, customized heads with a different chip socket or new headstages for other devices can easily be adapted and introduced to the system. The main amplifier has its own power supply unit and is connected to a PC by USB for control, and to a DAQ card for data acquisition. The customized BioMAS software runs a GUI and communicates with the DAQ card and the main amplifier by a *dynamic link library* (DLL) interface.

Within this thesis, functional versions of the main amplifier with power supply, the headstages for MEA and Mi-BeSAN chips, and major parts of the software were finished. In the following sections, these individual components of the system will be presented and explained in more detail.

4.3.1 BioMAS Head and Headstages

Figure 4.6 shows a photograph of two basic variants of the custom-made BioMAS head. The black anodized aluminum housing has a size of 92 mm × 68 mm × 10.5 mm (width × length × height). Each head can be connected to any headstage by a *peripheral component interconnect* (PCI) connector. For maximum flexibility when integrating the headstages with an experimental setup, two mirrored versions of the head were made so that the headstages can be turned upside down. The heads contain a 68-pin PLCC socket (IC51-0684-390, Yamaichi Electronics, Tokyo, Japan), which was customized in our mechanical workshop with a new lid for better access to inserted chips. Next to the lid, two sockets for the reference electrode are included - one for grounding and one for application of a stimulation signal to the bath electrolyte. Furthermore, a resistor heater with a PT 1000 temperature sensor for closed-loop control of the chip temperature and three *light-emitting diodes* (LEDs) for status indication were included. The head is constructed with an access opening on both sides so it can be used with upright and inverted microscopes.

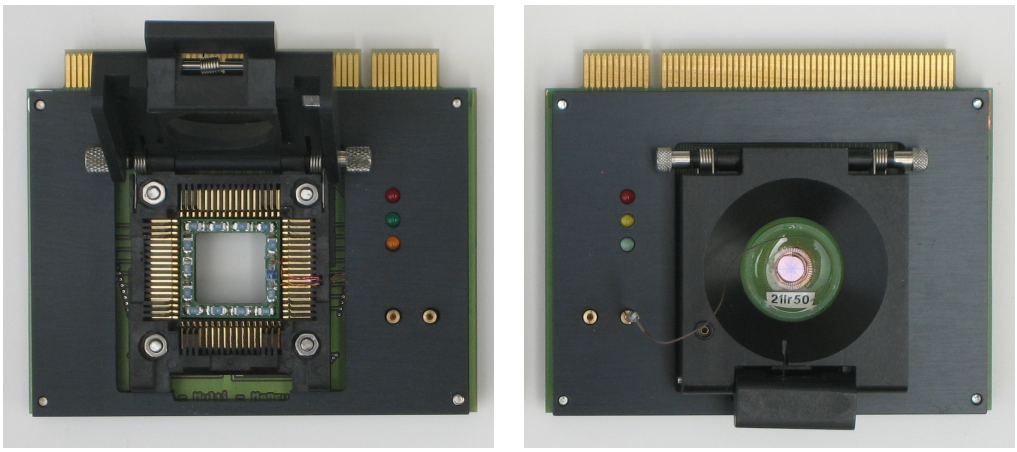

(a) (b)

Figure 4.6: Photographs of the variants of the BioMAS head. Two mirrored versions of the head were implemented for maximum flexibility. One head is shown with open chip socket revealing the 68 pins, the heater unit, and the opening for usage with an inverted microscope (a). The other head with closed chip socket carries a MEA and a Ag/AgCl wire as reference electrode (b).

An image of the housing of a BioMAS headstage is presented in Figure 4.7. The custom-made black anodized aluminum housing is horseshoe-shaped and has a size of 243.5 mm × 160 mm × 61.5 mm (width × length × height). It contains two PCI ports in a top and a lower position, either of which can be used to connect the head. The shape and the two ports were chosen to make the headstage as small as possible and still compatible with upright and inverted microscopes. Each headstage has two D-sub parallel ports with 25 and 78 pins on the backside for transmission of control signals and data, respectively. Additionally, one control PCB (e.g. for heater and LED control), two bus PCBs (to contact the PCI and the parallel ports), and a varying number of amplifier PCBs are built into the headstage. The following subsections will introduce the 64-channel MEA and the Mi-BeSAN headstage.

Figure 4.7: Photograph of the BioMAS headstage housing including a head in the lower position. The horseshoe-shaped headstage contains two PCI ports to allow an alternative connection of the head in a top position. Connection to the main amplifier is established by two parallel ports at the backside of the headstage.

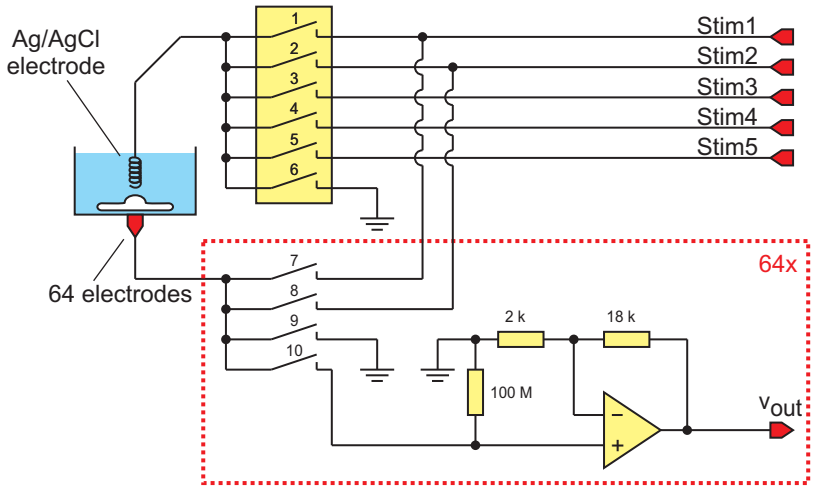

Figure 4.8: Schematic of signal paths in the 64-channel MEA headstage and head. The paths for recording and stimulation are described in detail in the text.

64-Channel MEA Headstage

In addition to the three standard PCBs, the 64-channel headstage for measurements with MEAs (see Section 3.1) contains two amplifier PCBs with electronics for 32 channels each. A schematic of the signal paths in the MEA headstage and the head is given in Figure 4.8.

A Ag/AgCl wire is mounted on the head and immersed in the electrolyte solution in the culture dish on the chip surface as a bath electrode. For standard extracellular recording, the wire is used as a reference electrode and connected to ground (switch 6 closed in Figure 4.8). However, for other applications including impedance measurements or *signal-to-noise ratio* (SNR) measurements, the wire can also be connected by five switches (1-5) to one of five stimulation lines (Stim1-5), which are fed with voltage signals from the main amplifier. Each of the 64 microelectrodes on the MEA is connected to four switches (7-10) in the amplifier headstage. Using those switches, each electrode can be individually connected to ground, to one of two stimulation lines (Stim1-2) for extracellular stimulation, or to the input of a first amplification stage for recording of cell signals. For high input impedance, the amplification stage is realized as a *non-inverting amplifier* composed of an *operational amplifier* (OPA) with an amplification of ten ($1 + 18\,\mathrm{k\Omega}/2\,\mathrm{k\Omega}$). A low-noise precision amplifier (OPA124) was used for this first amplification. The *output voltages* (v_{out}) of the 64 channels are passed to the main amplifier for further processing. The 100 MΩ resistor between the input of the amplifier and ground is introduced to suppress drift of the output voltage.

Mi-BeSAN Headstage

Electrophysiological measurements with Mi-BeSAN chips (see Section 3.2) require a headstage with electronics for measurements with FETs and stimulation experiments with microelectrodes. The chips either contain 16 FETs and 16 microelectrodes or 12 FETs and

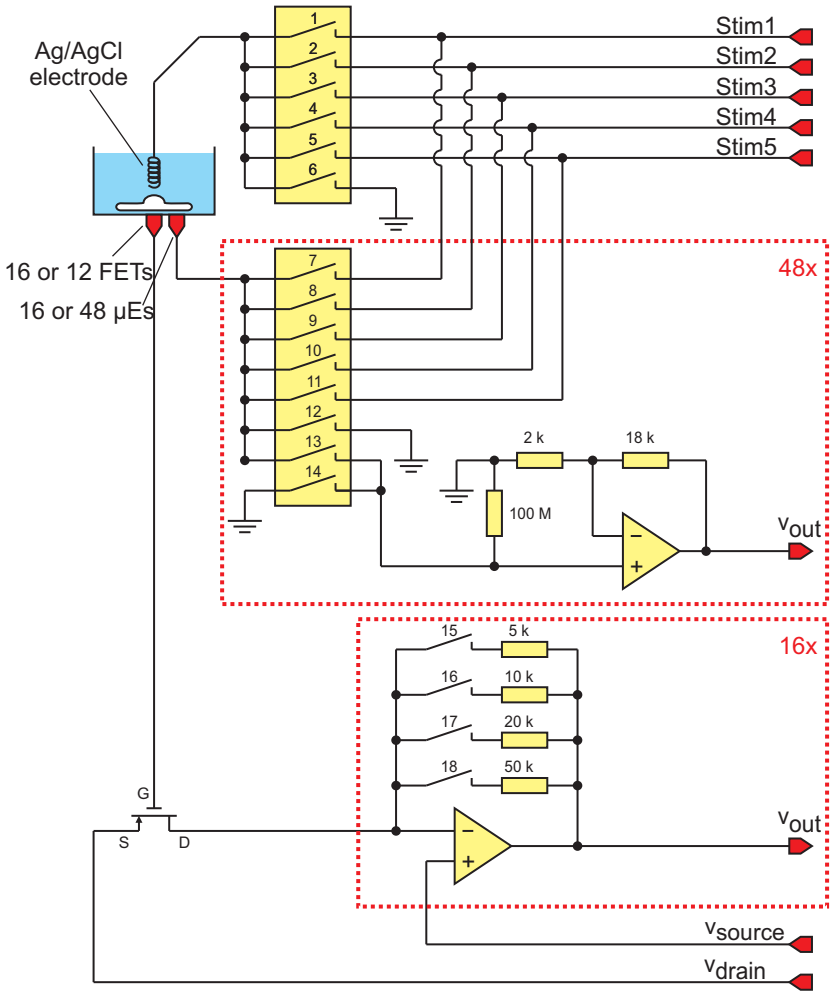

Figure 4.9: Schematic of signal paths in the Mi-BeSAN headstage and head. The paths for recording with FETs and stimulation with microelectrodes (µEs) are described in detail in the text. In addition, recording with the maximum 48 electrodes is also possible with an optionally included path.

48 microelectrodes. Therefore, the Mi-BeSAN headstage (signal path schematics in Figure 4.9) contains two PCBs with electronics for 24 electrode channels each and one amplifier PCB for 16 FET channels in addition to the three PCBs for control and the bus system.

As in the 64-channel MEA headstage, the Ag/AgCl bath electrode is connected by six switches (1-6 in Figure 4.9) to either ground or one of five stimulation paths (Stim1-5). The 48 paths for the microelectrodes each contain an eightfold switch (7-14) to individually connect the electrodes. Connection options are further discussed below. For stimulation, one of the five stimulation lines or ground can be connected to any electrode (one of switches 7-12 closed). Although in the Mi-BeSAN project the electrodes were only intended to be used for stimulation, a recording path as an alternative utilization method for the electrodes was additionally included. Therefore, the electrodes can be connected to the input of an OPA (only switch 13 closed), and voltage drops in the cleft can be recorded. Finally, the input of the OPA can also be connected to ground (switch 14 closed, switch 13 open) to prevent drift or voltage jumps during stimulation experiments. The electrode amplification stage is realized with the same electronic circuit as in the 64-channel MEA headstage, and

a maximum of 48 electrode output voltages (v_{out}) are passed to the main amplifier.

The 12 or 16 FETs are operated by application of the drain and source voltages (v_{drain} and v_{source}), which are generated in the main amplifier and passed to the headstage. When the FETs are set to an OP, a constant *drain-source current* (i_{DS}) flows, which is converted into the output voltage ($v_{out} = -R_{FB} \cdot i_{DS} + v_{drain}$) by a current-to-voltage converter. The *feedback resistor* (R_{FB}) of the converter can be switched to four different values between 5 kΩ and 50 kΩ (15-18 in Figure 4.9). Depending on i_{DS} of the device in the OP, the output voltage can be adjusted to the maximum *input voltage* (v_{in}, ±10 V) of the second amplification stage in the main amplifier. Any change in the gate potential (v_{gate}) causes a change of i_{DS} that is again transformed into a change of the output voltage $\Delta v_{out} = -R_{FB} \cdot \Delta i_{DS}$. This output voltage is then further processed in the main amplifier. The same operational amplifier (OPA124) was used for the first amplification stage in all 64 channels as in the MEA headstage.

4.3.2 BioMAS Main Amplifier

The BioMAS main amplifier is designed for maximum flexibility and can be used with several headstages specialized for certain chip types. The amplifier contains thirteen modular PCBs overall, which can separately be exchanged and further improved for extension of the system's capabilities.

The first PCB is used for communication with the PC and controlling the system by a microcontroller (TINY-Tiger 2, Wilke Technology GmbH, Aachen, Germany), which is programmed in Tiger-BASIC. A switch-PCB is directly controlled by the microcontroller and enables the connection of the various input ports for external signals and output ports for monitor signals to the desired circuit lines. The power supply and control of the closed-loop heater are situated on another PCB.

The basic circuits for recording and amplification of cell signals are located on two amplifier PCBs. The main amplifier board contains the electronics for the first 16 channels, which can be used for recording with FETs as well as microelectrodes. Furthermore, 16 and 32 identical channels solely for recording with microelectrodes are included on the main and the second amplifier board.

One PCB is used for control and generation of the stimulation signals and their application to the five stimulation lines (Stim1-5), which are passed to the headstages (compare Subsection 4.3.1). An electronic circuit with four DDS devices is used to generate up to four phase-selective sinusoidal or triangular voltage signals with any frequency up to 200 kHz and amplitudes up to ±5 V. Alternatively, rectangular signals with the same frequency range and amplitudes up to ±10 V can be generated. The four signals can each be applied to their corresponding stimulation line (Stim1-4), which again can either be connected to

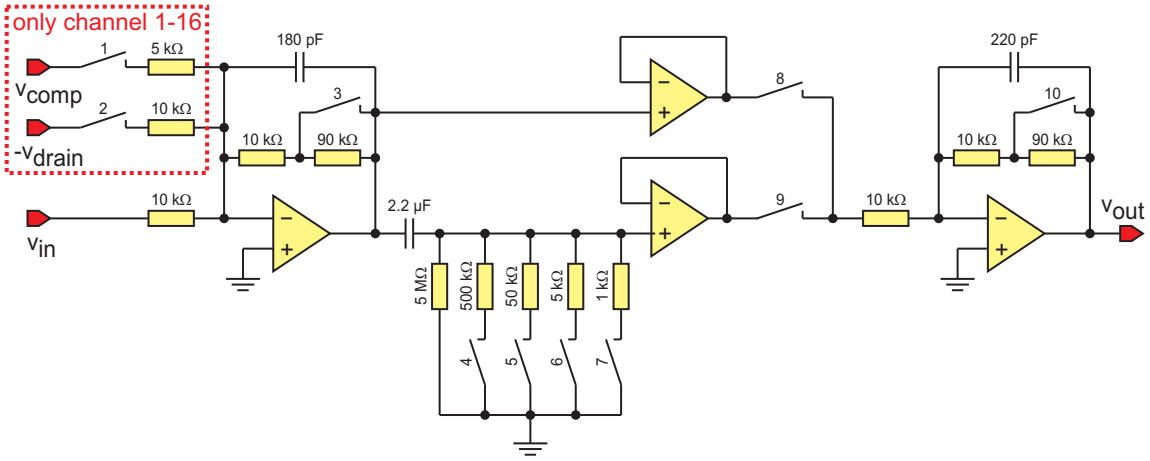

Figure 4.10: Schematic of the basic signal paths in the BioMAS main amplifier. The circuits including a compensation stage, two switchable amplification stages, and filter systems are described in the text in detail.

the bath electrode (e.g. for impedimetric or SNR measurements), or to any combination of microelectrodes (e.g. to test the functionality of the electrodes or for dielectrophoresis). Two DAC output signals of the DAQ card can alternatively be applied to the first two stimulation lines (Stim1-2). Furthermore, four input ports for external stimulation sources can also be linked to the same four stimulation lines (Stim1-4). Finally, any of the four DDS signals or another external signal source can be applied to the final stimulation channel (Stim5). This high variability of stimulation sources could even be extended in the future by adding another on-board stimulation source for the generation of current- or voltage-controlled stimulation pulses.

Seven more PCBs are needed for the various bus systems and connectors within the amplifier and to the front and back panel. In the future, another PCB for simultaneous frequency-dependent impedimetric TTF measurements with 16 channels (compare Section 4.2) will be implemented as another expansion of the system.

A schematic of the basic signal paths in the BioMAS main amplifier is shown in Figure 4.10 and can be divided into three stages. The 64 *input voltages* (v_{in}) from the headstage are fed into a first amplification stage. Because of the low output impedance of the headstage, this is realized as an *inverting amplifier* with a switch (3) for a variable amplification of either -1 ($-10\,\mathrm{k\Omega}/10\,\mathrm{k\Omega}$, switch 3 closed) or -10 ($-100\,\mathrm{k\Omega}/10\,\mathrm{k\Omega}$, switch 3 open). Furthermore, a capacitor of 180 pF is included with the resistors in the feedback loop of the amplifiers and operates as a passive first order low-pass filter to remove high frequency noise. With switch 3 closed, the cutoff frequency of this filter is approximately 8.8 kHz and thus does not attenuate any signal components within the spectrum of neuronal or cardiac cell action potentials, which approximately covers the frequencies between 1 Hz and a few kHz [45, 47, 143].

The first 16 channels of the amplifier are designed for the amplification of signals from a FET chip. The transistors are operated with a constant offset current, which is converted into a significant voltage offset at the output of the current-to-voltage converter of the headstage. This voltage offset is not of any particular interest for electrophysiological measurements, where usually only fast signal changes like action potentials (see 2.1.3) are investigated. Furthermore, the drain voltage applied to the current-to-voltage converter in the headstage is also added to the output voltage of the headstage, without containing any relevant information about the measured signal. Those two voltages add up to a relatively high offset voltage, which can easily exceed the maximum input voltage of the following amplifier stages. Therefore, two additional switches (1-2) are included in the circuit, enabling the addition of two compensation voltages ($-v_{drain}$ and v_{comp}) to the input of the inverting amplifier. By measuring the voltage offset of the transistor after setting the OP, the microcontroller can be used to set those two voltages by two DACs to compensate the output of the headstage to zero in the OP. Thus, the maximum dynamic range of the following amplifier stages and the DAQ card can be utilized to full extend. Since the DACs can introduce additional noise to the circuit, they can be switched off if the amplifier is used with microelectrodes. The other 48 channels of the main amplifier are always used with microelectrodes and do not include any compensation circuitry.

In the second stage of the main amplifier, two different signal paths can be chosen for further processing. With switch 8 open and switch 9 closed, the signal is filtered by a passive first order high-pass filter, which is realized by an RC-circuit with a capacitor of 2.2 µF and a resistor of 5 MΩ. This filter is included to suppress low-frequency drift of the measured signals, which often occurs e.g. for long-term measurements with microelectrodes. The *time constant* $\tau = 11$ s (and thus the *cut-off frequency* $f_c = 1/(2\pi\tau)$) of the high-pass filter can be adjusted by switching on one of four parallel resistors (switches 4-7). Thus, the time constant can be changed to a value of 1 s, 109 ms, 11 ms, or 2.2 ms. The resulting cut-off frequency of the filter can be chosen between approximately 14.5 mHz and 72 Hz to adjust the bandwidth of the amplifier to the expected signals. A *unity gain buffer* is used to reduce the load of the high-pass filter and pass the filtered signal to the input of the third stage. Alternatively, the output voltage of the first stage is passed without any further modification to the input of the third stage by another unity gain buffer when switch 8 is closed and switch 9 open. This path can be used if low frequency signal compartments or even the DC value are of interest for the user.

The third stage of the main amplifier constitutes a final amplification stage. Like the first stage, it is realized as an inverting amplifier with a switch (10) for a variable amplification of -1 or -10. Again, a capacitor is included to realize another passive first order low-pass filter. With a capacitance of 220 pF, the cutoff frequency of the second filter is about

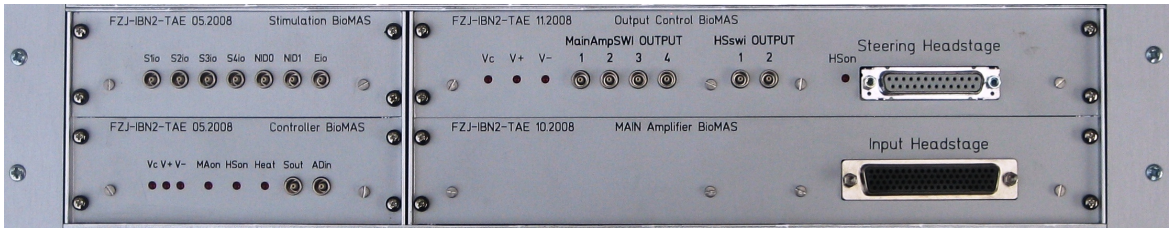

(a) Front panel.

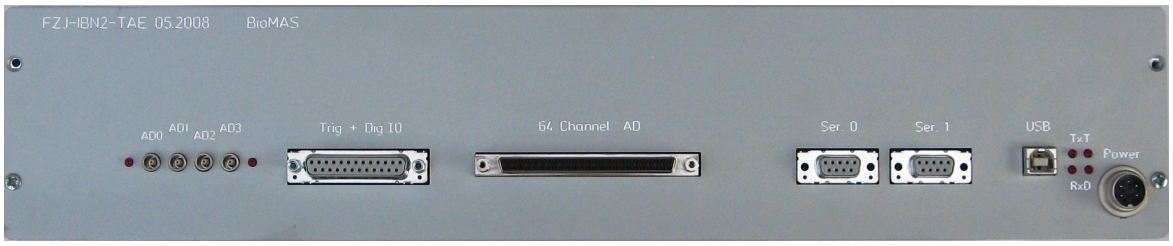

(b) Back panel.

Figure 4.11: Photographs of the BioMAS main amplifier front (a) and back panel (b). The various ports and status LEDs included in the housing are explained in the text.

7.2 kHz and thus serves as an *anti-aliasing* filter, before the output voltage of the third stage is finally passed to the PC and sampled by the DAQ card.

In the standard measurement mode (switch 3 and 10 open) for recording of cell signals, the main amplifier establishes an overall amplification of 100 and filters the signal with two first order low-pass filters, and if necessary one first order high-pass filter with variable cutoff frequency. However, by setting the switches within the circuit as desired, the user can modify the system with a wide variety of options to adjust the amplifier to his measurement specifications.

Two photographs of the BioMAS main amplifier housing are given in Figure 4.11. Figure 4.11.a shows the front panel of the housing, which is a gray anodized aluminum 19-inch housing (TEG/2HE, Daub CNC Technik, Wenden, Germany) with a length of 325 mm. The front panel contains two D-sub parallel ports to connect the main amplifier to the headstage. A 25-pin port is used for the exchange of control signals and to provide the voltage supply for the headstage. A 78-pin port is used for transmission of the five stimulation lines to the headstage and the output voltages from the first amplifier stage. Furthermore, the front panel holds LEDs to show the status of the main amplifier (MAon), the headstage (HSon), and the heater unit (Heat). The voltage supply status of the controller PCB and the amplifier PCB in the main amplifier are also indicated by LEDs (Vc, V+, V-). Additionally, multiple push-pull coaxial ports (LEMO 00, LEMO Elektronik GmbH, Ecublens, Switzerland) for signal in- or output are included. Four ports (MainAmpSWI OUTPUT 1-4) can each be used to monitor one out of the 64 main amplifier output signals, and two further (HSswi OUTPUT 1-2) each monitor one of 64 input voltages of the main amplifier

(corresponding to the output voltages of the headstage). Two ports (NID0, NID1) are used to monitor the stimulation voltages, which are generated by the DAC of the DAQ card. Another four monitor ports (S1io, S2io, S3io, S4io) are connected to the output voltages generated by the four internal DDS voltage sources. Alternatively, those four contacts can also be configured as input ports to introduce stimulation signals from external sources. Finally, one port (Eio) can either be configured as a general output or input port, and two other ports (Sout, ADin) are used as test lines for system analysis.

The back panel of the main amplifier (Figure 4.11.b) contains a Tuchel connector port for the power supply with ±15 V and +5 V, a galvanically isolated 2-channel USB port with four status LEDs for communication with the controlling PC, two D-sub 9 pin serial ports (Ser. 0, Ser. 1) as test interfaces for system analysis, and a 100 pin *small computer system interface* (SCSI) as connection to the DAQ card. In addition, a 25 pin D-sub parallel port is included to lead through the digital I/O ports and counters of the DAQ card (for example to be used as trigger input or output). Four LEMO 00 ports (AD0-3) can be used as alternative input ports which can be connected to the data lines for acquisition with the DAQ card.

4.3.3 BioMAS Software

The software for system control and data acquisition with BioMAS is organized in a two-layer hierarchy. Task-specialized modular GUIs for system and measurement control, and visualization of acquired data are programmed in a graphical programming language (LabVIEW 8, National Instruments). Each module is adapted to one particular function of the amplifier system (e.g. stimulation or recording with MEA or Mi-BeSAN headstage) and can be combined with other modules to be used for a combination of compatible tasks. The final software version will detect which headstage is connected to the main amplifier and automatically start only the modules that can be used to operate the present system configuration.

As the second software layer, a DLL was programmed in C++ and embedded into the LabVIEW software. The purpose of the DLL was to conduct the communication between the GUI and the microcontroller in the main amplifier, and to control the data acquisition as well as the stimulation signal generation by the DAQ card. When a measurement is started by the user, the DLL performs the acquisition and storage of the full data and automatically returns a downsampled amount of data of each active channel to the GUI for online visualization.

As an example, the GUI for the extracellular stimulation with MEAs, which was frequently used in the stimulation experiments presented in Chapter 5, is shown in Figure 4.12. The GUI is divided into three areas: the top area is a diagram visualizing a preview of the

pulse as it is designed by the user. In the center area, several pulse parameters (including the sampling ratio) of a stimulation signal, which is generated by one of the two DAC output channels of the DAQ card, can be selected. Rectangular, sinusoidal, triangular, or sawtooth pulse shapes can be chosen. In the lower area on the left, the user can select any combination of the 64 microelectrodes to which the pulse is applied. On the right side, the user can start the stimulation in one of three possible modes. If "Single Stimulation" is selected, one single stimulation pulse is generated by the DAQ board and applied to the selected electrodes. With the button "Finite Stimulation", a number of stimulation pulses defined by the "# of cycles" is applied consecutively. If the user sets this value to zero, a repetitive stimulation is activated until it is stopped by the user. Finally, the measurement and control of the chip temperature can be activated in the same area.

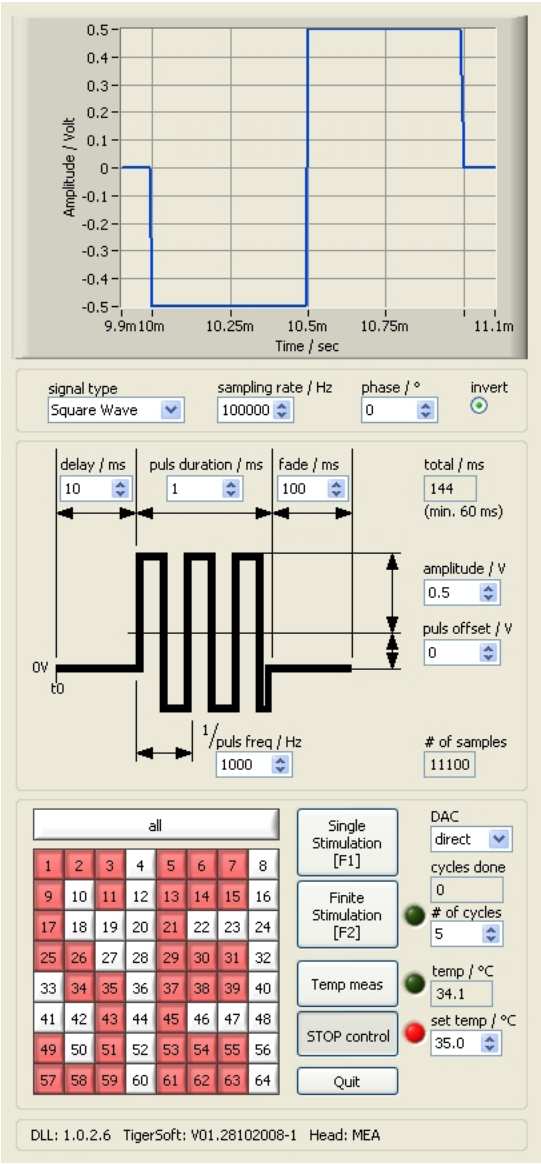

Figure 4.12: Graphical user interface of BioMAS software for the extracellular stimulation with MEAs. Three areas of the user interface are used for pulse visualization, selection of the pulse parameters, and control of the stimulation procedure.

A similar program for stimulation with the microelectrodes on Mi-BeSAN chips and two programs for the recording with a 16-channel FET chip or a 64-channel MEA are also already available. However, all software components are still in a developmental state and will be further improved and expanded in terms of functionality.

4.3.4 Electrophysiological Setup with BioMAS

In order to perform extracellular stimulation experiments, BioMAS was included in an electrophysiological setup similar to the configuration described in Section 4.1. Figure 4.13 shows a basic schematic of an electrophysiological setup including a patch-clamp amplifier and BioMAS.

A chip with a sensor array for bidirectional communication with electrogenic cells is mounted on the headstage. A Ag/AgCl wire is immersed into the the electrolyte solution in the culture dish on the chip as the bath electrode. The electrode can either be used as a grounded reference electrode for stimulation or recording experiments, or be connected to a stimulation signal from the main amplifier for other applications like impedimetric measurements. A patch-clamp amplifier (EPC 10 Double, HEKA) can be used to simultaneously control and record the transmembrane potential of one or two individually investigated

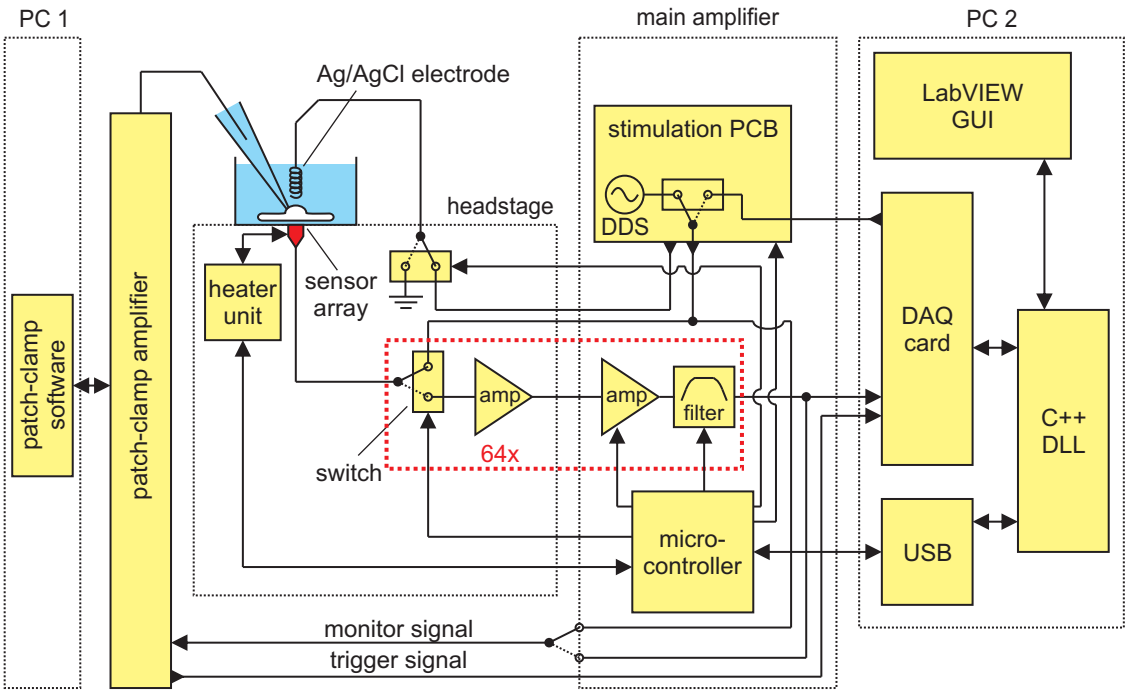

Figure 4.13: Schematic of electrophysiological setup for stimulation and recording with BioMAS. Similar to the setup used with the modified 20-channel MEA system (compare Figure 4.1), the experiment is controlled by two personal computers. A patch-clamp amplifier is used to simultaneously measure or control the transmembrane potential of the investigated cell during the experiment.

cells. The patch-clamp probes are again controlled by micromanipulators and a manual control unit (SM-5, Luigs & Neumann). The chip temperature is measured and controlled by a heater unit located in the headstage. Each of the sensors can be individually selected for extracellular recording or stimulation. If selected for stimulation, the sensor is connected to a stimulation line which is fed with a signal from the main amplifier or one of the DAC outputs of the DAQ card (e.g. PCI-6071E, National Instruments). In recording mode, the sensor potential is amplified in the first amplification stage of the headstage and then further amplified and filtered in the main amplifier. The microcontroller in the main amplifier is used to control the diverse switches in the system, as well as the heater temperature. It communicates with a second measurement PC by a USB connection. The amplified and filtered output signals are sampled by the ADCs of the DAQ card with a variable sampling ratio (depending on the used DAQ card). BioMAS was designed for use with the 64-channel PCI-6071E (National Instruments) with a combined sampling ratio of 1.25 Msamples, resulting in a sampling frequency of up to 19 kHz per channel if all channels are used for readout. Nevertheless, the BioMAS hard- and software are also compatible with any other DAQ card. The GUI interface is used to control the system by the DLL, which again controls the DAQ card and the USB connection for direct access to the BioMAS main amplifier. Finally, for synchronized intracellular and extracellular recording or stimulation with the patch-clamp amplifier and BioMAS, a trigger signal is generated by the patch-clamp clamp amplifier and used to trigger the start of the electrophysiological

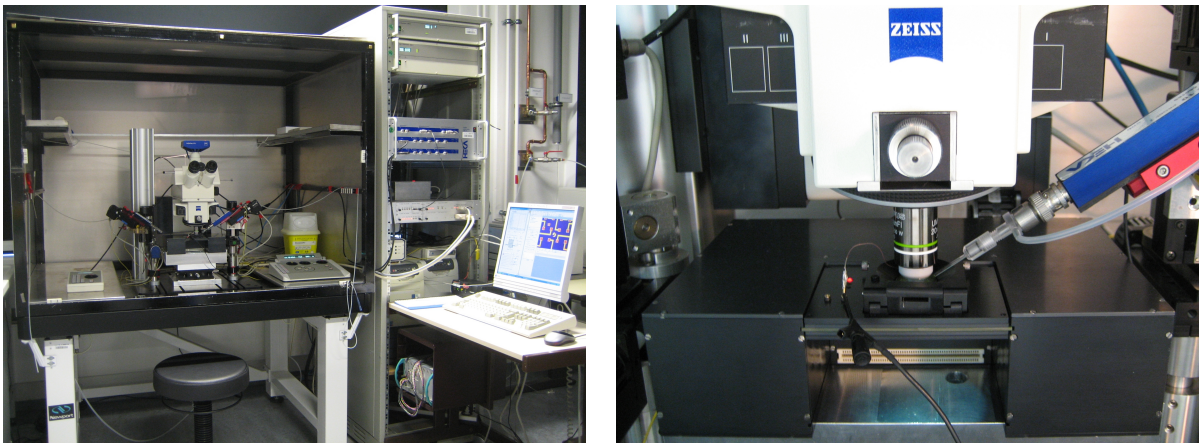

(a) (b)

Figure 4.14: Photographs of the electrophysiological setup with BioMAS. The setup is located on a vibration-isolation table in a Faraday cage (a). The headstage is mounted on an X-Y table underneath the immersion objective of a microscope for optical control of the experiment (b). Up to two micromanipulator-controlled patch-clamp pipettes are available to contact cells for comparative intracellular measurements. Alternatively, the system could also have been implemented on an inverted microscope.

measurement. Furthermore, either the stimulation voltage or the output voltage of up to four recording channels can be monitored by the patch-clamp amplifier using analog inputs.

Figure 4.14 shows two photographs of the experimental setup that was modified with the new amplifier system and used for most of the stimulation experiments presented in Chapter 5. The same upright microscope (Axiotech Vario, Carl Zeiss), immersion objective (UMPlanFl 20x, Olympus), digital camera (AxioCam MRc, Carl Zeiss) and micromanipulator with manual control unit (SM-6, Luigs & Neumann) are used for imaging and visual control. Again, a custom-made Faraday cage and the vibration-isolation table (VH3648W-OPT, Newport) are used as countermeasures to electromagnetic distortion and vibrations. The headstage is mounted on the same X-Y table (M-401, Newport) for positioning of the chip relative to the microscope. The two PCs for software-control are used with one keyboard and one monitor with a switch. The patch-clamp amplifier and the BioMAS main amplifier are located in a 19-inch rack next to the Faraday cage.

Chapter 5

Extracellular Stimulation and Recording

> The brain is the last and grandest biological frontier, the most complex thing we have yet discovered in our universe. It contains hundreds of billions of cells interlinked through trillions of connections. The brain boggles the mind.
>
> *James Dewey Watson (American molecular biologist and Nobel laureate, 1928-)*

In this chapter, the stimulation and recording experiments are presented that were performed with the chips developed in the scope of this thesis. The main focus of this work was the investigation of extracellular stimulation of electrogenic cells *in vitro* with simultaneous intracellular recording by patch-clamp experiments as shown in Figure 5.1. This combination of extra- and intracellular electrophysiological methods was chosen, since it enables the direct investigation of the influence of applied stimulation pulses on the membrane potential of the stimulated cell. In the case of neuronal cells, the purpose of the stimulation is the excitation of an *action potential* (AP, see Subsection 2.1.3). This combination with intracellular recording was already used in some of the first articles on extracellular stimulation with microelectrodes to prove stimulation success [33, 34, 144].

The first three sections of this chapter will deal with stimulation experiments performed with gold and modified *sputtered iridium oxide film* (SIROF) chips. In particular, Section 5.2 will give a detailed investigation of the stimulation with the newly processed 50 µm

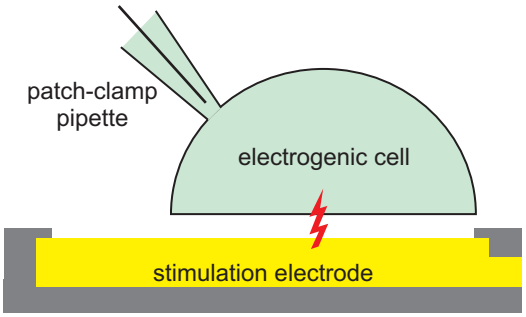

Figure 5.1: Experimental configuration for the investigation of extracellular stimulation. An electrogenic cell is located on top of the stimulation electrode and partly covers the electrode surface. The cell is additionally contacted by a patch-clamp pipette for simultaneous intracellular recording of the membrane potential.

iridium oxide (IrO_x) electrodes and compare measured data with simulations. Finally, Section 5.4 will present a few proof-of-principle experiments demonstrating the functionality of the new SIROF MEAs for extracellular recording, as well.

As already discussed in Subsection 2.5.1, the electrode potential of stimulation electrodes has to be kept within the *safe electrochemical window* (SECW), where only capacitive and reversible faradaic currents flow across the electrode-electrolyte interface. Therefore, voltage-controlled (instead of current-controlled) stimulation protocols were chosen for the experiments in this thesis to have complete control of the electrode potential and prevent damage to the electrode and the stimulated cells or tissue [54, 104].

Especially for single-cell experiments, the quality of the coupling between cell and electrode strongly varies from experiment to experiment depending on the cell size, position, and level of attachment to the electrode. Increasing stimulation pulse amplitudes have to be chosen for weak coupling. However, the SECW strictly limits the applicable stimulation voltage amplitude to a fixed maximum level, which sometimes may not be sufficient to achieve the desired stimulation effect. In that case, other stimulation pulse parameters like pulse form, frequency, phase sequence (monophasic or biphasic pulses, positive or negative phase first), and an increasing number of pulses can be applied for successful stimulation.

In a previous study by Wagenaar et al. [54], the effect of the pulse phase sequence on stimulation efficiency for voltage- and current-controlled stimulation was investigated using TiN electrodes. The authors used either current- or voltage-controlled pulses and evaluated the stimulation success by counting AP responses within a network of neuronal cells by recording with an array of 60 microelectrodes. Other studies investigated the influence of the pulse amplitude for current-controlled stimulation pulses on the stimulation with MEAs [34, 120], or the pulse number on voltage-controlled extracellular stimulation with capacitors [30] using direct intracellular recording. Section 5.1 will mainly deal with stimulation experiments with low coupling strength and the investigation of how some of the mentioned pulse parameters influence stimulation efficiency.

Finally, there are two different mechanisms to achieve extracellular stimulation. Firstly, the cell membrane can be depolarized by stimulation pulses until voltage-gated sodium channels in the membrane open and allow the influx of sodium ions [29, 30]. Secondly, high transmembrane voltages can cause *electroporation* or *electropermeabilization* of the cell membrane, generating a temporary permeabilization of the lipid bilayer [31, 145, 146] and a flow of ions along their electrochemical gradient into and out of the cell. The formation of nanopores with diameters up to 10 nm lasting for several nanoseconds induced by local electric field gradients at the water/lipid interface has been simulated by Tieleman [147]. Both mechanisms can lead to a further self-amplifying depolarization of the cell membrane and excitation of APs. However, electroporation should be prevented if possible, since high

electrical fields can cause irreversible membrane breakdown and cell damage. Theoretical investigations concerning cell models, stimulation mechanisms, and suitable stimulation pulse parameters can be found in the literature [104, 120, 148–151].

The stimulation experiments presented in this chapter were recorded with a temporal resolution higher than is feasible to print with markers for every data point. Therefore, if not stated otherwise, a subset of the data was chosen for each graph in a way that the markers are equally distributed and do not overlap, while a solid line shows the whole data.

5.1 Extracellular Stimulation with Standard Gold and Modified SIROF MEAs

In the past, the only electrode chips available for extracellular stimulation in our institute had been standard gold MEAs (zeroth chip generation, see Section 3.1.1). In previous work by Schindler [25], the extracellular stimulation of a rat cortical neuron by a voltage-controlled biphasic stimulation pulse had been shown in a proof-of-principle experiment.

One task of this thesis was to further optimize the setup used by Schindler and establish extracellular stimulation experiments with simultaneous intracellular monitoring by the patch-clamp technique in laboratory use. The first experiments performed in the scope of this thesis and all experiments presented in this section were done with a setup that was slightly modified from the one used for the proof-of-principle experiment, as explained in detail in Section 4.1.

5.1.1 Experiments with Gold MEAs

Using standard planar gold electrodes of the zeroth generation, a series of extracellular stimulation experiments with simultaneous intracellular recording by patch-clamp measurements was performed with rat cortical neurons and *Human Embryonic Kidney 293* (HEK293) cells. The chips were encapsulated as described in Section B.1. Cells were cultured on the gold MEAs, and patch-clamp experiments were performed on 5 to 14 *days in vitro* (DIV) for rat neurons or 2 to 4 DIV for HEK293 cells as described in the appendix (see Sections C.1 and C.2). For cells growing on top of one of the microelectrodes, extracellular stimulation experiments were conducted in whole-cell configuration (see Section 2.2).

Although numerous experiments were conducted, the yield of successful stimulation experiments was rather low and discouraging. Even for good patches with healthy neurons, no significant electrical activity could be excited by extracellular stimulation in most cases, although many different stimulation protocols, including various pulse shapes and amplitudes, were tested.

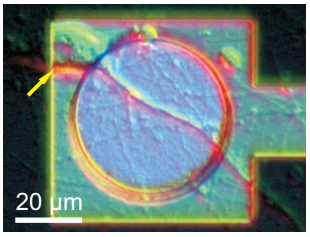

Figure 5.2: DIC image of a cell (yellow arrow) located at the edge of a planar gold stimulation electrode with a diameter of 50 µm. A big neurite (probably the axon) grew across the electrode. The cell was stimulated as shown in Figure 5.3.

The Figures 5.2 and 5.3 show one of the rare successful stimulation experiments performed with a planar gold MEA. A DIV 8 rat cortical neuron was stimulated using a planar gold electrode with a diameter of 50 µm. The cell body was located at the edge of the microelectrode, while a big cell process (probably the axon) grew across the electrode (see Figure 5.2). The membrane potential was measured intracellularly with a patch-clamp electrode in the current-clamp mode (v_P). The application of a biphasic voltage-controlled stimulation pulse with 950 mV amplitude caused the activation of ion channels in the cell membrane (see Figure 5.2). During the stimulation pulse, a passive reaction of the membrane potential could be seen, which followed the course of the stimulation pulse. Directly after this passive response, the membrane potential slowly started to rise until it reached a maximum value just above 0 mV after approximately 8 ms. Afterwards it slowly decayed to the initial value again.

Although the observed course of the membrane potential clearly indicates stimulated channel activity, the result is not satisfying for several reasons:

- With an overall duration of more than 15 ms, the time course of the membrane potential change is much too slow for a regular AP.
- The initial membrane potential (close to −40 mV) before the stimulation pulse was

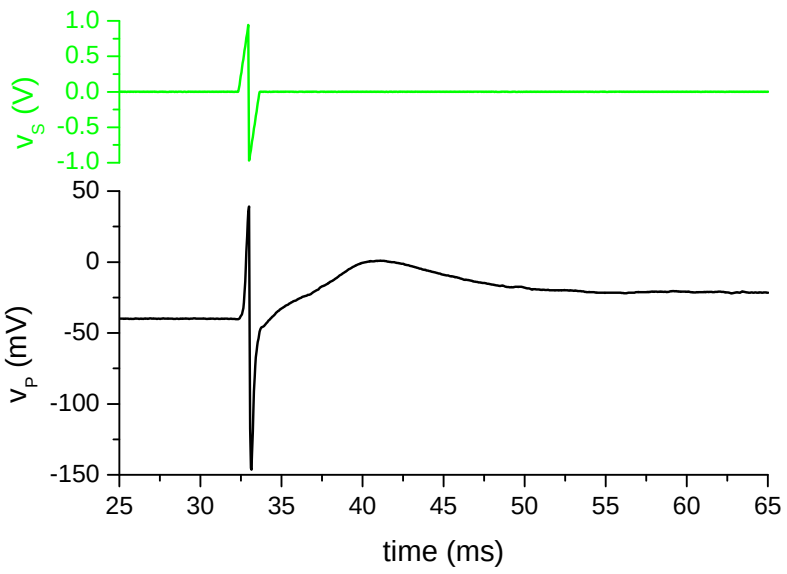

Figure 5.3: Extracellular stimulation experiment with cortical rat neuron located on the planar gold electrode shown in Figure 5.2. The membrane potential (black trace) was monitored intracellularly by a patch-clamp pipette (v_P). The application of a biphasic voltage pulse (green trace, (v_S)) to the gold electrode underneath the cell during a current-clamp experiment resulted in a cell response with opening of ion channels.

very high and close to the threshold for AP excitation for a neuronal cell. It is questionable if the stimulation would have caused channel activity for a lower (and more natural) initial membrane potential between −60 and −70 mV.

- The necessary stimulation voltage was rather high and close to or even above the potential of water electrolysis, which can cause electrode or cell damage.
- The successful stimulation was not reproducible before death of the patched cell and the end of the experiment.

Similar unsatisfying results were acquired for several other experiments, as well. For almost all experimental conditions it was found that the gold electrodes did not enable a significant cell response within reasonable stimulation voltages. Exceeding a stimulation voltage of about 1 V almost always caused a direct end of the experiment due to cell death. Obviously, the impedance of planar gold electrodes is too high to enable sufficient charge transfer for a reliable and efficient stimulator-cell contact.

A first approach to overcome the restrictions concerning the electrochemical properties of the stimulation electrodes was the electrochemical deposition of a rough platinum layer ("platinum black") on the gold, causing a significant increase of the electrode surface and decrease of the electrode impedance. The platinization was done by a method adapted from Thiébaud et al. [127] and is described in detail in Subsection 3.1.1 on page 39 of this thesis.

As shown in Subsection 3.1.1, the platinization caused an improvement of the electrochemical properties of the gold electrodes with a significant decrease in the impedance (see Figures 3.3). Nevertheless, there are two major disadvantages of the platinized electrodes restricting their usability for the stimulation experiments in this thesis. First, the electrochemically deposited platinum is very mechanically unstable and is mostly removed by the standard cleaning procedure for the MEA chips (see Section B.3). Therefore, the platinization has to be repeated before every cell culture to retain the full functionality of the chips. Second, the platinum black layer on the planar gold electrodes is visualized as a dense grainy black layer in *differential interference contrast* (DIC) images, completely concealing any cells located on the platinized electrodes. This makes patch-clamp experiments, which are necessary for the intracellular recording of the membrane potential, with cells on the platinized electrodes very difficult to impossible.

Figure 5.4.a shows a DIC image of a platinized gold electrode with a diameter of 100 µm. A culture of DIV 6 rat cortical neurons was grown on the chip surface. Several cortex cells growing in the vicinity of the electrode can easily be seen. However, the platinum black on the electrode surface makes it impossible to see if there are any cells located on the electrode. In order to locate any possible cells in position for stimulation, fluorescence microscopy was

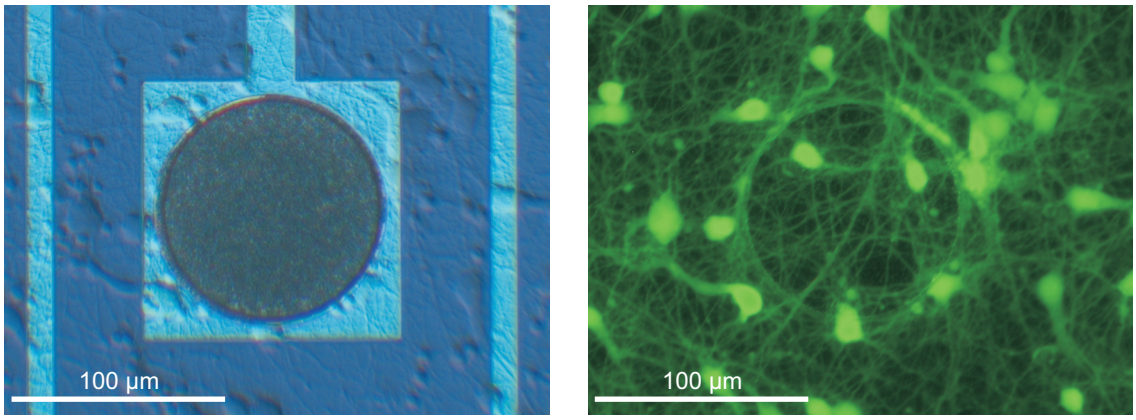

(a) (b)

Figure 5.4: DIC image (a) and fluorescence image (b) of a calcein-labeled rat cortical neuron culture on a platinized gold electrode, visualizing the experimental situation for a stimulation experiment. In order to locate the cells on the electrode, the cells have to be labeled with a fluorescent dye. During the patch-clamp experiment, repeated switching between DIC and fluorescence microscopy is necessary.

used. The cells were stained for at least 15 minutes with the fluorescent dye calcein AM (Sigma-Aldrich Chemie GmbH, Taufkirchen, Germany) in a concentration of approximately 1 µmol/l. Calcein AM can be transported through the cellular membrane into living cells, where it is enzymatically metabolized to calcein, resulting in green fluorescence. Altered in this way, the molecule cannot pass through the membrane anymore and stays within the cells. Figure 5.4.b shows an fluorescence image of the same area shortly after the DIC image in Figure 5.4.a was taken. Two cortical cells, which were previously not visible, can be found completely located on the 100 µm stimulation electrode.

Although a combination of DIC and fluorescence microscopy can be used to perform patch-clamp measurements with labeled cells on platinized electrodes, this combination of methods adds an additional error source and level of complexity. Experiments performed this way did not yield any successful stimulations.

5.1.2 Experiments with Modified SIROF MEAs

As a second approach to reduce the electrode impedance and increase the stimulation capabilities of the standard MEAs, the electrodes were coated with a SIROF. The design, production process, and characterization of these first generation SIROF MEAs are presented in Subsections 3.1.1 and A.1.2. The resulting MEAs carried electrodes with good electrochemical properties (low impedance and high charge storage capacity), but still bared technological challenges like fractured or missing SIROF surfaces from the production process or detachment during long-term cell culture. Nevertheless, the first generation

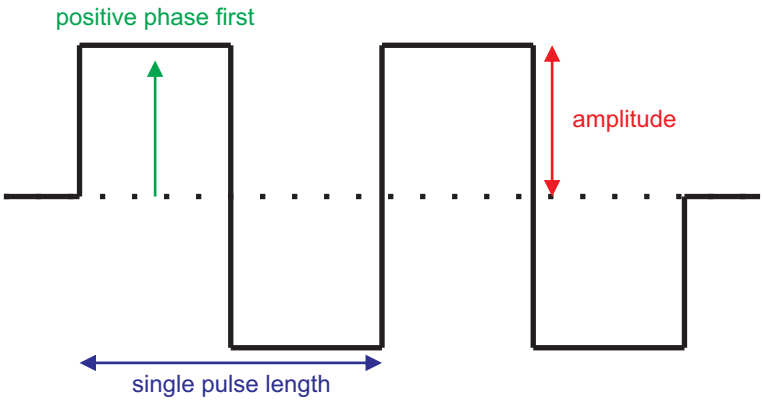

Figure 5.5: Example of a biphasic rectangular stimulation pulse with a pulse number of two for visualization of the three investigated pulse parameters. The shown pulse has a positive-phase-first phase sequence (indicated green). The pulse amplitude is shown in red, and a single pulse length is indicated in blue.

SIROF MEAs could be used for a series of successful stimulation experiments.

SIROF MEAs of the first generation were encapsulated as described in Section B.1, activated, coated with a protein mixture, and used for the culture of rat cortical neurons as described in Section C.1. The cells were grown on the chip surface for several days and all patch-clamp experiments were performed at 6 to 10 DIV as described in Section C.1. For extracellular electrical stimulation, voltage pulses were applied between one selected SIROF microelectrode and the reference electrode using the experimental stimulation setup with coupled intracellular recording as described in Section 4.1.

In all stimulation experiments presented in this section, biphasic, rectangular, voltage-controlled pulses with a single-pulse duration of 133 µs (corresponding to a pulse frequency of 7.5 kHz) were used. Seven neurons located on an IrO_x microelectrode with a diameter of 10 or 100 µm were successfully patched and stimulated. Using those experiments, the effect of the three stimulation pulse parameters phase sequence (positive or negative phase of the biphasic pulse first), amplitude, and pulse number on the stimulation efficiency (success ratio) and AP latency (time between start of the stimulation pulse and maximum of the AP) was analyzed. An overview of the pulse parameters examined is shown in Figure 5.5. All measurements considered in this section were performed at room temperature (22 to 24 °C).

The available time for investigating the stimulation greatly varies with every cell depending on the cell fitness and the time until the cell dies due to intracellular measurement with the patch pipette. Furthermore, the experimental conditions change for measurements with different cells, since the neurons vary in terms of cell fitness as well as their position on, and attachment to, the electrode. These variations in the experimental conditions are difficult to determine. For those two reasons, a statistical analysis of the results with various cells is very difficult. Therefore, only the results of the stimulation experiments with one particular neuron were taken into account for statistical evaluation. This particular cell showed good cell fitness and provided a long experimental time (70 minutes) for approximately 180 stimulation experiments. Due to the variation in the experimental situation between

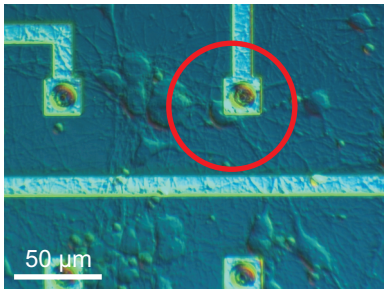

Figure 5.6: DIC image of the stimulated cell located at the edge of a modified SIROF stimulation electrode with a diameter of 10 µm. The red circle marks the position of the cell and the stimulation electrode.

cells, the results from this study cannot be used to give absolute numbers for ideal pulse parameters. However, the results show general tendencies for the influence of stimulation parameters. Furthermore, similar trends regarding the effect of the three pulse parameters investigated could be attained for the other cells investigated as well.

As can be seen in Figure 5.6, the investigated cell grew at the edge of a 10 µm SIROF microelectrode, partly covering it. The fact that the cell was only partly situated on the electrode suggests a sub-optimum coupling between electrode and cell with a comparably low seal resistance and low ratio of attached to free cell membrane area. Therefore, it could be expected that rather high voltages would be necessary for stimulation.

Before extracellular stimulation was conducted, the cell activity was tested using standard voltage-clamp and current-clamp protocols to show channel activity and the possibility of AP excitation. Figure 5.7 shows the results of a current-clamp experiment with the investigated cell. A bias pipette current (i_P) of −20 pA was injected to clamp the cell to a resting potential of approximately −55 to −60 mV. To test the ability of the cell to generate APs, a series of ten measurements was conducted, during which the cell was intracellularly stimulated for 50 ms by a depolarizing pipette current of +100 pA in addition to the bias current (red traces in Figure 5.7). Prior to the stimulation current, a

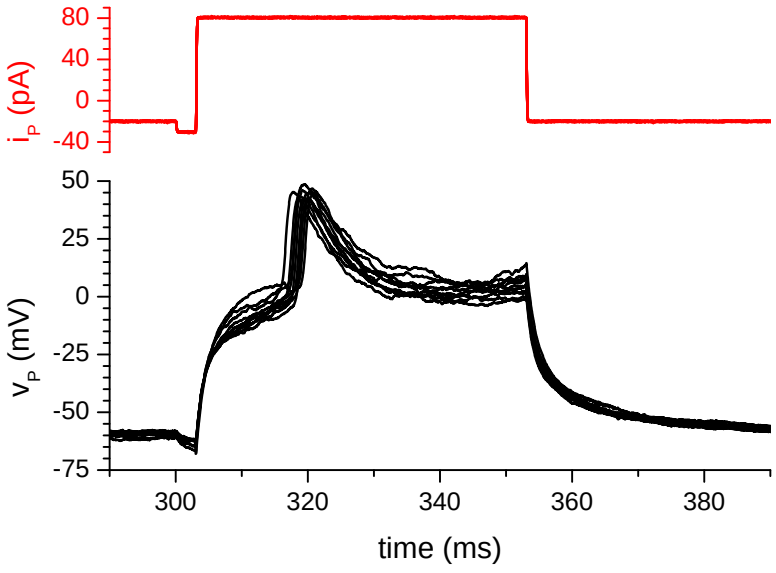

Figure 5.7: Ten current-clamp recordings of the cell located on the stimulation electrode (see Figure 5.6) to show the cell fitness. The cell was intracellularly stimulated with a pipette current (red traces, i_P), which caused a depolarization to the point of AP excitation.

negative pipette current of −10 pA was injected for 3 ms for an initial hyperpolarization to overcome resting fast sodium channel inactivation, as is regularly used in electrophysiology [9,152,153]. As can be seen by the course of the membrane potential (black traces in Figure 5.7, v_P), the stimulation of the cell by the pipette current caused a depolarization up to the point of AP excitation with a typical AP shape in all ten measurements. The measurements conducted proved the cell was a healthy neuron with reliable activation of ion channels and excitation of APs.

During the stimulation experiments, the current-clamp recording was continued with the same bias current of −20 pA to keep the membrane potential at a constant level. However, the actual membrane potential at the beginning of each stimulation experiment was not constant. As known from literature [154], the membrane potential of neuronal cells permanently fluctuates. Therefore, only the 129 stimulation experiments with a pre-pulse membrane potential within the standard deviation (±6.3 mV) of all measurements from a mean value of −57.4 mV were used for the analysis. Additionally, cellular responses were only regarded as APs if their amplitude (maximum during AP minus pre-pulse membrane potential) was higher than 45 mV and reached a maximum potential of at least −10 mV. Finally, only responses with a latency of less than 16 ms were considered to exclude responses evoked by spontaneous activity. Within these limitations, 43 stimulation experiments successfully caused the excitation of an AP.

Pulse Phase Sequence

The first pulse parameter investigated was the phase sequence. As previously described by Wagenaar et al. [54], the stimulation efficiency can be influenced by the order of the positive and negative phase within biphasic pulses. Therefore, the stimulation efficiency and AP latency was compared for experiments with biphasic pulses having a phase sequence with either the positive phase or the negative phase first.

Using the same stimulation frequency, pulse number, and amplitude, a higher stimulation probability and lower latencies were found for negative-phase-first pulses. Figure 5.8 shows an example of the membrane potential during extracellular stimulation with trains of two biphasic pulses (700 mV amplitude). While stimulation with positive-phase-first pulses only caused a small depolarization from the initial membrane potential, the negative-phase-first pulses caused a stronger depolarization, resulting in the excitation of an AP. For both traces, the onset of the extracellular stimulation pulse can be seen by the stimulation artifacts at about 30 and 32 ms.

Quantifying this result, Figure 5.9 shows a comparison of the stimulation efficiency for several measurements with positive- or negative-phase-first pulses with pulse amplitudes of 600 mV (3 to 5 pulses) and 700 mV (1 to 2 pulses). For both amplitudes, the efficiency

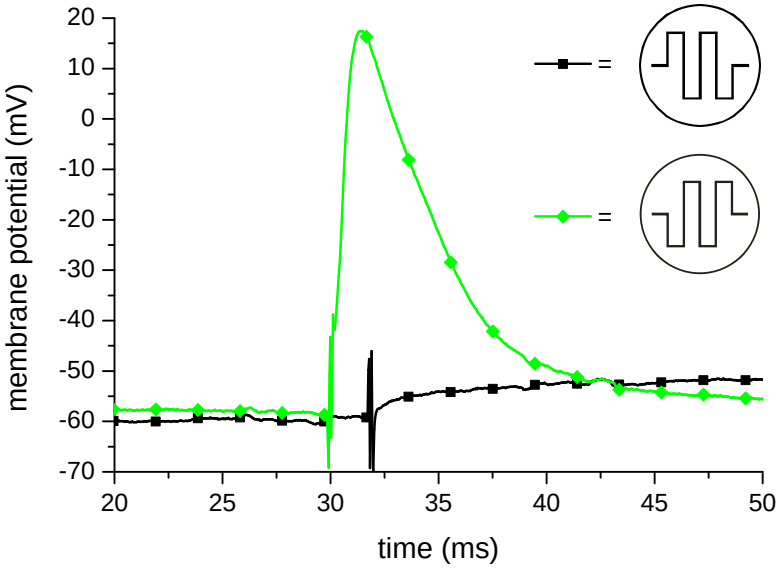

Figure 5.8: Influence of pulse phase sequence on the stimulation efficiceny. The cell membrane potential during application of two biphasic rectangular pulses with 700 mV amplitude with positive (black trace with squares) and negative (green trace with diamonds) phase first is shown. The stimulation pulses were applied at 30 and 32 ms. Only the negative-phase-first pulse could excite an AP.

of AP excitation was significantly higher for the negative-phase-first pulses. Additionally, the latency was also reduced in comparison to positive-phase-first pulses. However, further measurements by Wallys indicate that both effects of increased success ratio and reduced latency for negative-phase-first pulses slowly vanish with an increasing number of stimulation pulses [123].

Pulse Amplitude

Secondly, the pulse amplitude was analyzed with regard to its impact on stimulation efficiency. One important constraint of the pulse amplitude was to stay within the SECW of the electrode material to avoid irreversible electrochemical reactions at the electrodes. Therefore, the stimulation voltage was limited to a maximum value of ±800 mV.

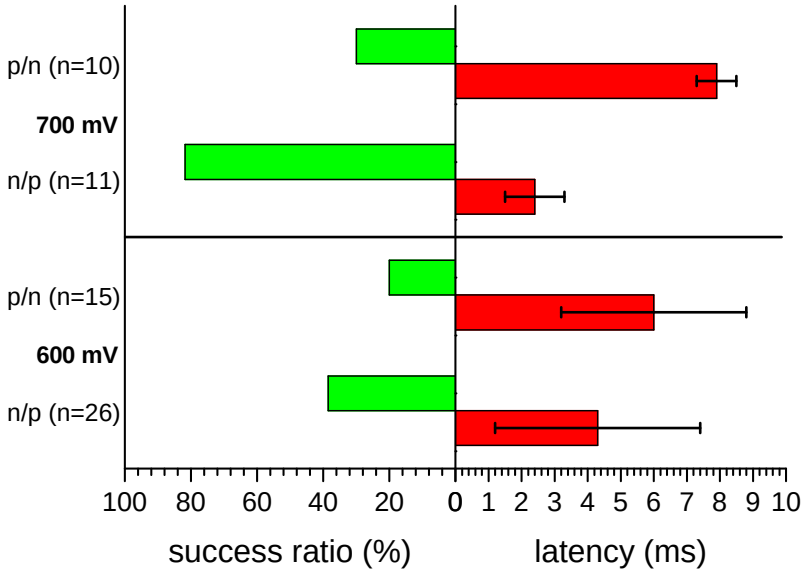

Figure 5.9: Results of quantitative investigation of the pulse phase sequence influence. The stimulation success rate and the AP latency are compared for pulses with positive (p/n) or negative (n/p) phase first at a pulse amplitude of 600 mV (3, 4, or 5 pulses) and 700 mV (1 or 2 pulses). The error bars in the latency plot represent the standard deviation.

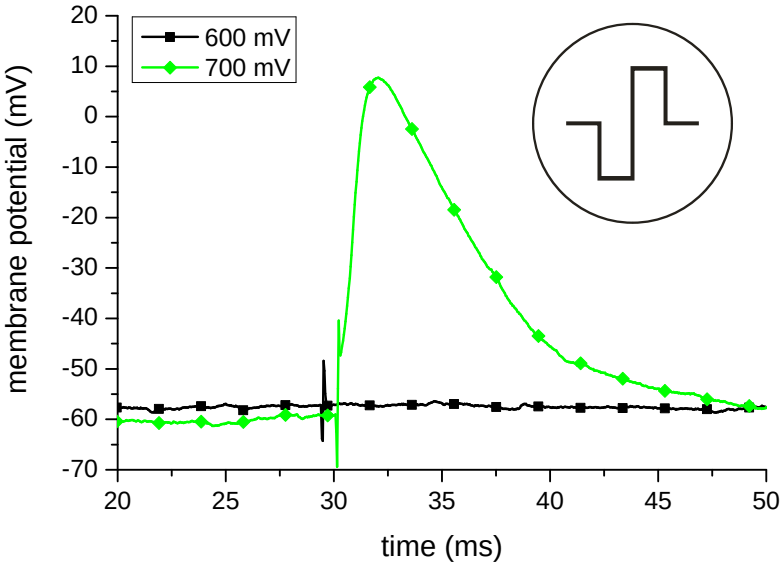

Figure 5.10: Effect of varying pulse amplitude on the stimulation efficiency. Two stimulation experiments with one biphasic negative-phase-first rectangular pulse with 600 mV (black trace with squares) or 700 mV (green trace with diamonds) amplitude. For the 700 mV pulse an AP was excited.

As expected, increasing the pulse amplitude enhances the stimulation success ratio and reduces the latency. While Figure 5.10 shows an example of two measurements with one negative-phase-first stimulation pulse with amplitudes of 600 and 700 mV, Figure 5.11 gives a quantitative comparison of experiments with trains of up to six negative-phase-first stimulation pulses for pulse amplitudes between 500 and 800 mV. For 500 mV, no experiment resulted in a successful stimulation. With increasing amplitude, the stimulation efficiency gradually increased, while the latency decreased at the same time. As can be seen by the large standard deviation for 600 mV, the latency varies greatly, thus, limiting the stimulation reliability for low amplitudes. Since stimulation was successful in all cases for pulse amplitudes of 800 mV, it was not further increased to prevent damage to the cell and the electrode.

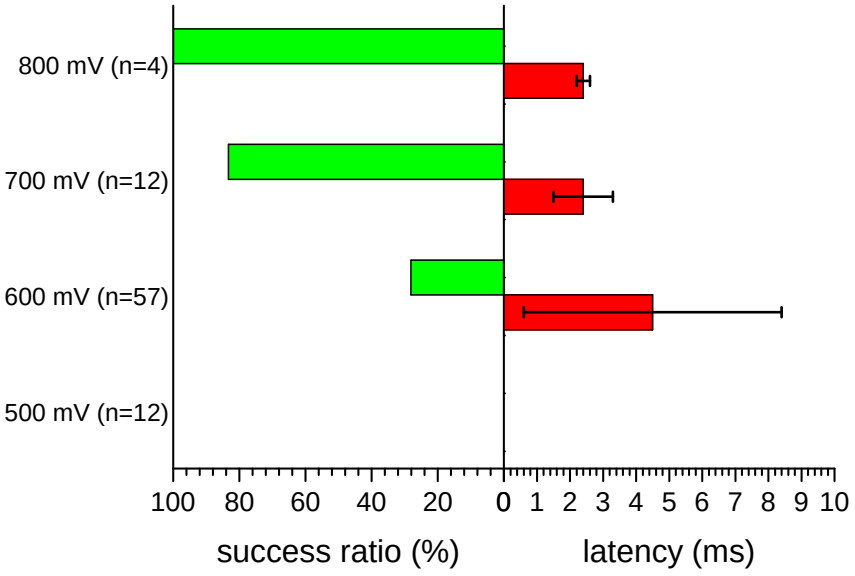

Figure 5.11: Quantitative analysis of the influence of the stimulation pulse amplitude. The stimulation reliability is compared for experiments with trains of up to 6 negative-phase-first stimulation pulses for different pulse amplitudes between 500 and 800 mV. Again, the error bars in the latency plot represent the standard deviation.

Pulse Number

Instead of raising the pulse amplitude of single pulses, the probability for AP excitation can be increased by using trains of pulses with increasing pulse numbers. As shown in the literature [30], repetitive weak activation of ion channels by trains of stimulation pulses is a method to depolarize the cell membrane stepwise to reach the threshold potential for the activation of APs in single cells. This effect is based on the asymmetric voltage dependence of sodium channel conductivity [10] and can be explained by the theory of periodic electrical stimulation [30, 155–157]. In this work, trains of up to 6 pulses were used for the stimulation of individual cells.

Figure 5.12 shows the intracellularly measured membrane potential of the stimulated neuron during application of trains of two, four, or six stimulation pulses with 600 mV amplitude. While two and four pulses were not sufficient to reach the threshold for sodium channel opening, six pulses caused a depolarization which finally led to excitation of an AP. The inset of Figure 5.12 shows a stepwise increase of the membrane potential with each stimulation pulse. Figure 5.13 gives quantitative results for the influence of the pulse number on stimulation efficiency and latency of APs with negative-phase-first stimulation pulses and 600 mV amplitude. While stimulation with one or two pulses could never excite an AP, the success ratio could be increased to about 24 % for three or four pulses and even to about 58 % for five or six pulses. However, it can be seen that the latency cannot be reduced by using more stimulation pulses. Instead, the latency seems to be distributed over a rather large time scale at longer stimulation pulse trains.

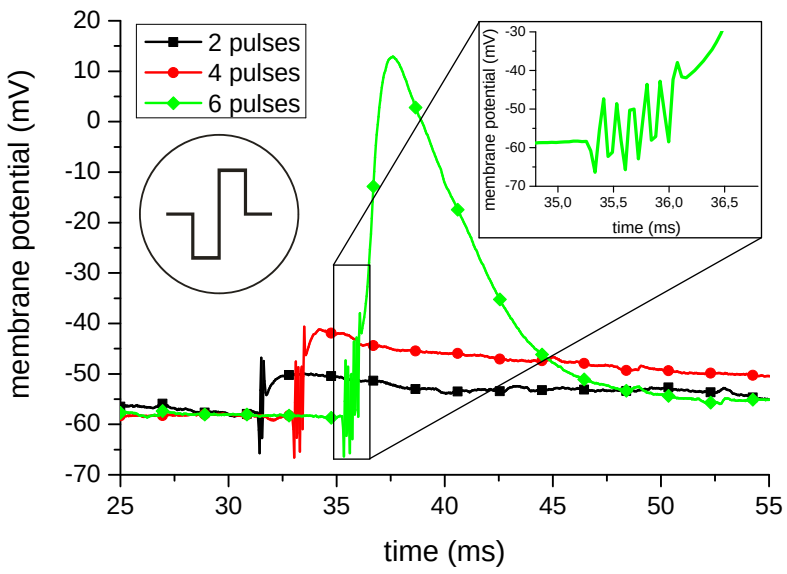

Figure 5.12: Impact of varying pulse number on the stimulation efficiency. The membrane potentials of a cell stimulated with trains of two (black trace with squares), four (red trace with circles), and six (green trace with diamonds) negative-phase-first pulses with 600 mV amplitude are shown. An AP only occurred for a train of six pulses. The figure inset shows a magnification of the time of stimulus application with the stepwise increase of the membrane potential from pulse to pulse.

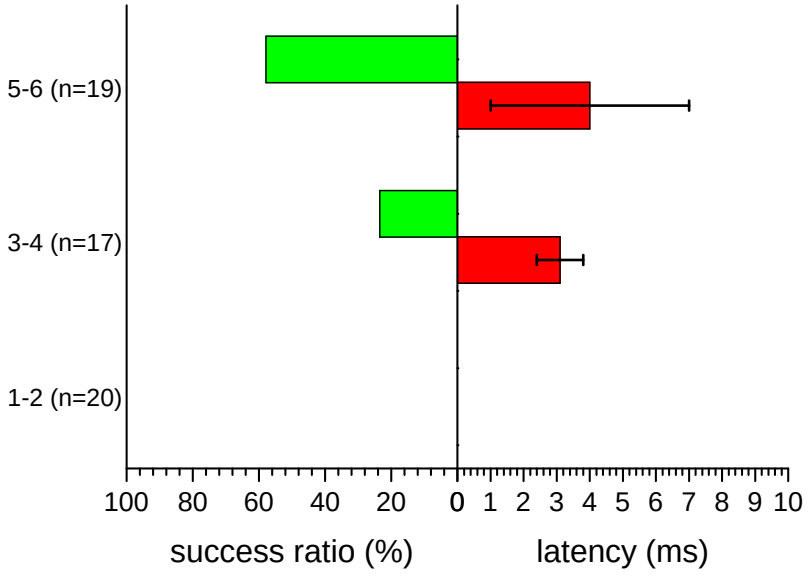

Figure 5.13: Quantitative analysis of the impact of the stimulation pulse number on the stimulation success rate and the AP latency. A comparison of both values is shown for stimulation with 1 to 2, 3 to 4, or 5 to 6 negative-phase-first rectangular stimulation pulses with 600 mV amplitude. The error bars in the latency plot indicate the standard deviation.

Electroporation

As discussed before, strong electrical fields applied to a cell membrane can cause irreversible electroporation to the point of cell damage [145–147]. In order to exclude the occurrence of this damage, further stimulation experiments with extracellular patch solution containing ethidium bromide were conducted in the scope of a diploma thesis [123]. While intact cell membrane is impermeable to this reagent, it can pass through electroporated membranes and bind to DNA in the cell's nucleus. Upon binding, the ethidium bromide changes its conformational structure to become fluorescent and detectable by fluorescence microscopy.

As shown by Wallys [123], no fluorescence could be detected after application of up to 100 stimulation pulses with amplitudes up to 1 V and frequencies up to 10 kHz using this method. However, a further increase of the pulse amplitude to voltages above 2 V caused damage to the cell membrane and detectable fluorescence. This leads to the conclusion that the cell membrane stays intact and no electroporation occurs within the amplitude and frequency range used for stimulation in this thesis.

5.1.3 Summary and Discussion of the Results

The experiments presented in this section show the usability of the modified SIROF MEAs of the first generation for electrophysiological experiments and especially the extracellular stimulation of individual neurons from dissociated cultures *in vitro*. In combination with intracellular recordings, stimulation pulse parameters were investigated for their influence on the stimulation efficiency.

For the given experimental situation, negative-phase-first voltage pulses were shown to be more efficient for extracellular stimulation in terms of success rate and lower AP latency

than positive-phase-first pulses. This result is in contradiction to the already mentioned publication by Wagenaar et al. [54], where positive-phase-first pulses were shown to be slightly more efficient for stimulation. This contradiction of the results could originate in differences in the experimental conditions and the data acquisition, since Wagenaar and colleagues evaluated the stimulation success from the number of measured APs from a whole electrode array with 60 microelectrodes within 20 ms after application of the stimulation pulse. This included responses from several cells that were probably stimulated by their processes growing across the microelectrodes used for stimulation. In the approach chosen in this thesis, the intracellularly measured response rather reflects the direct stimulation effect on a single-cell level.

A possible explanation for the increase in stimulation efficiency can be found in the two-domain stimulation model introduced in Subsection 2.5.2. As discussed there, any voltage applied to the stimulation electrode causes a voltage drop across the cell which is divided between attached and free membrane according to the ratio of both membrane domains' capacitances (capacitive voltage divider). Since the attached part of the membrane is usually smaller than the free part, the voltage drop across the attached membrane domain is larger. Every voltage applied to the electrode causes depolarization of one membrane domain and hyperpolarization of the other domain. For a negative-phase-first pulse, the initial negative voltage causes a hyperpolarization of the large free membrane domain which can partly remove the resting inactivation of the fast sodium channels in this area, similar to the brief hyperpolarizing current used in the current-clamp experiment presented in Figure 5.7. This effect of extracellular stimulation with biphasic pulses was already reported for neurons in the central nervous system [150,151]. Additionally, the depolarization of the attached membrane domain during this first pulse phase can cause the influx of sodium ions, leading to a residual depolarization at the end of the first pulse phase. Thus, the following depolarization caused by the positive voltage phase at the free membrane can easily excite an AP if the threshold for sodium channel activation is reached. Especially the high capacitive depolarization due to the increased step height between the negative and positive phase can cause a sufficient activation of ion channels to excite an AP in the free membrane. This also holds true in the case of low junction resistance (weak coupling), since the value of the junction resistance mainly influences the time constant describing the decay of the passive capacitive depolarization and not its initial amplitude.

For the opposite pulse sequence, the large free membrane will first be depolarized and the following hyperpolarization during the second pulse phase can suppress the excitation of an AP in the large free membrane. Even if an AP is excited in the smaller attached membrane domain during the depolarization in the second pulse phase, the hyperpolarization in the large free membrane at the same time will either suppress the AP or block its propagation

to other parts of the cell [29, 104]. However, this effect only occurs for a small number of stimulation pulses. With an increasing pulse number the improved stimulation reliability slowly vanishes, since the influence of the first phase of the first pulse and the initial phase sequence is reduced for later pulses.

As expected, increasing the stimulation pulse amplitude also increased the stimulation efficiency if the other parameters were kept constant. At the same time, the average AP latency was reduced, making the stimulation more reliable in general. However, since it is crucial for long-term experiments to prevent damage to electrodes and cells, the stimulation pulse amplitude should be limited to voltages within the SECW of the electrode's material to prevent irreversible electrochemical reaction such as gas evolution due to electrolysis. For the experiments presented here, reasonable success ratios were achieved at voltages well within the SECW despite the rather poor cell-electrode coupling.

A good alternative to increasing amplitude for higher stimulation success ratios is the use of trains of stimulation pulses. For every single pulse causing a depolarization higher than the threshold for sodium channel activation, a minor amount of positively charged sodium ions is injected into the cell, generating a small residual depolarization at the end of the pulse. This can lead to a stepwise increase of the membrane potential by summation of residual charges from several consecutive stimulation pulses. If the summed depolarization finally leads to a self-amplification, an AP can be excited. However, repetitive stimulation only suffices to elicit APs if two prerequisites are fulfilled: firstly, the passive repolarization of the cell membrane must be slow enough to leave substantial residual depolarization after each pulse, and secondly, the inactivation of sodium channels must be low enough to leave a sufficient number of channels excitable until the summed depolarization reaches the threshold for AP excitation [30]. Unfortunately, stimulation with a higher number of pulses leads to widely distributed latencies, since the threshold for AP excitation is reached at a different time of the pulse train for every experiment. Furthermore, the stepwise depolarization can lead to slower AP kinetics - comparable to intracellular stimulation with a small depolarizing current in a current-clamp experiment.

The extracellular stimulation of individual neurons in dissociated cultures is strongly influenced by coupling factors such as geometry of the electrode-cell contact area, which will not allow determination of absolute values for an optimum amplitude or pulse number. However, by adjusting stimulation pulse parameters, maximum stimulation reliability can be achieved without causing damage to the electrodes or the cells. In the next section, more experiments with well-defined experimental conditions and a better coupling between the cell and the stimulation electrode will be presented and evaluated to further elucidate the extracellular stimulation of electrogenic cells.

5.2 Extracellular Stimulation with SIROF MEAs

This section deals with stimulation experiments conducted with SIROF electrodes from the fourth generation MEAs. This generation of MEAs was developed in the scope of this thesis, and their design, production process and encapsulation procedure is described in detail in Subsections 3.1.2 and A.1.2 as well as Section B.1. The characterization of the chips (see Subsection 3.1.2) revealed electrodes with a stable and dense SIROF layer and, after conditioning and activation, good electrochemical properties with a low impedance and a high charge storage capacity. In particular the yield of working electrodes and the long-term stability was significantly improved in comparison to the first generation SIROF MEAs.

The zeroth and first generation MEAs were mainly used to show the feasibility of the stimulation experiments with the experimental configuration shown in Figure 5.1 and to investigate the influence of stimulation pulse parameters on the stimulation efficiency especially for weak coupling between cells and electrodes. The fourth generation MEAs were used for a detailed study of the cell-electrode coupling for extracellular stimulation. The big electrode size (diameter of 50 µm) allowed to generate a very defined experimental situation with exactly one cell completely situated on top of a single electrode. Since neuronal cells usually show a complex morphology with several dendrites, it is very difficult to estimate the size and position of the cell-electrode contact and which fraction of the cell membrane is attached to the electrode. Therefore, the first stimulation experiments and a detailed analysis of the the cell-electrode coupling with simulations presented in Subsection 5.2.1 were done with a HEK293 cell line. The HEK293 cells show a less complex morphology and an optically assessable cell-electrode contact. Subsection 5.2.2 shows results of stimulation experiments with rat cortical neurons conducted with the fourth generation MEAs. The results of this section are summarized and discussed in Subsection 5.2.3.

All experiments in this section were performed with the newly developed BioMAS amplifier system (see Section 4.3). The new amplifier was introduced in an electrophysiological setup for simultaneous intracellular recording experiments as shown in Figures 4.13 and 4.14 and as described in Subsection 4.3.4. The temperature control of the new amplifier system was used to regulate the temperature of the chip and the electrolyte solution to values between 35 and 36 °C for all experiments.

5.2.1 Extracellular Stimulation of HEK293 Cells

The first stimulation experiments with the fourth generation SIROF MEAs were done with a HEK293 cell line. HEK293 cells have been used widely in cell biology in the last decades. The cell line was originally generated in the 1970s by Graham [158] from human embryonic

kidney cells. Besides many other uses, they are regularly utilized for electrophysiological studies, since they can be easily transfected with genetic information e.g. for ion channels. While these channels are highly expressed, the HEK293 cells have a rather low number of endogenous ion channels [159]. The cells used in this study were taken from a stable cell line expressing the $Na_V1.4$ voltage-gated fast sodium channel from rat skeletal muscle [160,161]. It was used as a model system for extracellular stimulation, since this cell line expresses one type of the family of fast sodium channels, which are important for the excitation of APs (compare Section 2.1). The HEK293 cells have a size very similar to vertebrate neurons, but with a much simpler morphology and shape without the dendritic tree. Therefore, the size and position of the compartments of the free and attached membrane can much easier be optically estimated.

To prepare the electrophysiological experiments, the SIROF chips of the fourth MEA generation were cleaned as described in Section B.3, coated with a protein solution and used to culture the HEK293 cells as described in Section C.2. On 2 to 4 DIV, cells growing on top of one of the microelectrodes were patched and stimulated extracellularly after establishment of the whole-cell configuration (see Sections 2.2 and C.2).

Cell Fitness and Ion Channel Functionality

Figure 5.14 shows two DIC images of HEK293 cells that were used for stimulation experiments. The cells were each completely located on a 50 µm SIROF electrode and patched for the simultaneous intracellular monitoring of the membrane potential (shown for the first cell by the patch-pipette in Figure 5.14.a). The membrane capacitances were found to be 17.0 pF for the first cell and 16.9 pF for the second cell (see Figure 5.14.b), which are typical values for HEK293 cells.

Before the stimulation experiments, the cell fitness and the ion channel activity was

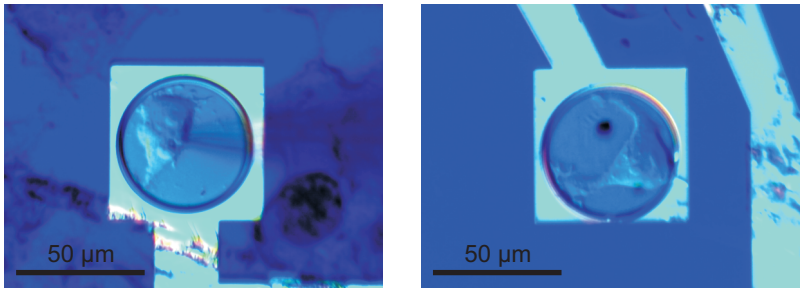

(a) (b)

Figure 5.14: DIC images of the two HEK293 cells used for stimulation experiments in this subsection. Both cells are completely located on a fourth generation SIROF stimulation electrode with a diameter of 50 µm. The cells were patched (see the patch-pipette in (a)), investigated in the whole-cell configuration, and used for stimulation experiments as described in the following.

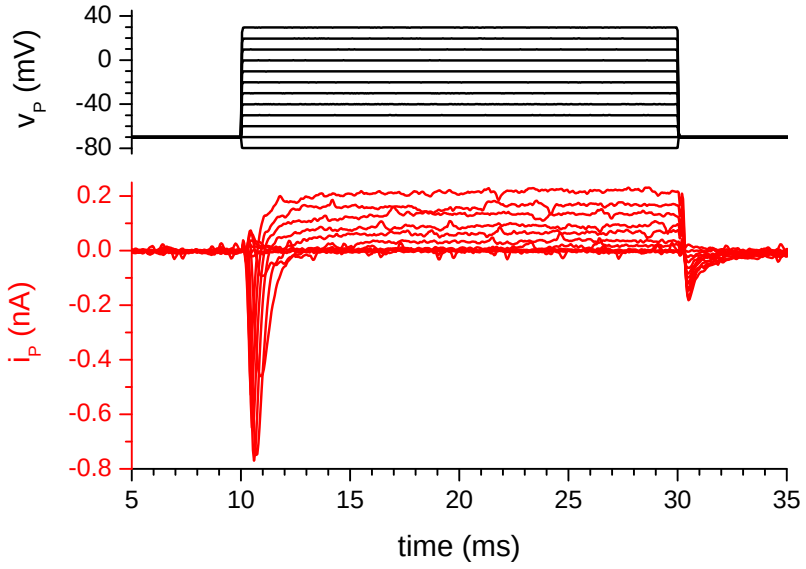

Figure 5.15: Voltage-clamp measurement of the HEK293 cell with $Na_V1.4$ fast sodium channels shown in Figure 5.14.a. The membrane current (red traces) is plotted in response to twelve membrane potential steps (black traces) to values between −80 and +30 mV.

tested using standard voltage-clamp and current-clamp protocols in the whole-cell configuration. Figure 5.15 shows the results of a voltage-clamp experiment conducted with the first HEK293 cell to test the activity of the $Na_V1.4$ sodium channels. A series of 23 measurements of the membrane current (red traces in Figure 5.15) during application of a stepwise membrane potential change (black traces) was done. In each measurement, the cell was initially clamped to the resting potential of −70 mV. After 10 ms, a stepwise change of the membrane potential was applied for 20 ms, before the resting potential was reinstated. The amplitude of the membrane potential step was increased by 5 mV for each experiment, ranging form a hyperpolarization to −80 mV in the first to a depolarization to +30 mV in the final measurement. Due to plotting density, only every second measurement is included in the figure.

The measured membrane current qualitatively resembles measurements found in literature [30, 161]. It can be divided into current conducted by the $Na_V1.4$ fast sodium channels and endogenous potassium channels [159]. Analyzing the voltage-clamp experiment, it can be found that the fast sodium channels open up at a membrane potential of approximately −35 mV, causing an inward (negative) sodium current into the cell. This threshold potential corresponds to values reported in literature [160, 161]. The peak sodium current increases with increasing membrane potential steps up to a maximum value of approximately −770 pA at a membrane potential of 0 mV. This value corresponds to the maximum sodium current that can be conducted by the $Na_V1.4$ channels in the cell membrane. With a further increase of the membrane potential steps, the peak current slowly depletes. The endogenous potassium channels of the cell cause a small outward-bound potassium current, which slowly increases in amplitude with increasing step voltage. The results of the voltage-clamp measurement are summarized in a current-voltage curve including the peak

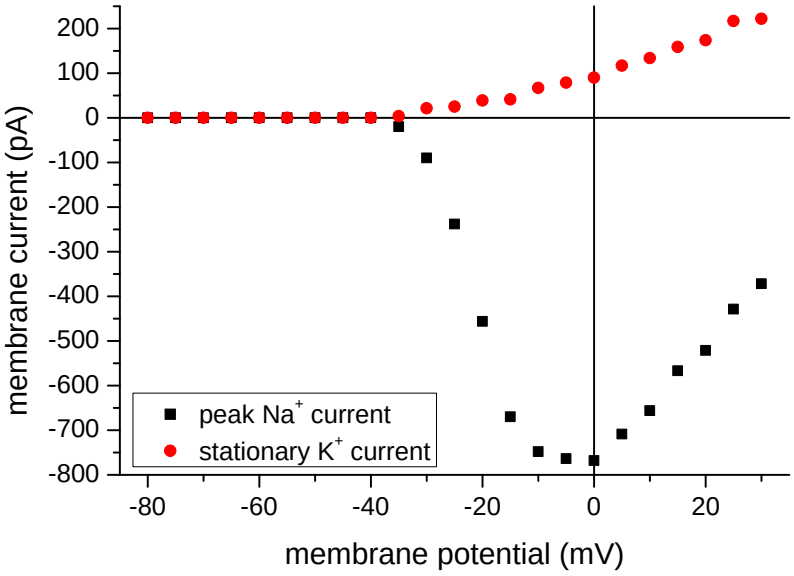

Figure 5.16: Current-voltage curve summarizing the results from the voltage-clamp characterization (see Figure 5.15) of the HEK293 cell shown in Figure 5.14.a. The peak sodium currents (Na^+, black squares) mediated by $Na_V1.4$ fast sodium channels and stationary potassium currents (K^+, red circles) mediated by endogenous potassium channels are plotted against the membrane potential applied during the voltage step.

sodium currents and the stationary potassium currents through the endogenous channels in Figure 5.16.

In the next step, the cell was clamped to a membrane potential of approximately −70 mV by injection of a bias current of −40 pA in the current-clamp configuration. In order to investigate the self-amplifying depolarization of the cell membrane by activation of the fast sodium channels, a current-clamp protocol was utilized as shown in Figure 5.17. Starting from the bias current, a rectangular current pulse with a stepwise increase of the amplitude between 0 (first measurement) and +250 pA (last measurement) in addition to the bias was applied to the cell for 10 ms. In each of the experiments, the depolarizing current causes an increase of the membrane potential. Starting with the fourth measurement with a

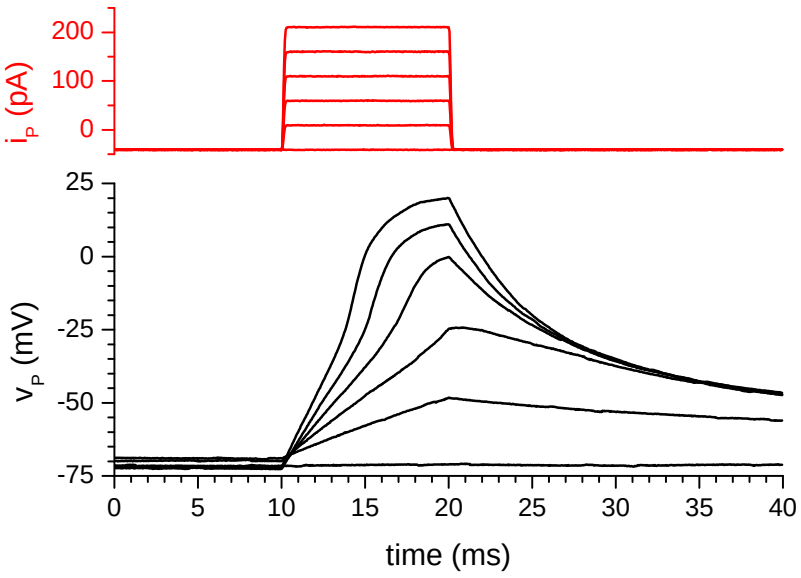

Figure 5.17: Current-clamp measurement of the HEK293 cell with $Na_V1.4$ fast sodium channels shown in Figure 5.14.a. The change of the membrane potential (v_P, black traces) in response to application of membrane current steps (i_P, red traces) with six different amplitudes between 0 and +250 pA in addition to the bias current is shown. The scans reveal the activation of pseudo-APs, when the threshold for ion channel activation is reached.

depolarizing current of 150 pA, the membrane potential reaches the threshold potential for the opening of the $Na_V1.4$ channels (approximately −35 mV, compare Figure 5.15), causing a self-amplification of the depolarization. For the final three measurements, this leads to a so-called pseudo-AP - a strong depolarization up to positive membrane potentials. Since the HEK293 cells only have a small amount of potassium channels, the repolarization at the end of the depolarizing pulse and the end of the pseudo-AP is slow and mostly passive.

The results presented for the first cell could also be achieved with similar values for the threshold potential and the current-voltage curve for the second HEK293 cell shown in Figure 5.14.b. For this cell, the current bias for maintaining the resting potential was −50 pA. Summing up the results from the voltage-clamp and current-clamp measurements, the presence of voltage-gated fast sodium channels with an approximate threshold potential of −35 mV could be affirmed. Furthermore, the cells showed a self-amplifying depolarization and the occurrence of pseudo-APs. Together with the facts that both cells were completely located on a stimulation electrode and had a size similar to a rat cortical neuron, this made them to excellent candidates to investigate the extracellular stimulation with SIROF microelectrodes. All stimulation experiments done with the two HEK293 cells presented in this subsection were done in the current-clamp configuration, and the cells were still injected with a bias pipette current of -40 respectively −50 pA.

Stimulation Experiments

Figure 5.18 shows the results of a series of extracellular stimulation experiments with voltage-controlled rectangular stimulation pulses with amplitudes of 300, 350, and 400 mV conducted with the first HEK293 cell. Similar to the experiments done with the first generation SIROF MEAs (see Subsection 5.1.2), biphasic negative-phase first pulses were chosen. A rather simple stimulation pattern with single pulses and a long pulse duration of 4 ms was chosen for clear result evaluation and simulation. 8 ms after beginning of each recording, the cell was extracellularly stimulated. Each trace shown in Figure 5.18 represents the average of five measurements.

As expected from the two-domain stimulation model and previous results with the first generation SIROFs, the leading negative pulse phase causes a measurable hyperpolarization of the free membrane domain, which is followed by a depolarization during the positive phase. The onset and offset of each pulse phase is clearly visible by strong capacitive peaks. For the 300 mV pulse, the depolarization quickly decays during the positive pulse directly after the capacitive peak, leaving no significant residual depolarization after the offset of the pulse. For the 350 and 400 mV pulse, however, an increasing depolarization can be measured during the positive phase, and even after offset of the stimulation pulse, clearly indicating activity of the fast sodium channels of the cell. As expected, the slope and

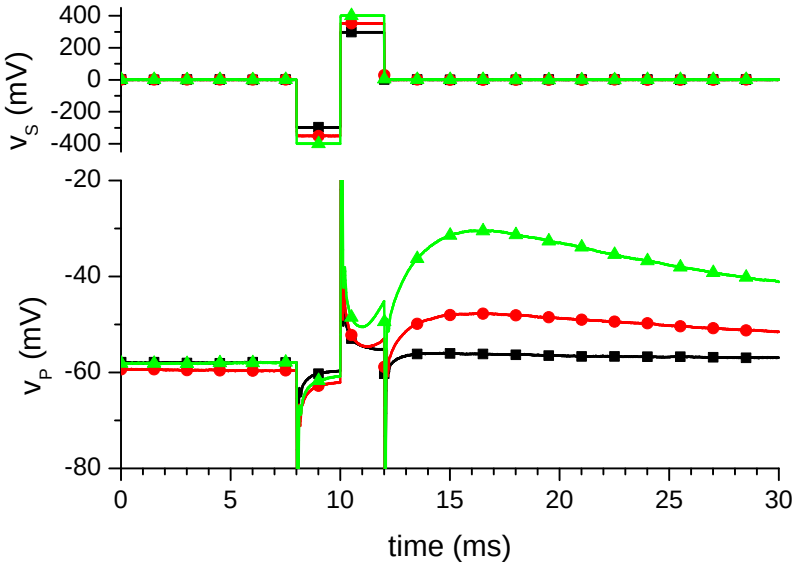

Figure 5.18: Stimulation experiments with biphasic rectangular pulses conducted with the first HEK293 cell with $Na_V1.4$ channels. The change of the membrane potential (v_P) in response to application of negative-phase-first pulses with pulse amplitudes of 300, 350, and 400 mV (v_S) is shown. Each trace represents the average of five measurements with the indicated pulse amplitude.

final amplitude of the depolarization increases with increasing stimulation voltage. For the 400 mV pulse, a maximum depolarization to a potential of −30.5 mV can be measured. Similar to the experiments with intracellular stimulation (see Figure 5.17), the membrane potential slowly repolarizes to its initial value after reaching the maximum depolarization.

In order to compare the stimulation with positive and negative-phase-first pulses, Figure 5.19 shows a comparison of stimulation experiments with rectangular biphasic pulses with identical pulse amplitude (350 mV), but opposite phase sequence. All other parameters were kept as in the experiments shown in Figure 5.18. Again, each trace represents the average of five measurements.

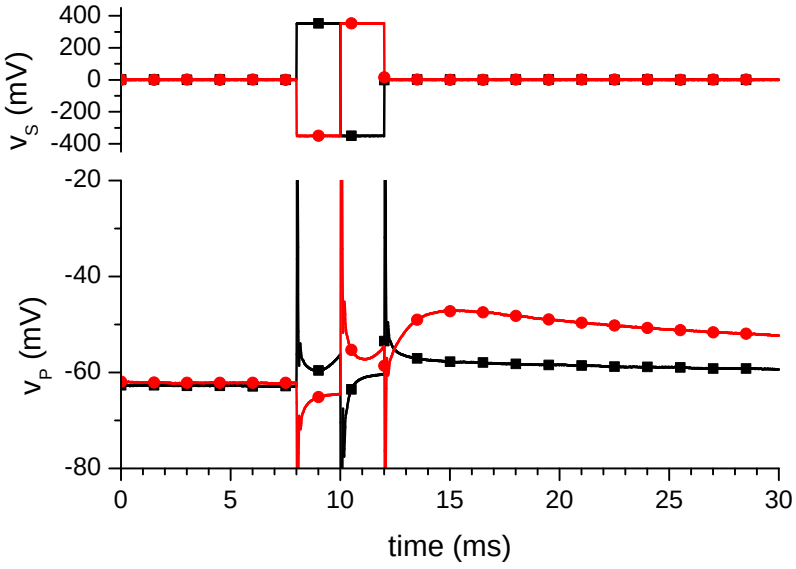

Figure 5.19: Stimulation experiments with rectangular pulses with a positive and a negative phase conducted with the first HEK293 cell. The membrane potential is measured intracellularly (v_P) to investigate the response to the application of a positive respectively a negative-phase-first stimulation pulse with an amplitude of 350 mV (v_S). Both traces show the average of five measurements.

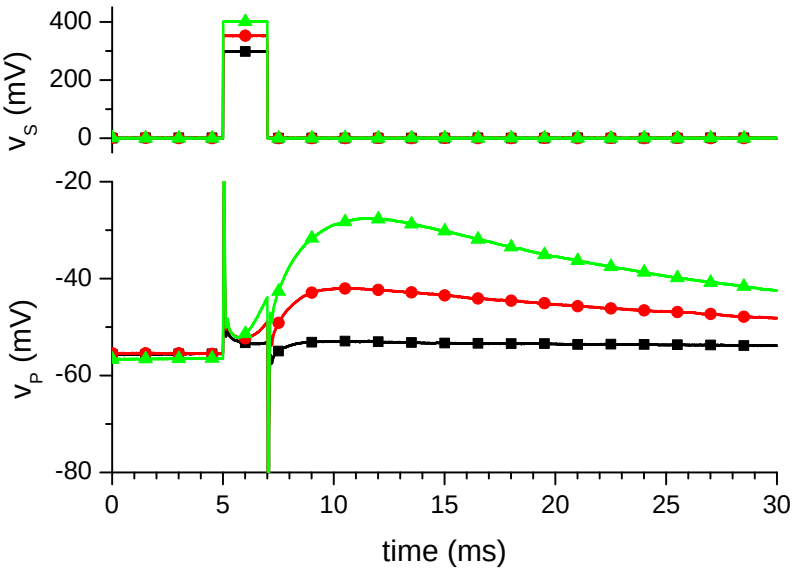

Figure 5.20: Stimulation of the first HEK293 cell with monophasic rectangular pulses. The membrane potential is measured intracellularly (v_P) during application of the stimulation pulses with amplitudes of 300, 350, and 400 mV (v_S). Each trace represents the average of five measurements.

In contradiction to the experiments with the negative-phase-first pulse, the positive-phase-first pulse does not result in a significant residual depolarization. Instead, the initial depolarization and opening of sodium channels during the positive phase is counteracted by the hyperpolarization during the following negative phase.

Since all previous experiments suggest that the depolarization mainly originates from the positive phase of the stimulation pulse, positive monophasic pulses with a pulse duration of 2 ms were used to stimulate the cell 5 ms after beginning of the recording. The results of a series of experiments with three different pulse amplitudes (300, 350 and 400 mV) are presented in Figure 5.20. As before, five measurements were averaged for every trace.

Similar to the results of the biphasic pulses, no significant residual depolarization could be measured for the 300 mV pulse. Again, higher amplitudes caused an increasing depolarization, which also continued to rise after the offset of the stimulation pulse. A maximum potential of -27.5 mV was measured for the 400 mV pulse. Since this value is even slightly higher than for the biphasic pulse, monophasic pulses with a pulse amplitude of 400 mV were used for further investigations.

In the next experiments, the influence of the pulse length on the stimulation effect and the depolarization was analyzed. Figure 5.21 shows the extracellular stimulation with lower (0.5, 0.6, and 1 ms) and higher (2, 4, and 8 ms) pulse lengths. All traces show averages of five measurements.

For decreasing pulse lengths (see Figure 5.21.a), the residual depolarization at the end of the pulses gradually decreases. For pulse length beneath 1 ms, this effects gets more and more pronounced and finally leads to a complete absence of a measurable depolarization for a pulse length of 0.5 ms or less, which can be explained by the opening kinetics of fast sodium channels. Literature values for the activation time constant are in the range of a

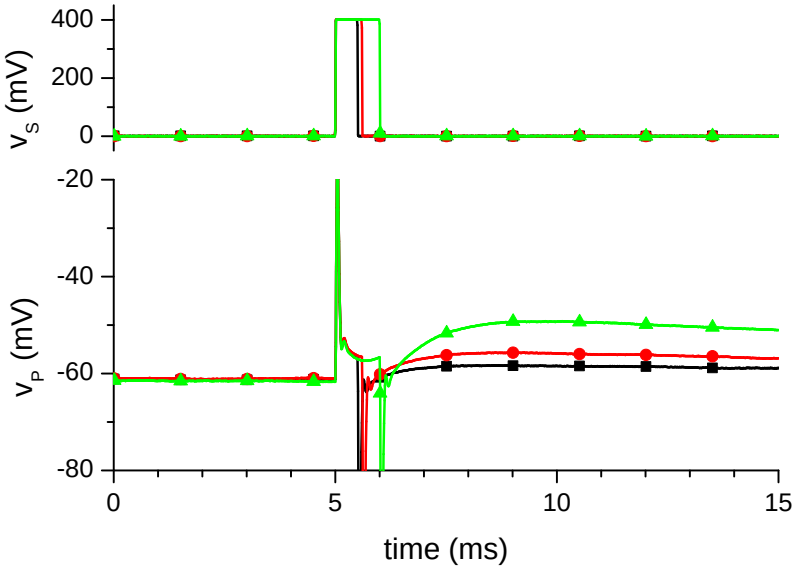

(a) low pulse durations

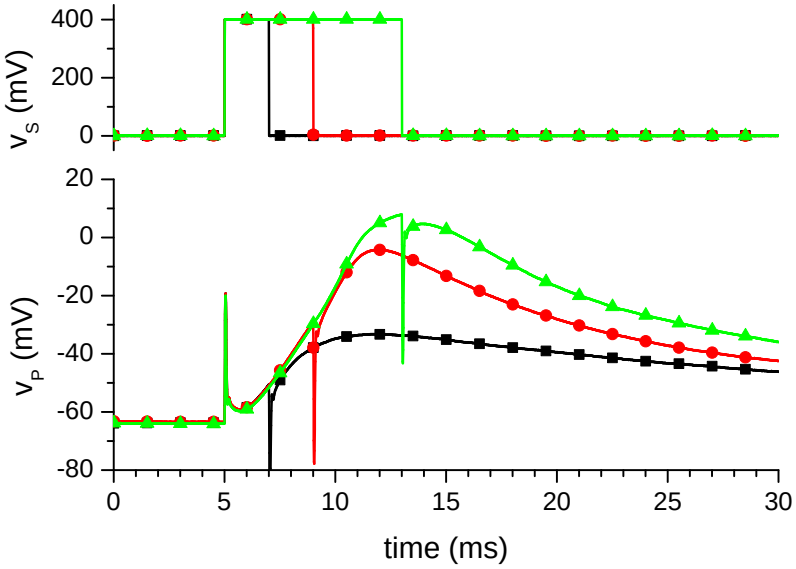

(b) high pulse durations

Figure 5.21: Stimulation of the first HEK293 cell with monophasic rectangular pulses with an amplitude of 400 mV. The intracellularly measured membrane potential (v_P) in response to stimulation pulses (v_S) with pulse lengths of 0.5, 0.6, and 1 ms (a) as well as 2, 4, and 8 ms (b) is shown. Note the different voltage and time scales for each graph. Each trace represents the average of five experiments.

few hundred microseconds up to a millisecond [10, 162]. If the pulse duration is too low, opening of a substantial fraction of the sodium channels cannot be achieved.

With increasing pulse durations, the depolarization rises further in comparison to shorter pulses. As can be seen in Figure 5.21.b, the depolarization continues to rise after the offset of the stimulation pulse for the 2 and 4 ms pulses. However, for a pulse length of 8 ms, the depolarization approaches a saturation at an approximate potential of 10 mV, before the pulse duration is over. Here, the membrane potential does not rise any further, but directly starts to repolarize after the falling edge of the stimulation pulse.

As can be seen in Figure 5.22, a further increase of the pulse length can be used to hold the membrane potential of the stimulated cell at an almost stationary depolarized value

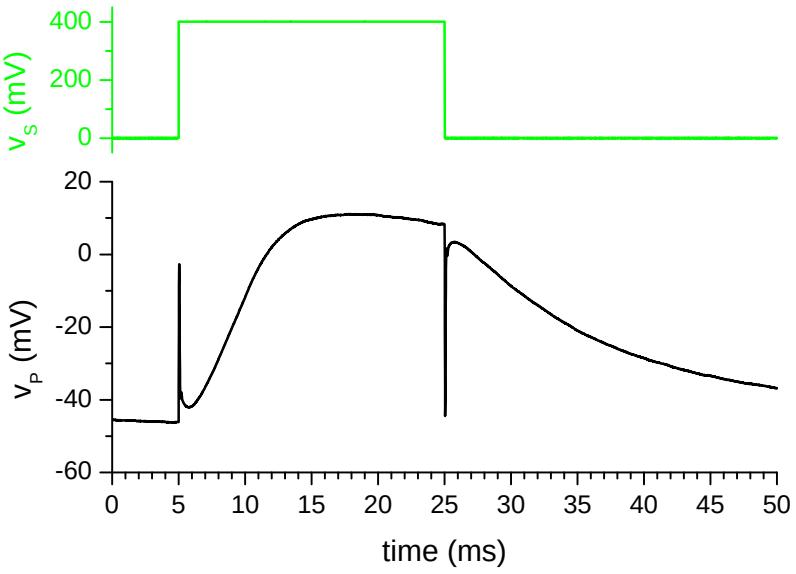

Figure 5.22: Stimulation experiment with first HEK293 cell using a 20 ms monophasic pulse (v_S) with a pulse amplitude of 400 mV. The intracellularly measured membrane potential (v_P) reaches a maximum after approximately 10 ms and is held at a high level until the end of the pulse. The traces correspond to the average of five measurements.

close to 10 mV. For a pulse duration of 20 ms, the potential can be kept at a rather constant value for more then 10 ms after the saturation is reached, as if the cell was clamped to a depolarized potential in a voltage-clamped mode. While the potential only wears of very slowly during the ongoing pulse duration, it directly decays with similar kinetics as in the case of intracellular stimulation (see Figure 5.17) after offset of the stimulation pulse.

A summary of the influence of the stimulation pulse amplitude and duration for monophasic pulses is shown in Figure 5.23. The black and the red symbols show the maximum depolarization after application of a stimulation pulse. For the black trace, all measurements were performed with a pulse amplitude of 400 mV, while the pulse duration was varied from 0.5 to 10 ms. For the red trace, the pulse duration was kept constant at 2 ms and the pulse amplitude was varied from 300 to 400 mV. Again, the average of five measurements was taken for this analysis. The depolarization linearly depends on the pulse length for durations up to 3 or 4 ms. For longer pulses, a saturation of the maximum depolarization is observed. This maximum value and the rather strong variation of the maximum depolarization can be explained by the maximum membrane potential in the pseudo-AP of the HEK293 cells and the variation of the resting potential at the beginning of the stimulation pulse. A linear fit of the black trace up to a duration of 3 ms revealed the intersection with the x-axis at a pulse duration of 0.34 ms, which is fits nicely to the time constants for the activation kinetics of fast sodium channels [10, 162] as already mentioned before.

A similar linear dependence of the maximum depolarization on the stimulation pulse amplitude was also found and fitted for voltages between 300 and 400 mV. Here, the intersection was found at a stimulation pulse amplitude of 291 mV. The stimulation voltage was not increased above 400 mV to preserve the cell for further experiments. In this regime, no saturation of the depolarization can be found for the dependence on the stimulation

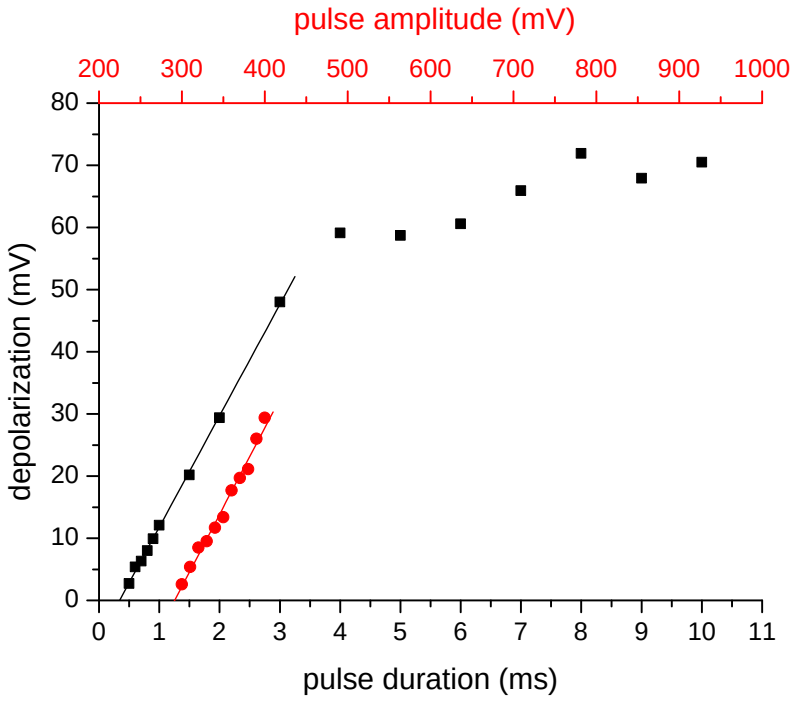

Figure 5.23: Summary of the influence of the stimulation pulse duration for 400 mV pulses (black squares) and amplitude for 2 ms pulses (red circles) on the maximum depolarization after application of the stimulation pulse. A linear fit for low pulse durations and amplitudes is integrated to show the minimum necessary pulse duration and amplitude at the intersection with the x-axes.

pulse amplitude.

In order to compare the extracellular stimulation by voltage pulses to the intracellular stimulation by current pulses, data from both kinds of experiments with the first HEK293 cell are plotted in Figure 5.24. In three current-clamp experiments with a bias current of −40 mV, the cell was stimulated intracellularly with a pipette current of 150 and 200 pA (red traces with circles and triangle) or extracellularly with a pulse amplitude of 400 mV (green trace with squares, average of five measurements). For both stimulation methods, the pulse was sustained for 10 ms.

As can be seen in the figure, the trace originating from extracellular stimulation looks similar to the measurement with intracellular stimulation. It also shows the increase in the depolarization slope around the threshold for the activation of the sodium channels which is characteristic for pseudo-APs. The maximum depolarization reached for the three pulses is also very similar, with the extracellular trace being situated right between the two intracellular traces. Besides the capacitive peaks at the pulse on- and offset, the biggest difference in the pulse shapes can be seen in the repolarization after the offset of the stimulation, which is slightly slower for the trace from the extracellular stimulation. However, this comparison shows that the extracellular stimulation can be used similarly to intracellular stimulation to produce very defined cell responses and even pseudo-APs if pulse parameters like pulse phase sequence, length, and amplitude are adjusted precisely.

The strong cell response with rather low stimulation pulse amplitudes in comparison to previous experiments (see Section 5.1) and the precise response modulation by pulse duration and amplitude indicate a good coupling between cell and sensor. Similar results

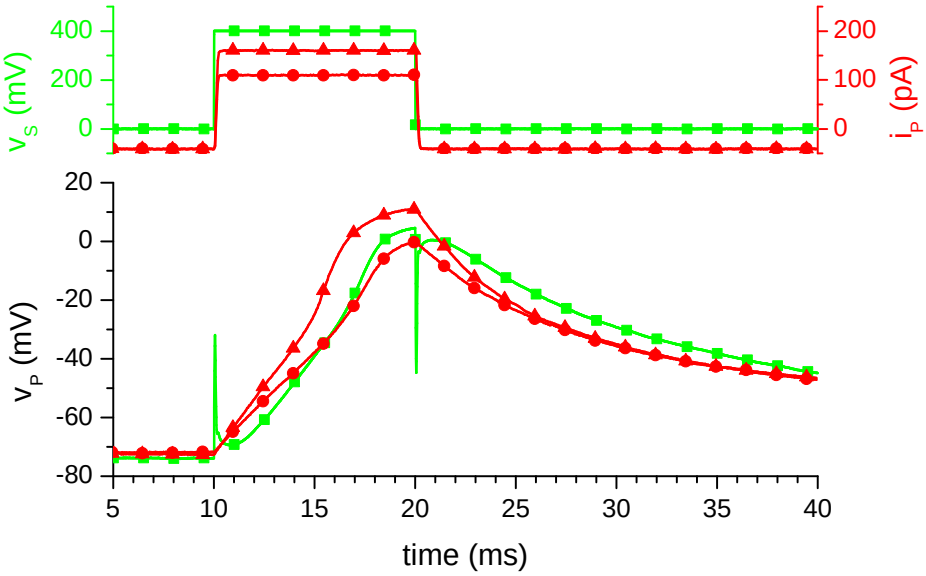

Figure 5.24: Comparison of extracellular (green trace, average of five measurements) and intracellular (red traces) stimulation of the first HEK293 cell with $Na_V1.4$ fast sodium channels. For both kinds of stimulation, pseudo-APs with similar time courses can be measured.

concerning the stimulation pulse phase sequence, amplitude and duration were also found for the second HEK293 cell. Here, even lower stimulation amplitudes were sufficient to evoke channel activity in the HEK293 cell. These results will be used for the investigation of the simulation model and the fitting of the simulations to the measured data on the following pages.

Simulation of Stimulation Experiments

Figure 5.25 shows the results of a series of extracellular stimulation experiments with voltage-controlled rectangular stimulation pulses conducted with the second HEK293 cell shown in Figure 5.14.b. In order to keep the pulse shape simple for the analysis and simulation of the stimulation situation, monophasic positive pulses with a pulse duration of 2 ms were chosen, which should cause a depolarization of the free membrane domain similar to the results acquired with the first HEK293 cell. The cell was stimulated extracellularly with pulses of varying amplitudes between 100 and 300 mV 5 ms after the recording was started. Each trace represents the average of five measurements.

Very similar to the results acquired with the first cell, the intracellular recording with the patch-pipette revealed a passive response to the stimulation pulse with fast capacitive peaks. While these fast passive peaks were the only measurable responses for the 100 mV stimulation pulse, slower membrane potential changes after the end of the stimulation pulse could be measured for increasing stimulation amplitudes. Since the slower potential changes reached their maximum levels of depolarization approximately 4 to 5 ms after the

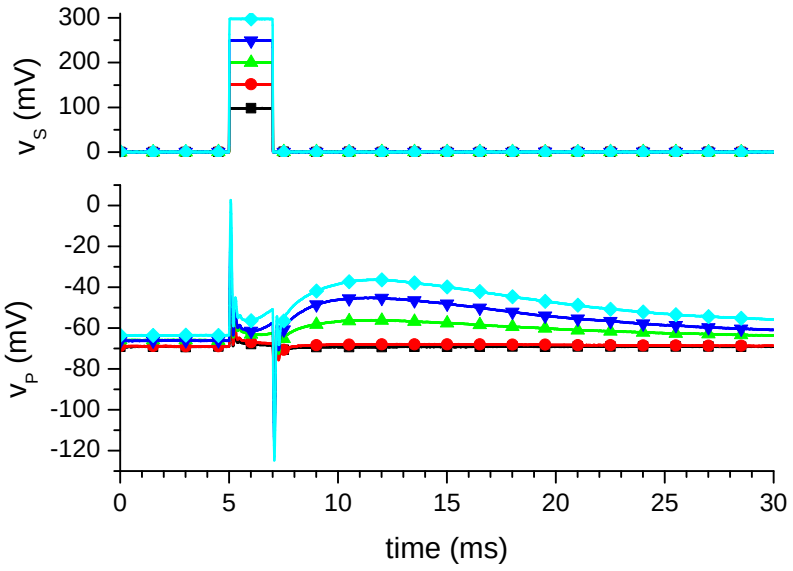

Figure 5.25: Extracellular stimulation experiments done with the second HEK293 cell with $Na_V1.4$ fast sodium channels shown in Figure 5.14.b. The change of the intracellularly measured membrane potential (v_P) in response to application of stimulation pulses (v_S) with five different pulse amplitudes between 100 and 300 mV is shown. Each trace shows the average of five measurements.

end of the stimulation pulse, they can again be contributed to activity of ion channels. For the stimulation pulse with an amplitude of 300 mV, the maximum measured membrane potential was approximately −36 mV.

In order to analyze the experimental situation more thoroughly and get an insight into the parameters that are important for extracellular stimulation, a simulation was done to retrace and reproduce the passive signal components. The model used for the simulation was introduced in Subsection 2.5.2. The numerical approach in the frequency domain introduced on page 30 ff. was used to solve the equations for the frequency responses (see Equations 2.34 to 2.38) of the relevant variables from th equivalent circuit shown in Figure 2.14. The MATLAB code presented in Appendix D was used to calculate the transformations between time and frequency domain, the frequency responses and the relevant output voltages from Equations 2.39 to 2.41. For the solution of the numerical simulation, a number of components of the electrical equivalent circuit describing the setup including the cell and the electrode had to be characterized.

Firstly, the impedance of the stimulation electrode was characterized by *electrochemical impedance spectroscopy* (EIS) as described in Section 3.1 and especially on page 38 ff. for various kinds of electrodes. In order to investigate the electrode impedance for conditions that resemble the stimulation experiment, the EIS scan was performed with the same electrode directly one day after the stimulation experiment. The MEA was cleaned as described in Section B.3 and the EIS scan was performed with a single electrode in extracellular patch solution (see Table C.2) as electrolyte.

Figure 5.26 shows the results of the EIS measurement of the electrode used for the stimulation experiments presented in Figure 5.25. Furthermore, a fit of the impedance data is included in the graph as well. The impedance scan could be fitted using an electrical

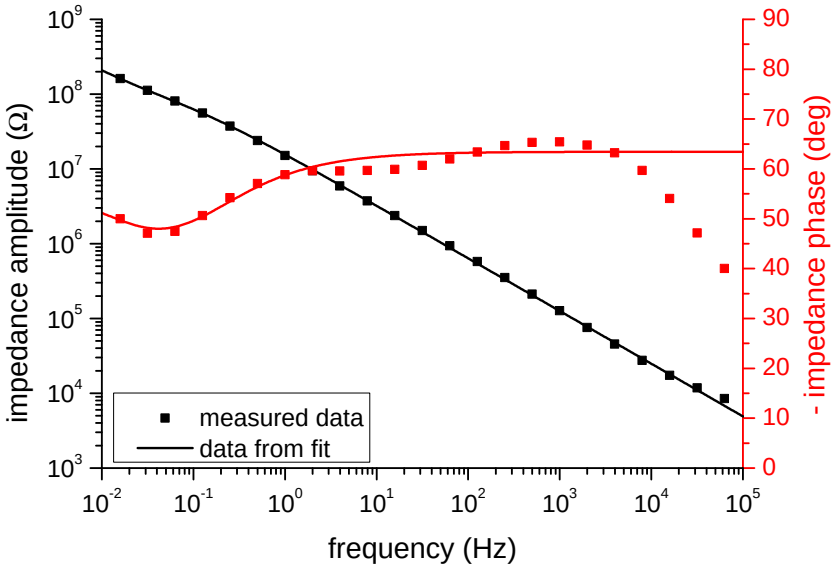

Figure 5.26: Impedance measurement and fit of the 50 µm SIROF electrode used for stimulation experiments with the second HEK293 cell. The deviation of the fit from the measured data in the high frequency range originates from the resistance of the electrolyte solution, which is not integrated in the impedance fit.

equivalent circuit composed of a serial connection of two circuits, each consisting of a parallel resistor and a constant phase element (see Figure 5.27).

This equivalent circuit was chosen as the most simple circuit giving good results in almost the complete relevant frequency range for fitting the measured data. It is not based on any physical model for the electrochemical properties of the interface between the SIROF electrode surface and the electrolyte solution, but only mathematically describes the course of the impedance well enough for the simulation of the stimulation experiments. The fit only deviates from the measured data for very high frequencies above 10 kHz. This deviation originates from the resistance of the electrolyte solution between working and counter electrode during the impedance scan, which is not integrated in the equivalent circuit for the electrode, but was included in another circuit element for the simulation.

A more detailed investigation of the impedance and an equivalent circuit, which is based on detailed interface models, is beyond the scope of this thesis. However, it can be stated that the porosity of the SIROF layer has to play an important role when explaining the course of the impedance. The interested reader is referred to the literature for good approaches to explain the impedance of porous electrodes made from IrO_x or other electrode materials [78, 109, 113, 132, 133].

With the impedance of a constant phase element ($\underline{X}_{CPE}$):

$$\underline{X}_{CPE} = \frac{1}{(j\omega)^n \cdot Q}, \tag{5.1}$$

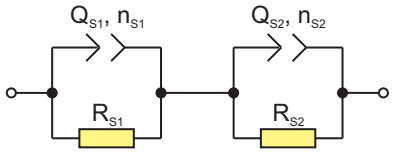

Figure 5.27: Equivalent circuit used to fit the data of the stimulation electrode impedance presented in Figure 5.26. It consists of two circuits each with a resistor and a constant phase element in parallel.

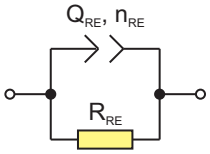

Figure 5.28: Equivalent circuit representing the impedance of the Ag/AgCl reference electrode. The circuit consists of a resistor and a constant phase element in parallel.

the impedance of the stimulating electrode ($\underline{X}_S$) can be calculated using the equivalent circuit presented in Figure 5.27:

$$\underline{X}_S = \frac{R_{S1}}{1 + (j\omega)^{n_{S1}} \cdot Q_{S1} R_{S1}} + \frac{R_{S2}}{1 + (j\omega)^{n_{S2}} \cdot Q_{S2} R_{S2}}. \tag{5.2}$$

Using this equation, the impedance measurement presented in Figure 5.26 was fitted with the parameters summarized in Table 5.1 on page 113.

Secondly, the impedance of the *silver/silver chloride* (Ag/AgCl) electrode was characterized with another EIS measurement. For that purpose, an impedance scan was done with the Ag/AgCl electrode as working electrode against a platinum wire with a large surface area as counter electrode. The results of the impedance scan were fitted to the elements of an equivalent circuit consisting of a parallel circuit of a resistor (R_{RE}) and a constant phase element (Q_{RE} and n_{RE}) as shown in Figure 5.28.

The values resulting from the fit of the impedance scan are also summarized in Table 5.1. Together with the resistance of the bath electrolyte (R_{EL}), they can be used to calculate the complex impedance of the electrolyte solution and the reference electrode ($\underline{X}_E$):

$$\underline{X}_E = R_{EL} + \frac{R_{RE}}{1 + (j\omega)^{n_{RE}} \cdot Q_{RE} R_{RE}}. \tag{5.3}$$

The third block of parameters listed in Table 5.1 summarizes all values concerning the cell and the contact between the cell and the electrode. The membrane capacitance (C_M) was derived from the patch-clamp experiment and used to calculate the whole membrane area (A_M) with the specific membrane capacitance $c_M = 1\ \mu\text{F/cm}^2$. Furthermore, the DIC image of the cell (see Figure 5.14.b) was used to approximate the area of the stimulation electrode, which was covered by the cell (A_{CS}). Using this area, the part of the cell membrane that is attached to the electrode was estimated. Since the cell membrane is assumed to be wavy rather than completely flat [82,83], an attached membrane area (A_{AM}) of twice the size of the covered electrode area was assumed. With these values and the electrode surface area (A_S), the scaling parameters α and β were calculated using the Equations 2.25 and 2.26. The calculated ratio of the attached membrane to the complete membrane area of $\alpha = 0.4723$ fits in the range of literature values for HEK293 cells that were cultured on similar substrates with the same protein coating [83].

As already stated in Subsection 2.5.2, the intracellular potential recorded by the patch-clamp amplifier (pipette potential v_P) will deviate from the real intracellular potential due to a filtering effect caused by the electronics. The properties of this filter are influenced by several parameters within the circuitry of the patch-clamp amplifier including compensation stages [69, 70] and experimental parameters such as the pipette capacitance and the serial resistance.

The filtering effect can easily be integrated in the simulations by filtering of the simulated data in the time or frequency domain. In this numerical approach, the filter was included in the MATLAB code (see Appendix D) and applied to the signals that were already transfered back into the time domain. A second order Chebyshev filter with a passband ripple [163, 164] was empirically identified to give the best results to implement the filter and resemble the measured signal. The values for the filter cutoff frequency (f_{co}) and passband ripple (R_P) resulting in the best fit and used for the simulation are included in Table 5.1 as well.

Using the values for the stimulation and bath electrode as well as the cell parameters, the simulation was manually fitted to the measured data in a recursive process, determining the values for the missing experimental parameters. Besides the filter cutoff frequency and passband ripple, this included the electrolyte resistance (R_{EL}) and the junction resistance (R_J). Especially the junction resistance is of special importance considering the coupling between the cell an the electrode. For the given experiments with the second HEK293 cell, a junction resistance of $R_J = 0.22\ \mathrm{M\Omega}$ was fitted. With the contact area of 400 $\mu\mathrm{m}^2$, this corresponds to a contact-area related specific conductivity of $1.14\ \mathrm{S/cm^2}$, which perfectly fits in the range of literature values between 0.2 and $3.2\ \mathrm{S/cm^2}$ for HEK293 cells on microelectronic devices [96]. The fitted value for the electrolyte resistance of $R_{EL} = 9.0\ \mathrm{k\Omega}$ also fits very well to the values that could be observed in the impedance measurements presented in Chapter 3.

Figure 5.29 shows the three most important frequency responses used for the simulation that were calculated with the numerical method introduced in Subsection 2.5.2 on page 30 ff. using the parameters summarized in Table 5.1. In the figure, the magnitude and the phase of the frequency responses for the potential change at the reference electrode and electrolyte solution ($\underline{H}_E$, see Equation 2.34), the free cell membrane ($\underline{H}_{FM}$, see Equation 2.38), and their sum ($\underline{H}_M = \underline{H}_E + \underline{H}_{FM}$) in response to a potential change at the stimulation electrode are shown. $\underline{H}_M$ is the frequency response for the potential change that is measured by the intracellular patch pipette. At a given frequency, the closer the frequency response is to one, the better a sinusoidal input signal will be transferred to the output of the system. In other words, a stimulation signal will cause the highest potential change at a certain element of the system if the frequency response for that element is

Parameter	Value	Parameter	Value
Q_{S1}	27.98 nF	Q_{S2}	40.99 nF
n_{S1}	0.6988	n_{S2}	0.7153
R_{S1}	56.9 MΩ	R_{S2}	4.01 GΩ
A_S	1963 µm^2		
Q_{RE}	1.24 mF	n_{RE}	0.7967
R_{RE}	25.49 kΩ	R_{EL}	9 kΩ
C_M	16.94 pF	A_M	1694 µm^2
A_{AM}	800 µm^2	A_{CS}	400 µm^2
α	0.4723	β	0.2038
R_J	0.22 MΩ		
f_{co}	6.5 kHz	R_P	5.2 dB

Table 5.1: Overview of the parameters used for the simulation of the stimulation experiments conducted with the second HEK293 cell. The first two blocks contain the parameters acquired from the characterization of the stimulation respectively the reference electrode. The parameters related to the cell and the position of the cell on the electrode respectively the low pass filter are summarized in the third and fourth block.

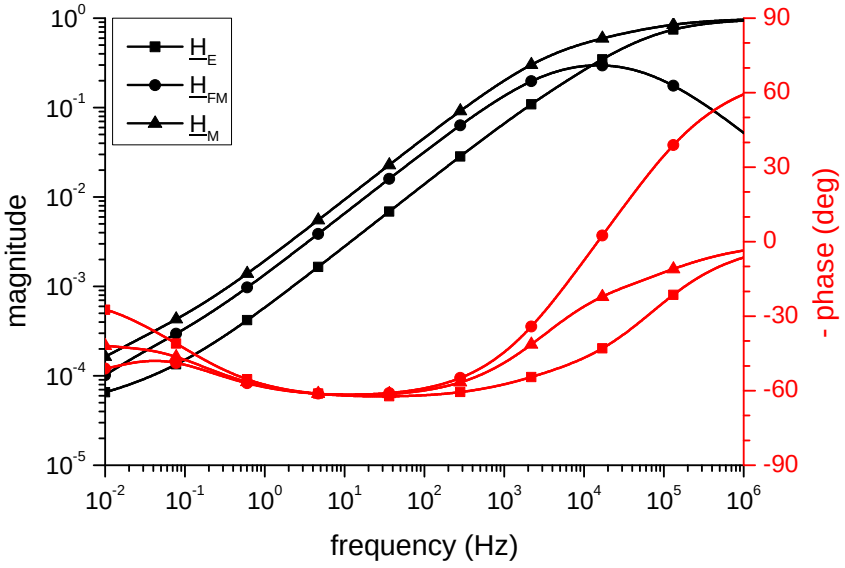

Figure 5.29: Frequency response magnitude and phase for the potential change at reference electrode and electrolyte solution ($\underline{H}_E$), free cell membrane ($\underline{H}_{FM}$), and measured by the intracellular patch pipette ($\underline{H}_M$) in response to a stimulating potential change. The traces were calculated for experiments with the second HEK293 cell.

close to one. Values far below one correspond to a significant attenuation of the signal components with that frequency.

All three curves show a strong and increasing attenuation of signals in the frequency range below 100 Hz. While $\underline{H}_E$ continuously rises and approaches a value of one for increasing frequencies, $\underline{H}_{FM}$ shows a maximum around 10 kHz. For stimulation experiments with the given electrode system this means that pulses should have their major frequency compartments in the frequency range above a few hundred hertz and below a few tens of kilohertz to result in a maximum potential change at the free membrane. However, since the opening kinetics of fast sodium channels, which are most important for the successful excitation of APs in cells, lie in the range of a few hundred microseconds to a millisecond [10, 162], the effect of pulses with frequencies higher than approximately 10 kHz is at

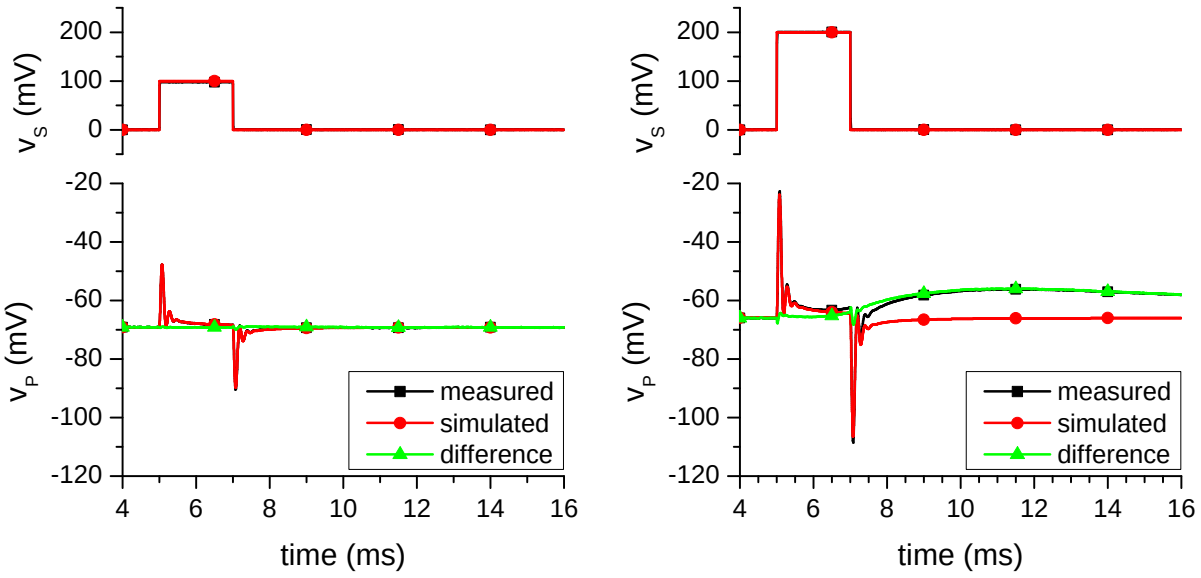

Figure 5.30: Comparison of measurements and simulations of membrane potential changes (v_P) during application of a monophasic rectangular stimulation pulse (v_S) with an amplitude of 100 (a) or 200 mV (b) for the second HEK293 cell. The simulation only includes the passive responses to the stimulation pulses and neglects any potential changes caused by channel opening. The measured data represents the average of five measurements.

least questionable. Since rectangular pulses of a certain basic frequency always include frequency components at multiples of the basic frequency, the pulse frequencies of a few hundred hertz to a few kilohertz used in this thesis lie in the right frequency range to realize a maximum effect at the free cell membrane.

Another important aspect which can directly be seen from the frequency responses is the effect of the potential change at the reference electrode and electrolyte solution on the measured signal. While the magnitude of $\underline{H}_M$ is mostly dominated by $\underline{H}_{FM}$ in the low frequency range, the influence of $\underline{H}_E$ gets bigger for higher frequencies, finally supersedes the magnitude of $\underline{H}_{FM}$, and causes the approach of $\underline{H}_M$ to a value of one. This means that rising frequencies will at a certain point cause an increase in the measured signal, while the actual voltage change at the free membrane decreases. This effect underlines the fact that the voltage drop at the electrolyte solution and the reference electrode cannot be neglected and that great care has to be taken when a measured signal is analyzed.

Using the frequency responses presented in Figure 5.29, the stimulation experiments with the second HEK293 cell can be simulated and compared to measured data (average of five measurements). The Figures 5.30 and 5.31 show the results of simulations (red traces with circles) of two stimulation experiments with pulse amplitudes of 100 and 200 mV and a comparison to the original measured data (black traces with squares), which was

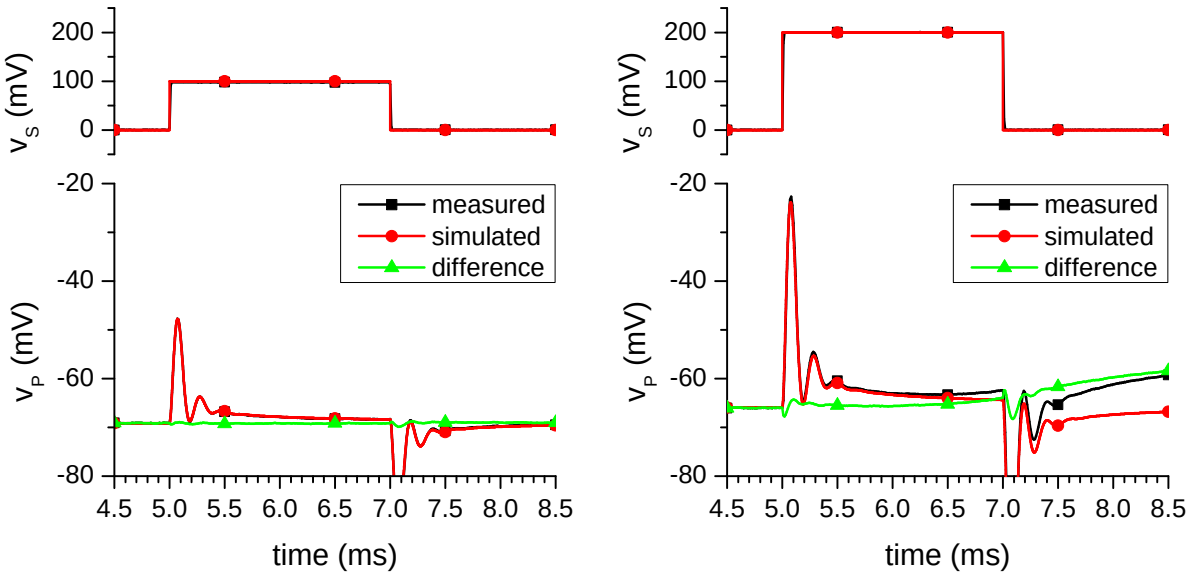

Figure 5.31: Magnification of data presented in Figure 5.30. The graph shows measurements and simulations (v_P) for stimulation experiments conducted with the second HEK293 cell and monophasic rectangular stimulation pulse (v_S) with an amplitude of 100 (a) or 200 mV (b). The measured traces show the average of five experiments.

already presented in Figure 5.25. Figure 5.31 shows a magnification of the signal at the beginning of the pulse, to allow the comparison of the traces with higher resolution. Since the simulations were only used to calculate the resulting change in the measured potential, an offset corresponding to the average pre-pulse membrane potential was added to the simulated data. The difference between simulation and measurement is shown as the green trace with triangles. The simulated data nicely reflects the passive stimulation response at the cell membrane. For the 100 mV pulse (see Figures 5.30.a and 5.31.a), the difference between simulated and measured signals is negligible for the complete duration of the stimulation experiment, since the response is purely passive. The passive response includes fast capacitive spikes at the beginning and the end of the stimulation pulses and a fast decay of the measured signal towards the pre-pulse potential. The spikes are superimposed by an oscillation that is determined by the filtering effect of the amplifier circuit.

An active response of the cell membrane can be seen for the stimulation experiment with the 200 mV pulse (see Figures 5.30.b and 5.31.b). Here, a rise of the measured potential can be seen at the end and after the stimulation pulse, which is not covered by the simulation. Therefore, the difference between both curves represents a change of the membrane potential that can be contributed to channel activity.

To investigate the influence of the already mentioned filter effect, Figure 5.32 shows a comparison of measured data with the filtered and unfiltered simulated change in the

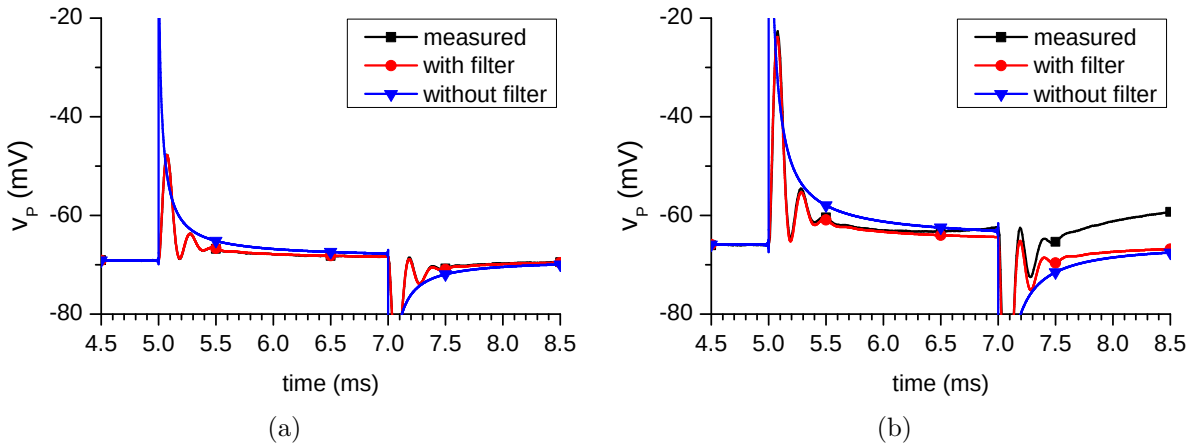

Figure 5.32: Influence of the filter realized by the patch-clamp amplifier including the compensation circuitry and the patch pipette on the recorded signal. A comparison of measured data to the filtered and unfiltered simulated change in the membrane potential for the same two stimulation experiments with 100 (a) or 200 mV (b) pulses as shown in Figures 5.30 and 5.31 is presented. Five measurements were averaged for the measured data traces.

membrane potential for the same two stimulation experiments as shown in Figures 5.30 and 5.31. While the filtered simulated signal precisely reflects the measured signal, the unfiltered signal shows a much more pronounced peak at the beginning and end of the stimulation pulse. Furthermore, the unfiltered potential change also has slightly higher amplitude during almost the complete experiment, indicating that the realized filter attenuates signal components of the stimulation pulse response.

For a deeper understanding of the effect of the stimulation pulse on the different com-

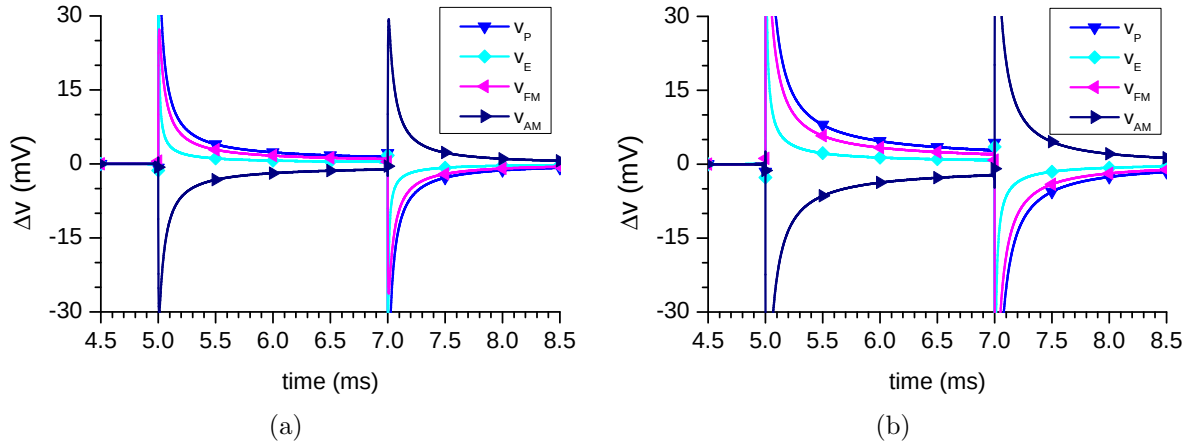

Figure 5.33: Voltage change at reference electrode and electrolyte solution (v_E), free membrane (v_{FM}), attached membrane (v_{AM}), and the unfiltered potential measured with the patch pipette (v_P) caused by an applied positive stimulation pulse with an amplitude of 100 (a) or 200 mV (b). The same experiments as already presented in Figures 5.30 to 5.32 are investigated.

ponents of the simulated system, Figure 5.33 visualizes the changes of the potential at reference electrode and electrolyte solution (v_E), free membrane (v_{FM}), attached membrane (v_{AM}), and the unfiltered potential measured with the patch pipette (v_P) for the same stimulation pulses as shown in the previous three figures.

As already predicted by the plot of the frequency responses (see Figure 5.29), the potential change at the electrolyte and reference electrode has a smaller amplitude than the change at the cell membrane for slower signal compartments, but shows a significant capacitive component at the beginning and the end of the pulse. For the slower parts of the signal, the potential change at the pipette is mainly dominated by the voltage drop at the free membrane. Because of the almost equal distribution of the cell membrane to the attached and the free domain ($\alpha = 0.4723$, see Table 5.1), the potential change at the attached membrane has about the same magnitude, but an opposite sign, in comparison to the change at the free membrane domain.

In order to explain the active response in case of the stimulation with the 200 mV pulse, one has to take a closer look at the potential change at the free membrane domain for both pulses. For a pulse amplitude of 100 mV the potential change at the free membrane quickly drops after onset of the pulse and reaches a magnitude of roughly 10 mV after 100 µs and just 6 mV after 200 µs. Starting from a resting potential of roughly −65 mV, such a depolarization is by far not high enough to open fast sodium channels in the cell membrane, since the threshold for channel activation lies at approximately −35 mV. Although a higher depolarization can be seen directly after the onset of the stimulation pulse, the opening kinetics of the fast sodium channels seem to be too slow to respond to such a brief depolarization. For the 200 mV pulse, the amplitude is doubled in all points in time. Nevertheless, the resulting depolarization of approximately 20 mV after 100 µs would still not be enough to exceed the threshold for channel activation. However, studies of the extracellular stimulation on single cells and simulations including an expansion of the two-domain stimulation model from a point-contact to a two-dimensional sheet conductor have already shown that the membrane potential change in each membrane domain greatly varies with distance to the boundary to the other domain. Thus, local depolarizations with maximum amplitudes of twice the average amplitude (which is simulated in the model used here) are expected for every stimulation experiment [29, 30]. Considering this doubling of the amplitude, the threshold for channel activation can easily be exceeded locally for at least 150 µs for the 200 mV pulse, causing the measurable depolarization. Accordingly, higher stimulation amplitudes can further prolong the time the threshold is exceeded and therefore cause an even higher depolarization.

The last three figures of this subsection will in the following be used to investigate, which parameters of the stimulation can be used to influence the efficiency of the extracellular

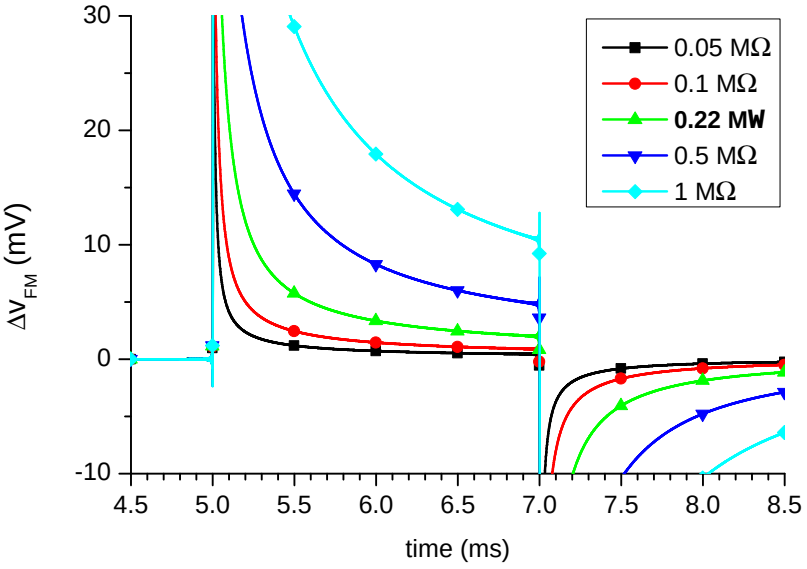

Figure 5.34: Influence of variations of the junction resistance from the experimentally determined value of 0.22 MΩ on the depolarization of the free cell membrane. An increase of the junction resistance causes a higher depolarization and a slower decay of the potential change.

stimulation on single cells. For that purpose, important parameters of the simulation have been varied, and the simulation results for the potential change at the free membrane were compared to the standard parameters. All the following simulations are based on the stimulation experiment with the second HEK293 cell and a rectangular stimulation pulse with a pulse amplitude of 200 mV.

Figure 5.34 shows a comparison of simulation results with a variation of the junction resistance (R_J). Obviously, the junction resistance plays a very important role in the coupling between the cell and the stimulation electrode. Starting from the experimental value of 0.22 MΩ determined from the fit, the simulated depolarization during the stimulation pulse significantly increases with an increasing junction resistance. Especially, the decay of the voltage change after the beginning of the pulse is prolonged, caused by the better seal of the junction area from the bulk electrolyte. This effect would allow a significantly increased activation of ion channels with the same pulse amplitude.

Accordingly, a decrease of the junction resistance causes a faster decay of the potential change at the free membrane. As a consequence, the membrane depolarization caused by the beginning of the pulse is not sustained, but quickly disappears again. Since it is necessary to guarantee a substantial depolarization for a time long enough to activate the fast sodium channels in the cell membrane, great care has to be taken to achieve an attachment of the cell to the electrode with a cleft as small as possible to get a high junction resistance for an optimized coupling. Studies investigating the tightness of attachment and the influence of various protein coatings on the cell adhesion help to optimize this parameter for stimulation as well as recording with microelectronic devices [80, 82, 83, 86].

Next, the impedance of the stimulation electrode ($\underline{X}_S$) was altered for the simulation to investigate its impact on the stimulation as presented in Figure 5.34. Considering

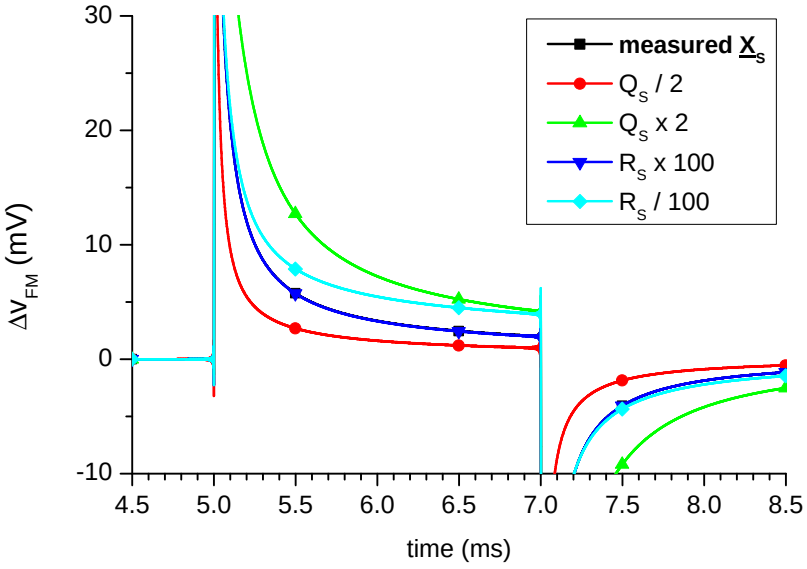

Figure 5.35: Influence of variations of the stimulation electrode impedance from the experimentally determined values summarized in Table 5.1 on the depolarization of the free cell membrane. A separate variation of the resistive (R_S) and capacitive (Q_S) components of the impedance was conducted and compared.

Equation 5.2 for the electrode impedance, either both resistive compartments (R_{S1} and R_{S2}, respectively) or both constant phase elements (Q_{S1} and Q_{S2}, respectively) were multiplied or divided by a factor of 2 and 100, respectively.

A change of the constant phase element by a factor of two already strongly influences the measured change in the potential of the free membrane. Comparable to the influence of a change of the junction resistance, an increase of Q_{S1} and Q_{S2} slows the decay of the potential change an thereby increases the depolarization during the whole stimulation pulse. Equivalently, decreased values for Q_{S1} and Q_{S2} cause a faster decay and a reduction of the depolarization. In comparison, the change of the resistive compartments of the electrode impedance only has a small effect on the depolarization of the free membrane (especially for the fast potential changes at the beginning of stimulation pulses). While an increase of the resistance by a factor of 100 does not cause any detectable change in the course of the membrane potential change, a decrease by a factor of 100 evokes an increase of the depolarization at the end of the stimulation pulse. This change can be explained by considering the equivalent electrical circuit of the stimulation system for low frequencies. In that case, the resistive component of the stimulation electrode and the junction resistance form a resistive voltage divider. This divider is dominated by the resistance of the stimulation electrode for the standard values, meaning that almost the complete voltage drops at the electrode and not at the cell. A further increase of the electrode resistance, therefore, does not change this voltage drop any more. A resistance decrease on the other hand causes the resistors to be in a similar range, thus increasing the voltage drop at the junction resistance and the whole cell especially towards the end of long stimulation pulses.

It can be concluded that the stimulation electrode should have a value as large as possible

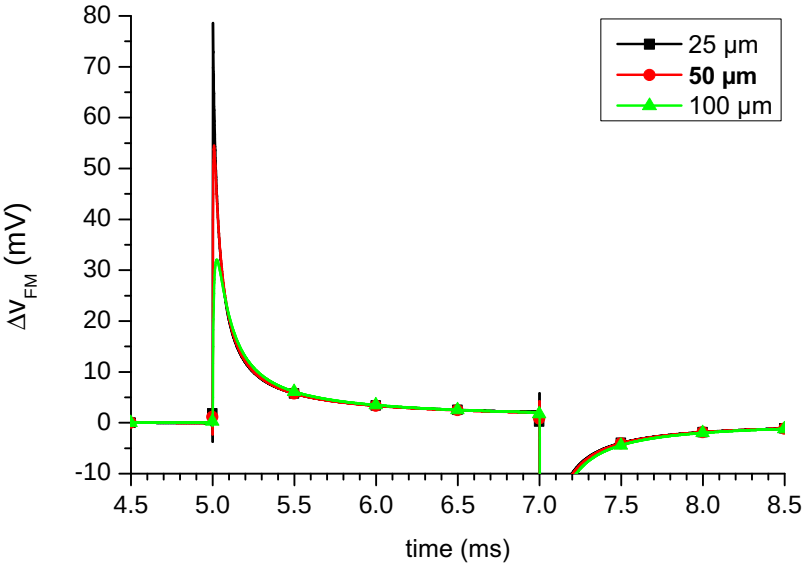

Figure 5.36: Influence of variations of the stimulation electrode diameter from the standard value of 50 µm on the depolarization of the free cell membrane. The electrode size mainly influences the depolarization directly at the beginning of the stimulation pulse.

for capacitive components like Q_{S1} and Q_{S2} or in general the double layer capacitance of the electrode/electrolyte interface. At the same time, a small resistive compartment is desirable to get a high resulting depolarization for slow signal compartments e.g. for long stimulation pulses. However for the given electrode material, a significant reduction of the resistance by a factor more than ten would be necessary to show a significant effect, while already an increase of Q_{S1} and Q_{S2} by a small fraction would cause a measurable improvement of the stimulation performance. Especially when comparing the impedance of the used SIROF electrodes to the previously used standard gold electrodes, it is obvious why stimulation experiments with the gold electrodes have at best just a slight chance of success.

Finally, the influence of the electrode size on the stimulation experiments was analyzed by simulating the pulse response for stimulation electrodes with diameters of 25, 50 and 100 µm. In all three cases, the cell was still considered to be completely located on the electrode. Therefore, the change in electrode diameter only caused a change in the impedance of the stimulation electrode and the size of the free and covered parts of the electrode surface. As can be seen in Figure 5.36, a variation of the electrode diameter from its standard value of 50 µm significantly alters the change in the free membrane potential directly after the beginning of the pulse. The enlarged free electrode surface reduces the high-frequency impedance of the stimulator-cell complex ($\underline{X}_{SC}$, compare Equation 2.33), resulting also in a reduced voltage drop at the cell. However, since only the impedance in the high-frequency range is significantly influenced, the potential change adjusts to a similar level for all compared electrode sizes after less than 100 µs. Without any experimental comparison with stimulation electrodes of varying sizes it cannot be completely discussed if this time shortly after application of the stimulation pulse is important for the

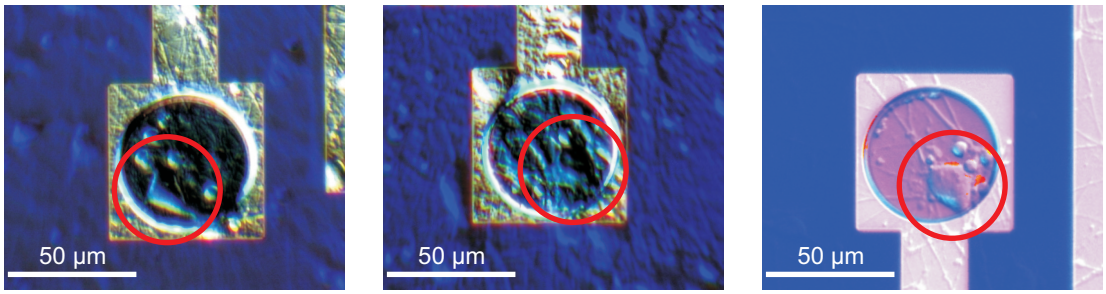

(a) (b) (c)

Figure 5.37: DIC images of three rat cortical neurons used for stimulation experiments presented in this subsection. The soma of all three cells (marked with red circles) was located on a fourth generation SIROF stimulation electrode with a diameter of 50 µm. The cells were investigated in the whole-cell patch-clamp configuration and used for stimulation experiments at DIV 8 (a, b) and DIV 7 (c) as described in the following.

stimulation efficiency. However, it can be concluded that the electrode size is important for the first microseconds after application of the stimulation pulse and thus influences the quality of the coupling between the cell and the electrode. At the same time, it has to be taken into account that the voltage drop at the reference electrode and the electrolyte solution is increased with larger electrode sizes. This increase in Δv_E also influences the measured change in the potential at the pipette (Δv_P) and has to be considered during any experiment and especially the data analysis.

5.2.2 Extracellular Stimulation of Rat Cortical Neurons

After the first stimulation experiments were successfully conducted with the HEK293 cells, the experiments were focused on the objective cell system, rat cortical neurons. The cells were equivalent to the rat neurons that were used for the experiments described in Subsections 5.1.1 and 5.1.2. Fourth generation SIROF MEAs were treated with the standard cleaning protocol (see Section B.3), activated, coated with proteins, and used to culture rat cortical neurons. The cells grew in the cell culture dish on the chip surface until the intracellular measurements and combined extracellular stimulation experiments were done at 6 to 8 DIV. The conditions and protocols for cell culture and patch-clamp experiments are described in Section C.1.

Using the experimental configuration with the new BioMAS amplifier (see Section 4.3) and the fourth generation SIROF electrodes with a diameter of 50 µm, successful extracellular stimulation of APs could be conducted with six different rat cortical neurons. The data analyzed and presented in this subsection was taken from experiments with the three rat neurons presented in Figure 5.37. For all three cells, the cell soma was located completely on a stimulation electrode (as indicated by red circles in the figure). However,

the cell processes including the axon with the axon terminals and the dendritic tree (see Section 2.1 and Figure 2.1) as usually covered a large area surrounding the cells. In comparison to the HEK293 cells, the morphology and shape of the neurons was much more complex and difficult to identify from DIC images. Especially the area and position of the free and attached membrane domains is difficult or even impossible to estimate optically for neurons. During the patch-clamp experiments, the cells' membrane capacitances were determined to 30.3, 38.0, and 22.5 pF for the first cell (DIV 8, see Figure 5.37.a), the second cell (DIV 8, see Figure 5.37.b), and the third cell (DIV 7, see Figure 5.37.c), respectively.

Cell Fitness and Ion Channel Functionality

Similar to the experiments with the HEK293 cells (see Subsection 5.2.1), the cell fitness and electroactivity was directly tested after establishment of the whole-cell configuration. Firstly, voltage-clamp experiments were conducted to characterize the conductivity and opening threshold for the sodium and potassium channels of the cells as shown for the first cell in Figure 5.38.

During each of the 23 measurements of the membrane current (i_P, red traces), the membrane potential (v_P, black traces) of the cell was changed from the initial resting potential of -70 mV for 20 ms with a changing potential step amplitude in every measurement. Starting from a hyperpolarization to -80 mV in the first experiment, the membrane potential was increased by 5 mV for each experiment, until a depolarization to $+30$ mV was reached in the final measurement. In the figure, only every second measurement is included for clarity.

In the recorded traces, a fast negative (inward) sodium current with a sharp peak can be seen, which arises for all traces starting from a threshold potential of approximately

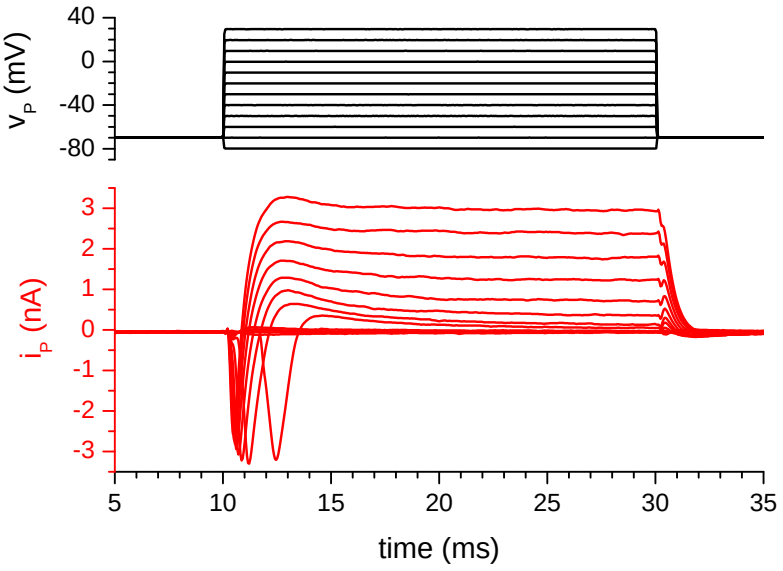

Figure 5.38: Voltage-clamp measurement of the first rat cortical neuron (see Figure 5.37.a). The membrane current (i_P, red traces) is plotted in response to twelve membrane potential (v_P, black traces) steps to values between -80 and $+30$ mV. A fast negative sodium current with a sharp peak and a slow positive potassium current can be identified.

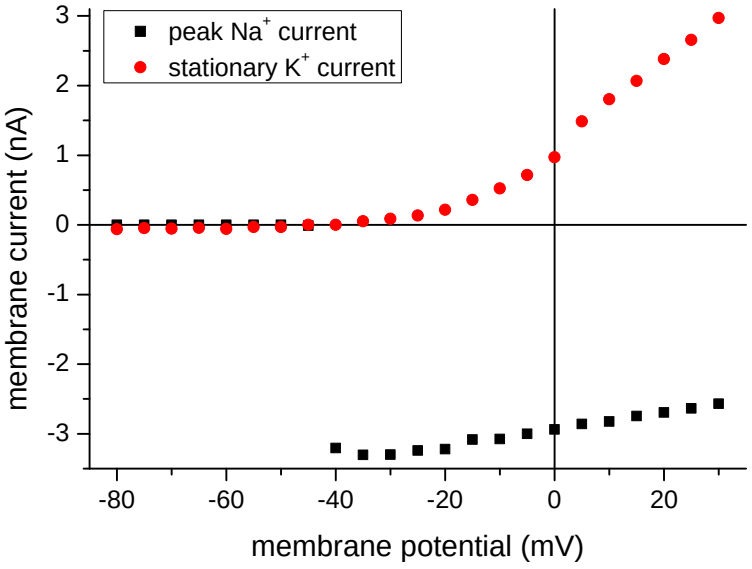

Figure 5.39: Current-voltage curve summarizing the results of the voltage-clamp measurements shown in Figure 5.38. The peak sodium currents (Na^+, black squares) and stationary potassium currents (K^+, red circles) are plotted against the membrane potential applied during the voltage step.

−40 mV. The peak originates from the fast opening and equally fast inactivation of voltage-gated fast sodium channels in the cell membrane. Roughly at the same potential, a positive (outward) potassium current arises, which quickly reaches a stationary phase and can be explained by the slower activation and missing inactivation of voltage-gated potassium channels.

The resulting peak sodium currents and the stationary potassium currents of the first neuron taken from the voltage-clamp measurements are summarized in Figure 5.39. The sodium current rapidly increases upon surpassing the threshold potential of approximately −40 mV and reaches its maximum at −35 mV with −3.30 nA. With membrane potential steps further increasing, the peak current is slowly reduced. Unlike the HEK293 cells, the neurons have a significant number of potassium channels, causing a big stationary outward potassium current. The measured potassium current of the first rat cortical neuron slowly increases in amplitude starting at −40 mV with increasing step voltages, without reaching a maximum within the experimental voltage range. For the final measurement with a depolarization to a value of +30 mV, a stationary potassium current of 2.97 nA could be measured.

After the voltage-clamp experiments, the mode was changed to current-clamp and the cell's membrane potential was adjusted to a value of approximately -65 to −70 mV by injection of a bias current of −70 pA. To investigate the excitation of APs in the neuronal cell, a current-clamp protocol was applied as shown in Figure 5.40 for the first neuron. Four measurements of the membrane potential (v_P, black traces) with 20 ms rectangular current pulses (i_P, red traces) with a stepwise amplitude increase between 100 and 250 pA in addition to the bias were conducted.

For the first current pulse, a slow depolarization of the membrane potential is caused,

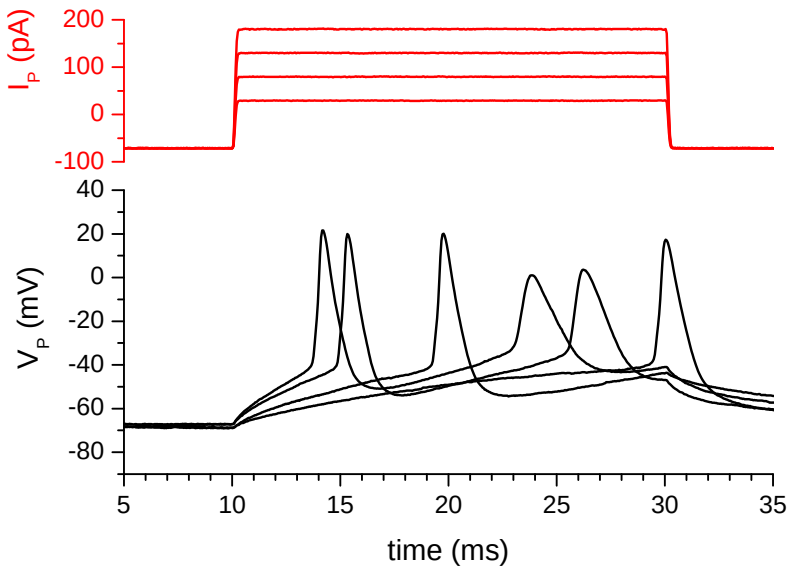

Figure 5.40: Current-clamp measurement of the rat cortical neuron shown in Figure 5.37.a. The change of the membrane potential (v_P, black traces) in response to application of four different membrane current steps (i_P, red traces) with amplitudes between 100 and 250 pA in addition to the bias current is shown. Upon reaching the threshold for sodium channel opening, the activation of APs can be observed. For strong depolarizing currents, even a repetitive AP excitation is achieved.

which finally leads to the excitation of an AP just at the end of the pulse. The typical shape of an AP with a fast rise of the membrane potential and a following fast repolarization to a negative potential can be seen. With increasing pulse amplitude, the depolarization is accelerated and the time of AP excitation is shifted closer to the onset of the pulse. For the final two experiments with the highest stimulating current, even a second AP is excited during the stimulation period. The fast and reliable AP excitation with a self-amplifying depolarization and the fast repolarization prove again the fitness of the neuron with strong sodium and potassium currents.

The results of the voltage- and current-clamp experiments indicate a healthy neuron with a high number of functional ion channels and a high excitability for the generation of APs. Similar results could also be generated for the other neuronal cells used for stimulation experiments, although the threshold for ion channel opening slightly varied in the range between −35 and −45 mV. Additionally, also the amplitude of the sodium and potassium currents and the maximum amplitude of the APs varied for the different cells. The necessary bias current to maintain a resting potential of approximately -65 to −70 mV was −60 pA for the second neuron (see Figure 5.37.b) and −50 pA for the third cell (see Figure 5.37.c).

The electrophysiological characterization and the position of the rat neurons on the stimulation electrodes made them excellent candidates for stimulation experiments with SIROF microelectrodes. The main difference in the electrophysiological properties of the rat cortical neurons in comparison to the HEK293 cells with the $Na_V1.4$ channels lies in the presence of a high number of voltage-gated potassium channels. It has to be kept in mind that these channels are activated in the same potential range as the fast sodium channels

and, therefore, will be influenced by the extracellular stimulation as well. Furthermore, the amplitude of the sodium currents is higher for the neurons and the fast sodium channels open much more rapidly and with a sharper threshold potential as can be seen in the current-voltage curves for both cell types (compare Figures 5.16 and 5.39). This should also influence the extracellular stimulation, as the sharper threshold and the increased current amplitude will more quickly lead to a self-amplifying depolarization in case of extracellular stimulation, as well.

Stimulation Experiments in Current-Clamp Mode

For all stimulation experiments in the current-clamp mode with the three cells, the bias current was maintained as determined during the electrophysiological characterization. Nevertheless, it has to be stated that the resting potential of the cells was not constant, but fluctuated between the stimulation experiments as is well known for cultured rat neurons [154] (compare page 91 in Subsection 5.1.2). Together with the influence of the voltage-activated potassium channels and the more complicated morphology of the rat cortical neurons, this increases the complexity of the investigated system and makes the interpretation of extracellular stimulation experiments much more complicated in comparison to experiments with HEK293 with just a single ion channel type.

Figure 5.41 shows the results of ten extracellular stimulation experiments conducted with

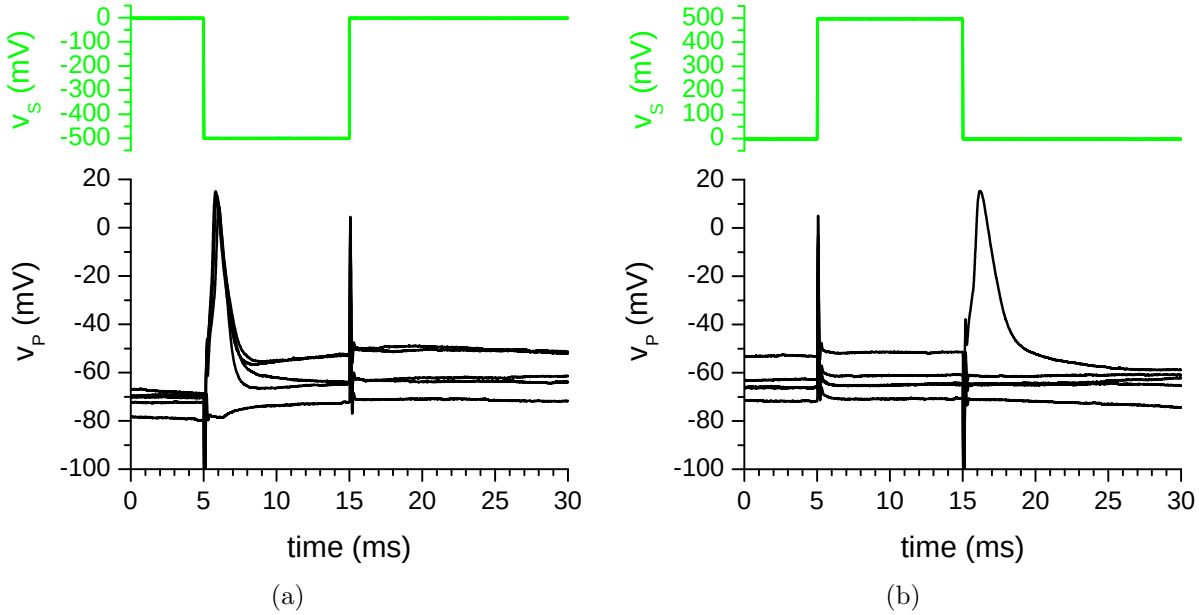

Figure 5.41: Stimulation experiments conducted with the first rat cortical neuron (see Figure 5.37.a) with negative (a) or positive (b) monophasic rectangular stimulation pulses (v_S) with an amplitude of 500 mV. The intracellular potential is measured simultaneously with a patch pipette (v_P).

the first rat cortical neuron in th current-clamp configuration. The cell was stimulated five times each with a negative (see Figure 5.41.a) or positive (see Figure 5.41.b) monophasic rectangular voltage pulse (v_S, green traces) with 500 mV amplitude. The intracellularly recorded potential (v_P, black traces) is directly influenced by the pulses and shows fast capacitive peaks at the beginning and end of the stimulation pulses. Furthermore, both kinds of pulses were able to excite APs in the cell. However, for the negative pulse, APs could be excited in four out of five cases, but only in one case for the positive stimulation pulse.

Looking at the membrane potential of the cells before the pulses, a strong fluctuation in the resting potential can be seen. The pre-pulse membrane potential seems to have a strong influence on the success of the stimulation experiment, as the only unsuccessful stimulation experiment with a negative pulse is recorded as the pre-pulse potential lies in the range of -80 mV and thus lower than in the other experiments. Accordingly, the only successful stimulation experiment with a positive pulse could be recorded for an initial membrane potential in the range of -50 mV, which is rather high in comparison to the other experiments. Nevertheless, the negative pulses seem to be more efficient for the given cell, since APs could be excited for several experiments with initial membrane potentials around -70 mV, while the positive pulses were not efficient even for membrane potentials around -65 mV in three cases.

Additionally, it is obvious that the AP is excited at different times for the two pulse polarities. For the negative pulse, the AP is excited directly at the beginning of the pulse, indicating a depolarization of the attached membrane at the falling flank of the pulse that directly exceeds the threshold of sodium channel opening and causes a self-amplifying depolarization and subsequently the AP. For the positive pulse on the other hand, the AP is excited directly after the end of the pulse. Thus, it can be speculated that the depolarization of the free membrane at the rising flank and during the pulse is not sufficient to reach the threshold of sodium channel opening. This can be explained by the larger area of the free membrane domain in comparison to the attached membrane, which causes any average potential change at the free membrane to be smaller than the potential change at the attached membrane for any stimulation pulse (compare Subsection 2.5.2). Instead, the falling flank at the end of the pulse again causes a depolarization of the attached membrane, which is only sufficient for the opening of fast sodium channels if the pre-pulse membrane potential is high enough. For that case, the depolarization caused by the sodium channel opening can spread to the free membrane domain for an AP in the whole cell.

Looking at these results from the first cell, it could be concluded that only the falling pulse flank is responsible for the excitation of APs and that negative pulses are more efficient in general. However, during some experiments it could be found out that this is

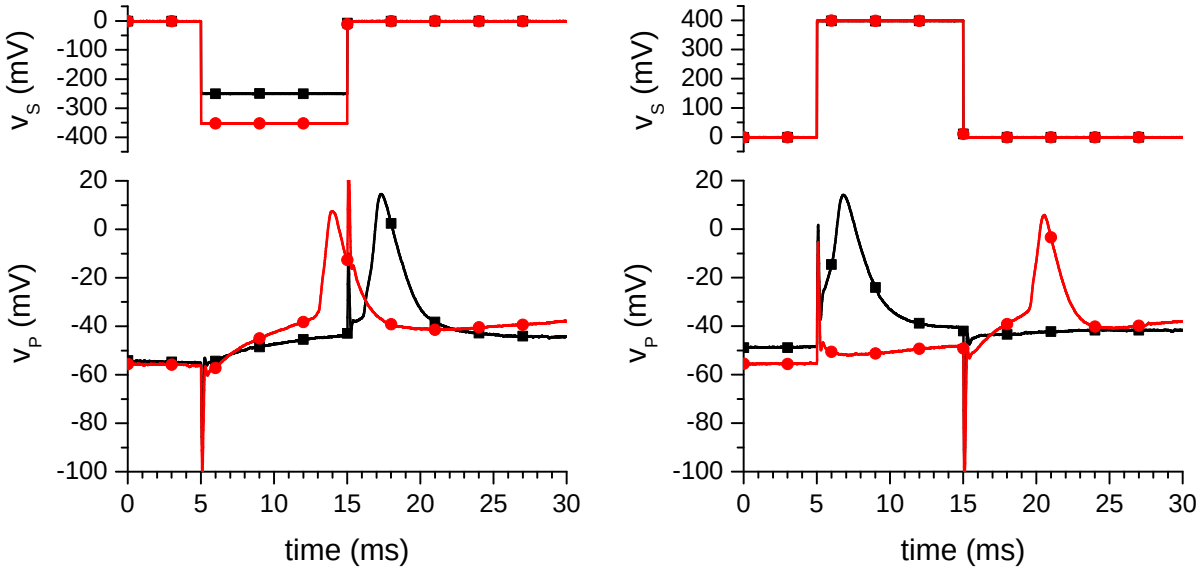

Figure 5.42: Stimulation experiments conducted with the second rat cortical neuron (see Figure 5.37.b) with negative (a) or positive (b) monophasic rectangular stimulation pulses (v_S) of varying amplitudes. Different excitation mechanisms can be identified in the recorded membrane potential (v_P) by the various times of AP occurrence.

not necessarily true in every case.

Four successful stimulation experiments with monophasic rectangular stimulation pulses with different polarities and amplitudes conducted with the second rat cortical neuron (see Figure 5.37.b) are presented in Figure 5.42. For the two negative pulses (see Figure 5.42.a), the APs were not excited directly at the beginning of the pulse (as shown for the first neuron in Figure 5.41.a), but directly before respectively after the end of the stimulation pulse. In this case, the membrane potential can be seen to gradually rise during the pulse duration, indicating a opening of sodium channels in the attached membrane and influx of sodium ions into the cell. For the higher pulse amplitude of 350 mV (red trace with circles), this depolarization is high enough to rise the membrane potential up to the threshold for excitation of an AP during the pulse. For a pulse amplitude of 250 mV (black trace with squares), however, the ion influx is not sufficient to reach that threshold during the pulse duration. Instead, the AP is excited directly at the rising flank of the stimulation voltage at the end of the pulse. The time of excitation and the increased AP amplitude in comparison to the pulse with the higher amplitude indicate that the AP is excited in the larger free cell membrane, which is excited by a combination of the depolarizing pulse flank and the residual depolarization caused by the influx of sodium ions during the pulse through the attached membrane.

For the positive stimulation pulses (both with 400 mV amplitude, see Figure 5.42.b), the

APs are either excited directly at the beginning of the positive pulse or with a short delay after the end of the stimulation pulse. The direct excitation (black trace with squares) is probably possible by direct exceeding of the sodium channel opening threshold in the free membrane due to the rather high pre-pulse membrane potential. For a lower initial resting potential (red trace with circles), the membrane potential slowly rises during the pulse due to open channels in the free membrane domain. After the end of the pulse, the residual depolarization together with the depolarization caused by the falling pulse flank excites an AP with a smaller amplitude in the attached membrane domain.

As can be seen from the stimulation experiments with the first two neurons, there are several mechanisms capable of causing a sufficient depolarization of the membrane potential to reach the threshold for the excitation of an AP. This is underlined by the various times of AP occurrence during or after the positive and negative stimulation pulses. In general, both pulse polarities can be sufficient and efficient for stimulation, and it is difficult to give a general description of a ideal stimulation pulse. The lowest stimulation amplitude sufficient for AP excitation in a cortical rat neuron recorded in this work was the negative pulse with an amplitude of 250 mV (black trace with squares in Figure 5.42.a).

Even more important for successful stimulation than the pulse polarity seems to be the pre-pulse resting potential of the cell. Figure 5.43 and Table 5.2 show the results of a series of 60 stimulation experiments done with the third rat cortical neuron shown in Figure 5.37.c. Each of the four diagrams in Figure 5.43 shows an example of a successful and an unsuccessful stimulation experiment with a negative (Figures 5.43.a and 5.43.c) or positive (Figures 5.43.b and 5.43.d) monophasic rectangular stimulation pulse with a pulse duration of 10 (Figures 5.43.a and 5.43.b) or 20 ms (Figures 5.43.c and 5.43.d). For each of the experiments, the pulse amplitude was 600 mV. In all four cases, an AP was excited when the pre-pulse membrane potential was approximately −64 mV, while no AP occurred for a initial membrane potential of approximately −72 mV. For the negative pulses, the APs were excited directly at the beginning of the pulse, and the excitation occured directly after the end of the pulse for the positive pulses, indicating the same excitation mechanisms as observed for the first rat neuron (compare Figure 5.41).

Table 5.2 summarizes the results of all 60 stimulation experiments with 600 mV amplitude and the two rather long pulse durations of 10 and 20 ms conducted with the cell. The ratio of successful AP excitation out of all experiments are listed for all four different pulse types. To investigate the influence of the pre-pulse resting potential, the experiments were separated in three pre-pulse membrane potential ranges ($v_P > -66$ mV, -66 mV $\leq v_P \geq -68$ mV, $v_P < -68$ mV).

The first and most dominant result of the data analysis is the influence of the pre-pulse membrane potential on the probability of AP excitation. While only a negligible number

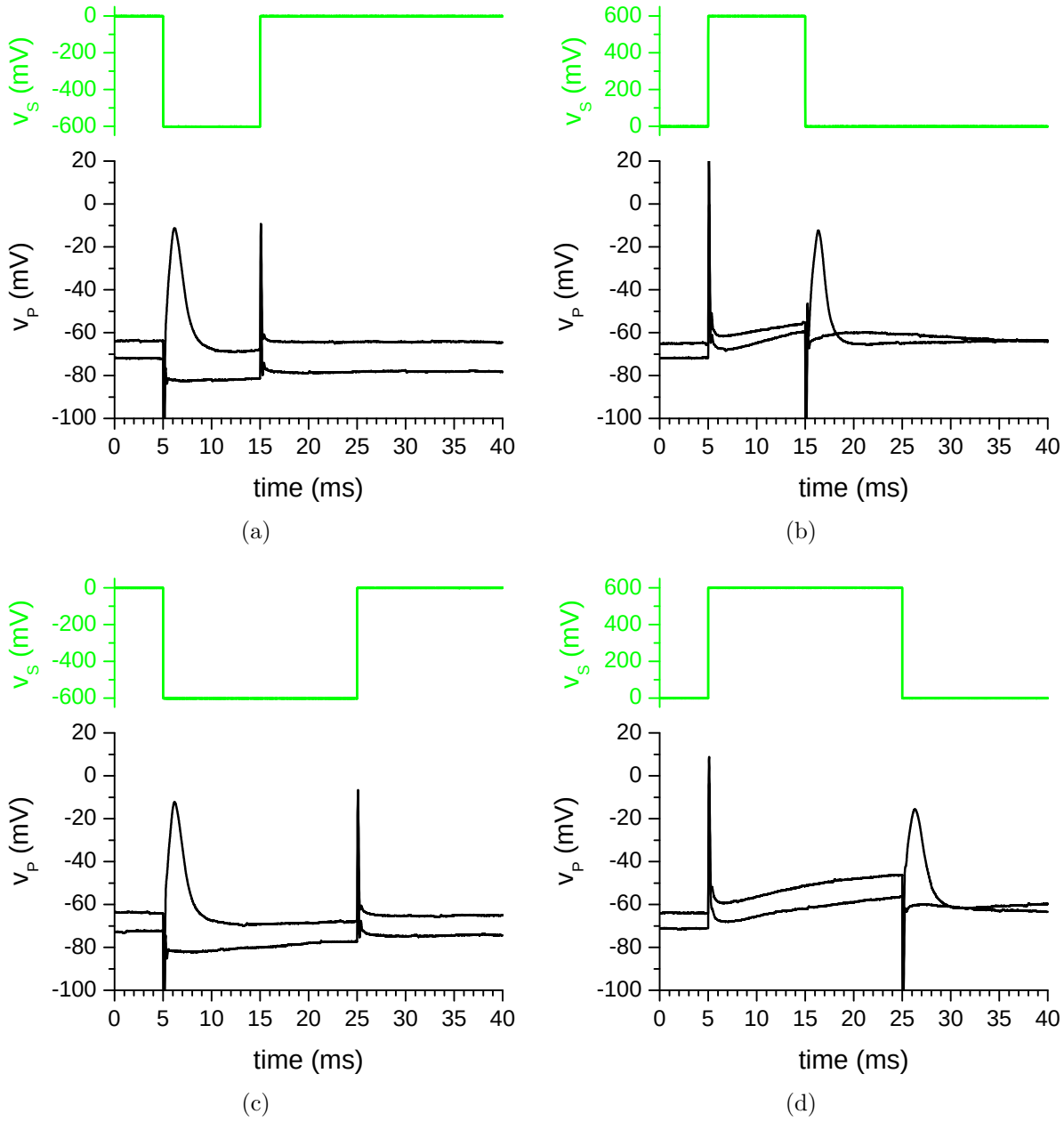

Figure 5.43: Two examples each for stimulation experiments conducted with the third rat cortical neuron (see Figure 5.37.c). Negative (a, c) or positive (b, d) monophasic rectangular stimulation pulses (v_S) with an amplitude of 600 mV and a duration of 10 (a, b) or 20 ms (c, d) were used. The intracellularly measured potential (v_P) shows only a successful stimulation for a higher initial resting potential in each case.

of stimulation experiments was successful for the lowest membrane potential range, the efficiency could be increased to 67 % and even 83 % in the potential ranges above −68 respectively −66 mV. This finding can easily be explained since the pre-puls membrane potential determines how much impact a stimulation pulse must have to rise the membrane potential of at least one membrane domain above the threshold for AP excitation.

Pulse duration (ms)	Pulse phase direction	Pre-pulse resting potential > -66 mV	-66 mV $\ldots -68$ mV	< -68 mV	Σ
10	positiv	9/10	0/0	0/5	9/15
10	negativ	3/5	1/3	1/7	5/15
20	positiv	5/5	4/4	1/6	10/15
20	negativ	3/4	5/8	0/3	8/15
Σ		20/24	10/15	2/21	
10	both	12/15	1/3	1/12	14/30
20	both	8/9	9/12	1/9	18/30
both	positiv	14/15	4/4	1/11	19/30
both	negativ	6/9	6/11	1/10	13/30

Table 5.2: Summary of the stimulation experiments conducted with a pulse amplitude of 600 mV with the third rat neuron. Negative or positive monophasic rectangular stimulation pulses with a duration of 10 or 20 ms were compared.

Additionally, the pulse length also seems to influence the stimulation efficiency, although this effect is not as clear as the effect of the initial membrane potential. However, doubling the pulse duration from 10 to 20 ms increases the overall excitation probability from 47 % to 60 %. This effect can also be seen for the single membrane potential ranges, and can be explained by the previously described slow depolarization of one of the two membrane domains during the pulse. This depolarization can cause the direct approach of the threshold for AP excitation in the depolarized membrane domain during the pulse (as shown for the red trace with circles in Figure 5.42.a) or improves the propability of AP excitation in the other membrane domain after the offest of the pulse by a residual depolarization (e.g. shown in Figure 5.43.d).

Finally, comparing the efficiency of positive and negative stimulation pulses, the positive pulses seem to be more efficient for the third rat neuron, resulting in a success probability of 63 % in comparison to 43 % for negative pulses. Although this can partially be explained by the higher number of stimulation experiments starting from a higher initial membrane potential for the positive pulses, the tendency is also visible if the potential ranges are examined seperately. However, due to the contradicting results from the different cells, it can be concluded that the impact of this effect severely depends on the morphology and ratio of free and attached membrane of the cell. Additionally, it can be presumed that it only occurs for rather long stimulation durations, since the slow depolarization of the free membrane needs time to accumulate a depolarization sufficient to lead to the excitation of an AP.

In order to visualize the impact of the pulse duration on the probability of successful stimulation, Figure 5.44 shows a direct comparison of stimulation experiments with a pulse

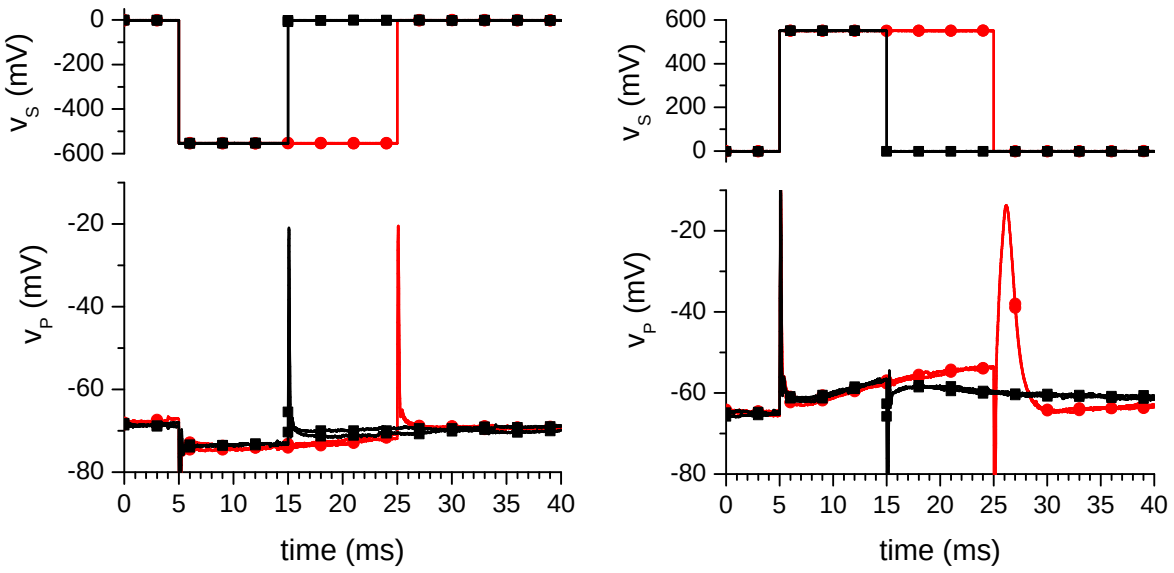

Figure 5.44: Comparison of stimulation experiments conducted with the third rat cortical neuron with pulse lengths of 10 and 20 ms. The effect of the pulse duration is investigated for negative (a) and positive (b) monophasic rectangular stimulation pulses (v_S) with an amplitude of 550 mV. The intracellular potential is measured with a patch pipette (v_P).

amplitude of 550 mV with pulse durations of 10 and 20 ms with the third neuron. For the positive pulses (see Figure 5.44.b), a slowly rising depolarization from the initial membrane potential can be observed, which increases with ongoing pulse duration. While no AP is excited at the end of the shorter pulse, the increased residual depolarization at the end of the longer pulse successfully helps to excite an AP. The negative pulses (see Figure 5.44.a) also cause a slow increase of the depolarization during the pulse, but neither for the short nor for the long pulse an AP is excited at the end of the pulse. Two reasons probably contribute to this. First, the smaller attached membrane depolarized by the negative pulse mediates an overall smaller influx of positive charges, which are distributed in the whole cell during and at the end of the pulse, resulting in a smaller residual depolarization at the end of the pulse. Secondly, the depolarizing effect of the falling flank on the larger free membrane at the end of the pulse is smaller and (together with the minor residual depolarization) not sufficient to cause an AP.

While a long pulse duration is important for the excitation of APs with positive pulses for the third neuron, the same does not hold true for negative pulses as can be seen in Figure 5.45. Five stimulation experiments with negative (see Figure 5.45.a) and positive (see Figure 5.45.b) monophasic rectangular pulses with a pulse amplitude of 600 mV and a duration of 4 ms starting from the same pre-pulse membrane potential were conducted. While the depolarization achieved during the pulse duration of the positive pulses was not

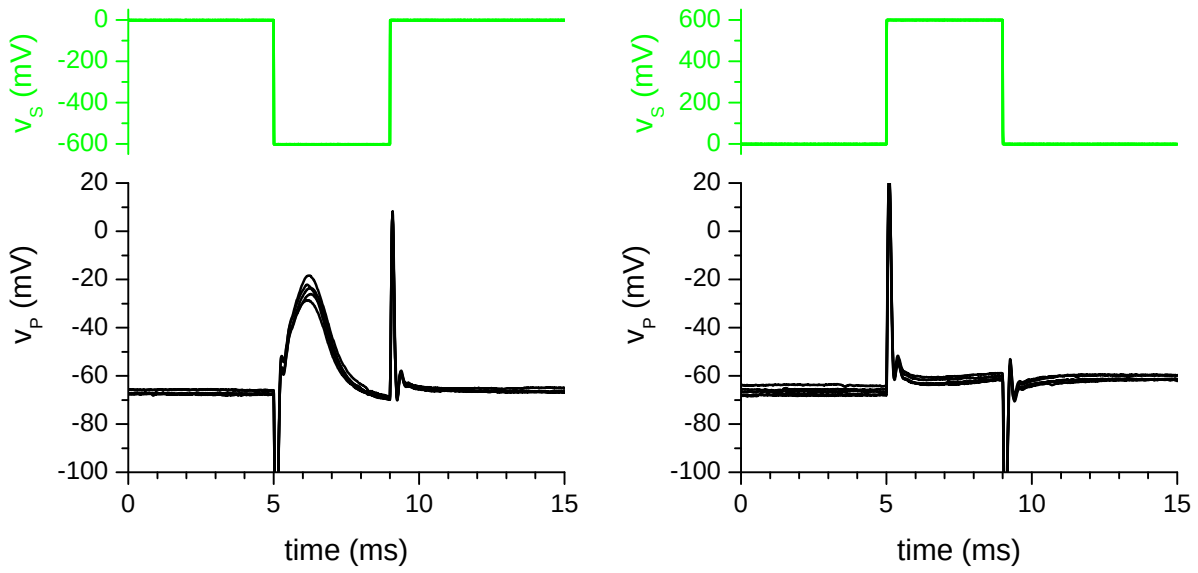

Figure 5.45: Comparison of stimulation experiments conducted with the third rat cortical neuron with a pulse length of 4 ms. The effect of a shorter pulse duration is investigated for negative (a) and positive (b) monophasic rectangular stimulation pulses (v_S) with an amplitude of 600 mV. The intracellular potential is measured with a patch pipette (v_P).

sufficient to prepare the excitation of APs at the end of the pulse, an AP was excited directly at the beginning of each of the negative stimulation pulses. Hence, it can be concluded that the pulse duration of negative pulses is not important for stimulation in case of the third neuron, as long as the pre-pulse membrane potential is high enough to directly excite an AP in the attached membrane at the leading falling flank of the pulse.

To support this conclusion, Figure 5.46 shows stimulation experiments with a further reduced pulse duration. Reducing the duration from 4 to 2, 1.5, and 1 ms does not prevent the excitation of an AP for the negative stimulation pulses. Even if the rising flank at the end of the pulse falls within the rising AP (as happened for the 1 ms pulse), the AP is not suppressed, but further rises to its maximum value after the pulse.

Finally, it can be concluded for the third cortical rat neuron that the pulse duration is mainly important for positive stimulation pulses. Here, the large free membrane area needs to be sufficiently depolarized by a sustained pulse to reach a sufficient depolarizing charge to guarantee an excitation of an AP in the attached membrane at the falling flank of the pulse. For a negative pulse, the pulse duration is not important, since the AP is usually generated directly at the beginning of the stimulation pulse if the depolarization of the smaller attached membrane area is high enough. Similar results could be acquired with most of the stimulated neurons. Nevertheless, the various stimulation mechanisms that occurred e.g. with the second cortical rat neuron (see Figure 5.42) showed that it is

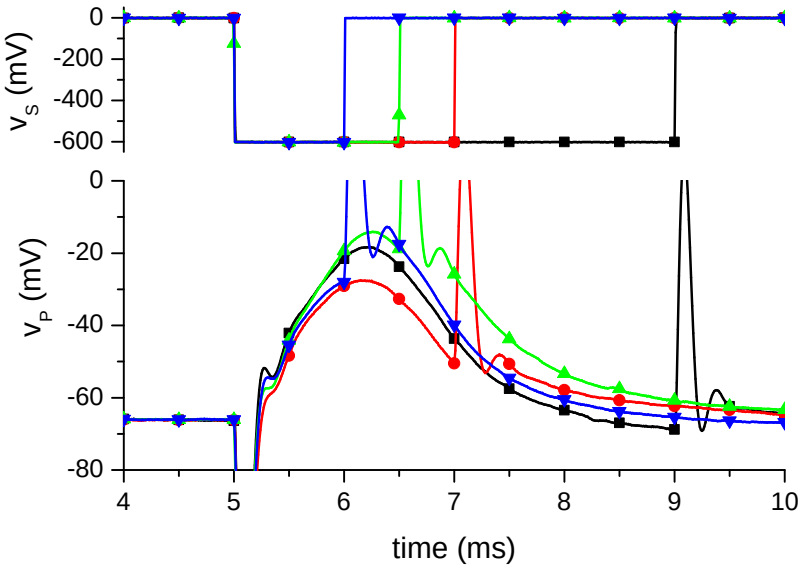

Figure 5.46: Stimulation experiments conducted with the third rat cortical neuron with negative stimulation pulses with 600 mV amplitude and durations of 4, 2, 1.5, and 1 ms. As can be seen by the intracellularly measured potential (v_P), the suitability of the negative pulses for AP excitation is also obtained with shorter pulse durations.

hard to define general rules for the ideal stimulation pulse. In any case, the most important parameter to determine the success probability of a stimulation experiment is the pre-pulse membrane potential. Unfortunately, there is no known method to extracellularly control the membrane potential.

Stimulation Experiments in Voltage-Clamp Mode

After the current-clamp experiments, the mode was switched back to voltage-clamp and the third rat cortical neuron was clamped to a resting potential of −70 mV and extracellularly stimulated. As already introduced in Subsection 2.5.2, the extracellular stimulation in the voltage-clamp is very different in comparison to the current clamp mode. Since the intracellular potential v_M is in this mode kept constant by the patch-clamp pipette, the two-domain stimulation model predicts that only the voltage drop across the attached membrane can be influenced by a stimulation pulse, while the potential at the free membrane stays constant. Therefore, only negative voltage pulses can be used in order to depolarize the attached membrane and stimulate an opening of ion channels. If the stimulation is successful, a measurable membrane current through the attached membrane should be measurable. Furthermore, the stimulation experiments in the voltage-clamp mode are more reproducible and do not underlie the strong membrane potential fluctuation that are common in the current-clamp mode.

Figure 5.47 shows the results of stimulation experiments in the voltage-clamp mode done with the third rat cortical neuron. For both experiments, the traces correspond to the average of five measurements. The cell was stimulated with positive and negative monophasic pulses with a duration of 10 ms and a pulse amplitude of 650 mV. For both kinds of stimulation pulses, a passive capacitive peak current with a brief post-pulse oscillation caused by

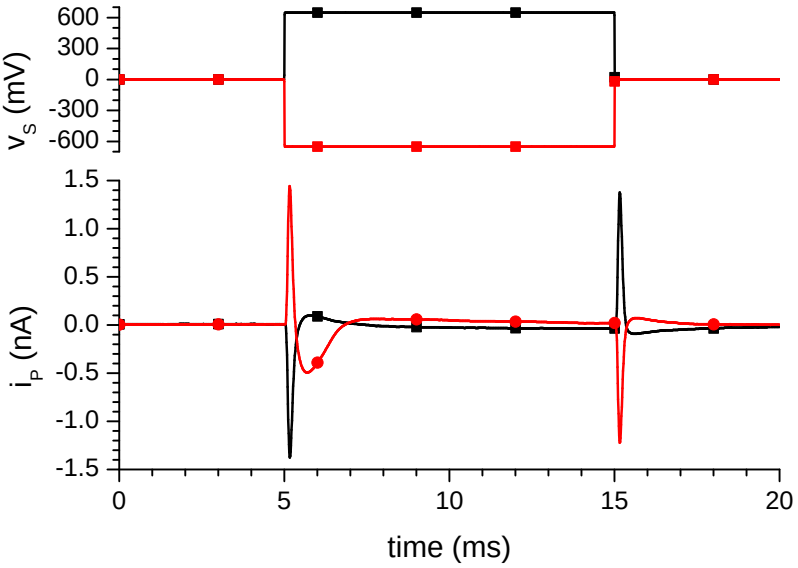

Figure 5.47: Stimulation experiments conducted with the third rat cortical neuron with monophasic rectangular stimulation pulses (v_S) with 10 ms duration and 650 mV amplitude in the voltage-clamp mode. As predicted by the stimulation model, only the negative pulse could stimulate ion channel activity and cause a pipette current (i_P), while the response to the positive pulse is purely passive. Both traces correspond to the average of five stimulation experiments.

the stimulation pulse could be measured at the beginning and the end of the pulse. In addition to that passive response, a negative current with a peak of approximately −500 pA was measured directly after the beginning of the negative pulse (red trace with circles), indicating the opening of fast sodium channels and an influx of sodium ions into the cell. Since the membrane potential was only briefly depolarized by the extracellular stimulation pulse, the potassium channels in the cell membrane did not contribute a significant membrane current during the stimulation experiment. As predicted by the two-domain stimulation model, the positive stimulation pulse (black trace with squares) did not cause any activation of ion channels and only the passive effects of the pulse could be measured.

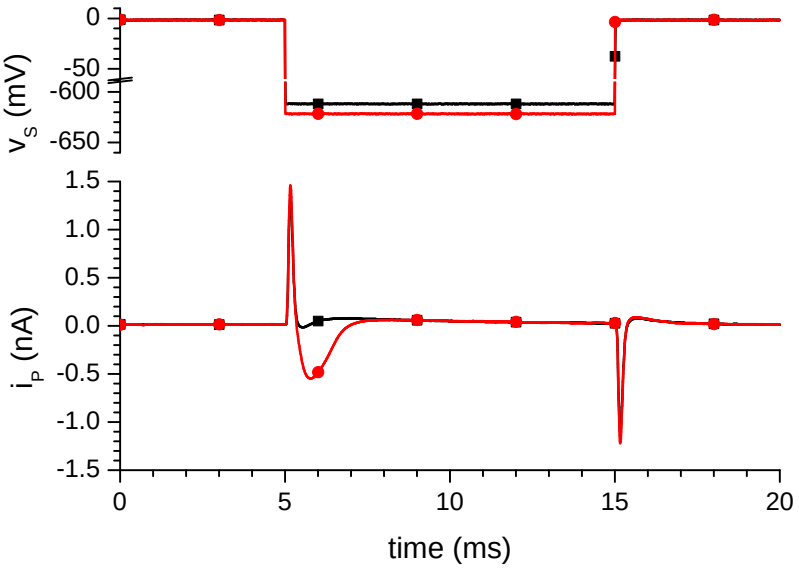

Figure 5.48: Stimulation experiments conducted with the third rat cortical neuron with negative monophasic rectangular stimulation pulses (v_S) with 10 ms duration in the voltage-clamp mode. For a stimulation pulse amplitude of 620 mV, ion channel activity could be excited and an active pipette current (i_P) could be measured, while the response to the 610 mV pulse was purely passive. Each trace corresponds to the average of five stimulation experiments.

In a second set of experiments, the threshold for the extracellular stimulation of the neuron was investigated. Since the membrane potential is precisely controlled by the patch pipette, the measurements were very reliable and a sharp threshold could be identified as shown in Figure 5.48. Starting from 650 mV, the stimulation pulse amplitude was reduced step by step by 10 mV in every set of five measurements, until no ion channel activity could be measured anymore. In the figure, the average of five measurements with stimulation pulse amplitudes of 610 (black trace with squares) and 620 mV (red trace with circles) each are compared. While the lower amplitude only resulted in capacitive current similar to the positive pulse in Figure 5.47, a significant potassium current with a peak amplitude of approximately −550 pA could be measured. Similar to the intracellular stimulation with the patch-clamp pipette in the voltage-clamp mode (compare Figures 5.38 and 5.39), the maximum potassium current could be measured very close to the threshold of channel opening, with a slow decrease of the peak amplitude for increasing stimulation pulse amplitudes. However, the stimulation voltage was not increased above 650 mV to prevent any damage to the cell. Furthermore, it has to be kept in mind that this threshold does not represent a general threshold for the extracellular stimulation of rat cortical neurons, but highly depends on the experimental situation and the coupling between the cell and the stimulation electrode.

5.2.3 Summary and Discussion of the Results

Within this section, the fourth generation SIROF MEAs with 50 µm electrodes produced in this thesis were shown to be suited for the extracellular stimulation of electrogenic cells *in vitro*. Stimulation experiments were successfully conducted with HEK293 cells expressing the $Na_V1.4$ fast sodium channel and rat cortical neurons, and cell responses could already be measured with very low stimulation amplitude of less than 200 (HEK293 cells) and 300 mV (rat neurons). In combination with intracellular recording by a patch-clamp electrode, the electrodes could be used to analyze the interactions between electrodes and cells during a stimulation experiment and to show the suitability of the two-domain stimulation model to explain the basic mechanisms involved in the stimulation of cell activity.

For experiments with HEK293 cells, a well-defined experimental situation with a simple cell morphology and cells completely positioned on the stimulation electrodes could be established. This precisely defined situation together with a rather slow increase of sodium current beyond the threshold for channel opening (compare Figure 5.16) allowed for a detailed experimental analysis. The measurements were reliable, could be averaged, and compared to simulations to identify the influence of several experimental parameters on the stimulation.

Experiments with bi- and monophasic stimulation pulses showed the defined influence

of the pulse amplitude and the pulse polarity on the achieved depolarization. Similar to the results found in the last section for rat neurons with weak coupling to the electrode, biphasic negative-phase-first pulses were found to result in a higher post-pulse depolarization than pulses with the positive phase first. Due to their depolarizing effect on the free cell membrane, the positive pulse phase was found to allow a precise and controlled stimulation with a direct intracellular measurement of the achieved depolarization. Therefore, positive monophasic pulses were used to gather information about the achieved depolarization, which could then be used to fit a linear relation to the applied stimulation pulse amplitude. However, the absolute threshold for a stimulation effect obviously depends on the experimental situation and the quality of the coupling between cell and electrode and cannot be given as an absolute value for every experiment. The lowest pulse amplitude found to result in a measurable depolarization for one of the investigated cells was in the range of 150 mV.

The pulse duration was found to play an important role for the stimulation with the HEK293 cells. Reducing the duration with a constant pulse amplitude caused a reduction of the achieved depolarization, which could be explained by the rather slow increase of the sodium current beyond the threshold of channel activation and the opening kinetics of the $Na_V1.4$ channels. On the other hand, an increased pulse duration could be used to achieve a higher depolarization of the cell, finally leading to the excitation of pseudo-APs with maximum membrane potentials and time courses comparable to intracellularly stimulated pseudo-APs. Also for the relation between the pulse duration and the depolarization, a linear dependence was found. However, a state of saturation of the depolarization was reached after a few milliseconds upon excitation of pseudo-APs. By further increasing the pulse duration beyond that point, the membrane potential could be kept at an almost constant high level around 10 mV. This maintenance of the depolarization is only possible, since the HEK293 cells contain almost no endogenous potassium channels, which prevents an active repolarization as in the case of neuronal cells.

Using the two-domain stimulation model and the numerical approach for its solution developed in this thesis (see Subsection 2.5.2), the passive signal components of the stimulation experiments conducted with the HEK293 cells could be precisely simulated. The necessary parameters for stimulation and reference electrode impedance as well as the geometry of the cell and its contact to the electrode were determined from impedance measurements and microscopic images. The values of the junction resistance, electrolyte resistance, and the filter parameters describing the influence of the patch-clamp amplifier were acquired from fitting the simulations to the measured data. The fitted electrolyte resistance was in the expected range, and the value for the junction resistance corresponded to literature values, underlining the accuracy of the used model and the numerical approach

for the simulation.

Using the simulation, it was possible to show that the intracellularly measured signal is composed of the potential change at the free membrane and the voltage drop at the reference electrode and the electrolyte solution. Also the filter effect of the recording system including the compensation circuitry on the measured signal could be quantified.

Furthermore, the influence of several experimental parameters on the achieved potential change at the membrane domains and thus the stimulation efficiency was analyzed. As expected, the junction resistance was found to be of uttermost importance for a good coupling between the electrode and the cell, with any slight change significantly altering the amplitude and the time course of the achieved passive depolarization. The higher the junction resistance, the longer an achieved depolarization of the membrane domains is sustained, resulting in a higher stimulation probability. Thus, the necessity to achieve a high junction resistance with a tight attachment of the cell to the electrode by a good surface treatment and good cell culture conditions is underlined.

Similarly important as the junction resistance is the impedance of the stimulation electrode. Especially the double layer capacitance of the electrode-electrolyte interface has a very high impact - comparable to the junction resistance - on the amplitude and time course of the potential changes at the membrane domains. The higher this capacitance, the longer a passive depolarization of the membrane domains is kept at a high value. The resistive component of the electrode impedance, on the other hand, rather determines the potential change to which the passive depolarization drops towards the end of a long stimulation pulse. However, the simulations showed that in order to play an important role on the achieved passive depolarization, the resistance needs to be reduced by more than one order of magnitude in comparison to the values determined from the impedance spectroscopy. Summing up the influence of these experimental parameters, the junction resistance and the electrode capacitance determine the time constant of the drop of any achieved passive depolarization (high frequency signal compartments), while the electrode resistance influences to which value the potential change drops towards the end of long stimulation pulses (low frequency signal compartments).

Finally, the electrode area was altered in the simulations to get information about the ideal size for stimulation electrodes. In general, for stimulation experiments with single cells, it is good to have big electrodes to get a high probability that a cell is located on the electrode. Additionally, for a systematic investigation, it is important to have a defined experimental situation, where the cell is completely and not only partly located on the electrode. However, big electrode sizes also come with drawbacks. As shown in Figure 5.36, the depolarization directly after the application of a stimulation pulse is reduced for high electrode surfaces, which could negatively influence the stimulation success for cells with

fast channel opening kinetics. Additionally, it has to be considered that most electrodes will also be used for recording cellular signals. For this purpose, the electrode size should be small to allow a complete coverage of the electrode with the cell and a good coupling of the cell signal to the sensor. In summary, the size of stimulation electrodes should be adjusted to the size of the cells and the desired application. Compromises between a large surface area for a high probability of cell positioning on the electrode as well as a defined experimental conditions, and a small surface area for complete coverage of the electrode for a good coupling have to be made. All these results for the experimental parameters are independent of the cell type and account for experiments with neurons, as well.

Being the actual objective cell system, several rat cortical neurons were successfully stimulated using the new SIROF microelectrodes in the next step. In comparison to the previously used HEK293 cells, neurons have a more complex morphology with a high number of cell processes, as well as a more complex electrophysiology with a significant number of repolarizing potassium channels. As show by the voltage-clamp experiments and the following current-voltage diagram (see Figure 5.39), the fast sodium channels in the investigated neurons have a very sharp threshold for channel activation and produce a strong self-amplifying depolarization upon opening. Together with the fluctuating resting potential of the neuronal cells, these differences complicate the analysis of the experimental data and the interpretation of the observations.

In contrast to the experiments with the HEK293 cells, good stimulation results could be achieved both with positive and negative monophasic stimulation pulses, leading to the excitation of APs. Comparing the experiments with several cells, no clear advantage of using positive or negative pulses could be found. Instead, the most important parameter for determining the probability of AP excitation was found to be the pre-pulse membrane potential of the cell. The higher the membrane potential of the cell before the stimulation, the higher the probability a stimulation pulse would cause an excitation of the cell leading to an AP. The lowest stimulation pulse amplitude that could be used to excite an AP of a rat neuron within this thesis was 250 mV.

For both pulse polarities, different times for the excitation of APs in relation to the time course of the stimulation pulse could be found. In the most simple case, a stimulation pulse directly caused a depolarization of one of the two membrane domains at the first pulse flank, which was sufficient to excite opening of fast sodium channels in the depolarized membrane domain and a resulting self-amplification of the depolarization. This effect could be investigated both for positive pulses, where the free membrane is depolarized (see Figure 5.42.b), as well as negative pulses, where the attached membrane is depolarized (see Figure 5.41.a). For this stimulation mechanism, the pulse duration was found not to have a significant influence on the stimulation effect. Since the initial stimulation at the beginning

of the pulse needs to be strong enough to directly cause a self-amplifying depolarization of the cell, it is not surprising that this mechanism was more often found for negative pulses. Since the attached cell membrane is in general smaller than the free membrane, the average potential change is here higher than at the free membrane, resulting in a higher possibility to directly achieve the desired depolarization to excite an AP.

Another stimulation mechanism is more similar to the results achieved with the HEK293 cells. It is characterized by a slowly rising depolarization of the membrane potential during the course of a stimulation pulse due to a depolarization of one of the two membrane domains. If the depolarization is high enough to achieve an ongoing accumulation of positive charges in the cell and if the stimulation pulse is sustained long enough, this can finally lead to the excitation of an AP during the stimulation pulse. However, if the pulse ends before the AP is excited, either no AP is excited at all, or the residual depolarization in combination with the sudden passive depolarization of the other membrane domain can excite an AP in that second domain, which then spreads to the whole cell. In contrary to the first stimulation mechanism, the stimulation success in this case severely depends on the duration of the pulse, as shown in this section. Here, a longer pulse duration increases the stimulation success ratio, due to the accumulated charge in the cell. For short pulses, the achieved depolarization at the end of the pulse is not high enough to excite an AP. Unlike the experiments with the HEK293 cells, a prolonged pulse duration after excitation of an AP could not be used to hold the membrane potential at a highly depolarized level, since the voltage-gated potassium channels in the rat neurons open up and cause a fast repolarization to the initial membrane potential. Although this stimulation mechanism could also be seen for negative pulses (see Figure 5.42.a), it occurred more often for positive stimulation pulses, which could be explained by the smaller size of the attached cell membrane. If a slow ionic depolarization is mediated through the rather small attached membrane domain, the positive charge transported by the current through this smaller domain will be distributed in the whole cell and any excitation can be suppressed by the large hyperpolarized free membrane domain [29, 104]. Thus, a rather small residual depolarization is left at the end of the stimulation pulse. In addition with the smaller following capacitive depolarization of the free membrane at the end of the pulse, this has a lower probability to cause a sufficient excitation of the cell.

In summary, two basic different mechanisms for the excitation of (pseudo) APs by monophasic pulses in electrogenic cells have been identified. The first mechanism with direct excitation of an AP in one of the two membrane domains was found to occur more often for neuronal cells, which had a rather steep increase of the sodium channel conductivity beyond the threshold for channel opening and a higher maximum current, leading to a higher probability of a self-amplification of the depolarization in comparison to the

HEK293 cells. This mechanism seems to occur more often for negative pulses, which can be explained by the usually smaller attached membrane and the resulting higher depolarization, directly exceeding the threshold potential for ion channel activation. Since this mechanism primarily depends on the direct passive depolarization at the beginning of a pulse, it is rather independent on the pulse length and, therefore, should not be severely influenced by the junction resistance, which is primarily important for sustaining the achieved depolarization for a longer pulse length.

In the second case, an indirect excitation of the (pseudo) AP was found during or at the end of the stimulation pulse after a slow depolarization of one membrane domain leading to an accumulation of charges in the cell. This stimulation mechanism was found for cortical rat neurons and especially HEK293 cells with the rather slow increase of the sodium current beyond the threshold for channel opening. As can be seen from the presented results, the pulse duration plays an important role in this stimulation mechanism with an increasing pulse duration producing a higher residual depolarization at the end of the pulse. Hence, a good coupling between cell and electrode with a high seal resistance is very important to sustain any achieved depolarization as long as possible for a further charge accumulation and increase of the depolarization.

Stimulation experiments with a rat cortical neuron were also conducted in the voltage-clamp mode, and the successful stimulation of ion channel activity in the neuron was shown. With these experiments, the influence of the pulse polarity was found to be as predicted by the two-domain stimulation model used in this thesis. Additionally, the simulation results of the experiments with the HEK293 cells show that the numerical solution in the frequency domain can be used to simulate the passive cell response to any given stimulation pulse and give an estimation of the resulting effect on the cell.

As shown by the results of this and the last section and the knowledge gained by various investigations and models about extracellular stimulation found in the literature, it is possible to comprehend and reconstruct the mechanisms of extracellular electrical excitation of (pseudo) APs in single electrogenic cells and especially neurons *in vitro*. However, contradictions and inconsistent results from previously published studies and experiments with different cells show the complexity of the stimulation situation. The high number of experimental parameters and coupling factors such as the geometry of the electrode-cell contact area strongly vary with the exact experimental configuration and from cell to cell and cannot be completely controlled or measured beforehand. In order to a priory predict the results of any particular stimulation experiment and the optimum stimulation parameters, complete knowledge of all these experimental conditions would be necessary. In this regard, the situation for extracellular stimulation is very similar to extracellular recording, were recent discussions about the interpretation of experimental data and regularly applied

models show that only the a posteriori modeling, but not the prediction of experimental data is possible so far [21, 165, 166]. As pointed out by Timko et al. [166], the significant variability in the cell-device interface leads to considerable uncertainty in the parameters used to describe this interface, which definitely holds true for the extracellular stimulation, as well.

5.3 Extracellular Stimulation with Mi-BeSAN MEAs

In parallel to the experiments with SIROF MEAs with 64 electrodes, first stimulation experiments were also conducted with the Mi-BeSAN MEAs (see Section 3.2 and especially Subsection 3.2.2). The aim of these experiments was to show the functionality of the Mi-BeSAN electrodes for the extracellular stimulation of electrogenic cells, which were later integrated with *field-effect transistors* (FETs) on the complete chips. Although the Mi-BeSAN MEAs of the third generation were later found to be unstable for lasting exposure to electrolyte solutions, they could beforehand be used for initial stimulation experiments. In one case, a SIROF ring electrode could be applied for a successful proof-of-principle stimulation experiment with a rat neuron.

The experiments shown in this section were done with the novel BioMAS amplifier system (see Section 4.3) with the Mi-BeSAN headstage. The electrophysiological setup for simultaneous intracellular recording is shown in Figures 4.13 and 4.14 and described in Subsection 4.3.4. After encapsulation and activation of the MEAs, the chip preparation and cell culture was done in the same way as previously described in Subsections 5.1.1, 5.1.2, and 5.2.2. The conditions and protocols for cell culture and patch-clamp experiments are described in Section C.1. The temperature control of the amplifier system was used to regulate the chip temperature to values between 35 and 36 °C during the experiments.

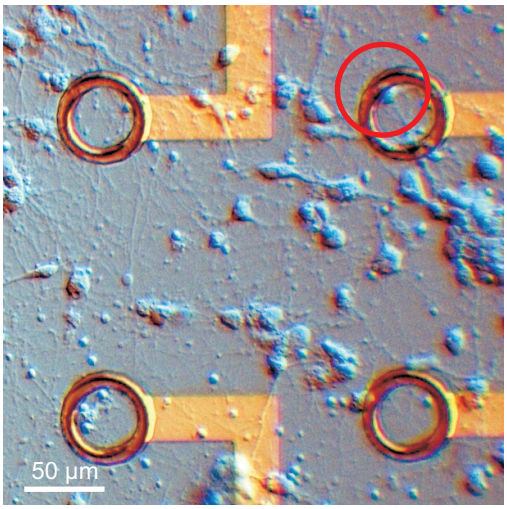

Figure 5.49: DIC image of the stimulated rat cortical neuron located at the edge of a SIROF ring electrode of a third generation Mi-BeSAN MEA. The red circle marks the position of the cell on the electrode.

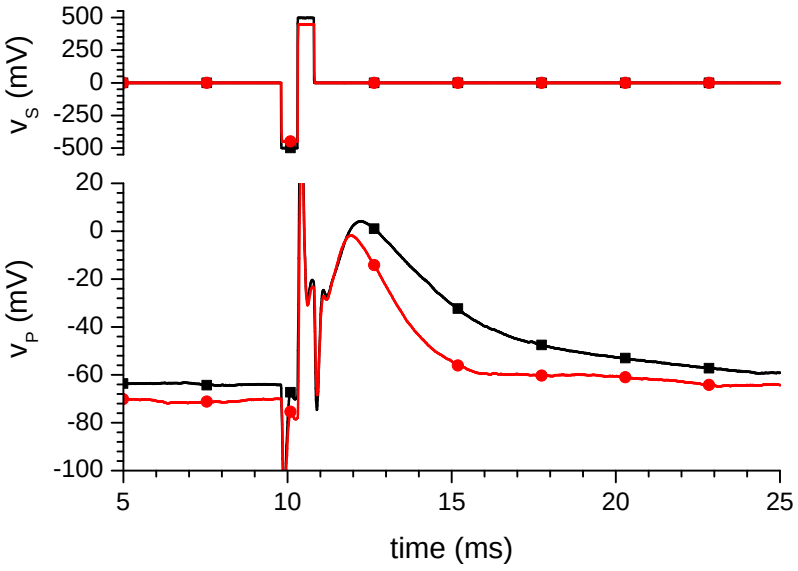

Figure 5.50: Extracellular stimulation of rat cortical neuron with a Mi-BeSAN SIROF ring electrode. The cell was successfully stimulated with biphasic negative-phase-first rectangular pulses with a pulse duration of 1 ms. The intracellularly measured membrane potential (v_P) in response to stimulation pulses (v_S) with 450 and 500 mV amplitude is shown.

Figure 5.49 shows rat cortex neurons (DIV 7) cultured on a third generation Mi-BeSAN MEA with SIROF ring electrodes. The cell marked by the red circle was patched and characterized with standard voltage- and current-clamp experiments, resulting in similar electrophysiological characteristics as already described for the other rat neurons in Subsection 5.2.1. In current-clamp mode, a bias current of −30 pA was injected to adjust the resting potential of the cell to an approximate value of −65 mV.

After characterization, the cell was extracellularly stimulated by application of biphasic negative-phase-first stimulation pulses with a duration of 1 ms. As shown in Figure 5.50, the successful stimulation of the rat neuron could be achieved with stimulation pulses with 450 and 500 mV amplitude.

The detachment of the SIROF layers could be overcome for the Mi-BeSAN MEAs of the fifth generation, and characterization of the electrodes revealed good electrochemical characteristics comparable to SIROF electrodes from 64 electrode MEAs (see Subsection 3.2.2). In combination with the successful proof-of-principal stimulation experiments, it can thus be concluded that the SIROF electrodes on the Mi-BeSAN chips are applicable for the *in vitro* extracellular stimulation of electrogenic cells.

5.4 Extracellular Recording with SIROF MEAs

In order to test the capabilities of the newly developed SIROF MEAs of the fourth generation for bidirectional communication with electrogenic cells, the chips were applied for the extracellular recording of APs from cells of the HL-1 cell line. For that purpose, the same encapsulated and activated MEAs were used as for the stimulation experiments presented in Section 5.2. To record the cell signals, the basic amplifier system with a standard

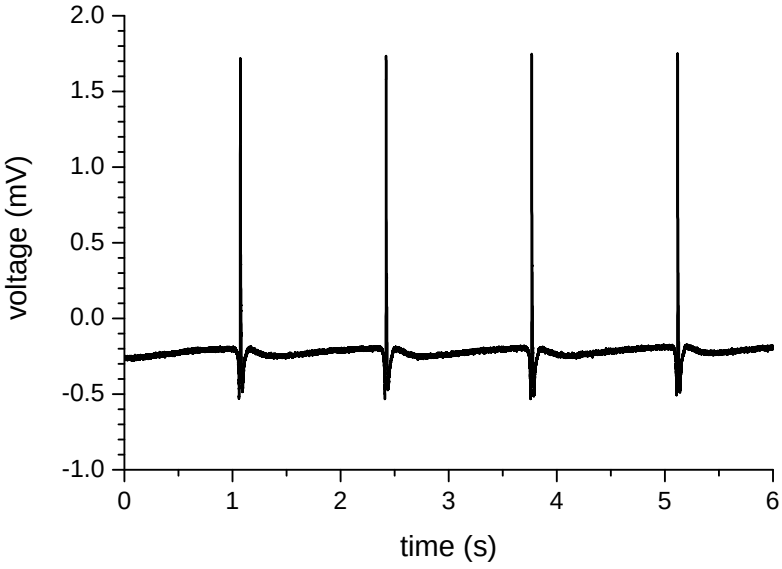

Figure 5.51: Example for an extracellular recording of HL-1 cell action potentials with a SIROF microelectrode with a diameter of 50 µm. The recordings show a peak-to-peak signal amplitude of approximately 2 mV and reappear with a frequency of roughly 0.7 Hz.

64-channel headstage presented in Section 4.1 was used.

The HL-1 cell line [167] is often used as a model system for extracellular recordings, since the cells are easy to culture and generate synchronized APs by themselves. The cell line was developed from mouse cardiomyocyte tumor cells and has electrophysiological properties similar to cardiac myocytes. For electrophysiological experiments, the SIROF MEAs were cleaned (see Section B.3) and used to culture the HL-1 cells as explained in Section C.3. On the chip surface, the cells continuously multiplied, until they built a functional syncytium being interconnected by electrical synapses (gap junctions). After reaching confluence, the HL-1 cells showed spontaneous APs that spread across the whole cell layer and the chip surface, resulting in synchronized cell activity that was recorded with the 50 µm SIROF microelectrodes.

Using this configuration, the synchronized APs of the HL-1 cells could be measured as extracellular signals with high signal amplitudes on all sensors. Figure 5.51 shows the recordings of four consecutive APs from one electrode. The recordings have a peak-to-peak signal amplitude of approximately 2 mV and uniformly reappear with a constant frequency of approximately 0.7 Hz. Similar recordings could be conducted with several MEAs, and maximum peak-to-peak signal amplitudes of 3 mV could be acquired. The high signal amplitude in combination with the peak-to-peak noise of approximately 30 µV in the recordings results in very good *signal-to-noise ratio* (SNR) in comparison to recently published HL-1 recordings with standard gold MEAs [168], diamond FETs [20], and silicon nanowires [23], as well as recordings from cardiac myocytes with planar silicon FETs [138, 139] and standard gold MEAs [122, 130].

Since the electric activity of the cells travels through the whole syncytium, the propagation of the signal could be measured with the array of 64 electrodes, as shown in Figure 5.52.

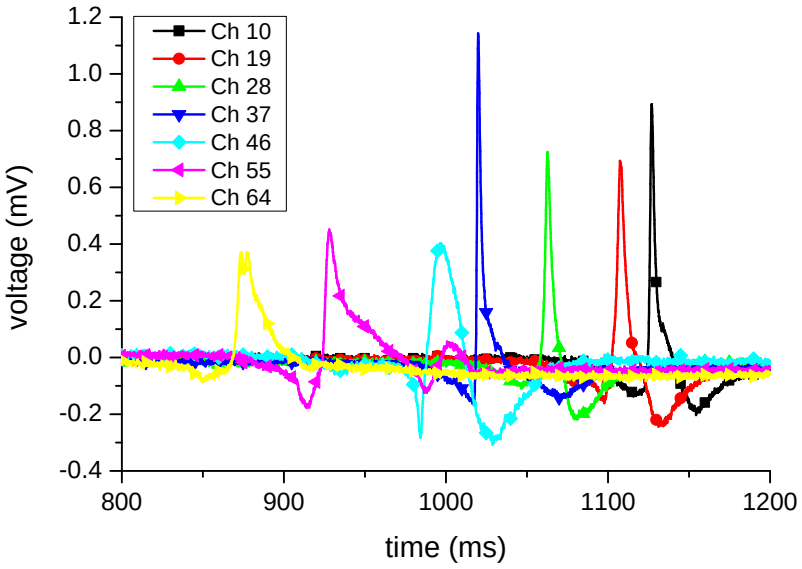

Figure 5.52: Propagation of HL-1 action potentials measured with a SIROF MEA with 50 µm electrodes. The self-propagating excitation wave of the HL-1 syncytium arrived from the lower right corner of the electrode array and spread to the top left corner. A time delay in the recordings of 7 channels on the array diagonal can clearly be seen and visualizes the propagation of the signal from channel 64 to channel 10.

In the figure, recordings from seven electrodes on the diagonal of the array can be seen. The excitation wave arrived from the lower right corner and propagated throughout the whole array, lastly reaching the top left corner. The time delay of the recordings from the 7 channels clearly visualizes the propagation of the signal from channel 64 to channel 10. Taking into account the distance of approximately 1.7 mm between electrode 10 and 64, an average propagation speed of roughly 6.7 mm/s can be calculated, which is in the range of recently reported propagation speeds for HL-1 cells [23, 169]. Comparing the signals from the seven electrodes, strong variations can be found for the signal amplitudes and shapes. These variations can be explained by differences in the cell positioning on and attachment to the microelectrodes, and especially the big size of the electrodes. Since the average cell size is much smaller than the electrode size, the recordings are not only from one cell, but represent the integration of the recording from several cells of the syncytium. Furthermore, it is well known from the literature that myocyte recordings can strongly vary in amplitude and shape for different recording sites [20, 122, 139]. Nevertheless, the time delay between the recorded events and the appropriate propagation speed prove the recorded spikes to be cell signals, since artifacts or distortions of any kind would occur at all channels simultaneously.

In combination with the good electrochemical properties, stability, biocompatibility, and successful stimulation experiments, these extracellular recordings from HL-1 cells show the quality of the manufactured MEAs and SIROF layers and the high potential for the bidirectional communication with electrogenic cells *in vitro*. Nevertheless, in order to optimize the devices especially for bidirectional investigations of vertebrate neurons, smaller electrodes that can be completely covered by a single cell are necessary. Electrodes with a diameter between 10 and 20 µm would improve the recording properties, allow analysis of

the signals in terms of amplitude and shape, and enable true bidirectional communication on a single-cell level.

Chapter 6

Conclusions and Outlook

Because things are the way they are, things will not stay the way they are.

Bertolt Brecht (German poet and playwright, 1898-1956)

6.1 Conclusions

In this work, the extracellular stimulation of individual electrogenic cells *in vitro* with surface-embedded microelectrodes was studied. In order to achieve this task, a new stimulation system, including devices and amplifiers, was developed. Newly designed chip systems included *multi-electrode arrays* (MEAs) with *sputtered iridium oxide films* (SIROFs) and integrated chips combining SIROF stimulation electrodes and recording *field-effect transistors* (FETs). An electrophysiological setup with the novel *Bioelectronic Multifunctional Amplifier System* (BioMAS) was implemented with a maximum flexibility for communication with cells. The new system was used for electrophysiological experiments with rat cortical neurons and electroactive cell lines. For the first time, *iridium oxide* (IrO_x) microelectrodes were successfully employed to extracellular stimulation of individual neurons from a dissociated culture.

To this end, arrays of 64 gold microelectrodes with SIROF stacks for improved electrochemical characteristics were developed in an iterative process. The final MEA generation carried large electrodes with a diameter of 50 µm for stimulation experiments with a defined cell-electrode geometry. The SIROF stacks consisted of a 20 nm titanium adhesive layer, a 100 nm platinum diffusion barrier, and a 200 to 300 nm IrO_x functional stimulation layer.

Investigation by scanning electron microscopy revealed a rough and porous IrO_x surface covering the electrodes and significantly increasing the electrochemically active surface area. The electrode impedance was significantly reduced in comparison to gold electrodes and was in the same range as, or even lower than, the impedance of platinized gold or *titanium*

nitride (TiN) electrodes. By comparison to literature values, the specific charge storage capacity of the SIROF electrodes was found to be in the same range as for other IrO_x electrodes and higher than for electrodes made of other materials including gold, platinum, and TiN.

After encapsulation and activation, the biocompatibility of the chips was proven by growth of rat neurons and *Human Embryonic Kidney 293* (HEK293) cells for electrophysiological experiments. Additionally, repeated cleaning and reuse for cell culture and electrophysiological measurements showed the mechanical and electrochemical stability of the chips. The electrochemical properties, stability, and biocompatibility, as well as the successful application for extracellular stimulation of neurons and recording from HL-1 cells showed the quality of the manufactured MEAs and SIROF layers and the suitability for bidirectional communication with electrogenic cells.

As a versatile platform for electrophysiological experiments, the novel BioMAS amplifier system was developed, merging previous amplifier systems and consolidating as many functions as possible. The system consisted of one general main amplifier for impedimetric and electrophysiological measurements (recording and stimulation) and multiple headstages specialized for individual chip types. The microcontroller-driven system and the data acquisition are controlled by a DLL hardware interface and a LabVIEW user interface. The system's hard- and software allow versatile applications, future customization, and system expansion e.g. for other devices.

Within this thesis, major parts of the software, functional versions of the main amplifier and the headstages for recording and stimulation of all channels from MEAs and integrated chips with FETs and microelectrodes were implemented. The system was tested and introduced to an electrophysiological measurement setup in combination with a patch-clamp amplifier. The functionality was proven by frequent experimental use, especially for extracellular stimulation experiments.

Successful stimulation was conducted with HEK293 cells expressing a fast voltage-gated sodium channel and rat cortical neurons. Simultaneously, the cell's membrane potential was recorded intracellularly using the patch-clamp method in the current-clamp mode. The data was analyzed by means of the two-domain stimulation model, which predicts passive depolarization of the large free membrane domain and hyperpolarization of the smaller attached membrane domain by a positive voltage flank or pulse, and vice versa for a negative flank or pulse.

The first stimulation experiments on rat cortical neurons in this thesis were performed using a preliminary amplifier system and an earlier chip generation. Analysis of the data revealed an increased probability of *action potential* (AP) excitation and reduced AP latency with higher stimulation pulse amplitudes. A similar effect was found using negative-phase-

first biphasic stimulation pulses instead of positive-phase-first pulses. This can be explained by a strong depolarizing effect of the large rising flank between the two pulse phases and the subsequent positive phase on the free cell membrane. This passive depolarization can be sufficient to raise the membrane potential above the threshold for AP excitation. Furthermore, it was found that trains of stimulation pulses with increasing pulse numbers can be used to increase the stimulation success rate. This is necessary if the pulse amplitude cannot be increased due to the threshold of irreversible electrochemical reactions at the electrodes. The underlying mechanism is the repetitive weak activation of sodium channels during each pulse, which stepwise depolarizes the cell membrane to reach the threshold for AP excitation.

The novel amplifier system and the new MEAs were successfully used for the stimulation of HEK293 cells. While negative-phase-first biphasic pulses were again found to be more efficient than positive-phase-first pulses, no significant difference could be seen when monophasic positive pulses were used, instead. The patch-clamp measurements showed that the depolarization of the free cell membrane slowly rises throughout the duration of the positive pulse, indicating an ongoing, slow influx of sodium ions. The pulse amplitude necessary for depolarization of the cell membrane varied for different cells. The lowest pulse amplitude that resulted in a measurable depolarization of one HEK293 cell was approximately 150 mV. Using the positive pulses, a linear relation between the achieved maximum depolarization and the pulse amplitude, as well as the pulse duration was found. When the pulse duration was long enough, even pseudo-APs could be extracellularly evoked with a time course similar to intracellularly stimulated pseudo-APs. If the pulse was sustained after the maximum of the pseudo-AP, the membrane potential remained almost constant and started to decay only at the end of the stimulation pulse. This happened due to the small number of endogenous potassium channels in the HEK293 cells, which cannot promote an active repolarization to the resting potential against the stimulation pulse.

A numerical approach for the solution of the two-domain stimulation model in the frequency domain was applied to simulate the passive response of the cell membrane to stimulation pulses. The impedance of the stimulation and reference electrodes was taken from impedance measurements. The surface areas of the cell membrane, the covered electrode, and the attached membrane domain were calculated from the patch-clamp experiment and approximated from microscopic images. The simulations were fit to measured data by adjustment of the unknown resistance of the junction and the electrolyte solution between the cell and the reference electrode. The fit values, and especially the junction resistance of 0.22 MΩ, were well within the range of literature values for HEK293 cells.

As shown by the simulations, the measured signal consists of the depolarization of the free cell membrane in combination with the voltage drop at the reference electrode and

electrolyte solution. It is then modified by the patch-clamp amplifier, which has the effect of a low-pass filter. The simulations further showed the significant influence of the junction resistance and the capacitive components of the electrode impedance on the potential change at both membrane domains. Increasing either of these parameters increases the time constant for the decay of the potential change at the membrane, and thus the overall passive stimulation effect. On the other hand, the resistive compartment of the electrode impedance and the size of the stimulation electrode seem to play a minor role in the outcome of the stimulation experiments, as long as they are kept within plausible experimental values. This again underlines the importance of good stimulation devices with a low impedance and a high charge storage capacity. Additionally, care should be taken to achieve a tight adhesion and precise positioning of the cell on the electrode.

The two-domain stimulation model and the solution in the frequency domain can easily be applied to investigate the passive response to applied stimulation pulses at the different components of the system. For the investigation of various pulse shapes and electrodes with complex impedances, the numerical approach and the calculations in the frequency domain are much easier than finding analytical solutions. Nevertheless, the lack of information on the spatial distribution of the potential changes in both membrane domains and the missing influence of active ion channels limit the absolute scope of the simulations in comparison to other approaches such as the finite element method.

In the next step, the reliable stimulation of several rat cortical neurons was achieved with low stimulation voltages, which varied from one neuron to the other. The lowest amplitude of a monophasic stimulation pulse, which was sufficient to excite an AP, was only 250 mV. With positive and negative monophasic stimulation pulses, two basic stimulation mechanisms could be identified. In the first case, the flank at the beginning of a pulse directly causes the excitation of an AP by activation of a sufficient number of sodium channels to achieve a self-amplifying depolarization. For this mechanism, the pulse duration has no significant influence on the stimulation success, since only the direct response at leading flank of the pulse is important.

In the second case, the stimulation pulse initiates an opening of just a few ion channels, causing a slowly increasing depolarization by accumulation of positive charges in the cell as long as the stimulation pulse is sustained. If this rising depolarization reaches a level sufficient to cause a self-amplification during the pulse duration, an AP is excited. However, if the pulse duration is too short and the pulse ends before an AP is excited, two outcomes are possible. Either, the slow depolarization is ended with the strong capacitive hyperpolarization of the same membrane domain at the end of the pulse, or the simultaneous depolarization happening at the other membrane domain now excites an AP, which can then spread to the whole cell. This stimulating effect of the pulse end can be

strengthened by the residual positive charge from the slow influx of sodium ions during the pulse. Obviously, this second stimulation mechanism is influenced by the duration of the stimulation pulse, with an increased probability of AP excitation for a longer pulse duration. Depending on the exact experimental situation, both mechanisms can occur either at the free or the attached membrane domain.

Besides the existing two stimulation mechanisms, the acquired data made especially clear that one of the most important parameters for the success of a stimulation experiment is the pre-pulse membrane potential, which constantly fluctuates in neurons. The higher the potential at the time of the pulse application, the higher the probability of initiating a self-amplifying depolarization.

The results of the stimulation experiments performed with the new stimulation system and the knowledge gained by various investigations and models about extracellular stimulation found in the literature enable us to comprehend and reconstruct the mechanisms and processes on the way to the extracellular electrical excitation of APs in single neuronal cells *in vitro*. However, detailed knowledge of all experimental conditions and coupling parameters would be necessary in order to precisely predict the time course and the outcome of a particular stimulation experiment.

6.2 Outlook

The MEAs produced in this thesis already proved to be well suited for stimulation as well as recording experiments with electrogenic cells. Nevertheless, there are several improvements that should help to further optimize the devices for investigations with vertebrate neuronal networks. First of all, the electrode size of 50 µm was optimized to achieve a high yield of cells completely located on the electrodes for a defined stimulation situation. Smaller electrodes that can be completely covered by a single rat cortical neuron should help to improve the recording properties of the electrodes and enable true bidirectional communication on a single-cell level. Electrodes with a diameter between 10 and 20 µm should be ideal for this goal. Secondly, the SIROF layer should be further optimized with our collaboration partners at RWTH Aachen University. The production process and especially the IrO_x layer thickness could be adapted to get even better electrochemical properties with a higher charge storage capacity and a lower impedance, which will be especially important if the electrode size is further reduced.

The manufacturing process of the Mi-BeSAN chip with p-type FETs for recording and SIROF microelectrodes for stimulation was finished in the scope of this thesis, but only a brief characterization of the transistors' characteristics could be done so far. However, the preliminary Mi-BeSAN MEAs revealed satisfactory electrochemical properties with com-

parable impedance and charge storage capacity to the MEAs with 64 electrodes and could be successfully applied for a proof-of-principle stimulation of a rat neuron. Nevertheless, a thorough characterization of the final chips is still to be done before the application for electrophysiological experiments with vertebrate and invertebrate neurons can be approached.

The BioMAS system proved its usefulness in laboratory use for stimulation experiments with standard and Mi-BeSAN MEAs and already offers functionalities for several applications with MEAs and Mi-BeSAN chips. Nevertheless, several extensions of the hardware and especially the software are necessary in order to unleash its full potential. For example, an improved stimulation board of the main amplifier, including a path for current-controlled stimulation and current measurement during voltage-controlled stimulation, is desired. Additionally, a novel headstage with a corresponding software for an alternative nanoribbon chip system is currently under development.

Using these new tools, the investigation of small neuronal networks and complex neurological processes such as learning and information processing will be facilitated. The SIROF microelectrodes developed here show especially promising characteristics for stable long-term investigations of neuronal networks with precise bidirectional interfaces on a single-cell level. Research in this field will not only broaden the basic understanding of neuronal networks, but also help to create better bioelectronic hybrid systems for medical purposes. The new application of IrO_x in basic neuroscience and the established application of IrO_x for neuroprosthetics could mutually enrich each other and promote advances in both fields.

Appendices

Appendix A

Chip Processes

> We live in a society exquisitely dependent on science and technology,
> in which hardly anyone knows anything about science and technology.
>
> *Carl Sagan (American astronomer, writer, and scientist, 1934-1996)*

All processes for the various chip types used in this thesis are explained in this appendix. The first section will introduce the processing for standard and modified *multi-electrode array* (MEA) chips, while the second section will present the more complex process of the Mi-BeSAN chip with microelectrodes and *field-effect transistors* (FETs).

A.1 MEA Processes

The standard process for the production of gold (Au) or titanium (Ti) MEAs was previously published [122, 129] and is frequently used in our institute. Therefore, the processing of standard gold MEAs, they have been used for the initial measurements in this work, will be presented in this section. With this process as a base, modifications for processing *iridium oxide* (IrO_x) MEAs in standard 64-electrode design and as Mi-BeSAN electrode arrays will be introduced here in detail.

A.1.1 Standard Gold MEAs

The standard gold MEAs are the basis for all other electrode arrays produced in this thesis, and will therefore be referred to as zeroth generation. Arrays with 8×8 microelectrodes and sensor pitches of 100 or 200 µm and electrode diameters of 6, 8, 10, 20, or 30 µm were fabricated on five inch glass wafers (Borofloat 33, Schott AG, Mainz, Germany, see Table A.1). On some chips, three electrodes in each corner with a diameter of 50 or 100 µm were included as stimulation electrodes. In the first step, the electrodes, contact lines, and

Table A.1: Different wafer types used for MEA processes.

	Borofloat 33	SiO_2-z-kat	Si/SiO_2
Company	Schott	CrysTec	Si-Mat
Diameter	100 or 125 mm	100 mm	100 mm
Thickness	500 µm	500 µm	500 ± 25 µm
Orientation	-	-	<100>
Dopant	-	-	phosphorus(n)
Resistivity	-	-	$1 - 10\ \Omega$cm
Pre-processing	-	-	1 µm wet SiO_2

bond pads were predefined by optical lithography followed by metalization with a stack of 30 nm titanium, 300 nm gold, and again 30 nm titanium in an electron beam evaporator. The structuring was completed with a lift-off process. The titanium layers were included to promote adhesion of the gold on the wafer and of the following passivation layer on the contact lines. The whole surface was then passivated with a stack of 500 nm silicon oxide (SiO_2), 500 nm silicon nitride (Si_3N_4) and 100 nm SiO_2 (ONO stack) using *plasma enhanced chemical vapor deposition* (PECVD). The electrodes and the bond pads were opened by a second optical lithography followed by *reactive ion etching* (RIE) in a fluoroform (CHF_3) atmosphere. Finally, the titanium layer on top of the electrodes and bond pads was opened either by overetching (RIE), or by a wet etch with an ammonium fluoride (NH_4F) mixture.

A schematic cross section showing the layer structure of an electrode, a contact line, and bond pad of a gold MEA is shown in Figure A.1. After fabrication was finished, the wafers were cut into chips and encapsulated for usage as described in Appendix B. The complete process for the zeroth MEA generation as described here was carried out at the *Institut für Mikrotechnik Mainz GmbH* (IMM, Mainz, Germany) [122, 129].

A.1.2 Iridium Oxide MEAs

In order to get MEAs with improved stimulation capabilities, several approaches to the production of chips with *sputtered iridium oxide film* (SIROF) microelectrodes were tested. A major challenge for this task was to find a new process for a dense and stable passivation layer, since the PECVD tool used for the standard MEA production in Mainz could not

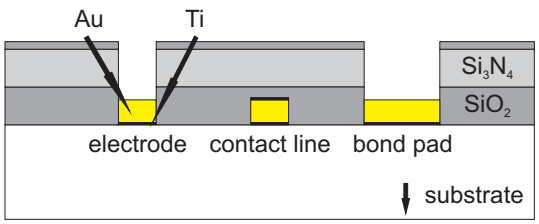

Figure A.1: Schematic of a standard gold MEA revealing the final layer structure of the electrodes, contact lines, and bond pads (not to scale).

be used anymore. The first two generations of IrO_x MEAs were produced and tested in the scope of a diploma thesis [123].

First MEA Generation

Existing gold MEAs which had already been fabricated a few years before (see Subsection A.1.1 and [129]) were subsequently cleaned and reprocessed to add an IrO_x layer to the electrode areas. Starting from the layer structure shown in Figure A.1, a third optical lithography was used to structure only the electrode areas for the SIROF deposition. A stack of approximately 20 nm titanium (adhesive layer) and 300 nm IrO_x was sputtered on the whole surface. A subsequent lift-off was used to remove the stack, leaving only the electrodes with a functional SIROF. The final layer structure of the modified MEAs is shown schematically in Figure A.2.

The sputtering of the amorphous IrO_x film was conducted in a first run by André van Ooyen at the *Institut für Werkstoffe der Elektrotechnik 1* (IWE1, Aachen, Germany) at RWTH Aachen University by reactive sputtering of iridium. It was done using a DC magnetron sputtering system (Nordiko NS 2550, Control Process Apparatus Inc., Fremont, USA) in argon and oxygen (Ar/O_2) plasma at room temperature with a six inch iridium disk of 99.9 % purity as described in [114]. The sputtering chamber was evacuated to $4 \cdot 10^{-6}$ mbar using a cryogenic pump, and a DC-power of 180 W was applied to the target. The gas flows were kept at 100 sccm (Ar) and 10 sccm (O_2), respectively, resulting in a chamber pressure of $1.4 \cdot 10^{-2}$ mbar. During sputtering, the oxygen partial pressure was measured with a Baratron gauge (MKS Instruments Inc., Andover, USA). Table A.2 shows the differences of the sputtering parameters in the process runs used for the various wafers in this thesis.

The chips resulting from this process were successfully used for stimulation experiments (see Section 5.1), but the SIROFs were not stable and sometimes detached from the electrodes. As a further disadvantage of this process, the number of available pre-processed wafers was strongly limited. More details about the chip process can be found in [123].

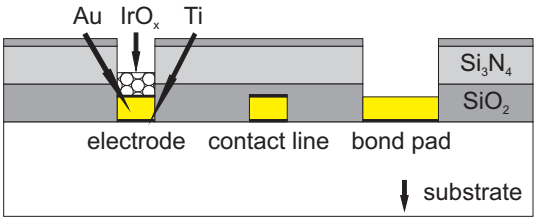

Figure A.2: Schematic of a first generation IrO_x MEA. The layer structure of the electrodes, contact lines, and bond pads is shown (not to scale). The chip process is described in the text.

sputtering run	Chip types (chip generations)	DC power (W)	Ar flow (sccm)	O_2 flow (sccm)	chamber pressure (mbar)
1^{st}	MEA 64 (1,2)	180	100	10	$1.40 \cdot 10^{-2}$
2^{nd}	MEA 64 (3) Mi-BeSAN MEA (3)	180	100	10	$1.70 \cdot 10^{-2}$
3^{rd}	MEA 64 (4) Mi-BeSAN MEA (4,5)	180	100	6.5	$1.57 \cdot 10^{-2}$
4^{th}	Mi-BeSAN MEA (5)	180	100	7	$1.58 \cdot 10^{-2}$
5^{th}	MEA 64 (4)	180	100	6	$1.23 \cdot 10^{-2}$

Table A.2: Differences in parameters of the sputtering processes used for the various 64-electrode MEA and Mi-BeSAN MEA wafers in this thesis.

Second MEA Generation

As a second approach, a complete new MEA process was started on four inch n-doped silicon <100> wafers (Si-Mat, Landsberg am Lech, Germany, see Table A.1) with a pre-processed wet oxide layer of 1 µm. The same steps for structuring of the electrodes (electrode diameters of 8, 10, 15, and 20 µm), contact lines, and bond pads were used as described above, but the metalization was thinner with a stack of 10 nm titanium, 200 nm gold, and again 10 nm titanium. In the next step, the SIROF was deposited in the same first sputtering run (see Table A.2) as the wafers from the first MEA generation. Here, the passivation was implemented at IWE1 with a layer of Parylen C, which was structured using a titanium hard mask and RIE with a *sulfur hexafluoride* (SF_6) plasma. However, the passivation layer of the resulting chips proved to be mechanically unstable and regularly detached after the first cell culture. Therefore, these chips were not used for any of the electrophysiological experiments in this thesis. For a more detailed description of the process and the characterization of the resulting MEAs, the reader is referred to Wallys [123].

Third MEA Generation

In order to overcome the problems with the Parylen C passivation and the detachment of the SIROFs, a third process was initiated on three different types of wafers: n-doped silicon <100> (Si-Mat), glass (Borofloat 33, Schott), and SiO_2 (SiO_2-z-kat, CrysTec GmbH, Berlin, Germany). For details about all wafer types used see Table A.1.

The structuring of the metal electrodes (same electrode diameters as in second generation), contact lines, and bond pads was done as described for the second generation. Then, the whole wafer was passivated with a stack of six alternating layers of PECVD nitride and oxide (NONONO stack, 150 nm Si_3N_4, 100 nm SiO_2, 150 nm Si_3N_4, 100 nm SiO_2, 150 nm Si_3N_4, and 200 nm SiO_2). This step was done by Detlev Cassel of our collaboration partner *Fachhochschule Kaiserslautern, Fachbereich Informatik und Mikrosys-*

temtechnik (Zweibrücken, Germany) and resulted in a dense and stable passivation layer, which was thoroughly characterized in another diploma thesis [131]. With a second optical lithography and RIE (CHF_3), the passivation was opened above the electrodes and the bond pads. A third optical lithography, a sputtering process, and a lift-off were used to deposit the IrO_x layer on the electrodes. To improve the long-term attachment on the metal electrodes, the SIROF stack was slightly modified. After sputtering the adhesive titanium layer (20 nm), a 150 nm thick platinum (Pt) layer was deposited to protect the titanium from the electrolyte solution, which can diffuse through the porous IrO_x and cause oxidation of the titanium. Finally, the IrO_x (300 nm) was sputtered by André van Ooyen at IWE1 in Aachen as described for the first generation (second sputtering run, Table A.2). A detailed process flow for this chip generation can be found in a diploma thesis [131]. Although the passivation layer of the resulting chips was dense and stable, they could still not be continuously used for electrophysiological measurements, because during usage of the chips for cell culture a detachment of the SIROF stack occurred.

Fourth MEA Generation

It was assumed that the detachment of the stack happened because of the SIROF deposition after the passivation layer, since the area for the stack deposition was slightly bigger than the electrode opening. Therefore, the sequencing of the passivation and SIROF stack deposition was changed for the fourth generation, which again was done on glass wafers (Borofloat 33, Schott, see Table A.1). Furthermore, the electrode size was changed to 50 µm for all electrodes to get chips for a high yield of possible stimulation experiments and defined experimental conditions. The masks used for processing of the electrodes are shown in Figure 3.6.

In the first step, the electrodes, contact lines, and bond pads were structured with an optical lithography, metalization and lift-off as described for the second chip generation. The SIROF stack was then deposited with a second lithography, a sputtering process (third run, Table A.2), and another lift-off as described for the third generation, with only the thickness of the platinum layer reduced to 100 nm. Then the complete wafer was passivated with a NONONO stack in Zweibrücken (again by Detlev Cassel as described for the third generation). The passivation was opened above the electrodes and the bond pads with a third optical lithography, resulting in the final layer structure which is depicted in figure (Figure A.3). Details about the different process steps can be found in the process flow for the third electrode generation [131].

This fourth generation of SIROF MEAs finally resulted in chips with a dense and stable passivation layer, as well as a stable SIROF stack. The chips could be used for stimulation experiments with a well defined experimental situation, where the stimulated cell is situated

Generation	Wafer size (mm)	Electrode sizes (µm)	Electrode material	Passivation material	Passivation as last step
0	125	6,8,10,20,30	Ti/Au	ONO	Yes
1	100	6,8,10,20,30	Ti/Au/Ti/IrO_x	ONO	No
2	100	8,10,15,20	Ti/Au/Ti/IrO_x	Parylen C	Yes
3	100	8,10,15,20	Ti/Au/Ti/Pt/IrO_x	NONONO	No
4	100	50	Ti/Au/Ti/Pt/IrO_x	NONONO	Yes

Table A.3: Differences in the processes for the five generations of MEAs used in this thesis.

completely on the device as described in Section 5.2. Therefore, several wafers of this MEA generation were processed for further usage (fifth sputtering run, Table A.2). A summary of the differences in the processes used for the production of gold and IrO_x MEAs is given in Table A.3.

A.1.3 Mi-BeSAN MEA Process

In the ongoing development of the process for the Mi-BeSAN chip (see Section 3.2), three different generations of Mi-BeSAN electrode wafers without FETs were processed to test the stability and stimulation capabilities of the SIROF microelectrodes. On each wafer, chips with the same three electrode designs (button, ring, and quad design, see Figure 3.18) were processed.

Third and Fourth Generation Mi-BeSAN MEA Process

The wafers of the first two iterations of Mi-BeSAN MEAs were processed at the same time, with the same process parameters, and on the same wafers as the standard 64-electrode MEAs of the third and fourth generation, and will therefore be called third and fourth generation Mi-BeSAN MEAs. For details about the processes, the reader is referred to Subsection A.1.2. Although the fourth generation MEAs with the standard 64-electrode design worked nicely for stimulation and were stable over several cell cultures, a detachment of the SIROF stack could still be found for the Mi-BeSAN MEAs, which were processed at the same time and with the same parameters.

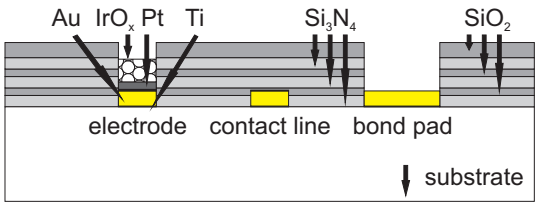

Figure A.3: Schematic of a fourth generation IrO_x MEA. The layer structure of the electrodes, contact lines, and bond pads is shown (not to scale). The chip process is described in the text.

Generation	Passivation as last step	Passivation opening smaller than electrode
3	No	No
4	Yes	No
5	Yes	Yes

Table A.4: Differences in the processes for the three generations of Mi-BeSAN MEAs developed in this thesis. For all three generations, a $Ti/Pt/IrO_x$ stack was deposited on the Ti/Au electrodes, and the passivation was achieved by a NONONO stack.

Fifth Generation Mi-BeSAN MEA Process

The reason for the detachment was assumed to originate in the mask design used for the Mi-BeSAN MEAs. The electrode opening through the passivation was done with a mask having the same electrode geometry as the masks, which were used for the SIROF stack deposition. Therefore, a very slight misalignment of the opening mask caused the exposure of the edges of the SIROF stack to the electrolyte solution. Thus, the titanium between gold and platinum could oxidize and cause the detachment of the whole stack.

To overcome this problem, a new mask with smaller openings for the electrodes was designed and used to open wafers, which were processed together with the fourth generation of chips. Besides the opening mask, all other process steps were identical, finally resulting in Mi-BeSAN MEAs of the fifth generation with a stable SIROF stack. For further tests, more Mi-BeSAN MEAs of this generation were processed on glass wafers (Borofloat 33, Schott, see Table A.1) with a fourth sputtering run (Table A.2). Details about the different process steps used for the MEA fabrication can again be found in the process flow for the third MEA generation [131]. A summary of the differences in the three Mi-BeSAN MEA generations can be found in Table A.4.

A.2 Mi-BeSAN Process

The Mi-BeSAN chip integrates planar FETs for recording and SIROF microelectrodes for stimulation of cells on one chip [131,137]. The process is, therefore, a combination of a FET process and an electrode process, as described in Section A.1. The FETs and electrodes are arranged in arrays of 4 × 4 sensor spots.

A.2.1 Mi-BeSAN FET Process

The processing of the planar p-type FET is based on a process including a planarization step with *local oxidation of silicon* (LOCOS) and selective etching [84, 137] on an <100> n-doped Si wafer (see Figure A.4). The wafers used for the process were supplied by two different companies (Si-Mat, Landsberg am Lech, Germany and Siltronic AG, München,

	Si	Si
Company	Siltronic	Si-Mat
Diameter	100 mm	100 mm
Thickness	$500 - 550$ µm	500 ± 25 µm
Orientation	<100>	<100>
Dopant	phosphorus(n)	phosphorus(n)
Resistivity	$2.5 - 8.5$ Ωcm	$1 - 10$ Ωcm

Table A.5: Different wafer types used for the complete Mi-BeSAN process.

Germany), and their characteristics are described in Table A.5.

At first, a stack of 30 nm thermal SiO_2 and 100 nm *low pressure chemical vapor deposition* (LPCVD) Si_3N_4 was prepared. With a first optical lithography, RIE (CHF_3), and a boron implantation, the conducting lines were defined and transferred to the stack. Then, the resist was removed by RIE using an oxygen plasma. Figure A.4.a shows a schematic of a cross section through the drain contact of a FET before this resist removal step.

In the second step, the gate plateau was defined with another optical lithography and RIE (CHF_3), leaving only the FETs' gate plateaus as elevated structures on the wafer (Figure A.4.b). Again, the resist was removed by RIE with oxygen plasma.

The planarization of the FET was achieved in three steps (Figure A.4.c). Firstly, the wafers were dry oxidized at 1000 °C to yield a local oxide growing everywhere on the wafer except on the gate areas (which were covered with the Si_3N_4). Additionally, this served as an annealing step for the boron implantation, because of the high temperature. The oxide thickness was determined by ellipsometry to an average thickness of 260 nm, with 44 % of the oxide grown into the silicon substrate and 56 % on top of it. Because of the growth of the oxide into the substrate, the implanted source and drain contacts moved downward deeper into the substrate, resulting in an elevated gate plateau in relation to the contact lines (first cross section in Figure A.4.c). Secondly, the local oxide was selectively etched down with 1 % hydrofluoric acid (HF) to the level of the gate-plateau oxide. Previously, the etch rate was investigated with test wafers, and the etching was done in several steps with repeated layer thickness and step height measurements using a surface profilometer or *atomic force microscopy* (AFM, center cross section in Figure A.4.c). Finally, the Si_3N_4 on the gate plateau was selectively etched with boiling *phosphoric acid* (H_3PO_4). After measurement of the achieved planarization by AFM, the remaining oxide was thinned to a 12 nm sacrificial layer (lowest cross section in Figure A.4.c).

In the next step (Figure A.4.d), the gate geometry including drain and source regions was defined with a third lithography and a second boron implantation (first cross section in Figure A.4.d). After removal of the resist by RIE with oxygen plasma, the wafers were cleaned, implantation was annealed, and the sacrificial oxide etched away with 1 % HF.

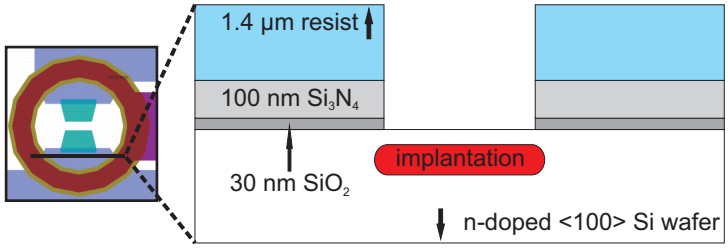

(a) Definition of contact lines.

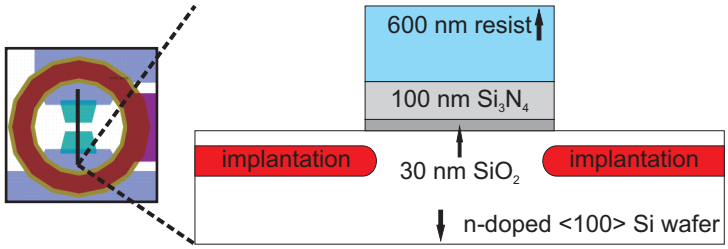

(b) Definition of gate plateau.

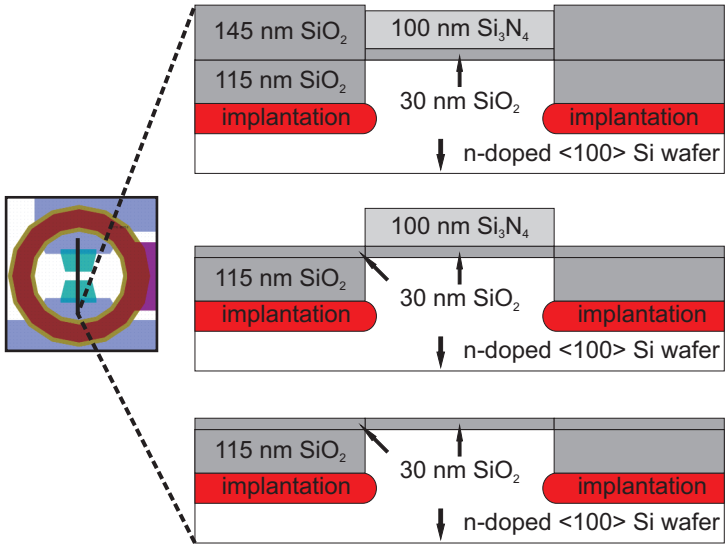

(c) Planarization.

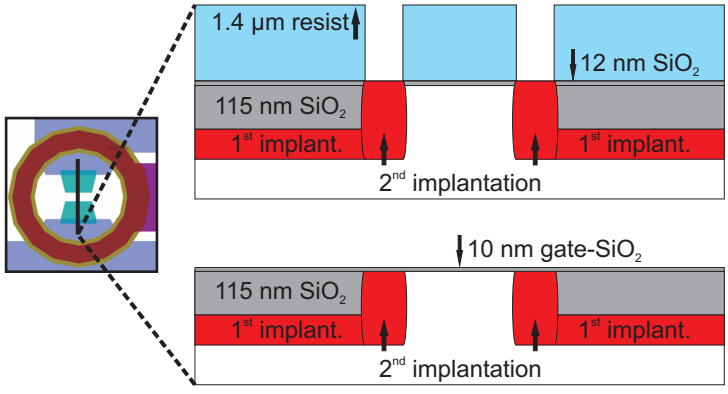

(d) Definition of gate geometry.

Figure A.4: Schematics of several cross sections during different steps in the Mi-BeSAN FET process (not to scale). (a) Contact line after first implantation before removal of resist. (b) Gate area after definition of the plateau before resist removal. (c) Gate area during three steps of planarization. After LOCOS (top), HF etch of LOCOS oxide (center), and selective etch of gate nitride (bottom). (d) Gate during definition of gate geometry. After implantation of drain and source areas (top), and growth of the gate oxide (bottom). The subsequent processing of the aluminum contacts is not shown in a cross section.

A 10 nm gate oxide was grown by dry oxidation (second cross section in Figure A.4.d) to finish the FET.

Finally, the implanted feed lines had to be contacted by aluminum contacts. Therefore, the SiO_2 passivation was opened with a fourth lithography and a wet etch with buffered 10 % HF. To apply the metal contacts to the implanted drain and source feed lines, a 150 nm aluminum layer was defined and deposited with a fifth lithography and a subsequent lift-off process, finishing the FET process. For more details about the FET process, the reader is referred to the complete process flow [131].

A.2.2 Mi-BeSAN Electrode Process

After finishing the FET process, the microelectrodes had to be processed on the planarized p-type FET. For this purpose, an electrode process very similar to the fifth generation Mi-BeSAN MEA process (see Subsection A.1.3) was used. The only differences to this process were:

- During the metalization, the aluminum contacts of the FET were also contacted to additional bond pads formed from the Ti/Au/Ti stack. Here, the titanium layer serves as an adhesive layer and additionally prevents alloying of gold and aluminum.
- After passivation of the chip surface with the NONONO stack, the electrodes and bond pads were not completely opened by RIE. Instead, the RIE was used to etch through the stack until the final Si_3N_4 layer. This final layer was then removed by selective etching with boiling H_3PO_4.
- In the same step, the passivation layer above the bond pads for the FETs was opened, too.

Appendix B

Packaging and Chip Cleaning

Sometimes life gives us lessons sent in ridiculous packaging.

Dar Williams (American singer-songwriter, 1967-)

The packaging or encapsulation of all chips used in this thesis is based on previous encapsulation protocols used with *multi-electrode arrays* (MEAs) and *field-effect transistor* (FET) chips [18, 122]. It is accomplished using a *flip chip* method [170] and differs only slightly for MEAs and Mi-BeSAN chips. In the first section, the complete encapsulation process will be explained for the MEA chips. The second section will explain the differences in the packaging of the Mi-BeSAN chips. Finally, the last section will introduce the cleaning procedure, which is repeatedly used to clean and prepare the chips before each cell culture.

B.1 Packaging of MEAs

After cutting the fully processed wafer, the MEA chips with a size of 11 mm × 11 mm were cleaned to remove any residues from processing by five minutes of sonication in a mixture of each 50 % (v/v) ethanol and acetone. The chips were mounted with a flip chip process (Figure B.1) to the backside of 1 mm thick PCB carriers (WI-KA GmbH, Baesweiler, Germany). The PCB carriers have an area of 24 mm × 24 mm, a circular opening in the center with a diameter of 9 mm, and 68 bond pads with contact lines of galvanized gold. The electrical contact between the bond pads on the chips and the carriers was formed by precisely printing a conductive two-component silver glue (Epo-Tek H20E-PFC, Polytec GmbH, Waldbronn, Germany) on the contact areas of the carrier using a laser perforated foil in a screen printer (SP-002, Essemtec AG, Aesch, Switzerland). Chips and carriers were then aligned and glued together using a precise X-Y positioning system (Fineplacer 96, Finetech GmbH & Co. KG, Berlin, Germany). The glue was cured at 150 °C for one

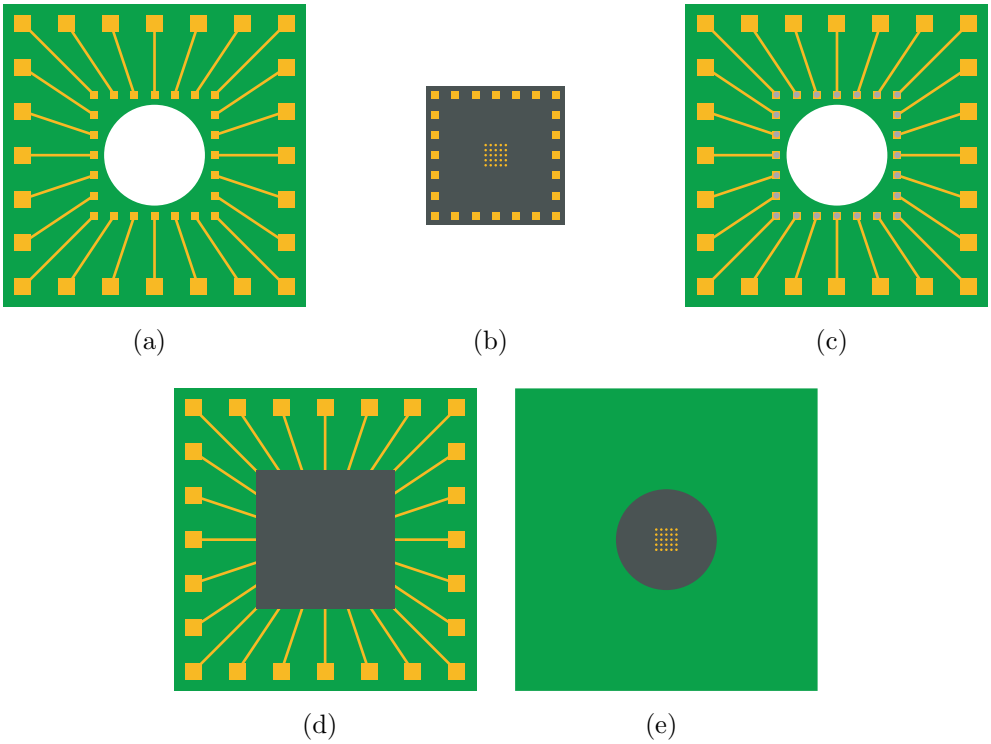

Figure B.1: Schematic of the flip chip procedure used to establish contact between the backside of the carrier (a) and the front of the chip (b). Silver glue is applied to the bond pads of the carrier (c), and the chip is glued with its top side to the backside of the carrier. After curing the glue, the chip is tightly attached to the carrier (backside (d) and front view (e)) and can be further encapsulated.

hour. Photographs of the screen printer with printing foil and the Fineplacer can be seen in Figure B.2.

To prevent shortcuts between the silver glue spots, the gaps between the contacts were filled with a dielectric two component underfill (Epo-Tek U300, Polytec), which was applied around the chip edges, drawn into the cleft by capillary forces, and cured for one hour at 150 °C. A petri-dish for the cell culture was formed on the chip by two glass rings with inner diameters of 7 mm and 16 mm and filling the space between the two rings (Figure B.3). Depending on the later use of the chips, both gluing and filling is done in two steps either with *polydimethylsiloxane* (PDMS) (Sylgard 96-083, Dow Corning Co., Midland, USA) or an epoxy resin (Epo-Tek 302-3M, Polytec). The epoxy resin is usually preferred, since in comparison to the PDMS, it results in a stiffer and more stable encapsulation without any significant swelling when in contact with electrolyte solutions. The PDMS was only utilized if the chips should be used with the HL-1 cell line, which does not grow on chips encapsulated with the epoxy resin. The curing was done for at least one hour in each step at 80 °C or 150 °C for epoxy resin or PDMS, respectively. The resulting free area for cell culture on the chips is 38.5 mm^2, and the culture dish holds approximately 600 µl of

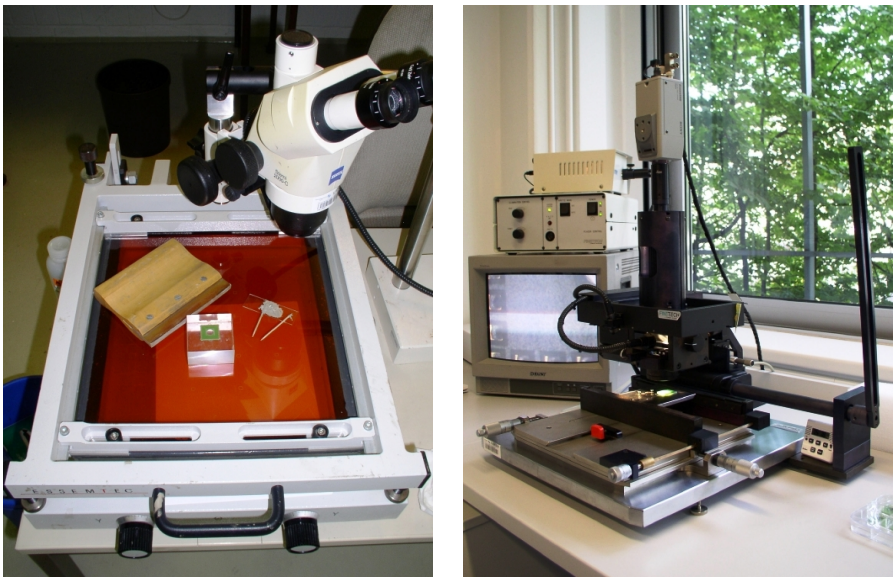

(a) (b)

Figure B.2: Photographs of screen printer (a) and Fineplacer (b) used for the flip chip process of the encapsulation procedure.

culture medium. In the filling step, a label with the chip name is usually added and sealed on the carrier surface between the glass rings. Finally, the edges of the chip on the backside of the carrier were sealed with epoxy resin or PDMS to protect the underfill from ethanol applied to the chip during the cleaning procedure.

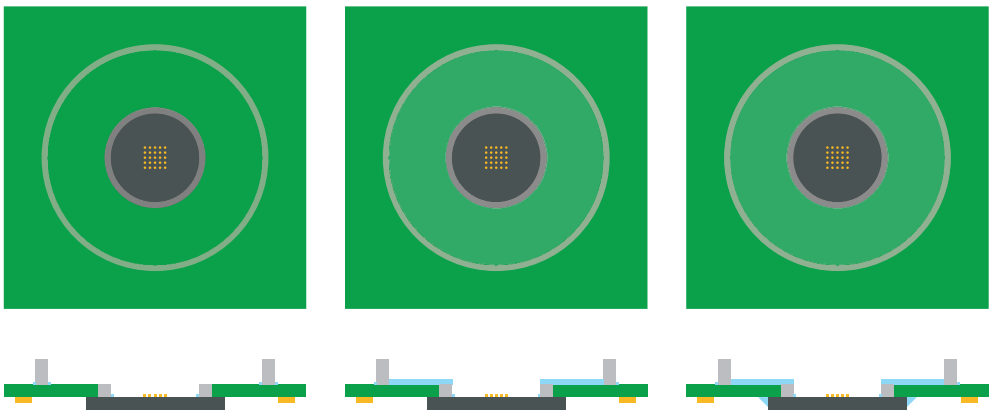

(a) (b) (c)

Figure B.3: Schematic of the encapsulation process for MEAs. After application and curing of the underfill, two glass rings are glued to the surface of the carrier and the chip (a), and the interspace is covered with epoxy resin or PDMS (b). Finally, the underfill and the edges of the chip are protected with epoxy resin or PDMS from underneath (c).

B.2 Packaging of Mi-BeSAN Chips

The packaging procedure of the Mi-BeSAN chips is almost identical to the procedure described for MEAs, including the flip chip procedure as a first step. The only differences in the packaging originate from the reduced chip size. Since the Mi-BeSAN chips are only 8.3 mm × 8.3 mm in size, the PCB chip carriers were produced with an inner opening diameter of 6 mm. Therefore, the inner glass ring had to be replaced by a different inner boundary with a reduced diameter. To still allow for patch-clamp experiments in the limited space between this boundary and underneath an immersed microscope objective, custom funnels made from either another PDMS (Sylgard 184, Dow Corning) or epoxy resin with a lower inner diameter of 2.8 mm were used instead of the glass rings. To keep the opening as big as possible for the approach with the patch pipette, the inner opening of the carrier was provided with a countersunk incline, so that the funnel could be glued directly on the chip surface without touching the carrier. Finally, the filling of the space between outer glass ring and inner funnel with PDMS or epoxy resin is carefully done, starting from the space between the funnel and the carrier. The remaining steps and parameters of the packaging remain unchanged, resulting in 6.2 mm^2 free area for cell culture, and approximately 600 µl volume for culture medium. To visualize the differences in the encapsulation procedure, a schematic view for Mi-BeSAN chips is given in Figure B.4.

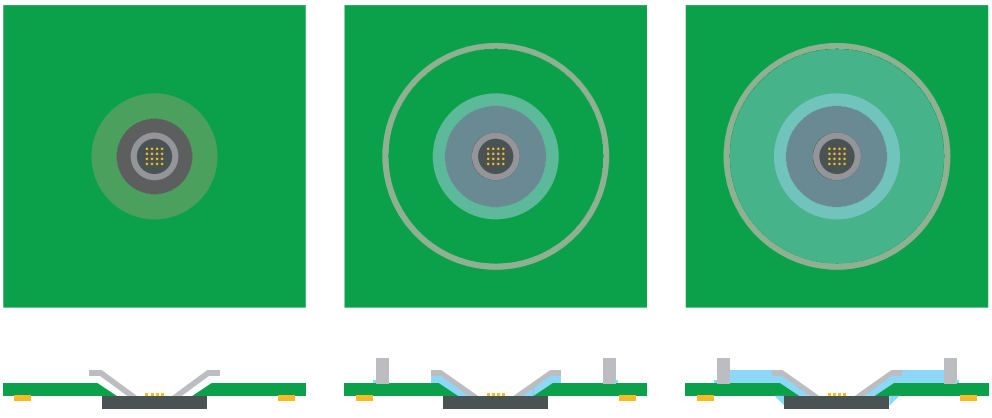

Figure B.4: Schematic of the encapsulation process for Mi-BeSAN chips. After application and curing of the underfill, a custom-made funnel is glued to the surface of the chip (a). In the next step, the space between funnel and carrier is filled up with PDMS or epoxy resin, and an outer glass ring is glued to the carrier (b). Finally, the space between glass ring and funnel is filled and the edges of the chip are protected with epoxy resin or PDMS (c).

B.3 Chip Cleaning Procedure

The encapsulated chips with culture chamber can be used and cleaned repeatedly for culturing cells. The cleaning procedure is identical for all chip types used in this work. It was adapted from Offenhäusser et al. [18, 122] with slight modifications.

As a first cleaning step, crude contaminations such as remains from previous cell cultures are mechanically removed from the chip surface by roughly rubbing the interior of the cell culture dish on the chip with cotton swaps soaked in 70 % (v/v) ethanol. In a second step, the complete chip including the carrier is sonicated in a detergent solution (2 % (v/v) Hellmanex II, Hellma GmbH, Müllheim, Germany) for five minutes. Afterwards, the detergent is rinsed off with deionized water. The whole chip is sonicated in bi-distilled water for additional five minutes, and dried with a nitrogen gun.

Appendix C

Cell Culture Protocols, Solutions, and Chemicals

Labels are your friends!

Vanessa Maybeck (American scientist, colleague, and friend, 1982-)

In the following sections, the cell culture protocols including the used solutions and chemicals will be introduced. The first three sections will each deal with the protocols used for one particular type of electrogenic cell, while the final two sections present a general list of all chemicals and recipes for the solutions used for cell culture.

C.1 Cortical Rat Neurons

This section introduces the culture conditions and protocols for cortical rat neurons, which were used as a model system to investigate the stimulation of vertebrate neurons. At the end of the section, the preparation of the cells for SEM imaging is introduced.

Chip Activation and Protein Coating

After performing the cleaning procedure (see Section B.3), the chip surface was activated by an oxygen plasma to form OH groups for better adhesion of the protein coating. The activation was done within a plasma chamber (PICO, Diener electronic GmbH & Co. KG, Nagold, Germany) at a pressure of 0.7 mbar and 40 % of maximum power.

The chips were sterilized with ultraviolet light for 30 minutes under a sterile bench. To promote adhesion of the neurons to the substrate, the sensor area of the chips was incubated for one hour with 50 µl of a solution of 10 µg/ml *poly-D-lysine* (PDL) and 100 µg/ml

extracellular matrix (ECM) gel in *Gey's Balanced Salt Solution* (GBSS). Afterwards, the protein solution was removed, and the chips were rinsed once with GBSS.

Cell Isolation, Preparation, and Culture

Rat embryonic cortical neurons were obtained from embryos of pregnant Wistar rats at 18 days gestation (E18) as described before [171]. Cortices were dissected from the embryonic brains and cooled in 1 ml *Hank's Balanced Salt Solution* (HBSS) without Ca^{2+} and Mg^{2+} ($HBSS^{-}$), 0.035 % $NaHCO_3$, 1 mmol/l sodium pyruvate, 10 mmol/l HEPES, and 20 mmol/l glucose at a pH-value of 7.3. The cells were mechanically dissociated by trituration with a fire-polished siliconized Pasteur pipette to avoid cell adhesion to the walls of the pipette. Afterwards, 2 ml $HBSS^{+}$ (with Ca^{2+} and Mg^{2+}, supplemented as above) were added.

Non-dispersed tissue was allowed to settle for three minutes, and the neuron-containing supernatant was centrifuged at 200 g for two minutes at room temperature. The pellet was resuspended in 1 ml supplemented *Neurobasal* (NB) medium (see Table C.4) per hemisphere isolated. An aliquot was diluted 1:4 with trypan blue (0.4 % solution), and dye-excluding cells were counted in a Neubauer counting chamber.

The remaining cells were diluted in supplemented NB medium, and 20,000 to 100,000 cells (depending on chip type and desired culture density) were plated in 50 µl medium on the sensitive area of each chip. After one hour incubation time at 37 °C and 5 % CO_2 atmosphere, the chips were filled up with 600 µl of supplemented NB medium.

After four hours, half a cover slip with a 7 DIV co-culture of rat cortical neurons was placed in the culture dish for Mi-BeSAN chips ("second floor culture") to supply neuronal growth factors and to increase the number of cells in the culture. This was not necessary for standard *multi-electrode arrays* (MEAs), since the chip area available for cell culture is significantly larger (see Appendix B). The chips with cells were kept at 37 °C and 5 % CO_2 atmosphere in a humidified chamber, and half of the culture medium was exchanged every two to three days.

Electrophysiological Measurements

The co-culture cover slips were removed directly before the electrophysiological experiments, and the cell culture medium was replaced by an extracellular recording solution (see Table C.2). For each individual chip, using an osmometer (Osmomat 030, GONOTEC GmbH, Berlin, Germany), the osmolality of the recording solution was adjusted to the osmolality of the culture medium with glucose. Micropipettes with resistances of $4 - 10$ MΩ were pulled from fire-polished borosilicate glass (BF150-86-10, Sutter Instrument Co., Novato, USA) using a laser pipette puller (P-2000, Sutter Instrument) and filled with an

intracellular recording solution (see Table C.2). Standard whole-cell patch-clamp recordings were conducted using a patch-clamp amplifier (EPC 10 Double, HEKA Elektronik) with Ag/AgCl wires in the pipette and within the bath solution. The silver wire in the bath solution was kept at ground potential during the measurements. The pipette capacitances were compensated after formation of the cell-attached configuration, and the membrane capacitances, series resistances, and leakage currents were compensated after establishment of the whole-cell mode.

Cell Fixation

The preparation of rat cortical neurons for SEM imaging was adapted from Wrobel et al. [82] with slight modifications. The cells were taken from the same preparation and kept under identical culture conditions as described above, but they were cultured on unencapsulated chips in petri dishes. In this case, the co-culture was not necessary, since the number of neurons in each well was high enough to support neuronal growth.

For SEM imaging, the wells were first rinsed with 37 °C warm *phosphate buffered saline* (PBS), then the cells were fixed with 3.4 % (v/v) glutaraldehyde in 20 mmol/l HEPES buffer (pH 7.3 adjusted with NaOH) for three hours. The wells were rinsed with Milli-Q water (Millipore, Billerica, USA) and serially dehydrated with increasing concentrations of isopropanol in Milli-Q water (30 % (v/v) and 50 % (v/v) for ten minutes each, 70 % (v/v) for at least 12 hours, 90 % (v/v) and 95 % (v/v) for ten minutes again, and finally 100 %). Before introducing the samples to the SEM (LEO1550, Carl Zeiss SMT AG, Oberkochen, Germany) they were removed from the isopropanol, dried in air, and finally coated with a $10 - 20$ nm thick gold layer by sputtering (SCD004 Sputter Coating Unit, Balzers AG, Liechtenstein).

C.2 HEK293 Cell Line

The *Human Embryonic Kidney 293* (HEK293) cell line used in this study stably expresses the $Na_V1.4$ voltage-gated fast sodium channel from rat skeletal muscle [160]. It was stably transfected [161] and provided to us by the group of Prof. Heinemann from the University of Jena.

Chip Activation and Protein Coating

To prepare chips for the culture of HEK293 cells, the same procedures for cleaning, activation, and sterilization of the chips were used as for cortical rat neurons (see Section C.1). Afterwards, the chip surface was coated with 50 µl of a solution of 100 µg/ml *poly-L-lysine*

(PLL) in bi-distilled water by incubation for one hour to improve the cell adhesion. The protein solution was removed, and the chips were rinsed once with PBS.

Cell Culture

The HEK293 cell line was cultured as described before for another HEK293 cell line expressing a different ion channel [96]. The cells were grown in M10 medium (see Table C.5) in T-flasks at 37 °C and 5 % CO_2 atmosphere in a humidified chamber. The antibiotic G418 was added in a concentration of 1 µl/ml as a selection marker to eliminate the non-transfected cells. The medium was replaced with fresh M10 every second day.

The cells were split once or twice per week, when they had proliferated to a roughly 80 % confluent layer. For splitting, the cells were detached from the culture dish by application of a solution containing 0.5 mg/ml trypsin and 0.2 mg/ml EDTA for five minutes at 37 °C. The trypsinisation was stopped by adding 5 ml M10 medium. The solution containing the detached cells was centrifuged for five minutes at 200 g. After centrifugation, the supernatent was removed and the cell pellet was resuspended in 1 ml of fresh M10 medium. Finally, $50 - 100$ µl of the cell suspension were seeded in a new T-flask.

For plating on the coated chips, the cell concentration in the remaining suspension was determined with a Neubauer counting chamber. Cells were plated in 50 µl M10 medium with G418 selection marker at densities of 10,000 to 40,000 cells per chip. After four hours of initial adhesion, the chips were filled with 600 µl of M10 medium, and then kept at 37 °C and 5 % CO_2 in a humidified chamber. Medium was exchanged daily.

Electrophysiological Measurements

The HEK293 cells were kept in culture for two to five days until the measurements were performed. Like the experiments with the cortical rat neurons, the cell culture medium was replaced by the same extracellular recording solution directly before the electrophysiological experiments. Again, the osmolality of the recording solution was adjusted to the osmolality of the culture medium with glucose. The same equipment, parameters, and protocols were used for micropipette preparation and patch-clamp experiments.

C.3 HL-1 Cell Line

The HL-1 cell line (Louisiana State University Health Science Center, New Orleans, USA), was derived from AT-1 cells (mouse cardiac myocyte tumor) and represents a hybrid between embryonic and adult myocytes [167]. The cell line can be used as a model system for extracellular recordings, since the cells are easy to culture, spread as a syncytium across

the whole chip surface, and generate synchronized APs with high extracellular signal amplitudes.

Chip Activation and Protein Coating

Again, the same procedures for cleaning, activation, and sterilization of the chips were used as for cortical rat neurons and HEK293 cells. The protein coating for the HL-1 cells was done by incubation of the chip surface with 50 µl of a solution of 0.2 % (v/v) gelatin together with 5 µg/ml fibronectin in bi-distilled water for one hour. The protein solution was removed, and the chips were rinsed once with PBS.

Cell Culture and Extracellular Recordings

The cell line was also cultured in T-flasks with supplemented Claycomb medium (see Table C.6) at 37 °C and 5 % CO_2 atmosphere in a humidified chamber with daily medium exchange. Whenever the cells had profilerated to confluence, they were split as descibed for HEK293 cells (see Section C.2).

Approximately 50,000 to 100,0000 cells were plated on each chip in a volume of 50 µl medium. The culture dish was filled with 600 µl of supplemented Claycomb medium after four hours of initial adhesion. The culture medium was changed daily until the measurements were performed. This was always done after cells reached confluence on the chip surface, usually at DIV 2 to 4. Approximately two hours before the measurement, the medium was exchanged by fresh supplemented Claycomb medium.

C.4 List of Chemicals

The chemicals used for all cell culture related protocols are listed here and were supplied by one of the following companies:

- Carl Roth GmbH & Co. KG, Karlsruhe, Germany (Roth)
- Honeywell Riedel-de Haën, Seelze, Germany (Riedel-de Haën)
- Invitrogen GmbH, Karlsruhe, Germany (Invitrogen)
- Merck KGaA, Darmstadt, Germany (Merck)
- Sigma-Aldrich Chemie GmbH, Taufkirchen, Germany (Sigma-Aldrich)

Table C.1: List of chemicals used for cell culture with rat cortical neurons and cell lines.

Reagent	Supplier
ascorbic acid	Sigma-Aldrich
B27 supplement	Invitrogen
$CaCl_2$	Sigma-Aldrich
Claycomb medium	Sigma-Aldrich
ECM gel	Sigma-Aldrich
EGTA	Sigma-Aldrich
Ethanol	Riedel-de Haën
fetal bovine serum	Invitrogen
fetal calf serum	Invitrogen
fibronectin	Sigma-Aldrich
G418	Invitrogen
GBSS	Sigma-Aldrich
gelatin	Sigma-Aldrich
gentamicin	Sigma-Aldrich
glucose	Sigma-Aldrich
glutaraldehyde	Sigma-Aldrich
$HBSS^+$	Invitrogen
$HBSS^-$	Invitrogen
HEPES	Sigma-Aldrich
isopropanol	Merck
KCl	Sigma-Aldrich
KH_2PO_4	Roth
KOH	Sigma-Aldrich
L-glutamine	Sigma-Aldrich
MEM	Sigma-Aldrich
Mg-ATP	Sigma-Aldrich
$MgCl_2$	Sigma-Aldrich
Na_2HPO_4	Roth
NaCl	Sigma-Aldrich
$NaHCO_3$	Merck
NaOH	Sigma-Aldrich
Neurobasal medium	Invitrogen
non-essential amino acids	Invitrogen
norepinephrine	Sigma-Aldrich

Table C.1: List of chemicals (continued).

Reagent	Supplier
PDL	Sigma-Aldrich
penicillin/streptomycin	Sigma-Aldrich
PLL	Sigma-Aldrich
sodium pyruvate	Sigma-Aldrich
trypan blue	Sigma-Aldrich
trypsin EDTA	Sigma-Aldrich

C.5 Solutions

Patch-Clamp and Buffer Solutions

Reagent	Extracellular concentration (mmol/l)	Intracellular concentration (mmol/l)
NaCl	125	2
KCl	3	120
$MgCl_2$	1	4
HEPES	10	5
$CaCl_2$	2	-
EGTA	-	0.2
Mg-ATP	-	0.2

Table C.2: Recipe for extra- and intracellular patch-clamp solutions used for HEK293 cells and cortical rat neurons. The reagents were dissolved in bi-distilled water, and the pH-value was adjusted to 7.4 with NaOH for extracellular and with KOH for intracellular solution.

Reagent	Concentration (mmol/l)
NaCl	137
KCl	2.7
Na_2HPO_4	8.1
KH_2PO_4	1.47

Table C.3: Recipe for phosphate buffered saline (PBS). The reagents were dissolved in bi-distilled water, and the pH-value was adjusted to 7.4 with NaOH.

Cell Culture Media

Ingredient	Concentration
B27 supplement	1 % (v/v)
L-glutamine	0.5 mmol/l
gentamicin	50 µg/ml

Table C.4: Recipe for supplemented Neurobasal medium for rat cortex cells. The medium was prepared by adding the listed ingredients to Neurobasal medium.

Ingredient	Concentration
fetal calf serum	10 % (v/v)
non-essential amino acids	1 % (v/v)
penicillin	100 units/ml
streptomycin	100 µg/ml
L-glutamine	2 mmol/l

Table C.5: Recipe for M10 medium for HEK293 cells. The medium was prepared by adding the listed ingredients to *minimal essential medium* (MEM).

Ingredient	Concentration
fetal bovine serum	10 % (v/v)
penicillin	100 units/ml
streptomycin	100 µg/ml
norepinephrine	0.1 mmol/l
ascorbic acid	0.3 mmol/l
L-glutamine	2 mmol/l

Table C.6: Recipe for supplemented Claycomb medium for HL-1 cells. The Claycomb medium is conditioned by addition of the listed ingredients.

Appendix D

MATLAB Code

> Measuring programming progress by lines of code is like measuring aircraft building progress by weight.
>
> *Bill Gates (American entrepreneur and founder of Microsoft, 1955-)*

The MATLAB code used for the simulation of stimulation experiments is printed in this appendix. The code includes all equations for the complex impedance values and frequency responses of the various elements of the equivalent electronic circuit (see Subsection 2.5.2). Furthermore, the calculation of the Fourier transform and the filter effect of the amplifier system are incorporated. In addition, the experimental and pulse parameters from the stimulation experiment that was simulated as described in Subsection 5.2.1 are included, as well. With these parameters and equations, the change of the intracellularly recorded filtered signal (v_P), the potential changes at the attached and free membrane (v_{AM} and v_{FM}, respectively), and the potential change at the reference electrode and electrolyte solution (v_E) can be numerically calculated for any defined stimulation pulse (v_S).

```
function StimSim

% define simulation parameters

% stimulation electrode
Qs1 = 27.98E-9;             % 1st stim. electrode CPE magnitude (F)
ns1 = 0.6988;               % 1st stim. electrode CPE exponent
Rs1 = 56.9E6;               % 1st stim. electrode resistance (Ohm)
Qs2 = 40.99E-9;             % 2nd stim. electrode CPE magnitude (F)
ns2 = 0.7153;               % 2nd stim. electrode CPE exponent
Rs2 = 4.01E9;               % 2nd stim. electrode resistance (Ohm)
As = 1963;                  % stim. electrode area (1963um^2 (d=50um))

% reference electrode and electrolyte
Qre = 1.24E-3;              % ref. electrode CPE magnitude (F)
nre = 0.7967;               % ref. electrode CPE exponent
Rre = 25.49E3;              % ref. electrode resistance (Ohm)
Rel = 9E3;                  % electrolyte resistance (Ohm)

% cell and contact area
Cm = 16.94E-12;             % cell membrane capacitance (F)
cm = 10E-15;                % spec. membrane capacitance (10fF/um^2)
Am = Cm/cm;                 % whole cell membrane area (um^2)
Acs = 400;                  % covered electrode area (um^2)
Aam = 800;                  % attached membrane area (um^2)
alpha = Aam/Am;             % ratio of attached to whole membrane
beta = Acs/As;              % ratio of covered to whole electrode
Rj = 0.22E6;                % junction resistance (Ohm)

% amplifier lowpass filter
fn = 2;                     % filter order
fco = 6500;                 % filter cuttoff frequency (Hz)
Rp = 5.2;                   % passband ripple (dB)

% additional calculated parameters
Cam = alpha*Cm;             % adhered cell membrane capacitance
Cfm = (1-alpha)*Cm;         % free cell membrane capacitance
```

```
% basic parameters and vectors in time and frequency domain

% sampling and time parameters for simulation
Fs = 1E6;                   % sampling frequency for simulation (Hz)
wholeT = 0.4;               % whole length simulated signal (s)
t = (1/Fs:1/Fs:wholeT);     % time vector (s)

% stimulation pulse parameters
Vs0 = 0.20;                 % stimulation pulse amplitude (V)
pDelay = 5E-3;              % delay before pulse (s)
pLength = 2E-3;             % pulse phase length (s)
dbins = Fs*pDelay;          % number of bins for delay
pbins = Fs*pLength;         % number of bins for pulse phase
fbins = Fs*(wholeT-(pDelay+pLength));   % remaining bins

% stimulation pulse generation (single monophasic rectangular pulse)
vs = [zeros(1,dbins) ones(1,pbins) zeros(1,fbins)]; % pulse shape
vs = Vs0*vs;                % signal amplitude

% two-sided frequency vector for frequency response calculation
f = [(0:1/wholeT:Fs/2) ((-Fs/2+1/wholeT):1/wholeT:-1/wholeT)];

% complexe impedance vectors in the frequency domain

% whole electrode impedance
Xs = Rs1./(1+(i*2*pi*f).^ns1*Qs1*Rs1)+Rs2./(1+(i*2*pi*f).^ns2*Qs2*Rs2);

% covered electrode impedance
Xcs = Xs./beta;

% free electrode impedance
Xfs = Xs./(1-beta);

% impedance of reference electrode and electrolyte
Xe = Rel + Rre./(1+(i*2*pi*f).^nre*Rre*Qre);
```

```
% cell impedance (including seal resistance)
Xc = Rj./(1+i*2*pi*f*Rj*Cam*Cfm./(Cam+Cfm));

% stimulator-cell impedance
Xsc = (Xcs+Xc).*Xfs./(Xcs+Xc+Xfs);

% calculate complex frequency responses in the frequency domain

% voltage drop at bath electrode and electrolyte
He = Xe./(Xe+Xsc);

% voltage drop at subcircuit
Hsc = Xsc./(Xe+Xsc);

% voltage drop at cell membrane (capacitance and seal resistance)
Hc = Hsc.*Xc./(Xc+Xcs);

% voltage drop at attached cell membrane (inverted voltage)
Ham = (-1)*Hc.*Cfm./(Cfm+Cam);

% voltage drop at free cell membrane
Hfm = Hc.*Cam./(Cfm+Cam);

% whole recorded voltage drop
Hm = He + Hfm;

% fourier tranform into frequency domain
Vs = fft(vs,length(vs))/length(vs); % DFT with normalization

% calculation of results by multiplication in frequency domain
Ve = Vs.*He;        % voltage at ref. electrode and electrolye
Vam = Vs.*Ham;      % voltage at attached membrane
Vfm = Vs.*Hfm;      % voltage at free membrane
Vm = Vs.*Hm;        % whole recorded voltage
```

```
% inverse fourier transform into time domain (iDFT)
ve = ifft(Ve,length(Ve))*length(Ve);
vam = ifft(Vam,length(Vam))*length(Vam);
vfm = ifft(Vfm,length(Vfm))*length(Vfm);
vm = ifft(Vm,length(Vm))*length(Vm);

% filter at patch pipette in time domain
[b,a] = cheby1(fn,Rp,2*fco/Fs);     % generate filter coefficients
vp = filter(b,a,vm);                % filter data
```

Bibliography

A lot of people ask me if I were shipwrecked, and could only have one book, what would it be? I always say: 'How to Build a Boat'!

Stephen Wright (American actor and writer, 1955-)

[1] Kandel, E. R., Schwartz, J. H., and Jessell, T. M. (2000) *Principles of Neural Science*. McGraw-Hill, 4th edition.

[2] Seeman, B. and Barry, J. E. (1967) *The Story of Electricity and Magnetism*. Harvey House.

[3] Enderle, J., Blanchard, S., and Bronzino, J. (2005) *Introduction to Biomedical Engineering*. Elsevier, 2nd edition.

[4] Malmivuo, J. and Plonsey, R. (1995) *Bioelectromagnetism: Principles and Applications of Bioelectric and Biomagnetic Fields*. Oxford University Press.

[5] Kirby, R. S. (1990) *Engineering in History*. Courier Dover Publications.

[6] Hodgkin, A. L., Huxley, A. F., and Katz, B. (April 1952) Measurement of current-voltage relations in the membrane of the giant axon of loligo. *The Journal of Physiology*, 116 (4), 424–448.

[7] Hodgkin, A. L. and Huxley, A. F. (April 1952) Currents carried by sodium and potassium ions through the membrane of the giant axon of loligo. *The Journal of Physiology*, 116 (4), 449–472.

[8] Hodgkin, A. L. and Huxley, A. F. (April 1952) The components of membrane conductance in the giant axon of loligo. *The Journal of Physiology*, 116 (4), 473–496.

[9] Hodgkin, A. L. and Huxley, A. F. (April 1952) The dual effect of membrane potential on sodium conductance in the giant axon of loligo. *The Journal of Physiology*, 116 (4), 497–506.

[10] Hodgkin, A. L. and Huxley, A. F. (August 1952) A quantitative description of membrane current and its application to conduction and excitation in nerve. *The Journal of Physiology*, 117 (4), 500–544.

[11] Neher, E. and Sakmann, B. (1976) Single-channel currents recorded from membrane of denervated frog muscle-fibers. *Nature*, 260 (5554), 799–802.

[12] Thomas, C. A., Springer, P. A., Okun, L. M., Berwaldn, Y., and Loeb, G. E. (1972) Miniature microelectrode array to monitor bioelectric activity of cultured cells. *Experimental Cell Research*, 74 (1), 61–66.

[13] Gross, G., Rieske, E., Kreutzberg, G., and Meyer, A. (November 1977) A new fixed-array multi-microelectrode system designed for long-term monitoring of extracellular single unit neuronal activity in vitro. *Neuroscience Letters*, 6 (2-3), 101–105. ISSN 0304-3940.

[14] Bergveld, P. (January 1970) Development of an ion-sensitive solid-state device for neurophysiological measurements. *IEEE Transactions on Biomedical Engineering*, 17 (1), 70–71.

[15] Bergveld, P. (September 1972) Development, operation, and application of the ion-sensitive field-effect transistor as a tool for electrophysiology. *IEEE Transactions on Biomedical Engineering*, 19 (5), 342–351.

[16] Bergveld, P., Wiersma, J., and Meertens, H. (March 1976) Extracellular potential recordings by means of a field effect transitor without gate metal, called OSFET. *IEEE Transactions on Biomedical Engineering*, 23 (2), 136–144.

[17] Fromherz, P., Offenhäusser, A., Vetter, T., and Weis, J. (1991) A neuron-silicon junction: A retzius cell of the leech on an insulated-gate field-effect transistor. *Science*, 252 (5010), 1290–1293.

[18] Offenhäusser, A., Sprössler, C., Matsuzawa, M., and Knoll, W. (1997) Field-effect transistor array for monitoring electrical activity from mammalian neurons in culture. *Biosensors & Bioelectronics*, 12 (8), 819–826.

[19] Steinhoff, G., Baur, B., Wrobel, G., Ingebrandt, S., Offenhäusser, A., Dadgar, A., Krost, A., Stutzmann, M., and Eickhoff, M. (January 2005) Recording of cell action potentials with AlGaN/GaN field-effect transistors. *Applied Physics Letters*, 86 (3), 033901.

[20] Dankerl, M., Eick, S., Hofmann, B., Hauf, M., Ingebrandt, S., Offenhäusser, A., Stutzmann, M., and Garrido, J. A. (September 2009) Diamond transistor array for extracellular recording from electrogenic cells. *Advanced Functional Materials*, 19 (18), 2915–2923.

[21] Patolsky, F., Timko, B. P., Yu, G., Fang, Y., Greytak, A. B., Zheng, G., and Lieber, C. M. (August 2006) Detection, stimulation, and inhibition of neuronal signals with high-density nanowire transistor arrays. *Science*, 313 (5790), 1100–1104.

[22] Timko, B. P., Cohen-Karni, T., Yu, G., Qing, Q., Tian, B., and Lieber, C. M. (February 2009) Electrical recording from hearts with flexible nanowire device arrays. *Nano Letters*, 9 (2), 914–918.

[23] Eschermann, J. F., Stockmann, R., Hueske, M., Vu, X. T., Ingebrandt, S., and Offenhausser, A. (2009) Action potentials of HL-1 cells recorded with silicon nanowire transistors. *Applied Physics Letters*, 95 (8), 083703.

[24] Eversmann, B., Jenkner, M., Hofmann, F., Paulus, C., Brederlow, R., Holzapfl, B., Fromherz, P., Merz, M., Brenner, M., Schreiter, M., Gabl, R., Plehnert, K., Steinhauser, M., Eckstein, G., Schmitt-Landsiedel, D., and Thewes, R. (December 2003) A 128x128 CMOS biosensor array for extracellular recording of neural activity. *IEEE Journal of Solid-State Circuits*, 38 (12), 2306–2317.

[25] Schindler, M. (2008) *Design of a High Density CMOS Array for the Bidirectional Coupling with Electrogenic Cells*. Ph.D. thesis, RWTH Aachen University. JUEL-4264.

[26] Fromherz, P. and Stett, A. (August 1995) Silicon-neuron junction - capacitive stimulation of an individual neuron on a silicon chip. *Physical Review Letters*, 75 (8), 1670–1673.

[27] Ulbrich, M. H. and Fromherz, P. (October 2005) Opening of K+ channels by capacitive stimulation from silicon chip. *Applied Physics A*, 81 (5), 887–891.

[28] Schoen, I. and Fromherz, P. (November 2005) Activation of Na+ channels in cell membrane by capacitive stimulation with silicon chip. *Applied Physics Letters*, 87 (19), 193901.

[29] Schoen, I. and Fromherz, P. (February 2007) The mechanism of extracellular stimulation of nerve cells on an electrolyte-oxide-semiconductor capacitor. *Biophysical Journal*, 92 (3), 1096–1111.

[30] Schoen, I. and Fromherz, P. (2008) Extracellular stimulation of mammalian neurons through repetitive activation of Na+ channels by weak capacitive currents on a silicon chip. *Journal of Neurophysiology*, 100 (1), 346–357.

[31] Meyburg, S. (2005) *Transistor Arrays for the Direct Interfacing with Electrogenic Cells*. Ph.D. thesis, RWTH Aachen University.

[32] Pine, J. (1980) Recording action-potentials from cultured neurons with extracellular micro-circuit electrodes. *Journal of Neuroscience Methods*, 2 (1), 19–31.

[33] Regehr, W. G., Pine, J., and Rutledge, D. B. (December 1988) A long-term in vitro silicon-based microelectrode-neuron connection. *IEEE Transactions on Biomedical Engineering*, 35 (12), 1023–1032.

[34] Jimbo, Y. and Kawana, A. (December 1992) Electrical-stimulation and recording from cultured neurons using a planar electrode array. *Bioelectrochemistry and Bioenergetics*, 29 (2), 193–204.

[35] Gross, G. W., Rhoades, B. K., Reust, D. L., and Schwalm, F. U. (November 1993) Stimulation of monolayer networks in culture through thin-film indium-tin oxide recording electrodes. *Journal of Neuroscience Methods*, 50 (2), 131–143.

[36] Maher, M. P., Pine, J., Wright, J., and Tai, Y. C. (February 1999) The neurochip: a new multielectrode device for stimulating and recording from cultured neurons. *Journal of Neuroscience Methods*, 87 (1), 45–56.

[37] Wagenaar, D. A., Madhavan, R., Pine, J., and Potter, S. M. (January 2005) Controlling bursting in cortical cultures with closed-loop multi-electrode stimulation. *Journal of Neuroscience*, 25 (3), 680–688.

[38] Jun, S. B., Hynd, M. R., Dowell-Mesfin, N., Smith, K. L., Turner, J. N., Shain, W., and Kim, S. J. (March 2007) Low-density neuronal networks cultured using patterned poly-l-lysine on microelectrode arrays. *Journal of Neuroscience Methods*, 160 (2), 317–326.

[39] Novak, J. L. and Wheeler, B. C. (March 1988) Multisite hippocampal slice recording and stimulation using a 32 element microelectrode array. *Journal of Neuroscience Methods*, 23 (2), 149–159.

[40] Egert, U., Schlosshauer, B., Fennrich, S., Nisch, W., Fejtl, M., Knott, T., Muller, T., and Hammerle, H. (June 1998) A novel organotypic long-term culture of the rat hippocampus on substrate-integrated multielectrode arrays. *Brain Research Protocols*, 2 (4), 229–242.

[41] Heuschkel, M. O., Fejtl, M., Raggenbass, M., Bertrand, D., and Renaud, P. (March 2002) A three-dimensional multi-electrode array for multi-site stimulation and recording in acute brain slices. *Journal of Neuroscience Methods*, 114 (2), 135–148.

[42] Gawad, S., Giugliano, M., Heuschkel, M., Wessling, B., Markram, H., Schnakenberg, U., Renaud, P., and Morgan, H. (2009) Substrate arrays of iridium oxide microelectrodes for in vitro neuronal interfacing. *Frontiers in Neuroengineering*, 2, 1.

[43] Stett, A., Barth, W., Weiss, S., Haemmerle, H., and Zrenner, E. (2000) Electrical multisite stimulation of the isolated chicken retina. *Vision Research*, 40 (13), 1785–1795.

[44] Grumet, A. E., Wyatt, J. L., and Rizzo, J. F. (August 2000) Multi-electrode stimulation and recording in the isolated retina. *Journal of Neuroscience Methods*, 101 (1), 31–42.

[45] Heer, F., Hafizovic, S., Franks, W., Blau, A., Ziegler, C., and Hierlemann, A. (July 2006) CMOS microelectrode array for bidirectional interaction with neuronal networks. *IEEE Journal of Solid-State Circuits*, 41 (7), 1620–1629.

[46] Heer, F., Hafizovic, S., Ugniwenko, T., Frey, U., Franks, W., Perriard, E., Perriard, J. C., Blau, A., Ziegler, C., and Hierlemann, A. (May 2007) Single-chip microelectronic system to interface with living cells. *Biosensors & Bioelectronics*, 22 (11), 2546–2553.

[47] Blum, R. A., Ross, J. D., Brown, E. A., and DeWeerth, S. P. (December 2007) An integrated system for simultaneous, multichannel neuronal stimulation and recording. *IEEE Transactions on Circuits and Systems I: Regular Papers*, 54 (12), 2608–2618.

[48] Wang, K., Fishman, H. A., Dai, H., and Harris, J. S. (September 2006) Neural stimulation with a carbon nanotube microelectrode array. *Nano Letters*, 6 (9), 2043–2048.

[49] Shein, M., Greenbaum, A., Gabay, T., Sorkin, R., David-Pur, M., Ben-Jacob, E., and Hanein, Y. (April 2009) Engineered neuronal circuits shaped and interfaced with carbon nanotube microelectrode arrays. *Biomedical Microdevices*, 11 (2), 495–501.

[50] Gabriel, G., Gómez, R., Bongard, M., Benito, N., Fernández, E., and Villa, R. (March 2009) Easily made single-walled carbon nanotube surface microelectrodes for neuronal applications. *Biosensors & Bioelectronics*, 24 (7), 1942–1948.

[51] Ludwig, K. A., Uram, J. D., Yang, J., Martin, D. C., and Kipke, D. R. (March 2006) Chronic neural recordings using silicon microelectrode arrays electrochemically deposited with a poly(3,4-ethylenedioxythiophene) (PEDOT) film. *Journal of Neural Engineering*, 3 (1), 59–70.

[52] Wilks, S. J., Richardson-Burn, S. M., Hendricks, J. L., Martin, D. C., and Otto, K. J. (2009) Poly(3,4-ethylene dioxythiophene) (PEDOT) as a microneural interface material for electrostimulation. *Frontiers in Neuroengineering*, 2, 7.

[53] Eytan, D., Brenner, N., and Marom, S. (October 2003) Selective adaptation in networks of cortical neurons. *Journal of Neuroscience*, 23 (28), 9349–9356.

[54] Wagenaar, D. A., Pine, J., and Potter, S. M. (September 2004) Effective parameters for stimulation of dissociated cultures using multi-electrode arrays. *Journal of Neuroscience Methods*, 138 (1-2), 27–37.

[55] Rizzo, J. F., Wyatt, J., Loewenstein, J., Kelly, S., and Shire, D. (December 2003) Methods and perceptual thresholds for short-term electrical stimulation of human retina with microelectrode arrays. *Investigative Ophthalmology & Visual Science*, 44 (12), 5355–5361.

[56] Cogan, S. F., Ehrlich, J., Plante, T. D., Smirnov, A., Shire, D. B., Gingerich, M., and Rizzo, J. F. (May 2009) Sputtered iridium oxide films for neural stimulation electrodes. *Journal of Biomedical Materials Research Part B: Applied Biomaterials*, 89B (2), 353–361.

[57] Weiland, J. D., Anderson, D. J., and Humayun, M. S. (December 2002) In vitro electrical properties for iridium oxide versus titanium nitride stimulating electrodes. *IEEE Transactions on Biomedical Engineering*, 49 (12), 1574–1579.

[58] Taketani, M. and Baudry, M. (2006) *Advances in Network Electrophysiology Using Multi-Electrode Arrays*. Springer Verlag.

[59] Shepherd, R. K. and Javel, E. (June 1997) Electrical stimulation of the auditory nerve. I. Correlation of physiological responses with cochlear status. *Hearing Research*, 108 (1-2), 112–144.

[60] McCreery, D. B. (August 2008) Cochlear nucleus auditory prostheses. *Hearing Research*, 242 (1-2), 64–73.

[61] Weiland, J. D., Liu, W. T., and Humayun, M. S. (2005) Retinal prosthesis. *Annual Review of Biomedical Engineering*, 7, 361–401.

[62] Wichmann, T. and Delong, M. R. (October 2006) Deep brain stimulation for neurologic and neuropsychiatric disorders. *Neuron*, 52 (1), 197–204.

[63] Perlmutter, J. S. and Mink, J. W. (2006) Deep brain stimulation. *Annual Review of Neuroscience*, 29, 229–257.

[64] Alberts, B., Johnson, A., Lewis, J., Raff, M., Roberts, K., and Walter, P. (2004) *Molekularbiologie der Zelle*. Wiley-VCH, 4th edition.

[65] Campbell, N. A. and Reece, J. B. (2005) Nervous systems. In *Biology*, book chapter 48. Benjamin Cummings, 7th edition, 1012–1043.

[66] Klinke, R. and Silbernagl, S. (2001) *Lehrbuch der Physiologie*. Thieme, 3rd edition.

[67] Adam, G., Läuger, P., and Stark, G. (2003) Biologische Membranen. In *Physikalische Chemie und Biophysik*, book chapter 9. Springer Verlag, 3rd edition, 288–357.

[68] Hamill, O. P., Marty, A., Neher, E., Sakmann, B., and Sigworth, F. J. (1981) Improved patch-clamp techniques for high-resolution current recording from cells and cell-free membrane patches. *Pfluegers Archiv / European Journal of Physiology*, 391 (2), 85–100.

[69] Numberger, M. and Draguhn, A. (1996) *Patch-Clamp Technik*. Spektrum Akademischer Verlag.

[70] Maertz, W. H., Adams, S. V., Chung, S. C., Figl, T., and Verdnik, D. J. (2007) *The Axon Guide - A Guide to Electrophysiology & Biophysics Laboratory Techniques*. MDS Analytical Technologies, 3rd edition.

[71] von Helmholtz, H. L. F. (1879) Studie über elektrische Grenzschichten. *Annalen der Physik*, 7, 337–382.

[72] Gouy, G. J. (1910) Sur la constitution de la charge électrique à la surface d'un électrolyte. *Journal de Physique Théorique et Appliquée*, 9, 457–468.

[73] Chapman, D. L. (1913) A contribution to the theory of electrocapillarity. *Philosophical Magazine*, 25 (148), 475–481.

[74] Hamann, C. H., Hamnett, A., and Vielstich, W. (1998) *Electrochemistry*. Wiley-VCH, 2nd edition.

[75] Stern, O. (1924) Zur Theorie der elektrolytischen Doppelschicht. *Zeitschrift für Elektrochemie und Angewandte Physikalische Chemie*, 30, 508–516.

[76] Bard, A. J. and Faulkner, L. R. (2001) *Electrochemical Methods: Fundamentals and Applications*. Wiley, 2nd edition.

[77] Bockris, J. O., Reddy, A. K. N., and Gamboa-Aldeco, M. E. (2000) The electrified interface. In *Modern Electrochemistry*, 2A, book chapter 6. Kluwer Academic, 2nd edition, 771–1034.

[78] Bard, A. J., Stratmann, M., and Unwin, P. R. (2003) *Instrumentation and Electroanalytical Chemistry*, volume 3 of *Encyclopedia of Electrochemistry*. Wiley-VCH, 1st edition.

[79] Yates, D. E., Levine, S., and Healy, T. W. (1974) Site-binding model of electrical double-layer at oxide-water interface. *Journal of the Chemical Society, Faraday Transactions 1*, 70, 1807–1818.

[80] Braun, D. and Fromherz, P. (1998) Fluorescence interferometry of neuronal cell adhesion on microstructured silicon. *Physical Review Letters*, 81 (23), 5241–5244.

[81] Engelhardt, S. (2007) *Characterization of the Cell-Sensor Contact with Total Internal Reflection Fluorescence Microscopy*. Diploma thesis, RWTH Aachen University. JUEL-4255.

[82] Wrobel, G., Höller, M., Ingebrandt, S., Dieluweit, S., Sommerhage, F., Bochem, H. P., and Offenhäusser, A. (February 2008) Transmission electron microscopy study of the cell-sensor interface. *Journal of The Royal Society Interface*, 5 (19), 213–222.

[83] Sommerhage, F., Helpenstein, R., Rauf, A., Wrobel, G., Offenhäusser, A., and Ingebrandt, S. (October 2008) Membrane allocation profiling: a method to characterize three-dimensional cell shape and attachment based on surface reconstruction. *Biomaterials*, 29 (29), 3927–3935.

[84] Schäfer, S. (2008) *Electrical Characterization of the Cell-Sensor Adhesion with Transistor Transfer Function Measurements*. Diploma thesis, University Köln. JUEL-4261.

[85] Dufaux, T. (2008) *Design and Development of Amplifier Electronics for Silicon-Nanowire Biosensors*. Diploma thesis, RWTH Aachen Köln. JUEL-4269.

[86] Schäfer, S., Eick, S., Hofmann, B., Dufaux, T., Stockmann, R., Wrobel, G., Offenhäusser, A., and Ingebrandt, S. (January 2009) Time-dependent observation of individual cellular binding events to field-effect transistors. *Biosensors & Bioelectronics*, 24 (5), 1201–1208.

[87] Krause, G., Lehmann, S., Lehmann, M., Freund, I., Schreiber, E., and Baumann, W. (2006) Measurement of electrical activity of long-term mammalian neuronal networks on semiconductor neurosensor chips and comparison with conventional microelectrode arrays. *Biosensors & Bioelectronics*, 21 (7), 1272–1282.

[88] Hutzler, M., Lambacher, A., Eversmann, B., Jenkner, M., Thewes, R., and Fromherz, P. (September 2006) High-resolution multitransistor array recording of electrical field potentials in cultured brain slices. *Journal of Neurophysiology*, 96 (3), 1638–1645.

[89] Offenhäusser, A., Rühe, J., and Knoll, W. (1995) Neuronal cells cultured on modified microelectronic device surfaces. *Journal of Vacuum Science & Technology A - Vacuum Surfaces And Films*, 13 (5), 2606–2612.

[90] Cohen, A., Spira, M. E., Yitshaik, S., Borghs, G., Shwartzglass, O., and Shappir, J. (2004) Depletion type floating gate p-channel MOS transistor for recording action potentials generated by cultured neurons. *Biosensors & Bioelectronics*, 19 (12), 1703.

[91] Meyburg, S., Stockmann, R., Moers, J., Offenhausser, A., and Ingebrandt, S. (December 2007) Advanced CMOS process for floating gate field-effect transistors in bioelectronic applications. *Sensors and Actuators, B: Chemical*, 128 (1), 208–217.

[92] Regehr, W. G., Pine, J., Cohan, C. S., Mischke, M. D., and Tank, D. W. (1989) Sealing cultured invertebrate neurons to embedded dish electrodes facilitates long-term stimulation and recording. *Journal of Neuroscience Methods*, 30 (2), 91–106.

[93] Ingebrandt, S., Yeung, C. K., Krause, M., and Offenhäusser, A. (2005) Neuron-transistor coupling: Interpretation of individual extracellular recorded signals. *European Biophysics Journal*, 34 (2), 144–154.

[94] Weis, R., Müller, B., and Fromherz, P. (1996) Neuron adhesion on a silicon chip probed by an array of field-effect transistors. *Physical Review Letters*, 76 (2), 327–330.

[95] Brittinger, M. and Fromherz, P. (2005) Field-effect transistor with recombinant potassium channels: Fast and slow response by electrical and chemical interactions. *Applied Physics A*, 81 (3), 439–447.

[96] Wrobel, G., Seifert, R., Ingebrandt, S., Enderlein, J., Ecken, H., Baumann, A., Kaupp, U. B., and Offenhäusser, A. (2005) Cell-transistor coupling: Investigation of potassium currents recorded with p- and n-channel FETs. *Biophysical Journal*, 89 (5), 3628–3638.

[97] Pabst, M., Wrobel, G., Ingebrandt, S., Sommerhage, F., and Offenhäusser, A. (September 2007) Solution of the poisson-nernst-planck equations in the cell-substrate interface. *European Physical Journal E: Soft Matter*, 24 (1), 1–8.

[98] Abe, H., Esashi, M., and Matsuo, T. (1979) ISFETs using inorganic gate thin-films. *IEEE Transactions on Electron Devices*, 26 (12), 1939–1944.

[99] Wallrapp, F. and Fromherz, P. (June 2006) TiO2 and HfO2 in electrolyte-oxide-silicon configuration for applications in bioelectronics. *Journal of Applied Physics*, 99 (11), 114103.

[100] Jenkner, M., Müller, B., and Fromherz, P. (March 2001) Interfacing a silicon chip to pairs of snail neurons connected by electrical synapses. *Biological Cybernetics*, 84 (4), 239–249.

[101] Brummer, S. B., Robblee, L. S., and Hambrecht, F. T. (June 1983) Criteria for selecting electrodes for electrical-stimulation - theoretical and practical considerations. *Annals of the New York Academy of Sciences*, 405, 159–171.

[102] Huang, C. Q., Carter, P. M., and Shepherd, R. K. (September 2001) Stimulus induced pH changes in cochlear implants: an in vitro and in vivo study. *Annals of Biomedical Engineering*, 29 (9), 791–802.

[103] Harnack, D., Winter, C., Meissner, W., Reum, T., Kupsch, A., and Morgenstern, R. (September 2004) The effects of electrode material, charge density

and stimulation duration on the safety of high-frequency stimulation of the subthalamic nucleus in rats. *Journal of Neuroscience Methods*, 138 (1-2), 207–216.

[104] Merrill, D. R., Bikson, M., and Jefferys, J. G. R. (February 2005) Electrical stimulation of excitable tissue: design of efficacious and safe protocols. *Journal of Neuroscience Methods*, 141 (2), 171–198.

[105] Cogan, S. F. (2008) Neural stimulation and recording electrodes. *Annual Review of Biomedical Engineering*, 10, 275–309.

[106] Schindler, M., Kim, S. K., Hwang, C. S., Schindler, C., Offenhäusser, A., and Ingebrandt, S. (January 2008) Novel post-process for the passivation of a CMOS biosensor. *Physica Status Solidi RRL*, 2 (1), 4–6.

[107] Jimbo, Y., Kasai, N., Torimitsu, K., Tateno, T., and Robinson, H. P. C. (February 2003) A system for MEA-based multisite stimulation. *IEEE Transactions on Biomedical Engineering*, 50 (2), 241–248.

[108] Robblee, L. S., Lefko, J. L., and Brummer, S. B. (1983) Activated Ir - an electrode suitable for reversible charge injection in saline solution. *Journal of the Electrochemical Society*, 130 (3), 731–733.

[109] Aurian-Blajeni, B., Beebe, X., Rauh, R. D., and Rose, T. L. (June 1989) Impedance of hydrated iridium oxide electrodes. *Electrochimica Acta*, 34 (6), 795–802. ISSN 0013-4686.

[110] Lee, I. S., Whang, C. N., Park, J. C., Lee, D. H., and Seo, W. S. (June 2003) Biocompatibility and charge injection property of iridium film formed by ion beam assisted deposition. *Biomaterials*, 24 (13), 2225–2231.

[111] Schiavone, L. M., Dautremontsmith, W. C., Beni, G., and Shay, J. L. (1979) Electrochromic iridium oxide-films prepared by reactive sputtering. *Applied Physics Letters*, 35 (10), 823–825.

[112] Klein, J. D., Clauson, S. L., and Cogan, S. F. (September 1989) Morphology and charge capacity of sputtered iridium oxide-films. *Journal of Vacuum Science & Technology A - Vacuum Surfaces And Films*, 7 (5), 3043–3047.

[113] Aurian-Blajeni, B., Boucher, M. M., Kimball, A. G., and Robblee, L. S. (March 1989) Physicochemical characterization of sputtered iridium oxide. *Journal of Materials Research*, 4 (2), 440–446.

[114] Slavcheva, E., Vitushinsky, R., Mokwa, W., and Schnakenberg, U. (2004) Sputtered iridium oxide films as charge injection material for functional electrostimulation. *Journal of the Electrochemical Society*, 151 (7), E226–E237.

[115] Wessling, B., Mokwa, W., and Schnakenberg, U. (2006) RF-sputtering of iridium oxide to be used as stimulation material in functional medical implants. *Journal of Micromechanics and Microengineering*, 16 (6), 142–148.

[116] Slavcheva, E., Schnakenberg, U., and Mokwa, W. (December 2006) Deposition of sputtered iridium oxide - influence of oxygen flow in the reactor on the film properties. *Applied Surface Science*, 253 (4), 1964–1969.

[117] Oppenheim, A. V., Schafer, R. W., and Buck, J. R. (1998) *Discrete-Time Signal Processing*. Prentice-Hall, 2nd edition.

[118] Ohm, J.-R. and Lüke, H. D. (2007) *Signalübertragung: Grundlagen der digitalen und analogen Nachrichtenübertragungssysteme*. Springer Verlag, 10th edition.

[119] Kammeyer, K.-D. and Kroschel, K. (2006) *Digitale Signalverarbeitung. Filterung und Spektralanalyse mit MATLAB-Übungen*. Vieweg+Teubner, 6th edition.

[120] Buitenweg, J. R., Rutten, W. L. C., and Marani, E. (December 2002) Extracellular stimulation window explained by a geometry-based model of the neuron-electrode contact. *IEEE Transactions on Biomedical Engineering*, 49 (12 Pt 2), 1591–1599.

[121] Buitenweg, J. R., Rutten, W. L. C., and Marani, E. (April 2003) Geometry-based finite-element modeling of the electrical contact between a cultured neuron and a microelectrode. *IEEE Transactions on Biomedical Engineering*, 50 (4), 501–509.

[122] Ecken, H., Ingebrandt, S., Krause, M., Richter, D., Hara, M., and Offenhäusser, A. (September 2003) 64-channel extended gate electrode arrays for extracellular signal recording. *Electrochimica Acta*, 48 (20-22), 3355–3362.

[123] Wallys, J. (2007) *Stimulation of Individual Electrogenic Cells with Micro-Scale SIROF Electrodes*. Diploma thesis, RWTH Aachen University.

[124] Horch, K. W. and Dhillon, G. S. (2004) *Neuroprosthetics - Theory and Practice*, volume 2 of *Series On Bioengineering & Biomedical Engineering*. World Scientific.

[125] Weiland, J. D. and Anderson, D. J. (July 2000) Chronic neural stimulation with thin-film, iridium oxide electrodes. *IEEE Transactions on Biomedical Engineering*, 47 (7), 911–918.

[126] Wessling, B., Mokwa, W., and Schnakenberg, U. (2008) Sputtered Ir films evaluated for electrochemical performance - I. Experimental results. *Journal of the Electrochemical Society*, 155 (5), 61–65.

[127] Thiébaud, P., de Rooij, N. F., Koudelka-Hep, M., and Stoppini, L. (November 1997) Microelectrode arrays for electrophysiological monitoring of hippocampal organotypic slice cultures. *IEEE Transactions on Biomedical Engineering*, 44 (11), 1159–1163.

[128] Wessling, B., van Ooyen, A., Mokwa, W., and Schnakenberg, U. (2006) Iridium sputtered at varying pressures and target-substrate-distances evaluated for use as stimulation electrode material. In *2006 28th Annual International Conference of the IEEE Engineering in Medicine and Biology Society, Vols 1-15*. 474–477. 28th Annual International Conference of the IEEE-Engineering-in-Medicine-and-Biology-Society, New York, NY, AUG 30-SEP 03, 2006.

[129] Krause, M., Ingebrandt, S., Richter, D., Denyer, M., Scholl, M., Sprössler, C., and Offenhäusser, A. (November 2000) Extended gate electrode arrays for extracellular signal recordings. *Sensors and Actuators, B: Chemical*, 70 (1-3), 101–107.

[130] Wrobel, G., Zhang, Y., Krause, H.-J., Wolters, N., Sommerhage, F., Offenhäusser, A., and Ingebrandt, S. (January 2007) Influence of the first amplifier stage in MEA systems on extracellular signal shapes. *Biosensors & Bioelectronics*, 22 (6), 1092–1096.

[131] Kotman, N. (2008) *Bidirectional Coupling of Neurons with a Microchip Integrating Microelectrodes and Field-Effect Transistors*. Diploma thesis, University Kassel. JUEL-4285.

[132] Meyers, J. P., Doyle, M., Darling, R. M., and Newman, J. (August 2000) The impedance response of a porous electrode composed of intercalation particles. *Journal of the Electrochemical Society*, 147 (8), 2930–2940.

[133] La Mantia, F., Vetter, J., and Novak, P. (May 2008) Impedance spectroscopy on porous materials: A general model and application to graphite electrodes of lithium-ion batteries. *Electrochimica Acta*, 53 (12), 4109–4121.

[134] van Ooyen, A. (2009) Personal communication. Institute of Materials in Electrical Engineering 1 - Micro Structure Integration (IWE1), RWTH Aachen University, Aachen, Germany.

[135] Blau, A., Ziegler, C., Heyer, M., Endres, F., Schwitzgebel, G., Matthies, T., Stieglitz, T., Meyer, J. U., and Gopel, W. (1997) Characterization and optimization of microelectrode arrays for in vivo nerve signal recording and stimulation. *Biosensors & Bioelectronics*, 12 (9-10), 883–892.

[136] Stett, A., Muller, B., and Fromherz, P. (February 1997) Two-way silicon-neuron interface by electrical induction. *Physical Review E: Statistical, Nonlinear, and Soft Matter Physics*, 55 (2), 1779–1782.

[137] Eick, S., Kotman, N., Prömpers, M., Van Ooyen, A., Schnakenberg, U., Ingebrandt, S., and Offenhäusser, A. (September 2008) Combination of field-effect transistors and microelectrodes for the bi-directional coupling of neuronal cells. In *MME 2008 - 19th MicroMechanics Europe Workshop - Technical Digest.* 389–392. ISBN: 978-3-00-025529-8.

[138] Sprössler, C., Richter, D., Denyer, M., and Offenhäusser, A. (September 1998) Long-term recording system based on field-effect transistor arrays for monitoring electrogenic cells in culture. *Biosensors & Bioelectronics*, 13 (6), 613–618.

[139] Ingebrandt, S., Yeung, C. K., Krause, M., and Offenhäusser, A. (September 2001) Cardiomyocyte-transistor-hybrids for sensor application. *Biosensors & Bioelectronics*, 16 (7-8), 565–570.

[140] GhoshMoulick, R., Vu, X. T., Gilles, S., Mayer, D., Offenhäusser, A., and Ingebrandt, S. (March 2009) Impedimetric detection of covalently attached biomolecules on field-effect transistors. *Physica Status Solidi A*, 206 (3), 417–425.

[141] Ingebrandt, S., Han, Y., Nakamura, F., Poghossian, A., Schöning, M. J., and Offenhäusser, A. (June 2007) Label-free detection of single nucleotide polymorphisms utilizing the differential transfer function of field-effect transistors. *Biosensors & Bioelectronics*, 22 (12), 2834–2840.

[142] Ingebrandt, S., Han, Y. H., Sakkari, M. R., Stockmann, R., Belinskyy, O., and Offenhäusser, A. (2005) Electronic detection of nucleic acid molecules with a field-effect transistor. *Semiconductor Materials for Sensing*, 828, 307–312.

[143] Kovacs, G. T. A. (June 2003) Electronic sensors with living cellular components. *Proceedings of the IEEE*, 91 (6), 915–929.

[144] Breckenridge, L. J., Wilson, R. J., Connolly, P., Curtis, A. S., Dow, J. A., Blackshaw, S. E., and Wilkinson, C. D. (October 1995) Advantages of

using microfabricated extracellular electrodes for in vitro neuronal recording. *Journal of Neuroscience Research*, 42 (2), 266–276.

[145] Tsong, T. Y. (August 1991) Electroporation of cell membranes. *Biophysical Journal*, 60 (2), 297–306.

[146] Zimmermann, U. and Neil, G. (1996) *Electromanipulation of Cells*. CRC Press.

[147] Tieleman, D. P. (July 2004) The molecular basis of electroporation. *BMC Biochemistry*, 5, 10.

[148] Ranck, J. B. (1975) Which elements are excited in electrical-stimulation of mammalian central nervous-system - review. *Brain Research*, 98 (3), 417–440.

[149] Rattay, F. (March 1999) The basic mechanism for the electrical stimulation of the nervous system. *Neuroscience*, 89 (2), 335–346.

[150] McIntyre, C. C. and Grill, W. M. (February 1999) Excitation of central nervous system neurons by nonuniform electric fields. *Biophysical Journal*, 76 (2), 878–888.

[151] McIntyre, C. C. and Grill, W. M. (October 2002) Extracellular stimulation of central neurons: Influence of stimulus waveform and frequency on neuronal output. *Journal of Neurophysiology*, 88 (4), 1592–1604.

[152] Magistretti, J. and Alonso, A. (October 1999) Biophysical properties and slow voltage-dependent inactivation of a sustained sodium current in entorhinal cortex layer-II principal neurons - a whole-cell and single-channel study. *Journal of General Physiology*, 114 (4), 491–509.

[153] Thio, L. L. and Yamada, K. A. (June 2004) Differential presynaptic modulation of excitatory and inhibitory autaptic currents in cultured hippocampal neurons. *Brain Research*, 1012 (1-2), 22–28.

[154] Vogt, A. K., Lauer, L., Knoll, W., and Offenhausser, A. (September 2003) Micropatterned substrates for the growth of functional neuronal networks of defined geometry. *Biotechnology Progress*, 19 (5), 1562–1568.

[155] Gildemeister, M. (April 1944) Untersuchungen über die Wirkung der Mittelfrequenzströme auf den Menschen. *Pfluegers Archiv / European Journal of Physiology*, 247 (4), 366–404.

[156] Bromm, B. and Lullies, H. (December 1966) Über den Mechanismus der Reizwirkung mittelfrequenter Wechselströme auf die Nervenmembran. *Pfluegers Archiv / European Journal of Physiology*, 289 (4), 215–226.

[157] Bromm, B. (September 1968) Die Natrium-Gleichrichtung der unterschwellig erregten Membran in der quantitativen Formulierung der Ionentheorie. *Pfluegers Archiv / European Journal of Physiology*, 302 (3), 233–244.

[158] Graham, F. L., Smiley, J., Russell, W. C., and Nairn, R. (July 1977) Characteristics of a human cell line transformed by DNA from human adenovirus type 5. *Journal of General Virology*, 36 (1), 59–74.

[159] Zhu, G., Zhang, Y., Xu, H., and Jiang, C. (June 1998) Identification of endogenous outward currents in the human embryonic kidney (HEK 293) cell line. *Journal of Neuroscience Methods*, 81 (1-2), 73–83.

[160] Trimmer, J. S., Cooperman, S. S., Tomiko, S. A., Zhou, J. Y., Crean, S. M., Boyle, M. B., Kallen, R. G., Sheng, Z. H., Barchi, R. L., Sigworth, F. J., Goodman, R. H., Agnew, W. S., and Mandel, G. (July 1989) Primary structure and functional expression of a mammalian skeletal-muscle sodium-channel. *Neuron*, 3 (1), 33–49.

[161] Chen, H. J., Gordon, D., and Heinemann, S. H. (February 2000) Modulation of cloned skeletal muscle sodium channels by the scorpion toxins Lqh II, Lqh III, and LqhαIT. *Pfluegers Archiv / European Journal of Physiology*, 439 (4), 423–432.

[162] Baranauskas, G. and Martina, M. (January 2006) Sodium currents activate without a hodgkin-and-huxley-type delay in central mammalian neurons. *Journal of Neuroscience*, 26 (2), 671–684.

[163] Moschytz, G. S. (August 1999) Low-sensitivity, low-power active-RC allpole filters using impedance tapering. *IEEE Trans. Circuits Syst. Express Briefs*, 46 (8), 1009–1026.

[164] Tietze, U. and Schenk, C. (2008) *Electronic Circuits - Handbook for Design and Application*. Springer Verlag, 2nd edition.

[165] Fromherz, P. and Voelker, M. (2009) Comment on "detection, stimulation, and inhibition of neuronal signals with high-density nanowire transistor arrays". *Science*, 323 (5920), 1429b–.

[166] Timko, B. P., Patolsky, F., and Lieber, C. M. (2009) Response to comment on "detection, stimulation, and inhibition of neuronal signals with high-density nanowire transistor arrays". *Science*, 323 (5920), 1429c–.

[167] Claycomb, W. C., Lanson, N. A., Stallworth, B. S., Egeland, D. B., Delcarpio, J. B., Bahinski, A., and Izzo, N. J. (March 1998) HL-1 cells: A cardiac muscle cell line that contracts and retains phenotypic characteristics of the adult cardiomyocyte. *Proceedings of the National Academy of Sciences of the United States of America*, 95 (6), 2979–2984.

[168] Law, J. K. Y., Yeung, C. K., Hofmann, B., Ingebrandt, S., Rudd, J. A., Offenhäusser, A., and Chan, M. (February 2009) The use of microelectrode array (MEA) to study the protective effects of potassium channel openers on metabolically compromised HL-1 cardiomyocytes. *Physiological Measurement*, 30 (2), 155–167.

[169] Hofmann, B. (2009) Personal communication. Institute of Bio- and Nano Systems 2 - Bioelectronics (IBN-2), Forschungszentrum Jülich, GmbH, Jülich, Germany.

[170] Lau, J. H. (1995) *Flip Chip Technologies*. McGraw-Hill, 1st edition.

[171] Brewer, G. J., Torricelli, J. R., Evege, E. K., and Price, P. J. (August 1993) Optimized survival of hippocampal-neurons in B27-supplemented neurobasal, a new serum-free medium combination. *Journal of Neuroscience Research*, 35 (5), 567–576.

Abbreviations, Symbols, Constants

Abbreviations

A^-	negatively charged organic ion
AC	alternating current
ADC	analog-to-digital converter
AFM	atomic force microscopy
Ag/AgCl	silver/silver chloride
Al	aluminum
AM	attached membrane
AP	action potential
Ar	argon
ATP	adenosine triphosphate
Au	gold
BioMAS	bioelectronic multifunctional amplifier system
Ca^{2+}	calcium ion
$CaCl_2$	calcium chloride
CC	current-clamp
CHF_3	fluoroform
Cl^-	chloride ion
CNS	central nervous system
CMOS	complementary metal-oxide-semiconductor
CO_2	carbon dioxide
CS	covered stimulator
CV	cyclic voltammetry
D	drain
DAC	digital-to-analog converter
DAQ	data acquisition
DC	direct current
DDS	direct digital synthesis
DFT	discrete Fourier transform
DIC	differential interference contrast

DIV	days in vitro
DLL	dynamic link library
e^-	electron
E18	18 days gestation
ECM	extracellular matrix
EDTA	ethylenediaminetetraacetic acid
EGTA	ethyleneglycoltetraacetic acid
EIS	electrochemical impedance spectroscopy
FET	field-effect transistor
FG-FET	floating-gate field-effect transistor
FIB	focused ion beam
FM	free membrane
FS	free stimulator
G	gate
GBSS	Gey's Balanced Salt Solution
GUI	graphical user interface
H^+	hydrogen ion (proton)
H_3O^+	hydronium ion
H_3PO_4	phosphoric acid
HBSS	Hank's Balanced Salt Solution
HEK293	Human Embryonic Kidney 293
HF	hydrofluoric acid
I/O	input/output
iDFT	inverse discrete Fourier transform
IHL	inner Helmholtz layer
IMM	Institut für Mikrotechnik Mainz GmbH
Ir	iridium
IrO_x	iridium oxide
ISFET	ion sensitive field-effect transistor
ITO	indium tin oxide
IWE1	Institut für Werkstoffe der Elektrotechnik 1
K^+	potassium ion
KCl	potassium chloride
KH_2PO_4	monopotassium phosphate
KOH	potassium hydroxide
LED	light-emitting diode
LOCOS	local oxidation of silicon

LPCVD	low pressure chemical vapor deposition
LTI	linear time-invariant
MEA	multi-electrode array
MEM	minimal essential medium
Mg^{2+}	magnesium ion
$MgCl_2$	magnesium chloride
MOSFET	metal-oxide-semicondutor field-effect transistor
Na^+	sodium ion
Na_2HPO_4	disodium phosphate
NaCl	sodium chloride
$NaHCO_3$	sodium bicarbonate
NaOH	sodium hydroxide
NB	Neurobasal
NH4F	ammonium fluoride
NONONO	$Si_3N_4/SiO_2/Si_3N_4/SiO_2/Si_3N_4/SiO_2$
O_2	Oxygen
OG-FET	open-gate field-effect transistor
OH^-	hydroxide ion
OHL	outer Helmholtz layer
ONO	$SiO_2/Si_3N_4/SiO_2$
OP	operating point
OPA	operational amplifier
PBS	phosphate buffered saline
PC	personal computer
PCI	peripheral component interconnect
PCB	printed circuit board
PDL	poly-D-lysin
PECVD	plasma enhanced chemical vapor deposition
PLL	poly-L-lysin
PDMS	polydimethylsiloxane
Pt	platinum
RIE	reactive ion etching
S	source
SCSI	small computer system interface
SECW	safe electrochemical window
SEM	scanning electron microscope
SF_6	sulfur hexafluoride

Si_3N_4	silicon nitride
SiO_2	silicon oxide
SIROF	sputtered iridium oxide film
SNR	signal-to-noise ratio
Ti	titanium
TiN	titanium nitride
TTF	transistor transfer function
USB	universal serial bus
VC	voltage-clamp
vs. SSE	against the potential of a silver/silver chloride electrode
w.r.t.	with respect to open circuit potential
OCP	
µE	microelectrode

Formula Symbols

A_{AM}	area of attached cell membrane
A_{CS}	area of covered stimulator
A_{FM}	area of free cell membrane
A_{FS}	area of free stimulator
A_M	area of whole cell membrane
A_S	area of whole stimulator
C_{AM}	capacitance of attached cell membrane
C_{CS}	capacitance of covered stimulator
C_{DL}	double layer capacitance
c_{DL}	specific double layer capacitance
C_f	patch-clamp pipette capacitance
C_{FM}	capacitance of free cell membrane
C_{FS}	capacitance of free stimulator
C_S	capacitance of whole stimulator
c_S	specific capacitance of stimulator
C_G	Gouy capacitance
C_H	Helmholtz capacitance
C_M	capacitance of whole cell membrane
c_M	specific membrane capacitance
C_M^*	effective capacitance of cell membrane
C_{OX}	gate oxide capacitance
d	distance

E_0^i	equilibrium potential for ion species i
f_c	cutoff frequency
G_{CS}	conductance of covered stimulator
G_E	conductance of electrolyte solution (and bath electrode)
G_{FS}	conductance of free stimulator
G^i	membrane conductance for ion species i
g^i	specific membrane conductivity for ion species i
G_{FM}^i	attached membrane conductance for ion species i
G_{FM}^i	free membrane conductance for ion species i
G_J	junction conductance
g_M	summarized specific membrane conductivity for all ions
g_m	transconductance of a field-effect transistor
$\underline{H}$	frequency response of a system
$\underline{H}_{AM}$	frequency response for voltage drop at attached membrane
$\underline{H}_C$	frequency response for voltage drop at complete cell
$\underline{H}_E$	frequency response for voltage drop at electrolyte and bath electrode
$\underline{H}_{FM}$	frequency response for voltage drop at free membrane
$\underline{H}_{SC}$	frequency response for voltage drop at stimulator and cell
i_{DS}	drain-source current
$[i]_{in}$	concentration of ion species i inside a cell
i^{K+}	potassium current caused by sodium-potassium exchanger
i^{Na+}	sodium current caused by sodium-potassium exchanger
$[i]_{out}$	concentration of ion species i outside a cell
i_P/I_P	pipette current
j	imaginary unit
L_D	Debye length
n_0	bulk ion concentration
P^i	membrane permeability for ion species i
Q_{CSC}	charge storage capacity
q_{CSC}	specific charge storage capacity
R_{CS}	resistance of covered stimulator
R_E	resistance of electrolyte solution (and bath electrode)
R_{FB}	feedback resistor
R_{FS}	resistance of free stimulator
R_J	junction resistance
R_S	series resistance
T	absolute temperature

t	time
$v_{AM}/\underline{V}_{AM}$	voltage drop at attached membrane
v_B	bulk voltage
$\underline{V}_C$	voltage drop at complete cell impedance
v_{comp}	compensation voltage
v_{drain}	drain potential
v_{DS}	drain-source voltage
$v_E/\underline{V}_E$	electrolyte potential close to cell
v_{EC}	extracellular potential
$v_{FM}/\underline{V}_{FM}$	voltage drop at free membrane
v_{gate}	gate potential
v_{GS}	gate-source voltage
v_{IC}	intracellular potential
$v_{in}/\underline{V}_{in}$	input voltage of a circuit
v_J	junction potential
v_M	membrane potential or intracellular potential
$v_{out}/\underline{V}_{out}$	output voltage of a circuit
$v_P/\underline{V}_P$	pipette potential
v_{source}	source potential
$v_S/\underline{V}_S$	stimulator potential
V_S^0	amplitude of potential step at stimulator
$\underline{V}_{SC}$	voltage drop at impedance of subcircuit including stimulator and cell
$\underline{X}$	impedance
$\underline{X}_C$	impedance of complete cell
$\underline{X}_{CS}$	impedance of covered stimulator
$\underline{X}_E$	impedance of electrolyte solution and bath electrode
$\underline{X}_{FS}$	impedance of free stimulator
$\underline{X}_{SC}$	impedance of subcircuit including stimulator and cell
$\underline{Y}$	admittance
$\underline{Y}_{CS}$	admittance of covered stimulator
$\underline{Y}_E$	admittance of electrolyte solution and bath electrode
$\underline{Y}_{FS}$	admittance of free stimulator
$\underline{Y}_S$	admittance of whole stimulator
z^i	valence of ion species i
α	scaling parameter for ratio between attached and whole membrane area
β	scaling parameter for ratio between covered and whole stimulator area
ϵ	Heaviside step function

τ	time constant
Φ	potential
Φ_0	surface potential
φ	phase
ω	angular frequency

Constants

F	8.314472 $\mathrm{JK^{-1}mol^{-1}}$	Faraday constant
R	96485.3399 $\mathrm{Cmol^{-1}}$	gas constant

Author's List of Publications

Hofmann, B., Maybeck, V., **Eick, S.**, Meffert, S., Ingebrandt, S., Bamberg, E., and Offenhäusser, A. Combined light triggered cardiac pacemaker defibrillator. Submitted to *Proceedings of the National Academy of Sciences of the United States of America.*

Eick, S., Wallys, J., Hofmann, B., van Ooyen, A., Schnakenberg, U., Ingebrandt, S., and Offenhäusser, A. (November 2009) Iridium oxide microelectrode arrays for in-vitro stimulation of individual rat neurons from dissociated cultures. *Frontiers in Neuroengineering, 2, 16.*

Dankerl, M.*, **Eick, S.***, Hofmann, B.*, Hauf, M.*, Ingebrandt, S., Offenhäusser, A., Stutzmann, M., and Garrido, J. A. (September 2009) Diamond transistor array for extracellular recording from electrogenic cells. *Advanced Functional Materials, 19 (18), 2915 - 2923.* *These authors contributed equally to this work.

Schäfer, S., **Eick, S.**, Hofmann, B., Dufaux, T., Stockmann, R., Wrobel, G., Offenhäusser, A., and Ingebrandt, S. (January 2009) Time-dependent observation of individual cellular binding events to field-effect transistors. *Biosensors & Bioelectronics, 24 (5), 1201 - 1208.*

Eick, S., Kotman, N., Prömpers, M., Van Ooyen, A., Schnakenberg, U., Ingebrandt, S., and Offenhäusser, A. (September 2008) Combination of field-effect transistors and microelectrodes for the bi-directional coupling of neuronal cells. In *MME 2008 - 19th MicroMechanics Europe Workshop - Technical Digest.* 389 - 392. ISBN: 978-3-00-025529-8.

Eick, S., Wallys, J., Ingebrandt, S., Hofmann, B., van Ooyen, A., Schnakenberg, U., and Offenhäusser, A. (July 2008) Extracellular stimulation of individual rat cortical neurons with sputtered iridium oxide microelectrodes. In *Conference Proceedings of the 6th International Meeting on Substrate-Integrated Micro Electrode Arrays.* 159 - 160. ISBN: 3-938345-05-5

Danksagung

Zum Abschluss möchte ich mich bei den Personen bedanken, die zum erfolgreichen Gelingen meiner Arbeit beigetragen haben. Mein besonderer Dank gilt

- Prof. Dr. A. Offenhäusser für das Ermöglichen dieser Dissertation und die regelmäßige fachliche und moralische Unterstützung auf dem Weg zu ihrem erfolgreichen Abschluss. Danke für das Vertrauen in meine Person und die Ermutigung, meinen Horizont durch die interdisziplinäre Arbeit und die Zeit in Südkorea zu erweitern.
- Prof. Dr. W. Mokwa für die Übernahme der Betreuung und Korrektur meiner Arbeit im Fachbereich für Elektrotechnik und Informationstechnik der RWTH Aachen.
- Prof. Dr. S. Ingebrandt für die gute Betreuung als Gruppenleiter und zahlreichen Denkanstöße während der ersten beiden Jahre in Jülich und darüber hinaus aus der Ferne. Dank Dir konnte ich die Breite der Forschungsfelder in unserem Institut kennen lernen und mehr als einmal über den Tellerrand hinaus blicken.
- Dr. B. Wolfrum für die inoffizielle Übernahme meiner Betreuung im letzten Jahr, die beinahe unerschöpflichen Ansätze für Problemlösungen und die gründliche Korrektur meiner Arbeit. Deine gute Laune und deine Begeisterung für die Wissenschaft waren für mich immer wieder Motivation und Antrieb, meinen Weg weiter zu gehen.
- S. Bippus für die regelmäßige Unterstützung in der Überwindung der bürokratischen Hürden.
- M. Banzet und M. Prömpers für die zahlreichen arbeitsreichen Stunden im Reinraum bei der Prozessierung der Bauelemente und Chips.
- U. Schnakenberg und A. van Ooyen für die gute Zusammenarbeit im Rahmen des Mi-BeSAN Projekts und die ausgezeichneten Iridiumoxidschichten.
- D. Cassel für die zuverlässige und zügige Passivierung aller Chips in Zweibrücken und die stets freundliche Korrespondenz.
- E. Brauweiler-Reuters für die schönen REM-Aufnahmen.

- D. Eßer für die ausgezeichneten FIB Schnitte.

- B. Bruns, W. Hürttlen, D. Lomparski, R. Otto und N. Wolters für die hervorragende Arbeit bei der Entwicklung und Implementierung der zahlreichen Hard- und Softwarekomponenten des neuen Verstärkersystems. Ohne Euch wäre BioMAS nie realisiert worden.

- D. Strobl und seinem Team für die zahlreichen mechanischen Maßanfertigungen für diverse Anwendungen.

- W. Briell für die gute und schnelle Konstruktion für die TIRFM-Motorsteuerung.

- M. Dankerl, J. Garrido und M. Hauf für die erfolgreiche und unkomplizierte Zusammenarbeit im Rahmen des DREAMS Projekts und die schönen gemeinsamen Stunden bei den Projekttreffen und im Labor.

- K. Adamiak, J. F. Eschermann, S. Gilles, M. Hüske, E. Kätelhön, Dr. K. Michael, Dr. A. Reska, N. Sanetra, Dr. M. Schindler, F. Sommerhage, und G. Wrobel für die schöne und inspirierende Institutsatmosphäre. Ihr Sputtologen füllt die Wissenschaft mit Leben.

- T. Dufaux, S. Engelhardt, N. Kotman, S. Schäfer und J. Wallys für die gute und zuverlässige Arbeit als fleißige Labor-Elfen und Jung-Wissenschaftler. Eure Betreuung war immer fordernd und Lehrreich und machte vor allem viel Spaß.

- J. Brusius, M. Hitzbleck und X. T. Vu für die gemeinsame tägliche Stunde auf der Autobahn. Ob Comedyclub oder Selbsthilfegruppe - jede Minute mit euch war schön und wertvoll.

- V. Maybeck für die unbezahlbaren und arbeitsintensiven Stunden bei der Korrektur meiner Arbeit. Ich habe unsere gemeinsamen Gespräche über Sprachen, Arbeit and Everything sehr genossen und viel gelernt.

- R. Fricke für die unzähligen Arbeitsstunden in der Zellkultur und die vielen präparierten Nervenzellen. Vielen Dank auch, dass du immer ein offenes Ohr hast und da bist, wenn man Dich braucht.

- B. Hofmann für die vielen schönen, interessanten, abwechslungsreichen und manchmal auch therapeutischen Stunden im Büro, Labor und dem Rest der Welt. Erst warst Du mein Zwilling, dann wurdest Du zum Freund fürs Leben. Vielen Dank dafür, und dass Du in mir die Freude am Segeln wieder erweckt hast.

- meiner Familie und meinen Freunden für die fortwährende Unterstützung während der Zeit in Jülich, Aachen und all den Jahren vorher. Ihr habt immer an mich geglaubt und wart da, wenn ich Euch brauchte.

- meiner Sonja, die mein Halt und meine Konstante ist, und auf die ich mich immer verlassen kann. Vielen Dank, dass Du mich dasselbe für Dich sein lässt und wir gemeinsam in die Zukunft gehen.

Cleared the fog that was veiled around me
And blurred my sights
Suddenly, I'm no longer aching
To honor my plights

Rising moon and my skin is peeling
Past undone
Suddenly, I can't justify
What I had become

Mikael Åkerfeldt (Swedish musician, 1974-)
Lyrics of the song Atonement *from the album* Ghost Reveries *by* Opeth